2015

# Exploring novel anode materials for sodium-ion storage

Yunxiao Wang
*University of Wollongong*

UNIVERSITY OF WOLLONGONG

# Exploring Novel Anode Materials for Sodium-ion Storage

**This thesis is presented as part of the requirements for the Award of the Degree of**

**Doctor of Philosophy**

**from the**

**University of Wollongong**

**by**

**YUNXIAO WANG**
**B. Sc., M. Sc.**

**Institute for Superconducting and Electronic Materials**

**Faculty of Engineering**

**January 2015**

## CERTIFICATION

I, Yunxiao Wang, declare that this thesis, submitted in fulfilment of the requirements for the award of Doctor of Philosophy, in the Institute for Superconducting & Electronic Materials, Faculty of Engineering, University of Wollongong, is wholly my own work unless otherwise referenced or acknowledged. This document has not been submitted for qualifications at any other academic institution.

Yunxiao Wang

29/01/ 2015

**DEDICATION**

*To my family and friends, who stand by me all the time.*

## ACKNOWLEDGEMENTS

My thesis was undertaken with the support of all the people in the Institute for Superconducting and Electronic Materials (ISEM) at the University of Wollongong in Australia, the Korea Electronics Technology Institute (KETI) in Korea, and the Fudan University in China.

Firstly, I wish to express my deepest gratitude to my research supervisors, Professor Shi Xue Dou and Professor Hua Kun Liu, for their academic supervision and guidance, constant support and encouragement, and invaluable advice throughout my doctoral degree. I would like to express my utmost appreciation to my co-supervisor, Dr. Shu Lei Chou, for his professional suggestions and instruction, including the design of experiments and imparting new research techniques. He spent large amounts of time on mentoring me, helping me to build my self-confidence and future orientation as well. I am deeply grateful to Dr. Minsik Park for his support and guidance in my research when I was an exchange student at KETI in Korea. I also wish to thank Professor Dong Yuan Zhao for his supervision and guidance when I was a visiting student at his laboratory in Fudan University.

Furthermore, I wish to express my appreciation to Professor Jia Zhao Wang, for her suggestion and guidance during group meetings. I am grateful to Professor Jung Ho Kim, who spent his valuable time on TEM observations of my samples and manuscript revision. My deep gratitude goes to my co-workers, Dr. Jian Ping Yang, Dr. Kuok Hua Seng and Ms. Young Gun Kim, who have been very helpful, sharing

their experience and knowledge. I would also like to thank Dr. Tania Silver for her critical reading of my manuscripts and thesis.

I would also like to thank the staff members and technicians at ISEM for their kind assistance, including Dr. Germanas Peleckis (XRD), Dr. David Wexler (TEM), Dr. Kosta Konstantinov (BET, TGA/DTA), Mr. Darren Attard (SEM), Mr. Tony Romeo (SEM, EDS), Mrs. Crystal Login, Mrs. Narelle Badger, Mrs. Joanne George (OH&S), Mr. Robert Morgan, Mr. Mathew Davis, and Mrs. Candace Gabelish.

Moreover, many thanks to Dr. Jian Tie Xu, Mr. Zhi Jia Zhang, Ms. Yi Shi, Ms. Xin Liang, Mr. Jun Wang, Mr. Yue De Pan, Ms. Wei Jie Li, Ms. Xuan Wen Gao, Ms. Dan Li, Ms. Li Li, Ms. Sha Li,Ms. Kathrin Bogusz, Ms. Jung Woo Park, Dr. Jae Gun Kim, Dr. Jin Xiu Wang, and other students and staff at ISEM, KETI, and Fudan University, for their kind help and valuable advice.

Finally, I would like to express my deep appreciation and love to my parents, brother and sisters, who are standing by me and encouraging me to move forward all the time.

## ABSTRACT

Lithium-ion batteries (LIBs) have been widely used since the early 1990s as the power sources for the small electronic devices that are ubiquitous in our daily lives, due to their high energy densities. With the increasing demand for Li commodity chemicals and geographically-constrained Li mineral reserves, however, LIBs are confronting a huge challenge to satisfy the demands of the ever growing electronics market and the markets for electric vehicles (EVs) or hybrid electric vehicles (HEVs), and stationary energy storage systems. Rechargeable sodium ion batteries (NIBs), therefore, are currently regaining interest for use in large-scale applications because of their huge advantages in terms of low cost and the abundance of sodium resources. My doctoral work focuses on the sodium-storage properties of anode materials, including reduced graphene oxide, tin oxide/reduced graphene oxide composite, molybdenum disulfide/carbon composite, molybdenum disulfide/reduced graphene oxide composite, and iron disulfide/carbon composite. The obtained active materials were characterized for their physical characterization and electrochemical properties. The corresponding sodium-storage mechanisms were studied as well.

Reduced graphene oxide (RGO) was fabricated via the facile Hummers' method, which achieved by exfoliating the graphite through oxidation by a strong acid. The obtained RGO is a compound of carbon, oxygen, and hydrogen in the form of C-C, C=O and C-OH species. With large *d*-spacing, high surface area, high conductivity, and high density of cavities and/or holes and/or defects in the graphene nanosheets, its structural properties result in excellent cycling stability for sodium ion batteries. The reaction mechanism between sodium and the graphene layer is capacitive behavior, showing outstanding cycling stability without capacity decay over 1000

cycles. Excellent rate capability is delivered due to its adsorption mechanism, and the reversible capacity is as high as 217.2 mAh $g^{-1}$at 0.2 C, which slightly decreases to 95.6 mAh $g^{-1}$ when the applied current rate increase to 5 C.

Tin oxide/ reduced graphene oxide ($SnO_2$/RGO) nanocomposite was prepared via a simple hydrothermal method, and it possesses a lacunose structure with large amounts of buffering space between the small $SnO_2$ nanoparticles and nanovoids amongst the agglomerated $SnO_2$ clusters. This unique nanostructure is able to tolerate the large volume expansion during charge/discharge processes, and is favourable to fast $Na^+$ diffusion. Furthermore, the synergistic effects due to RGO in the composite are capable of increasing the overall conductivity of the electrode. $SnO_2$/RGO thus shows good cycling performance (330 mAh $g^{-1}$ after 150 cycles) and outstanding rate capability. The mechanism is deduced to be a reversible alloying/dealloying reaction between tin and sodium, while RGO contributes to the capacity via the absorption reaction.

Exfoliated molybdenum disulfide (E-$MoS_2$) was prepared by chemical exfoliation, and the E-$MoS_2$/C composite was further fabricated by the hydrothermal method. E-$MoS_2$/C composite shows a graphene-like structure, with an enlarged interlayer distance of 0.64 nm (*d*-spacing of 0.61 nm for pristine $MoS_2$) and higher conductivity. When it was applied as anode material in sodium-ion batteries, different electrolytes were used to optimize the electrochemical properties. The composite exhibits a high capacity of 400 mAh $g^{-1}$ at 100 mA $g^{-1}$ over 100 cycles in electrolyte consisting of 1.0 M $NaClO_4$ with propylene carbonate / ethylene carbonate and 5 wt. % fluoroethylene carbonate additive (PC/EC + 5 wt. % FEC). Meanwhile, the anode was tested at different cut-off voltages, which correspond to different sodium-storage mechanism, thereby

showing various cycling performance. Furthermore, ex-situ X-ray diffraction (XRD) and X-ray photoelectron spectroscopy (XPS) were conducted to investigate the conversion reaction mechanism between sodium and $MoS_2$.

Exfoliated molybdenum disulfide / reduced graphene oxide ($MoS_2$/G) composite was synthesised by attachment of exfoliated $MoS_2$ nanosheets onto a graphene nanosheets matrix. The $MoS_2$/G composite has a graphene-like structure with interlayer spacing of 0.69 nm, so that it was first investigated as an anode for sodium-ion batteries. The reaction mechanism between $MoS_2$ and Na was clearly confirmed by ex-situ XRD, and it is supposed to be an intercalation reaction at first discharge process, with a following conversion reaction for the subsequent cycles. The reversible capacity was 313 mAh $g^{-1}$ at 100 mA $g^{-1}$ after 200 cycles. Due to the voltage hysteresis in the conversion reaction, the $MoS_2$/G composite can be applied in sodium-ion pseudocapacitors. The $Na_nMoS_2$/G electrodes from the sodiation of $MoS_2$ were utilized to construct symmetric sodium-ion pseudocapacitors. The full cell exhibits outstanding cycling performance of ~ 50 F $g^{-1}$ during prolonged 2000 cycles at 600 mA $g^{-1}$.

## TABLE OF CONTENTS

## LIST OF FIGURES

## LIST OF TABLES

## NOMENCLATURE

List of Abbreviations

| Abbreviation | Full name |
|---|---|
| a.u. | Arbitrary unit |
| 1D | One-dimensional |
| AFM | Atomic force microscope |
| ARC | Accelerating rate calorimetry |
| BET | Brunauer-Emmett-Teller |
| CMC | Carboxymethyl cellulose |
| CNTs | Carbon nanotube |
| CV | Cyclic voltammogram |
| DEC | Diethyl carbonate |
| DEGDME | Diethylene glycol dimethyl ether |
| DFEC | Transdifluoroethylene fluorinated EC |
| EC | Ethylene carbonate |
| EDLCs | Electric double layer capacitors |
| EDS | Energy dispersive X-ray spectroscopy |
| EELS | Electron energy loss spectra |
| EES | Electrical energy storage |
| EIS | Electrochemical impedance spectroscopy |
| ES | Ethylene sulphite |
| EV | Electric vehicle |
| FEC | Fluoroethylene carbonate |
| FESEM | Field-emission scanning electron microscopy |
| hcp | Hexagonal close packed |
| HEVs | Hybrid electric vehicles |
| HRTEM | High-resolution transmission electron microscopy |
| JCPDS | Joint Committee on Powder Diffraction Standards |
| LIBs | Lithium ion batteries |
| MWCNTs | Multi-walled carbon nanotubes |
| NIBs | Sodium ion batteries |
| NICs | Sodium ion capacitors |

| | |
|---|---|
| NMP | 1-methyl-2-pyrrolidinone |
| OCP | Open circuit potential |
| PAA | Polyacrylic acid |
| PC | Propylene carbonate |
| PHEVs | Plug-in hybrid electric vehicles |
| PVDF | Polyvinylidene fluoride |
| RGO | Reduced graphene oxide |
| SAED | Selected area electron diffraction |
| SEI | Solid electrolyte interphase |
| SEM | Scanning electron microscopy |
| SHE | Standard hydrogen electrode |
| STEM | Scanning transmission electron microscopy |
| TEM | Transmission electron microscopy |
| Tf | Trifluoromethane sulfonate |
| TFSI | Bis(trifluoromethanesulfonyl)imide |
| TGA | Thermogravimetric analysis |
| VC | Vinylene carbonate |
| XAS | X-ray absorption spectroscopy |
| XPS | X-ray photoelectron |
| XRD | X-ray diffraction |

List of Symbols

| Symbol | Name | Unit |
|---|---|---|
| $2\theta$ | Peak position of XRD | ° |
| $C$ | Charge or discharge rate | C |
| $C_m$ | Specific capacitance | F $g^{-1}$ |
| $d$ | Lattice spacing | nm |
| $I$ | Current | mA |
| $L$ | Crystal size | nm |
| $m$ | Active material weight | g |
| $N$ | Avogadro's number = $6.022 \times 10^{-23}$ | $mol^{-1}$ |
| $P/P0$ | Relative pressure | |
| $PD$ | Power density | W $L^{-1}$ |
| $Q$ | Specific capacity | mAh $g^{-1}$ |
| $R$ | Resistance | Ω |
| $SBET$ | Specific BET surface area | $m^2$ $g^{-1}$ |
| $SE$ | Specific energy | Wh $kg^{-1}$ |
| $SP$ | Specific power | W $kg^{-1}$ |
| $t$ | Time | s |
| $T$ | Temperature | K or °C |
| $t_{Na}$ | Sodium transference number | |
| $V$ | Voltage | volt |
| $\eta$ | Coulombic efficiency | % |
| $\lambda$ | X-ray wavelength | Å |

# CHAPTER 1 INTRODUCTION

## 1.1 General background

For several decades, rechargeable lithium ion batteries (LIBs) have long been successfully used in portable electronics, and they are currently being considered for energy demanding applications such as electric vehicles. Lithium sources, however, are too geographically constrained and limited to meet the increasing demands. Therefore, sodium ion batteries (NIBs) are currently regaining extensive interest for large-scale electric storage applications due to the low cost of sodium sources and the similar chemistry of sodium and lithium. NIBs certainly are a promising option for large-scale applications.

Sodium electrodes, not strictly isostructural to their lithium counterparts, have various thermodynamically stable phases due to the influence of the alkali size/charge ratio. Different electrochemical performance, therefore, have been demonstrated between the Li and Na systems, especially in the case of electrode materials based on intercalation chemistry. For example, hard carbons, rather than the graphitic materials used as anode in Li-ion batteries, have been confirmed to be active sodium-ion intercalation compounds at low potential. Furthermore, modelling studies have revealed that the activation energy for Na-ion hopping is often lower than for Li ions because of less polarization of sodium electrode, which leads to lower voltage of Na compounds. For the sodium anodes, lower voltages are beneficial for increasing the overall voltage and hence the energy density. The lower voltages of sodium cathode lead to lower energy density, and they offer the opportunity to explore materials where the lithium analogues have too high a potential to support many conventional electrolytes. However, Na-ion transport in

NIBs requires higher activation energy and much larger volume expansion/contraction occurs in the cathode and anode electrode materials. It has been proven that open and layered structures are better able to accommodate the larger $Na^+$ ions, which hold the most promise of intercalation compounds. It is manifest that the nanostructure and framework of electrode materials plays the most crucial role in the advancement of sodium-ion storage.

This doctoral work aims to realize higher sodium-storage via constructing nanostructured electrode materials and optimizing electrolyte systems. Specifically, the emphases of this doctoral work are outlined as follows: 1) Choosing simple and scalable synthesis methods for commercialization, including the wet chemical method and the hydrothermal method. 2) Enhancing the Na-storage capacity via an exfoliation strategy, such as with exfoliated graphite and exfoliated molybdenum disulfide. 3) Constructing special nanostructures via the incorporation of active materials in a conductive matrix, such as graphene-like molybdenum disulfide / amorphous carbon ($MoS_2$/C) composite and lacunose tin dioxide nanoparticles / reduced graphene oxide ($SnO_2$/RGO) composite. 4) Optimizing the electrolyte systems by employing various solvents with different viscosity and ionic conductivity. The effect of additive is investigated as well. 5) Utilizing various techniques to deduce the probable reaction mechanisms between active material and sodium, such as *ex-situ* powder X-ray diffraction (XRD) and X-ray photoelectron spectroscopy (XPS).

## 1.2 Chapter overview

Chapter 2 contains basic background knowledge on the sodium-ion energy storage system. Various topics are briefly introduced, including the history of sodium ion batteries, the reaction mechanism of sodium-ion storage, and an overview on the general battery components, such as the positive and negative electrode materials, and the electrolyte.

Chapter 3 presents the experimental and characterization methods used in this thesis, including the details of chemicals, synthesis procedures, physical characterization techniques, and electrochemical characterization methods.

Chapter 4 discusses the electrochemical properties of reduced graphene oxide (RGO), which achieves the sodium storage by expansion and distortion of graphite via the Hummers' method. A capacity of 141 mAh $g^{-1}$ is maintained over 1000 cycles at the current rate of 1 C (20 mA $g^{-1}$), which is a significant enhancement compared to the inactive graphite in sodium-ion batteries. The corresponding reaction mechanism between reduced graphene oxide and sodium is likely to be an adsorption mechanism according to its charge/discharge curves and cyclic voltammogram (CV) behavior.

The application of RGO in sodium-ion batteries is extended in Chapter 5, where it is used as an active matrix for $SnO_2$/RGO composite. The composite is prepared by loading ultrafine $SnO_2$ on RGO nanosheets via a simple hydrothermal method. The construction of unique nanostructures with large amounts of nanovoids and free space is proven to be an effective strategy for optimizing electrochemical performance. The alloying/dealloying reaction mechanism is deduced based on its

CV curves for sodium-ion batteries and comparison with its lithium-storage performance.

Chapter 6 presents an exfoliation strategy that is utilized to improve the electrochemical performance of $MoS_2$ in sodium-ion batteries. The exfoliation strategy can effectively enlarge the interlayer distance and degree of disorder, which is favorable for the acceptance of the larger sodium ion, thereby tolerating severe volume expansion. Exfoliated $MoS_2$ delivers a high capacity of 400 mAh $g^{-1}$ at 0.25 C (100 mA $g^{-1}$) after 100 cycles. The impacts of various electrolytes are investigated, which confirms that the electrolyte with ethylene carbonate/propylene carbonate as solvent achieves the best sodium-storage properties due to its good viscosity and ionic conductivity. The cycling stability can be further optimized by adding fluoroethylene carbonate additive, which is favourable for forming thinner and more stable solid electrolyte interphase films due to the participation of additive during electrolyte decomposition during the first discharge process. Furthermore, the probable conversion reaction mechanism is confirmed by *ex-situ* X-ray photoelectron spectroscopy (XPS) and *ex-situ* X-ray diffraction (XRD).

Chapter 7 is a study of the electrochemical properties of exfoliated $MoS_2$ that is attached on graphene nanosheet matrix ($MoS_2$/G) for sodium-ion batteries and pseudocapacitors. It is obvious that this $MoS_2$/G composite shows better cycling stability and rate capability than $MoS_2$/C (Chapter 6). This is ascribed to the benefits of the graphene matrix, which is able to improve the conductivity and stability of the active materials, and effectively protect exfoliated $MoS_2$ sheets from aggregation. On the other hand, $MoS_2$/G interfaces show a synergistic effect, which leads to higher Na storage capacity in the $MoS_2$/G composite. In addition, Chapter 7 discusses a symmetric sodium-ion

pseudocapacitor that was constructed using sodium-doped $MoS_2$/G ($Na_nMoS_2$/G) electrodes, which shows a capacitance of ~ 50 F $g^{-1}$ for 2000 cycles with outstanding cycling stability. Meanwhile, this pseudocapacitor delivers excellent rate capability. Furthermore, the Na-storage mechanism is confirmed in detail by ex-situ XRD of pristine $MoS_2$, in which it is easier to detect the phase changes during the charge/discharge process due to its good crystallization and high intensity diffraction peaks. It is speculated that the $MoS_2$ and Na undergo an irreversible intercalation reaction during the first charge, followed by a highly reversible conversion reaction.

# CHAPTER 2 LITERATURE REVIEW

Owning to the increased demand for energy and the need to reduce carbon emissions, energy storage innovation has been a constant global concern over the past decade. The traditional fossil fuels suffer from drastic increases in the price and have led to serious environmental problems, such as global warming. Some renewable energy resources, such as wind, wave, and solar power are becoming increasingly popular in several industrialized countries, however, they provide intermittent energy; Rechargeable lithium ion batteries (LIBs) have become successful and sophisticated energy storage devices for portable electronic devices since the first commercialization of the carbon//$LiCoO_2$ cell in 1991. The demand for lithium-ion batteries for large-scale applications is rapidly emerging throughout the world, such as for hybrid electric vehicles (HEVs) and plug-in hybrid electric vehicles (PHEVs), which could reduce the energy dependence on fossil fuels for a transportation system in the future. In addition, a large-scale energy storage system for the grid is necessary to utilize electrical energy with high efficiency and for peak shift operation.[1-3] Indeed, some battery companies have already developed LIBs on the megawatt hour (MWh) scale and plan to begin a demonstration testing for electrical energy storage (EES). Such MWh-class batteries can also probably be used to store electricity generated from solar cells and wind turbines as green and renewable energy resources. In consequence of the enormous application potentials of lithium ion batteries for EV and EES, and the limitations of available global lithium resources, concerns over lithium supply have arisen both in terms of its cost and its long-term sustainability. As shown in Figure 2.1, the distribution of lithium is wide in the Earth's crust, but it is regarded as a scarce element. Its relative abundance in the Earth's crust is only 20

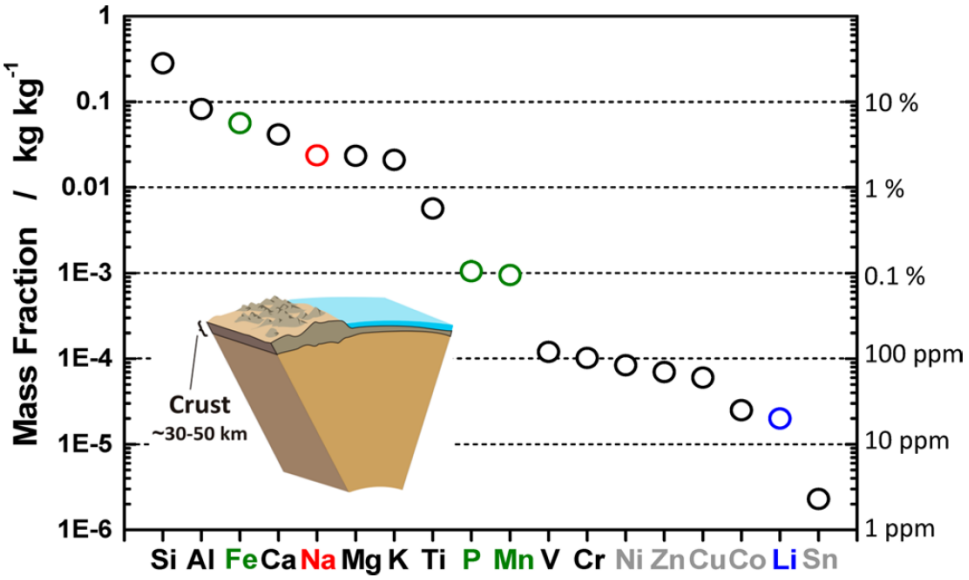


**Figure 2.1** Elemental abundance in the Earth's crust [4]

ppm. Moreover, lithium resources are unevenly distributed, and they are mainly located in remote or in politically sensitive areas (such as South America).[5, 6] It is not surprising that the cost of the main lithium source ($Li_2CO_3$) has soared during this past decade.[7] In contrast to lithium, sodium is one of the most abundant elements in the Earth's crust; and the distribution of sodium resources is extensive everywhere. Practically unlimited sodium resources are found in the ocean as well. Based on this material abundance, similar intercalation chemistry to Li and standard electrode potential, rechargeable sodium energy storage system hold promise as a complement or even substitute for lithium-based technology.[8, 9]

In the first place, all-solid-state sodium batteries with inorganic solid electrolytes are promising power sources for a wide range of applications because of their safety, long-cycle life and versatile geometries.[10] Recently, new developments in room-temperature sodium–sulfur batteries (Na-S), Na-ion batteries (NIBs), and novel Na–$O_2$ batteries are rapidly taking place. The details of these technologies and some of

the significant issues and opportunities provided by the field of sodium-ion batteries will be discussed herein.

## 2.1 General background

Historically, studies of $Li^+/Na^+$ ions for electrochemical energy storage at ambient temperature started before 1980. The application of $TiS_2$ in energy storage devices was first proposed in the 1970s.[11-13] Electrochemical and highly reversible sodium insertion into $TiS_2$ at room temperature was also demonstrated as soon as in 1980.[14] Lithium cobalt oxides ($LiCoO_2$), a lithium-containing layered oxide, was first reported in 1980.[15] It is still widely used as the high energy positive electrode materials in LIBs. Similarly, sodium containing layered oxides ($Na_xCoO_2$) were also reported for NIBs.[16] Apart from few of reports on sodium insertion materials after that period[17, 18] nevertheless, studies on sodium insertion materials for energy storage almost disappeared. In the past three decades, significant research efforts have been made only for LIBs. This big rush of Li battery research after 1980 resulted from the fact that the energy density of the Li system was believed to be much higher compared with the Na system. Furthermore, the absence of suitable negative materials hindered the development of Na-ion batteries for a long period of time. In the mid-1980s, carbonaceous materials were believed to hold promise as Li insertion (intercalation) anodes, in such forms as disordered carbons[19, 20] and graphite.[21, 22] The advancement of LIBs was further accelerated by the commercialization of graphite, which delivers a high reversible capacity of 372 mAh $g^{-1}$ and possesses a low and flat operating potential (0.1-0.2 V vs. $Li^+/Li$). Graphite, however, was proven to be an inactive host for sodium ions according to early research.[23, 24] Before the 1990s, only a few materials were feasible as potential negative electrode materials for NIBs, including disordered carbon[24] and Na−Pb alloy.[25] The first turning point on anodes for NIBs was reported by Stevens and Dahn in 2000,[26] which demonstrated hard

carbon in NIBs with a high reversible capacity of 300 mAh $g^{-1}$, close to that for lithium insertion in graphitic carbon; even though its cyclability was insufficient for

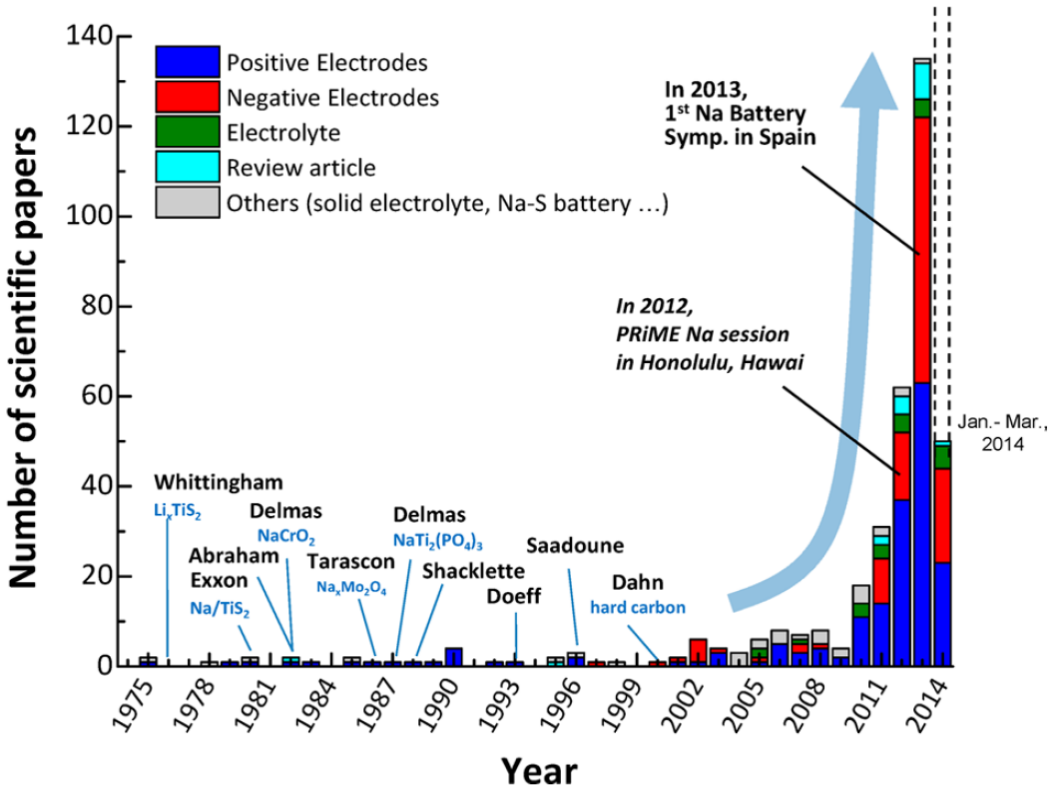


**Figure 2.2** Numbers of publications relevant to NIBs during the past three decades.[27]

battery applications at that time. Hard carbon is now extensively studied as a potential candidate for the negative electrode material for NIBs. As shown in Figure 2.2, studies on Na-ion batteries have increased rapidly from 2010. With the positive electrode materials extensively investigated, important negative electrode materials have been also newly found in the past few years. An important difference was noticed in the chemistry between Li and Na in aprotic polar solvents. For instance, surface passivation processes are clearly different in both systems. The design of

better electrolyte and suitable interphase for the Na system is quite important for realizing long cycle life.

The structures, components, systems, and charge storage mechanisms of NIBs are essentially the same as for LIBs, except that lithium ions are replaced with sodium ions as shown in Figure 2.3. A NIB consists of two sodium insertion materials, the positive and negative electrodes, which are electronically separated by electrolyte (in general, electrolyte salts dissolved in aprotic polar solvents) as a pure ionic conductor. The battery performance depends on the battery components selected, and many different NIBs for different purposes can be assembled.

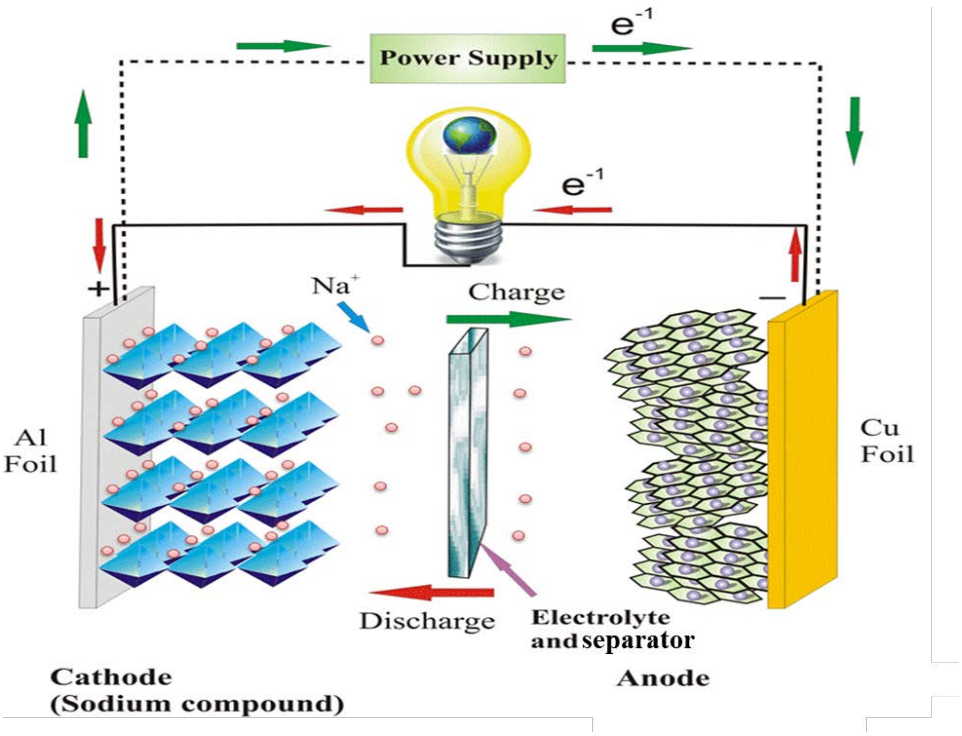


**Figure 2.3** Schematic illustration of operation and charge storage mechanism of Na-ion batteries

## 2.2 Positive electrode materials

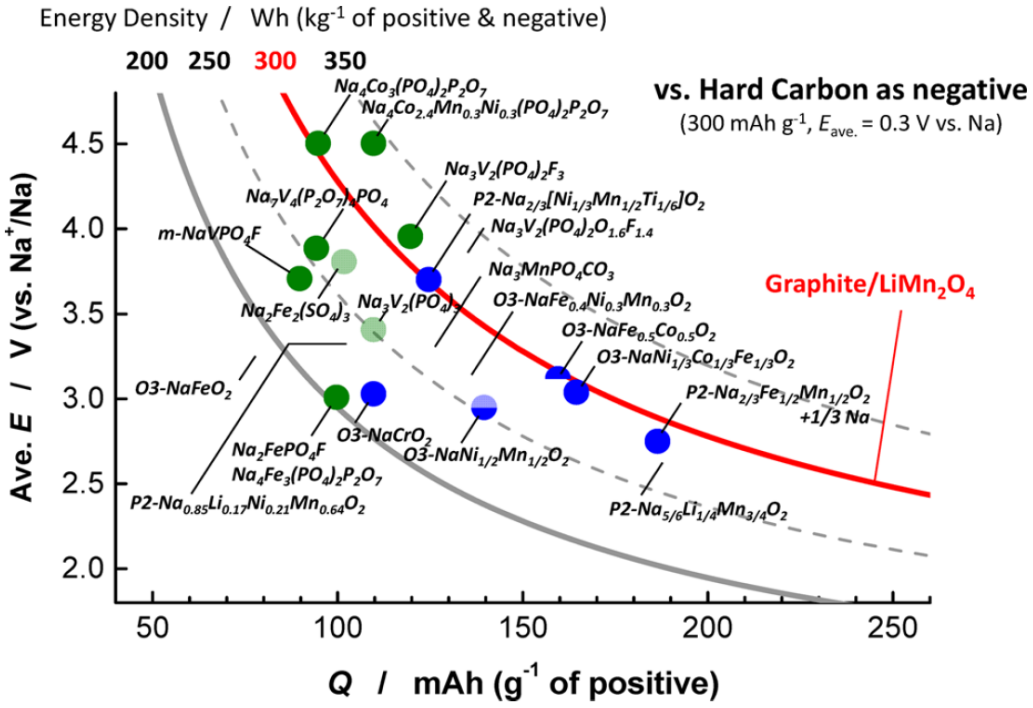


**Figure 2.4** Average voltage and energy density versus gravimetric capacity of cathode materials for NIBs.[27]

The recent research NIBs focuses on the sodium-ion based electrochemistry, with a focus on intercalation compounds for positive electrode materials for sodium intercalation (including layered transition metal oxides and polyanionic compounds). Many different compounds are being studied as possible cathode materials as shown in Figure 2.4, from oxides to phosphates, fluorophosphates or pyrophosphates. Each compound presents its own advantages and disadvantages for its real application in energy storage systems. It is clear that the gravimetric energy density of NIBs, which combine various cathodes with hard carbon, is estimated to be from 200-350 mWh $g^{-1}$. The energy density of NIBs is now competitive with the graphite/$LiMn_2O_4$ system. Hopefully, research progress on cathode materials will further improve the energy

density of NIBs in the future. The following sections explain the main features of each compound family.

### 2.2.1 Layered structure oxides ($NaMO_2$, where M is a metal)

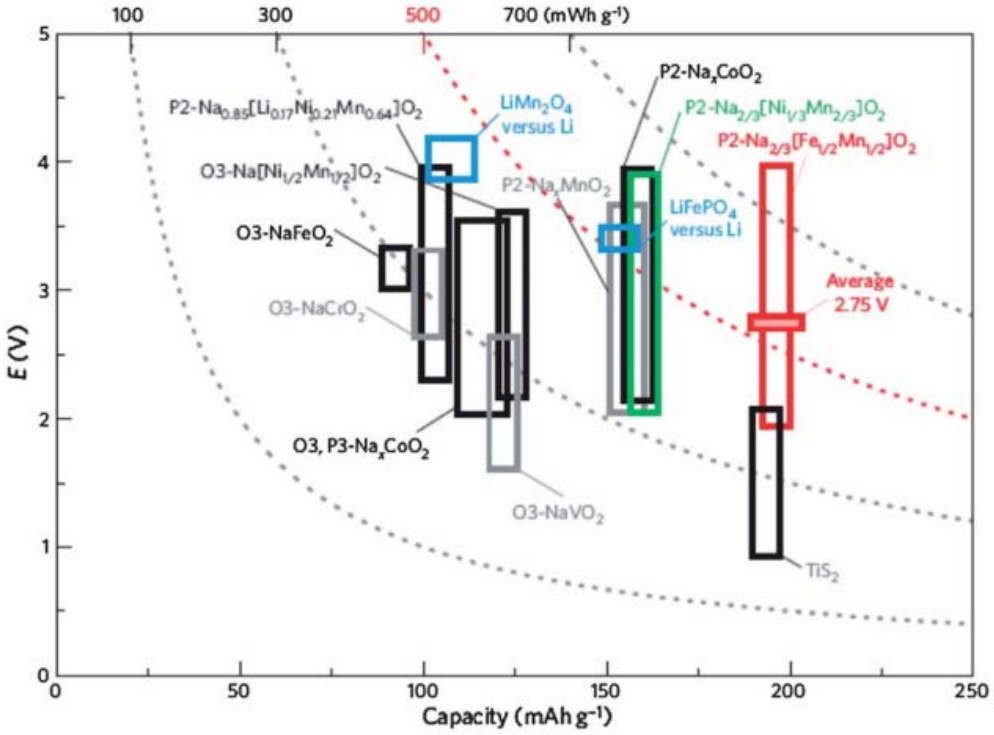


**Figure 2.5** A comparison of reversible capacity and operating voltage ranges of the layered sodium insertion materials. The energy density was calculated on the basis of the voltage versus metallic sodium for simplicity. $LiFePO_4$ and $LiMn_2O_4$ are also shown for comparison based on the voltage versus Li metal.[28]

As shown in Figure 2.5, a great range of transition metals and their combinations can result in layered structure oxides. All of them deliver different operating voltages and specific capacities, which correspondingly decide their energy densities.[28] The most common layered structures are built up of a sheet of edge sharing MeO6 octahedra, with Me a transition metal. Polymorphisms appear when the sheets of edge-sharing

MeO6 octahedra are stacked with different orientations along the *c*-axis direction. As shown in Figure 2.6, sodium-based layered materials can be categorized into two main groups using the classification proposed by Delmas *et al.*[29] O3 type or P2 type, in which the sodium ions are accommodated at octahedral and prismatic sites,

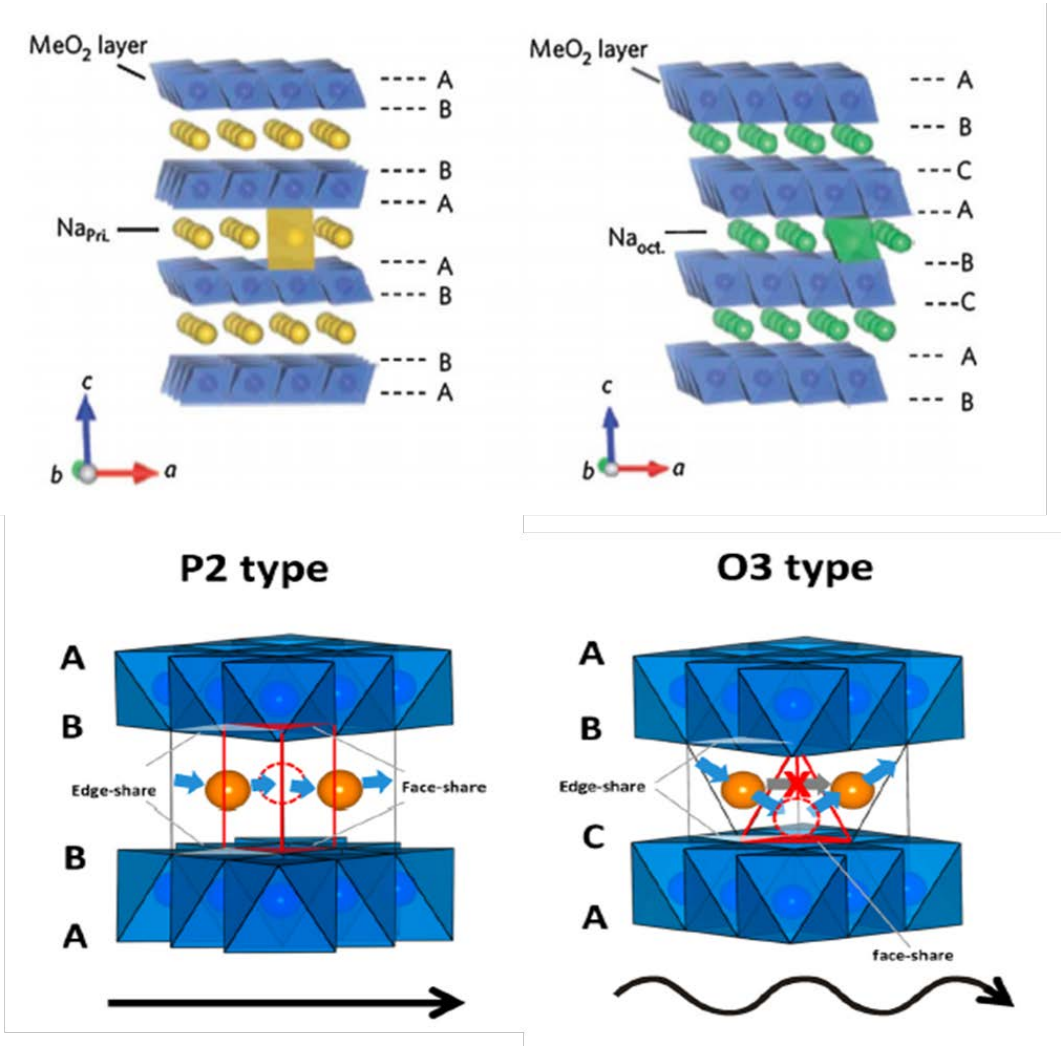


**Figure 2.6** Layered structures and different Na migration paths of P2-type and O3-type $NaMO_2$ with sheets of edge-sharing MeO6 octahedra.[28]

respectively. In the P2-phase, Na occupies the trigonal prismatic sites (P, entirely face-sharing or entirely edge-sharing) of the ABBA oxygen stacking sequence. In the O3-phase, Na occupies octahedral sites (O, face-sharing) with ABC oxygen stacking.

When the sodium source is off-stoichiometry (typically $0.6 < x < 0.7$ in $Na_xMO_2$), the P2-type phase is structurally stabilized, so that it has open paths for Na ions and a low diffusion barrier. Typically, P2 compounds are accepted as better cathode materials because of their high diffusion rate and prohibited slab-gliding.

#### 2.2.1.1 O3-type $NaNiO_2$

Fielden and Obrovac reported an irreversible capacity of 40 mAh $g^{-1}$ and a reversible capacity of 80 mAh $g^{-1}$ within the voltage range of 2.0 – 3.5 V at C/10 after the first cycle for $NaNiO_2$.[30] Vassilaras *et al.* investigated the same system and showed that a large amount of Na can be deintercalated/intercalated.[31] Multiple plateaux were observed due to phase change during charge/discharge cycling (Figure 2.7). Overall, a 147 mAh $g^{-1}$ discharge capacity (0.62 Na) within the voltage range of 2.0 - 4.5 V at C/10 was achieved. Large capacity loss was observed, however, probably due to an irreversible phase change which is evidenced by the formation of an unidentifiable phase after cycling. Cycling the cell over the voltage range of 1.25 - 3.75 V resulted in a 123 mAh $g^{-1}$ discharge capacity (0.52 Na) with fairly stable capacity retention at C/10. Significant improvement in Coulombic efficiency at lower cut-off voltage indicated that the phase changes below 3.75 V are highly reversible, although the fully sodiated phase is never achieved and $Na_{0.91}NiO_2$ is obtained instead.

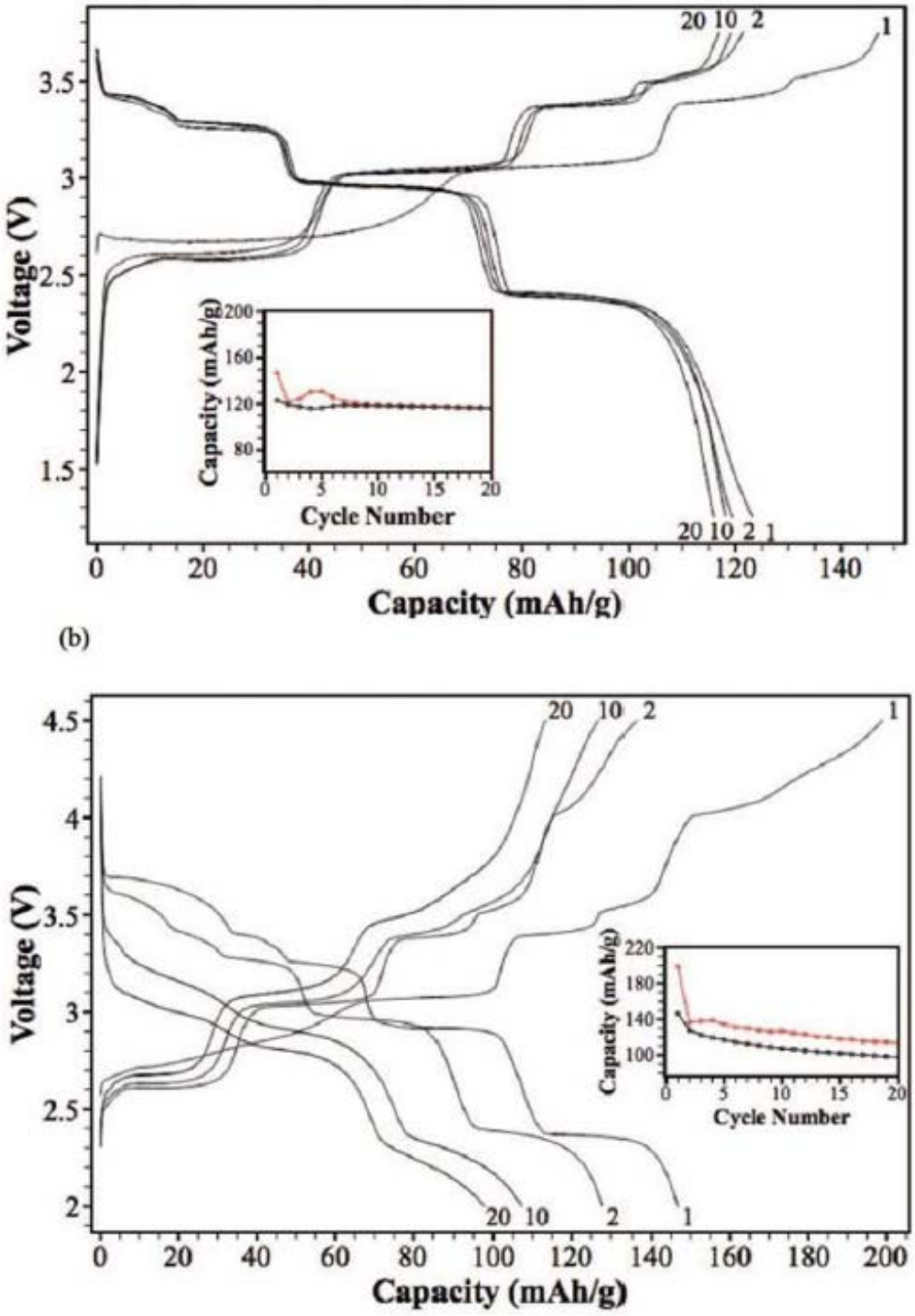


**Figure 2.7** Voltage profile of $NaNiO_2$ after multiple cycles at C/10. The cell is galvanostatically cycled between (a) 1.25–3.75 V, and (b) 2.0–4.5 V. The insets show the cycling performance for the first 20 cycles. [31]

2.2.1.2 O3-type $NaFeO_2$

$\alpha$-$NaFeO_2$ is known as a typical example of a O3-type layered structure and easily prepared by conventional solid-state reaction.[32] Electrochemical Na extraction from $NaFeO_2$ in a non-aqueous Li/ $NaFeO_2$ cell was first demonstrated by Takeda and co-workers.[33] Charge/discharge curves during sodium extraction/insertion processes for a single phase of O3-type $NaFeO_2$ are shown in Figure 2.8. It is clear that reversibility in electrode materials is significantly influenced by the cut-off conditions on the charge (sodium extraction) process. Although the charging capacity, corresponding to amounts of sodium ions extracted from the crystal lattice, increases as a function of cut-off voltage, the reversible capacity obviously decreases when the cell is charged beyond 3.5 V. Excellent reversibility with small polariza-

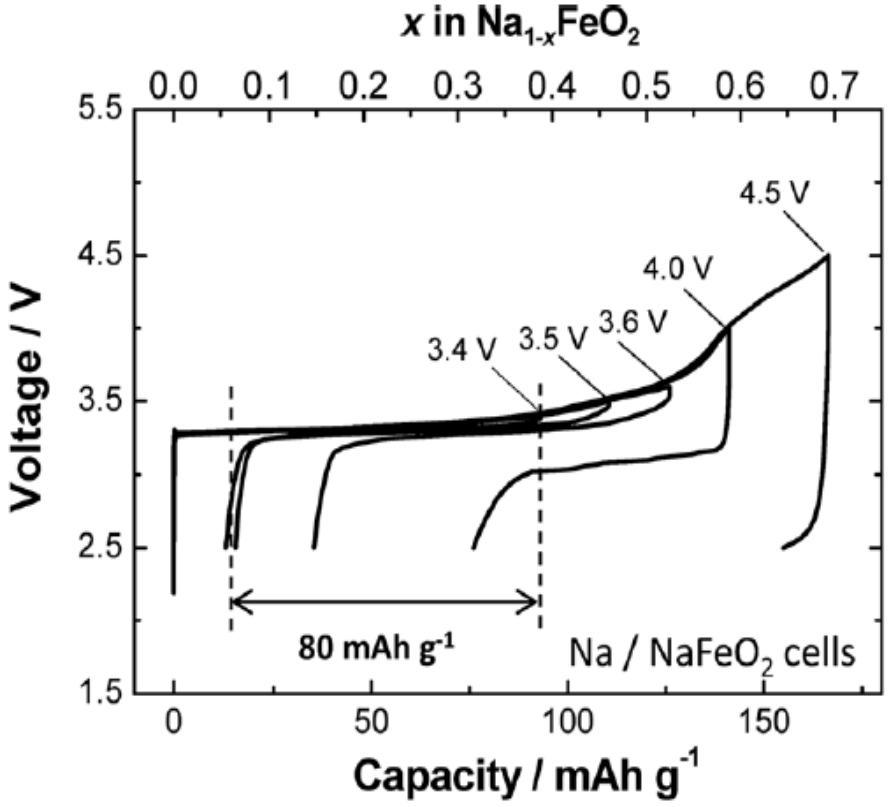


**Figure 2.8** Galvanostatic charge/discharge curves of Na/NaFeO2 at different cut-off voltages.[33]

-tion is observed with a cut-off voltage of 3.4 V. The observed reversible capacity reaches 80 mAh $g^{-1}$, indicating that approximately 0.3 mol Na is reversibly extracted from $NaFeO_2$ and inserted into the $Na_{0.7}FeO_2$ host structure. The deterioration of the electrode properties beyond 3.5 V originates from an irreversible phase transition as suggested by *ex-situ* X-ray diffraction (XRD) [34] and X-ray absorption spectroscopy (XAS).[35] These facts suggest that part of the $Fe^{3+}$ ions could migrate into the neighbouring tetrahedral sites, when sodium ions are extracted from the crystal lattice; vacancies are created at face-sharing tetrahedral sites with $FeO_6$ octahedra. Significant irreversible structural change takes place, which is caused by the migration of iron into the inter-slab spaces at high voltage.

#### 2.2.1.3 O3-type $NaCrO_2$

The electrode performance of O3-type $NaCrO_2$ was first reported in 1982, and it shows a complicated phase transition on sodium extraction.[36] The reversibility of the Na extraction/reinsertion process was revisited in 2009, and it was reported to be that approximately 50% of sodium ions can be reversibly extracted from $NaCrO_2$ with small polarization based on the $Cr^{3+}/Cr^{4+}$ redox couple.[37] A voltage plateau at nearly 3.0 V vs $Na^+/Na$ is observed in the high sodium content region, and the voltage shifts up gradually to 3.3 V. An additional plateau at 3.6 V appears near $x \approx 0.5$ in $Na_{1-x}CrO_2$. Dahn and his co-workers reported the electrochemical performance of $NaCrO_2$ as a positive electrode material for sodium-ion batteries in 1M $NaClO_4$/PC electrolyte. It delivered a reversible capacity of 110 mAh $g^{-1}$ during the first charge and had good cycling stability. The reaction between deintercalated $Nax CrO_2$ ($x \approx 0.5$) in ethylene carbonate/diethyl carbonate (EC/DEC) solvent was studied via accelerating rate calorimetry (ARC). In contrast to analogous results for

$Li_{0.5}CoO_2$ and $Li_0FePO_4$ under the same conditions, $Na_{0.5}CrO_2$ showed an unexpected excellent thermal stability in solvent with no heat release in the ARC test temperature range. The results proved that $Na_xCrO_2$ is a fundamentally safe family of positive electrode materials for NIBs with liquid electrolytes.[38] In order to study the effects of surface coating, carbon coated $NaCrO_2$ was synthesized by Ding *et al* by adding an appropriate amount of citric acid in a solid-state reaction.[39] Carbon-coated $NaCrO_2$ maintained a stable 100 mAh $g^{-1}$ discharge specific capacity after 40 cycles as opposed to rapid capacity fading of nearly 20% after 20 cycles in previous reports.[37] The multiple peaks on the CV curve (Figure. 2.9 b) were identified as due to a phase change from hexagonal O3 to monoclinic O3 to monoclinic P3 and the sharp peaks were associated with the partial oxidation of $Cr^{3+}$ to $Cr^{4+}$. The better performance of coated particles is due to the fact that the coating prevents direct contact between the active material and the electrolyte. This coating effectively reduces side reactions between the electrode material and the electrolyte, and decreases the polarization by increasing electronic conductivity.[40, 41]

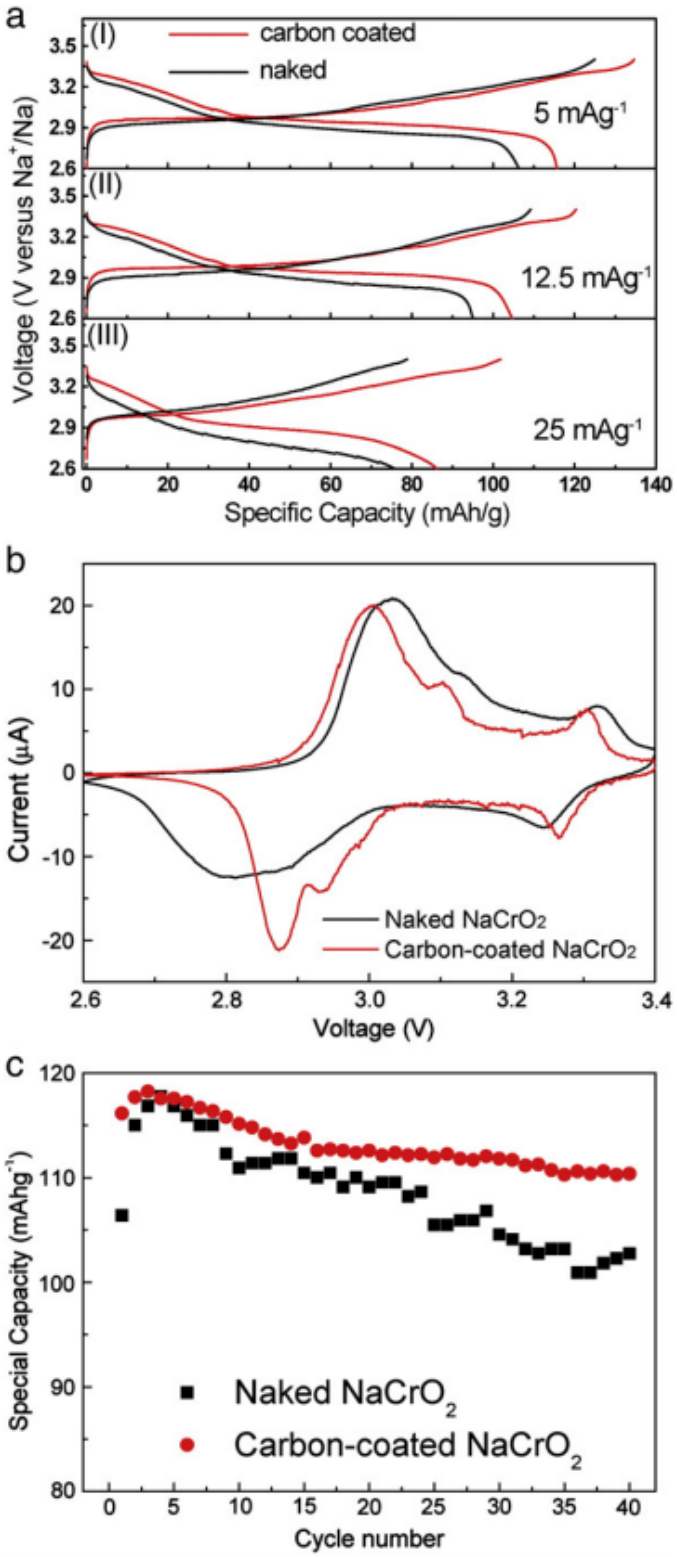


**Figure 2.9** (a) Galvanostatic charge/discharge curves of $NaCrO_2$ at different current densities; (b) Cyclic voltammogram during 2.6-3.4 V at a scan rate of 0.1 mV $S^{-1}$; (c) Cycling performance of $NaCrO_2$ at the current of 5 mA $g^{-1}$.[39]

2.2.1.4 P2-type Na$x$$CoO_2$

P2-type $Na_xCoO_2$ has been studied to investigate its thermal stability by accelerating rate calorimetry (ARC). X-ray diffraction was used to detect the products after the ARC experiments, which indicates that the de-intercalated P2-Na$x$$CoO_2$ reacts strongly with both the electrolyte salt ($NaPF_6$) and the solvent, leading to formation of $NaCoF_3$.[42] In order to investigate the effects of the ionic diffusion length and particle size, the electrochemical properties of two P2-$Na_{0.71}CoO_2$ samples with different microstructures were studied.[43] The P2-$Na_{0.71}CoO_2$ with smaller particle size exhibited a higher specific capacity of 105 mAh $g^{-1}$ during the voltage range of 2.0 - 3.9 V at C/25, while the P2-$Na_{0.71}CoO_2$ with larger particle dimensions only achieved a capacity of 70 mAh $g^{-1}$ with the same voltage range and current density. Meanwhile, the smaller particles resulted in higher capacity retention and less polarization. These results confirmed that smaller particle dimensions induced shorter ionic diffusion paths, thereby leading to better kinetics. Ding *et al.* studied a similar composition of P2-type $Na_{0.74}CoO_2$ as cathode material.[44] As shown in Figure 2.10, it delivered a discharge capacity of 107 mAh $g^{-1}$ ($Na_{0.93}CoO_2$) at C/10 within the voltage range of 2.0 - 3.8 V in $NaPF_6$ electrolyte. When starting on charge, $Na_{0.5}CoO_2$ could also be obtained with a capacity of 55.7 mAh $g^{-1}$. Multiple plateaux at 2.72 V, 3.00 V, 3.30 V, and 3.60 V were observed, which implied a series of phase changes during cycling. The voltage polarization was 150 - 250 mV. Figure 2.10b shows the charge/discharge curves of P2-phase $Na_{0.74}CoO_2$ in $NaClO_4$ electrolyte. The test was conducted using the same cut-off voltage at a current density of 0.05 C. The initial charge/discharge capacities were ~ 54.86 and 110.2 mAh $g^{-1}$, respectively. $Na_{0.74}CoO_2$ showed similar electrochemical performance in $NaClO_4$ and $NaPF_6$ electrolyte, while poor capacity retention in $NaClO_4$ electrolyte. Interestingly,

the Coulombic efficiency of the cell with $NaClO_4$ electrolyte was higher than that with $NaPF_6$. Regardless of the electrolyte, the Coulombic efficiency was reported to be very consistent up to 40 cycles (Figure 2.25c). *Ex-situ* XRD showed expansion / compression in the *c*-axis upon cycling, which indicates stable deintercalation / intercalation of $Na^+$ in the inter-slab spaces. XPS measurements confirmed the $Co^{3+}/Co^{4+}$ redox reaction during the charge/discharge processes.

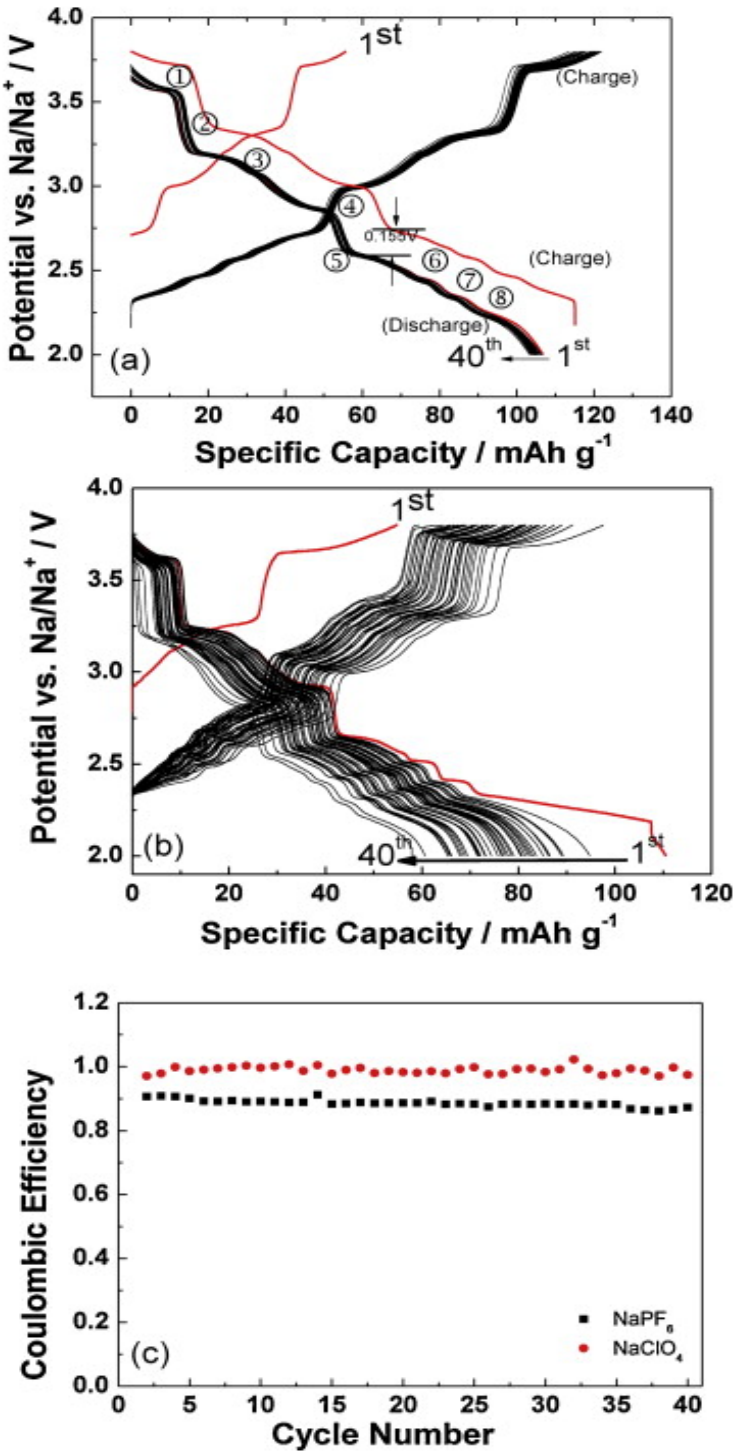


**Figure 2.10** (a) Galvanostatic curves of P2-$Na_{0.74}CoO_2$/$NaPF_6$/Na cells at the current rates of 0.1 C; (b) galvanostatic curves of P2-$Na_{0.74}CoO_2$/$NaClO_4$/Na cells at the current rates of 0.05 C, and (c) Coulombic efficiency of the cells as a function of cycle numbers.[44]

2.2.1.5 O3-type and P2-type $Na[Fe_{1/2}Mn_{1/2}]O_2$

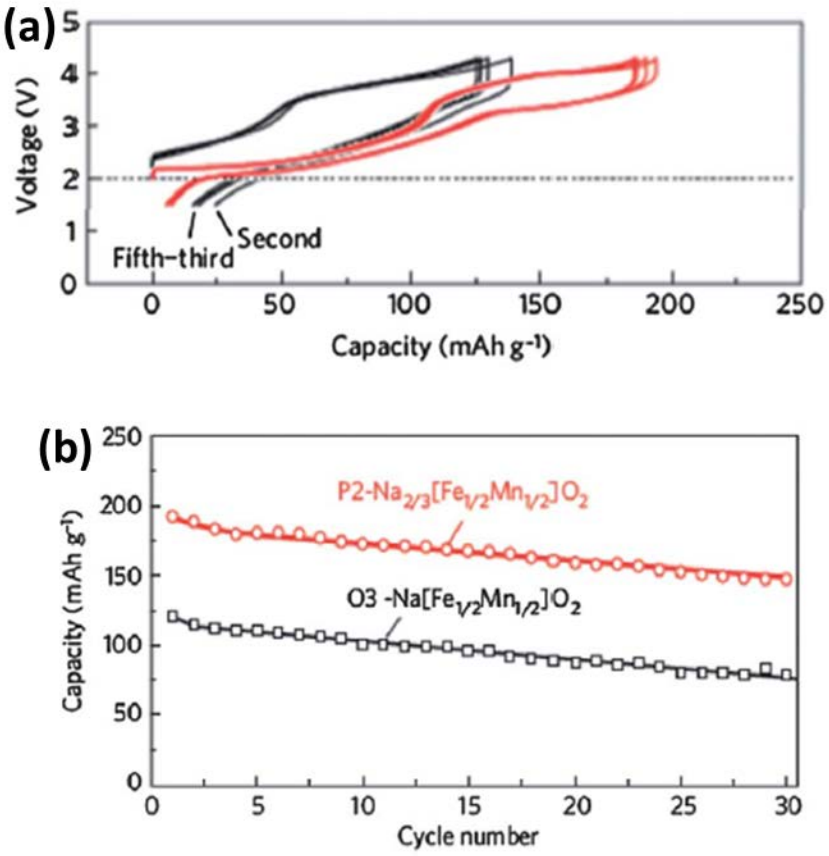


**Figure 2.11** (a) Galvanostatic charge/discharge curves; (b) cycling performance of P2-$Na[Fe_{1/2}Mn_{1/2}]O_2$ and O3-type $Na[Fe_{1/2}Mn_{1/2}]O_2$ at a current density of 12 mA $g^{-1}$ within a voltage window of 1.5 - 4.3 V.[45]

Yabuuchi *et al.* prepared P2- and O3-type $Na[Fe_{1/2}Mn_{1/2}]O_2$ as single phase materials, respectively.[45] The comparison of these two cathodes is displayed in Figure 2.11. O3-type $Na[Fe_{1/2}Mn_{1/2}]O_2$ was able to achieve a capacity of 100 - 110 mAh $g^{-1}$ in the voltage range of 1.5-4.2 V at C/20, showing large polarization at approximately 1 V. In contrast, P2-type $Na_{2/3}[Fe_{1/2}Mn_{1/2}]O_2$ displayed a high capacity value of 190 mAh $g^{-1}$ under the same testing conditions, which is 72 % of the theoretical capacity based on the $Fe^{3+}/Fe^{4+}$ redox process (Figure 2.11a). Both electrodes showed similar

cycling behavior (Figure 2.11b) with relatively higher capacity and better cycling stability for P2-type $Na_{2/3}[Fe_{1/2}Mn_{1/2}]O_2$. This implies that the structural transformations do not degrade the material upon cycling.

#### 2.2.1.6 P2-type $Na_{0.67}[Mn_{0.65}Ni_{0.15}Co_{0.2}]O_2$

Metal substitution is one of the most effective methods to improve the electrochemical performance of layered oxides via stabilization of the inter-slab spaces. The electrochemical performance of P2-phase $Na_{0.67}[Mn_{0.65}Ni_{0.15}Co_{0.2}]O_2$ (NaMNC) and Al-substituted $Na_{0.67}[Mn_{0.65}Ni_{0.15}Co_{0.15}Al_{0.05}]O_2$ (NaMNCA) using a citric acid assisted combustion method were reported.[46] The obtained NaMNC and NaMNCA particles formed micro-flakes with almost the same XRD features and peaks. The cyclic voltammogram (CV) curves of NaMNC in Figure 2.12a indicates that there are three pairs of reversible redox peaks at the potentials of 4.25, 3.65, and 2.3 V, corresponding to the redox reaction of $Ni^{2+}/Ni^{4+}$, $Co^{3+}/Co^{4+}$, and $Mn^{3+}/Mn^{4+}$, respectively. The specific capacity of NaMNC was 141 mAh $g^{-1}$ at 20 mA $g^{-1}$ between 2 and 4 V, with capacity retention of 89 % of the specific capacity after 30 cycles. The capacity became stable with prolonged cycling. NaMNCA exhibited almost the same CV features as NaMNC except for a slight splitting of the oxidation peak at 4.30 V. Interestingly, the NaMNCA electrode showed excellent capacity retention of 95.4% over 50 cycles. It should be noted that the discharge capacity at 4.25 V was highly reversible with only 6 mAh $g^{-1}$ capacity loss over 50 cycles. More importantly, NaMNCA showed good electrochemical performance at current density of 100, 200, and 400 mA $g^{-1}$, delivering 78, 64, and 50% of the initial capacity (Figure 2.12c).

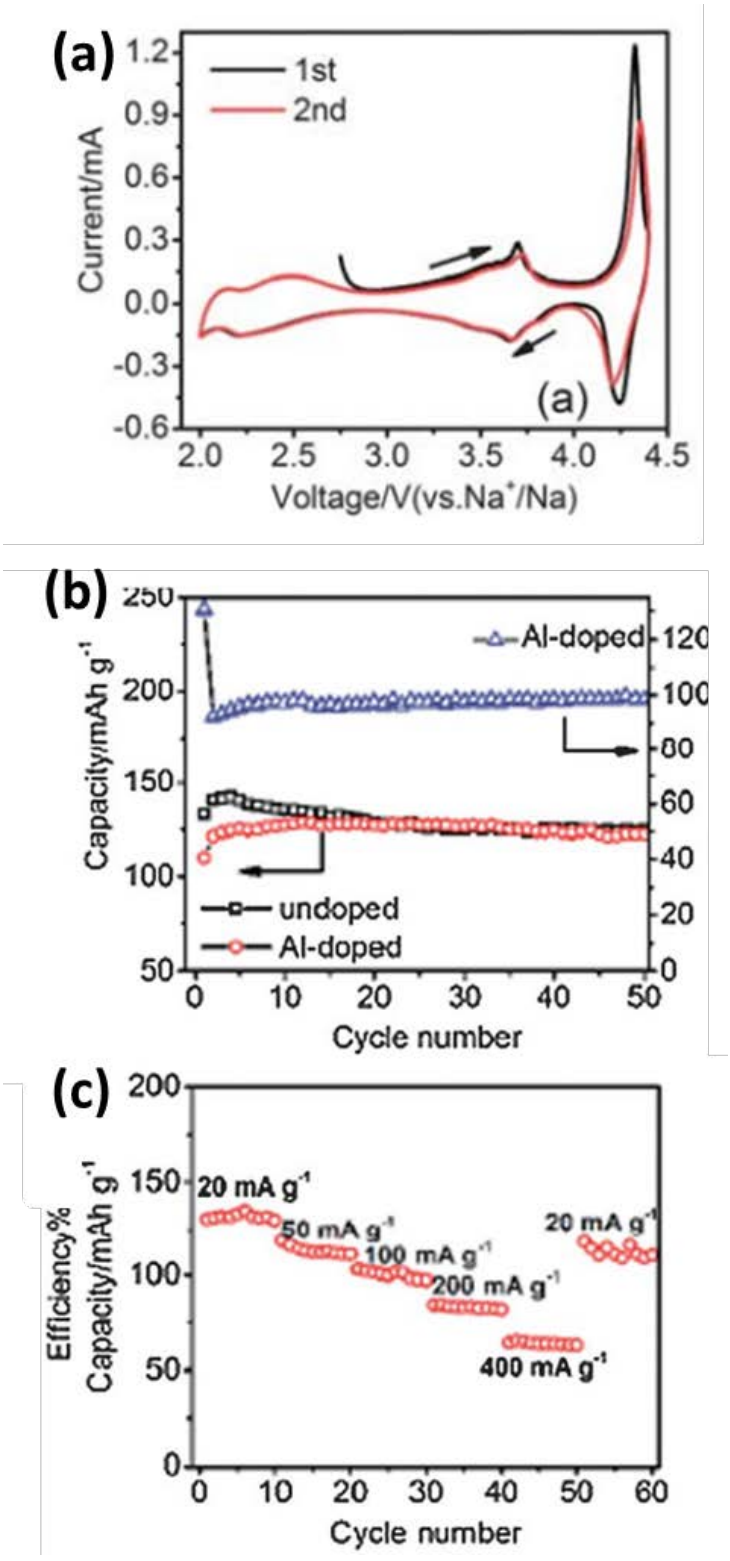


**Figure 2.12** (a) Cyclic voltammograms of NaMNC microflakes measured at a scan rate of 0.5 mV $s^{-1}$; (b) cycling performance of NaMNC and NaMNCA at a current density of 20 mA $g^{-1}$; (c) rate capability of NaMNCA at various current rates. [46]

### 2.2.2 Phosphate and fluorophosphate polyanionic compounds

#### 2.2.2.1 Olivine $NaFePO_4$

Olivine $NaFePO_4$ has been thoroughly studied as it has the highest theoretical specific capacity ((154 mAh $g^{-1}$) among phosphate polyanion cathode materials. In addition, it is interesting that the electrochemical behavior of $NaFePO_4$ is quite

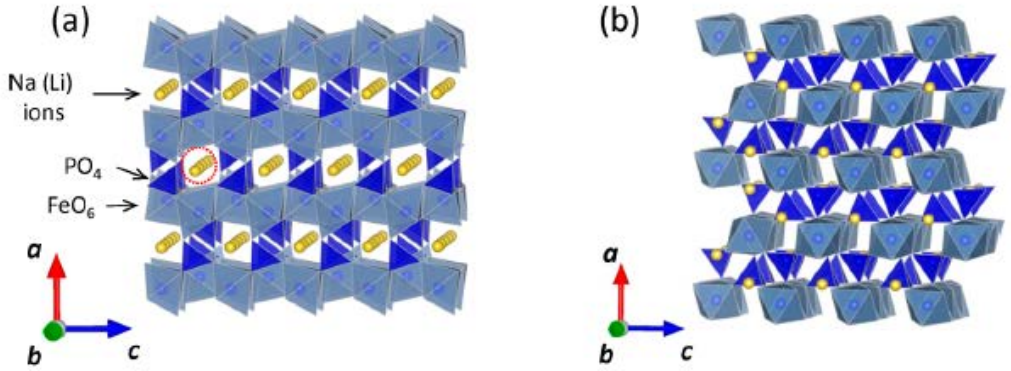


**Figure 2.13** Crystal structure of (a) $Na(Li)FePO_4$ (triphylite-type) and (b) $NaFePO_4$ (Maticite-type).[47]

different from electrochemical behavior of $LiFePO_4$, even though they have the same phase structure. As shown in Figure 2.13b, $NaFePO_4$ crystallizes in the maricite-type structure as the thermodynamically stable phase. Its crystal structure is also closely related to the olivine-type structure with a distorted hexagonal close packed (hcp) oxygen lattice. In comparison with triphylite-type $LiFePO_4$ (Figure 2.13a), there is a large gap in the ionic radii between Na and Fe, which results in significant distortion of the hcp oxygen lattice. Iron ions are located at octahedral sites, and the $FeO_6$ octahedra share edges, forming one-dimensional (1D) chains. The structure of 1D chains of $FeO_6$ in the maricite phase is essentially the same as the 1D $LiO_6$ chains in the triphylite phase. Sodium ions are located at large tetrahedral sites, which share corners with $PO_4$ tetrahedra (Figure 2.13b). Since sodium sites are isolated in the

structure as shown in Figure 2.28b, a large barrier for sodium migration is expected in the maricite-type $NaFePO_4$. Indeed, the reversibility of Na extraction/insertion for maricite-type $NaFePO_4$ as an electrode material seems to be unacceptable.[47, 48] In contrast, triphylite-type $NaFePO_4$ (olivine), which is a metastable polymorph of $NaFePO_4$, is electrochemically active.[47, 49] Triphylite-type $NaFePO_4$ can be prepared

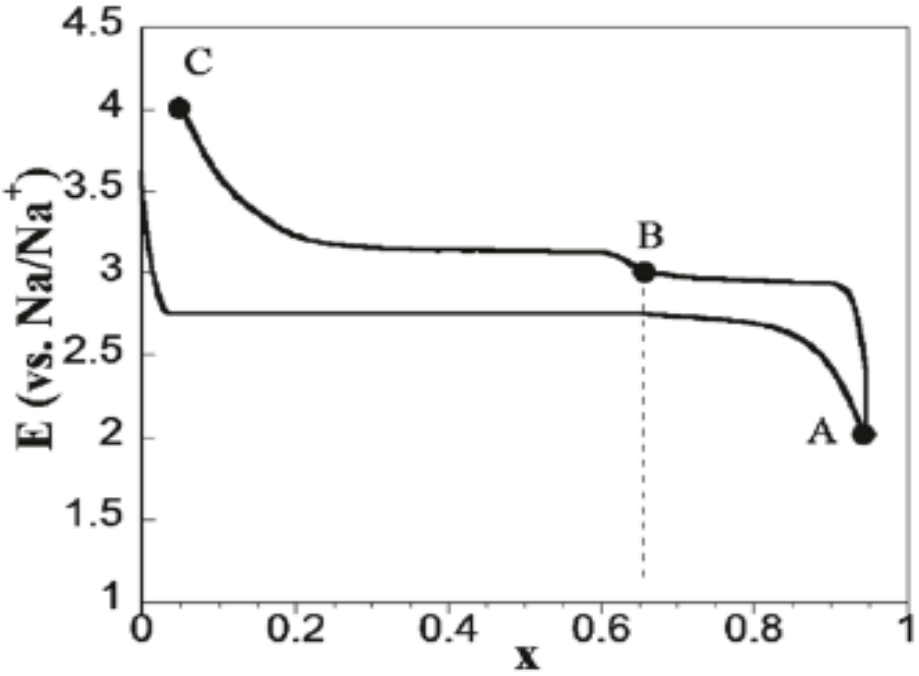


**Figure 2.14** Charge/discharge curves of NaFePO4 (triphylite-type) in NIBs.[49]

by an ion-exchange method from $LiFePO_4$, including chemical and electrochemical extraction of Li. Heterosite-type $FePO_4$ is formed without destruction of its core structure. Na+ is correspondingly inserted into heterosite-type $FePO_4$ to form triphylite-type $NaFePO_4$, which possesses the same framework structure as triphylite-$LiFePO_4$. Triphylite-type $NaFePO_4$ is stable below 480 °C under steady nitrogen flow and is able to transform into maricite-$NaFePO_4$ on further heating above 480 °C.[49, 50] The typical charge/discharge curves of triphylite-$NaFePO_4$ in a Na cell[49] are shown in Figure 2.14. Nearly 1 mol Na ions is reversibly

inserted/extracted into/from triphylite-$NaFePO_4$. Since the ionic radius of the sodium ion is much larger than that of the lithium ion, the unit cell volume of triphylite-$NaFePO_4$ is approximately 10% larger than that of triphylite-$LiFePO_4$. Two voltage plateaus are observed on discharge (Figure 2.14). The open-circuit voltage on the plateaus is observed to be between 2.87 and 2.97 V,[49] which is slightly lower than that of ~ 3.1 V vs Na expected from $LiFePO_4$ (3.45 V vs Li). The appearance of two voltage plateaus originates from the formation of an intermediate phase (a sodium-ion ordered phase) in the form of $Na_{0.4}FePO_4$ (point B in Figure 2.14). Such an intermediate phase is not generally found for $Li_xFePO_4$ under equilibrium conditions. The larger interaction of Na ions, in comparison to Li ions, could result in the occurrence of an intermediate phase,[49, 51] similar to the case of layered oxides. Wang's group prepared carbon-coated olivine $NaFePO_4$ (C-$NaFePO_4$) spherical particles by chemical delithiation and subsequent electrochemical sodiation of carbon-coated olivine $LiFePO_4$ (C-$LiFePO_4$).[51] From Figure 2.30a, C-$NaFePO_4$ can deliver a reversible capacity of ~ 100 mAh $g^{-1}$ over 100 cycles, with the Coulombic efficiency higher than 94%. Similar to Figure 2.14, two voltage plateaus appeared during charge and only one for discharge. Poor rate capability is shown in Figure 2.15c and d, and it implies the poorer kinetics of C-$NaFePO_4$ at high rate.

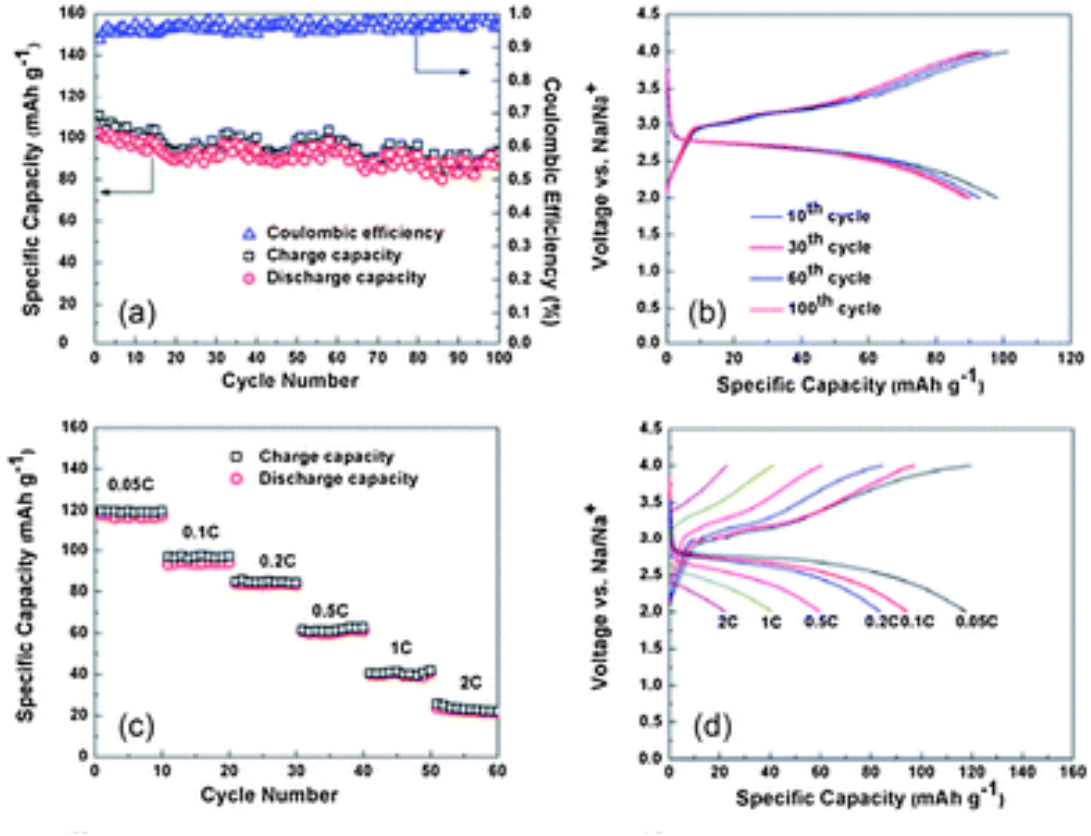


**Figure 2.15** (a) Cycling performance and Coulombic efficiency of C-$NaFePO_4$; (b) charge/discharge curves of C-$NaFePO_4$ tested at 15.4 mA $g^{-1}$(0.1 C). (c) Rate capability and (d) charge/discharge curves of C-$NaFePO_4$ tested at various C-rates.[52]

2.2.2.2 NASICON $Na_3V_2(PO4)_3$

Sodium vanadium (III) phosphate, $Na_3V_2(PO_4)_3$, has the sodium super-ionic conductor (NASICON)-type framework structure consisting of corner-sharing $FeO_6$ octahedra and $PO_4$ tetrahedra. It originates from $Na_{l+x}Zr_2P_{3-x}Si_xO_{12}$, which has a superior $Na^+$ network (Figure 2.16a). The name NASICON is an acronym for "$Na^+$ super ionic conductivity".[52,53] Ordering of Na ions in $Na_3V_2(PO_4)_3$ is observed to be

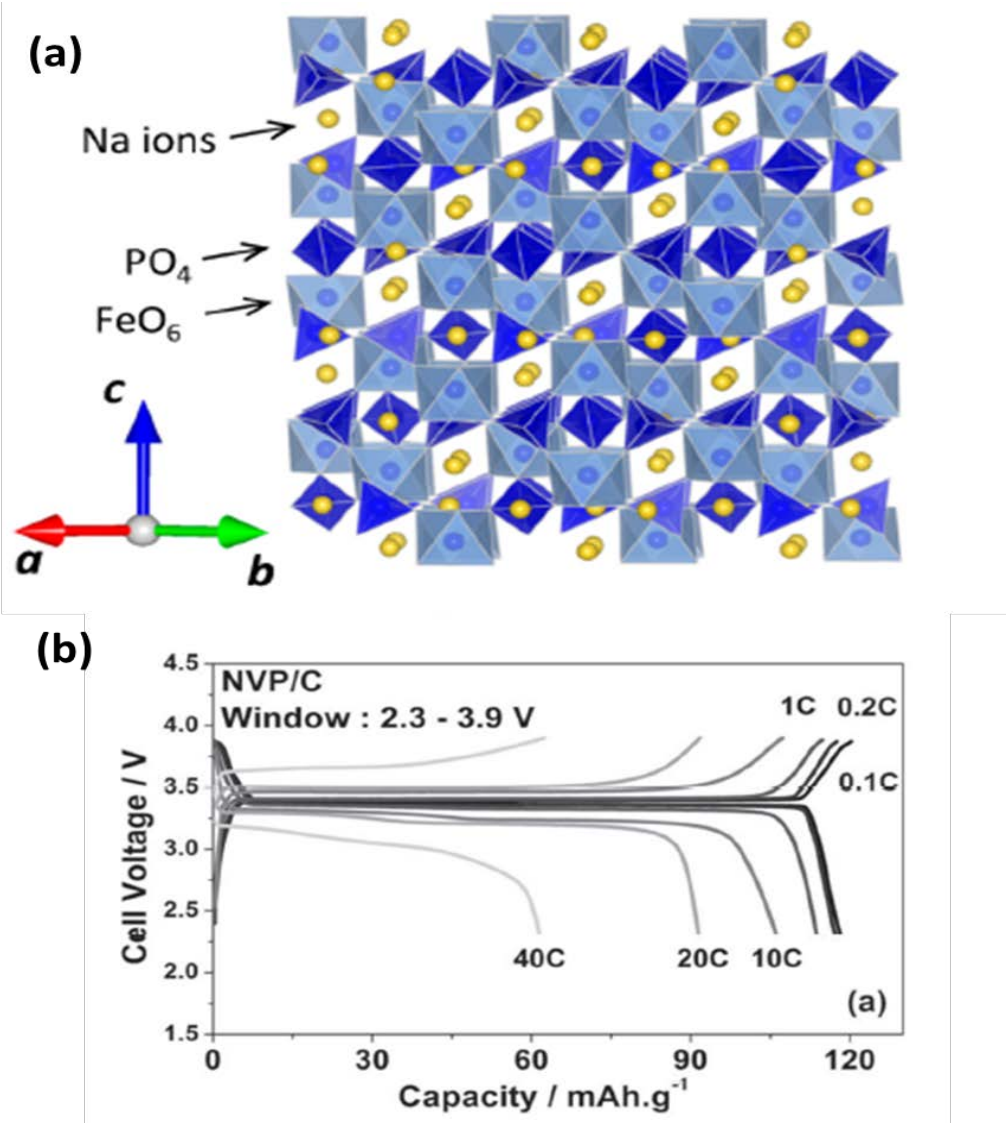


**Figure 2.16** (a) Crystal structure of $Na_3V_2(PO_4)_3$; (b) charge/discharge curves of $Na_3V_2(PO_4)_3$/C.[59]

the NASICON-type framework structure.[54] The full sodium-extracted phase ($V_2(PO_4)_3$) is prepared by chemical oxidation using $Cl_2$ gas without destruction of the framework structure.[55] $Li_3V_2(PO_4)_3$ can be prepared by $Na^+/Li^+$ exchange from $Na_3V_2(PO_4)_3$, and its electrode performance in Li cells has been reported.[54] Saravanan *et al.* reported the synthesis of carbon-coated nanosized $Na_3V_2(PO_4)_3$ by a solution-based approach. The $Na_3V_2(PO_4)_3$/C delivers reversible capacity of 120 mAh $g^{-1}$ (Figure 2.16b) with excellent capacity retention.[56] Recently, Ji's group reported that the open three-dimensional framework of NASICON-type NVP has two different Na sites, and that the ions extracted from the Na(2) sites would be mainly responsible for its electrochemical performance. The ion occupation of 0.75 for all Na sites is suitable for the configuration of $[Na_3V_2(PO_4)_3]_2$, and the two-step extraction is accompanied by structural reorganization.[57] The atomic structure and kinetics of sodium insertion into NASICON $Na_xV_2(PO_4)_3$ are studied in detail.[58]

#### 2.2.2.3 $Na_3V_2(PO4)_2F_3$

As shown in Figure 2.17a, the framework structure of $Na_3V_2(PO_4)_2F_3$ comprises $VO_4F_2$ octahedra and $PO_4$ tetrahedra, The $VO_4F_2$ and $VO_5F$ octahedra share four corners with $PO_4$ tetrahedra, forming $V_2(PO_4)_2O_2F$ and $V_2(PO_4)_2F_3$ layers. The $VO_4F_2$ and $VO_5F$ octahedra in the $V_2(PO_4)_2O_2F$ and $V_2(PO_4)_2F_3$ layers further share corners, forming the framework structure with two-dimensional (2D) paths for sodium along the *a-b* plane. Recently, $Na_3V_2(PO_4)_2F_3$ has been revisited, and excellent electrode performance has been reported.[60,61] $Na_3V_2(PO_4)_2F_3$ delivers 120 mAh $g^{-1}$ of reversible capacity (Figure 2.17b) with excellent cyclability and rate capability. The two voltage plateaus appear at 3.6 and 4.1 V.[60] The 2D diffusion paths for sodium ions in $Na_3V_2(PO_4)_2F_3$ were also evidenced by the results of first-

principles calculations.[61] $Na_3V_2(PO_4)_2O_2F$, as an isostructural composite of $Na_3V_2(PO_4)_2F_3$, has been studied. $Na_3V_2(PO_4)_2O_2F$/graphene composite demonstrated a high reversible capacity of 120 mAh $g^{-1}$ over 200 cycles, showing two plateaus at approximately 3.65 and 4.05 V on charge, and 4.0 and 3.6 V on discharge.[62]

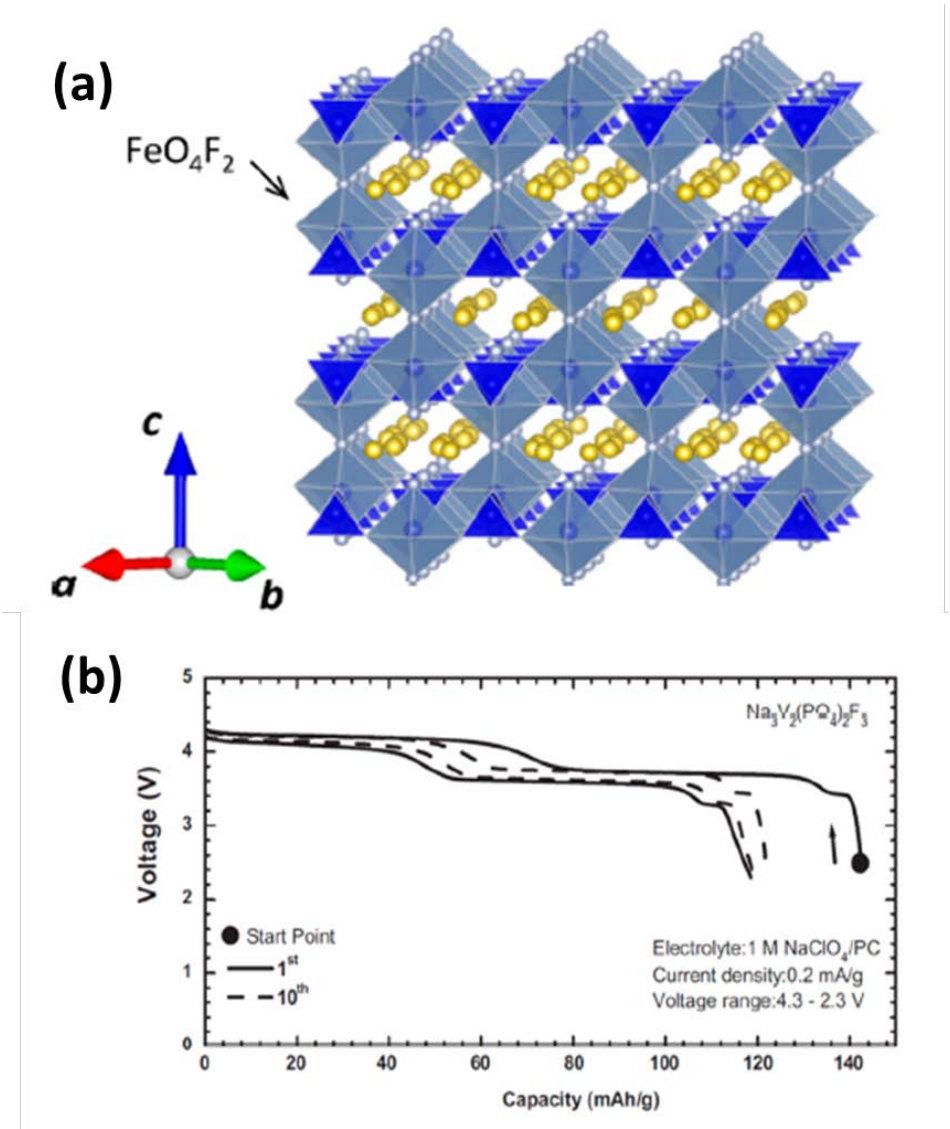


**Figure 2.17** (a) Crystal structure of $Na_3V_2(PO_4)_2F_3$; (b) charge/discharge curves of $Na_3V_2(PO_4)_2F_3$ for the 1st and 10th cycles.[60]

In summary, the most reported cathode materials with their reported capacities and operating voltages for NIBs can be found in Table 2.1.

**Table 2.1 Summary of cathode materials with their reversible capacity and operating voltage for sodium ion batteries.**

| Compound | Reversible capacity (mA h $g^{-1}$) | Operating voltage (V vs. $Na/Na^+$) |
|---|---|---|
| O3-$NaNiO_2$ | ~120 | ~3.4, 3.3, 3.0, 2.4 |
| O3- $NaFeO_2$ | ~80 | ~3.4 |
| O3-$NaCrO_2$ | ~100 | Slope curve during 3.3-3.0 |
| P2- $NaxCoO_2$ | ~140 | Multiple plateaux 2.25-3.75 |
| P3- $NaxCoO_2$ | ~130 | 2.25-3.75 |
| O3- $NaxCoO_2$ | ~120 | 2.25-3.75 |
| P2-$Na_{0.67}[Mn_{0.65}Ni_{0.15}Co_{0.2}]O_2$ | ~120 | 4.25, 3.65, 2.3 |
| Olivine $NaFePO_4$ | 154 | ~2.9 |
| NASICON $Na_3V_2(PO_4)_3$ | 117 | 3.5 |
| $Na_3V_2(PO_4)_2F_3$ | 130 | 3.6, 4.1 |
| $Na_3V_2(PO_4)_2O_2F$ | 120 | 3.6, 4.0 |
| $P_2$-$Na_x[Fe_{1/2}Mn_{1/2}]O_2$ | 190 | ~2.75 |
| O3-$Na[Ni_{1/3}Fe_{1/3}Mn_{1/3}]O_2$ | 100 | 2.75 |
| $Na_{0.44}MnO_2$ | 160 | ~2.75 |
| $Na_{0.45}[Mn_{0.66}Ni_{0.22}Co_{0.11}]O_2$ | 141 | 2.3, 3.65, 4.25 |
| $Na_3V_2O_{2x}(PO_4)2F_{3-2x}$ | 130 | 3.6, 4.1 |
| $NaFePO_4F$ | 124 | 2.9-3.0 |
| $Na_2FeP_2O_7$ | 97 | 2.5, 3.2 |
| $Na_2MnP_2O_7$ | 98 | ~3.5 |
| $NaFeSO_4F$ | 138 | 3.5 |
| Prussian blue analogues | ~200 | ~3.5 |
| Polymeric cathodes | ~173 | ~3.2 |
| $Na_7V_4(P_2O_7)_4PO_4$ | ~80 | 3.9 |
| $Na_2Fe_2(SO_4)_3$ | ~100 | 3.8 |
| $Na_2[Fe_{1/2}Mn_{1/2}]PO_4F$ | ~110 | 3.36, 3.04, 2.86 |
| P2-$Na_{1.0}Li_{0.2}Ni_{0.25}Mn_{0.75}O_\delta$ | ~100 | 2.0-4.2 |
| $Na_{2/3}[Ni_{1/3}Mn_{1/2}Ti_{1/6}]O_2$ | 127 | 3.7 |
| O3-$NaVO_2$ | ~120 | 2 |
| P2- $Na_{0.7}VO_2$ | ~120 | 2 |

### 2.3 Negative electrode materials

Significant progress on negative electrode materials for NIBs has been made during the past several years, extending from carbonaceous materials to alloy materials, phosphorus and phosphides, and metal oxides and sulfides. As shown in Figure 2.18, when various anode materials are paired with P2-$Na_{2/3}Fe_{1/2}Mn_{1/2}O_2$ cathode, the specific and volumetric energy densities of sodium full cells can reach 80-200 W h $kg^{-1}$ and 120-550 W h $L^{-1}$, respectively. When high-capacity anodes, such as P, Sn, or $SnO_2$, were applied, the energy density of NIBs was comparable to the performance of commercialized LIBs (150-200 W h Kg $^{-1}$, 400-650 W h $L^{-1}$). Since the electrode potential is generally low around 0-1 V vs. $Na/Na^+$, decomposition of the electrolyte solution at the negative electrode is a serious issue in terms of realizing long cycle life for battery applications. Therefore, selection of binders, additives, and electrolyte

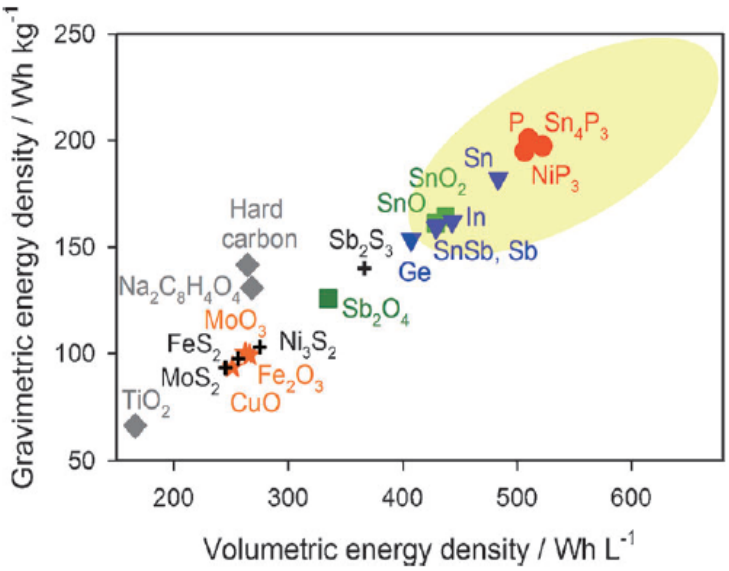


**Figure 2.18** Theoretical gravimetric and volumetric energy densities of full cells with various reported anode materials paired with P2-$Na_{2/3}Fe_{1/2}Mn_{1/2}O_2$ cathode for Na-ion batteries. The region of the yellow ellipse represents the energy density of commercialized LIBs.[64]

has a significant impact on the electrochemical behavior of negative electrodes, which is associated with the formation of surface passivation layers, namely, the solid electrolyte interphase (SEI) film.[63]

### 2.3.1 Carbon materials

#### 2.3.1.1 Graphite

Graphite is used as the commercial anode for LIBs due to its high gravimetric and volumetric capacity. It is electrochemically less active in NIBs, however, since $Na^+$ ions do not intercalate between carbon sheets.[65-67] Recently, Kim. *et al* reported unusual $Na^+$-solvent co-intercalation behavior in natural graphite in 2014.[68] As

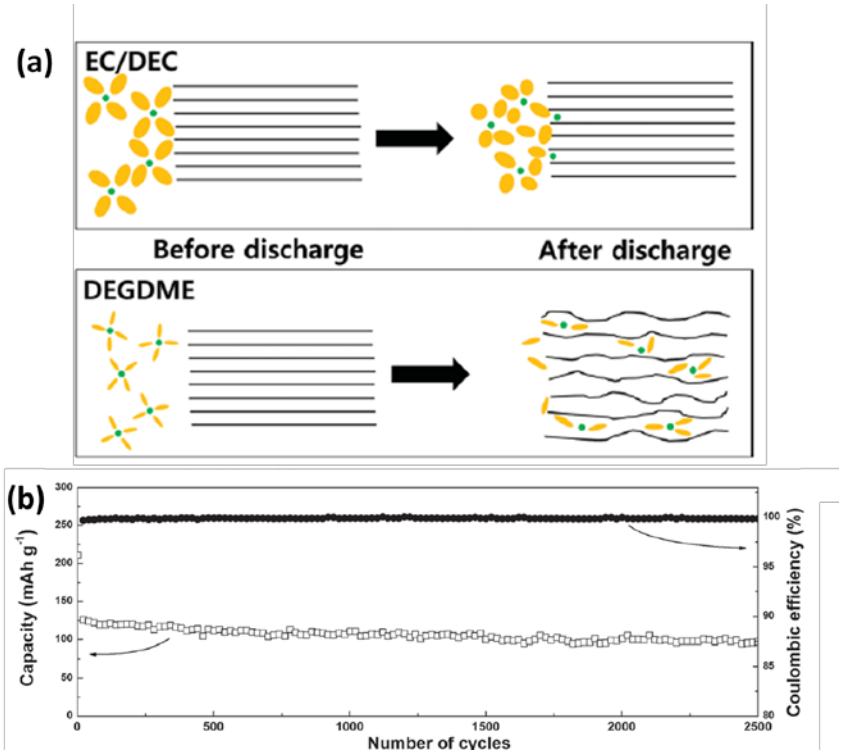


**Figure 2.19** (a) Proposed schematic of Na storage in nature graphite using selected electrolyte systems; (b) Cycling performance of natural graphite at 500 mA $g^{-1}$.[68]

shown in Figure 2.19a, the ether-based electrolyte, diethylene glycol dimethyl ether (DEGDME), has a high donor number. Ether-based electrolytes with a high donor

number can form stable $Na^+$ solvated species with non-polar characteristics for co-intercalation into natural graphite.

In addition, ether-based electrolytes could suppress electrolyte decomposition, resulting in the formation of a negligible SEI film on the graphite surface, enabling $Na^+$-solvent transport to the graphite lattice. On the other hand, carbonate-based electrolytes form relatively thick insulating SEI layers on the graphite surface, which block $Na^+$-solvent transport. Natural graphite delivered a reversible capacity of ~ 150 mAh $g^{-1}$ and the voltage could be varied from 0.6 V to 0.78 V (vs. $Na/Na^+$) by adjusting the chain length of the electrolyte solvents. Without any modification or treatment, natural graphite exhibited excellent cycling stability (~ 2500 cycles) and rate capability (~ 100 mAh $g^{-1}$ at 5000 mA $g^{-1}$).

2.3.1.2 Hard carbon

Hard carbon (HC) is composed of two domains, that is, carbon layers (graphene-like) and micropores (nanosized pores) formed between disorderly stacks of carbon layers. The electrochemical reversibility of Na insertion/extraction into/from HC at room temperature was first reported by Stevens and Dahn in 2000.[26] They prepared a HC sample by carbonization of glucose at 1000 °C, which delivered ~ 300 mAh $g^{-1}$ of reversible capacity in Na cells. Zhao *et al.*[69] fabricated HC by carbonization of organic polymer compound with an aromatic ring at 1600 °C, delivering a capacity higher than 300 mAh $g^{-1}$. In contrast to graphite, a much higher amount of Na ions can be reversibly inserted into hard carbon. Recently, Ponrouch *et al.*[70] demonstrated a capacity of ~ 326 mAh $g^{-1}$ at C/10 for HC anode with large particle size and low degree of graphitization prepared through pyrolysis of sugar. It maintained excellent

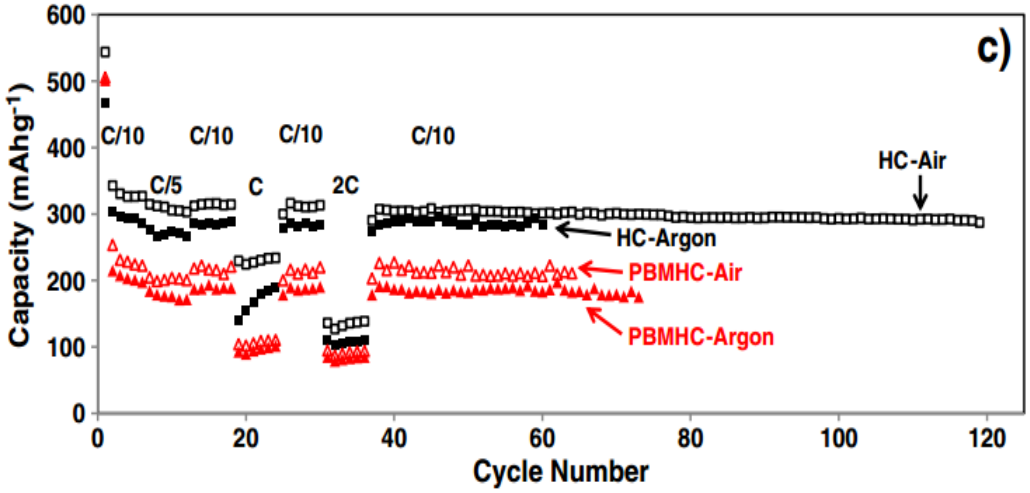


**Figure 2.20** Cycling performance of HC (black curves) and PBMHC (red curves) electrodes prepared through slurry mixed in air (dashed curves) or argon (solid curves).[70]

capacity retention (~ 300 mAh $g^{-1}$ after more than 120 cycles) and rate capability (~ 230 mAh $g^{-1}$ at 1C). A possible reaction mechanism is proposed, in which sodium ions are firstly inserted into the extended interstitial space, sandwiched between hexagonally bonded carbon layers, then further inserted into the micropores.[71,72] Meanwhile, some carbonaceous materials with disordered structure have been investigated. The reversible capacity of hollow carbon spheres reached 200 mAh $g^{-1}$ at a current density of 50 mA $g^{-1}$.[73] Hollow nanowires showed 251 mAh $g^{-1}$ reversible capacity for 400 cycles at 50 mA $g^{-1}$.[74] Hollow nanotubes deliver 250 mAh $g^{-1}$ reversible capacity at the same current of 50 mA $g^{-1}$ but over a narrower voltage range of 1.2–0.01 V vs. $Na^+/Na$ with 82% capacity retention for 400 cycles. The good cyclability is attributed to the short diffusion distance that sodium ions need to travel in the hollow carbon and the quite large average graphitic interplanar distance in the as-prepared nanowires. The N-doped material polypyrrole has also acted as the precursor for the synthesis of N-doped carbon nanosheets,[75] which exhibited larger

capacity (~ 300 mAh $g^{-1}$) than the nanofibres at the low current density of 50 mA $g^{-1}$, but only 50 mAh $g^{-1}$ at 20 A $g^{-1}$. Nevertheless the capacity retention over 10 cycles was less than 70 %.

### 2.3.2 Alloy materials

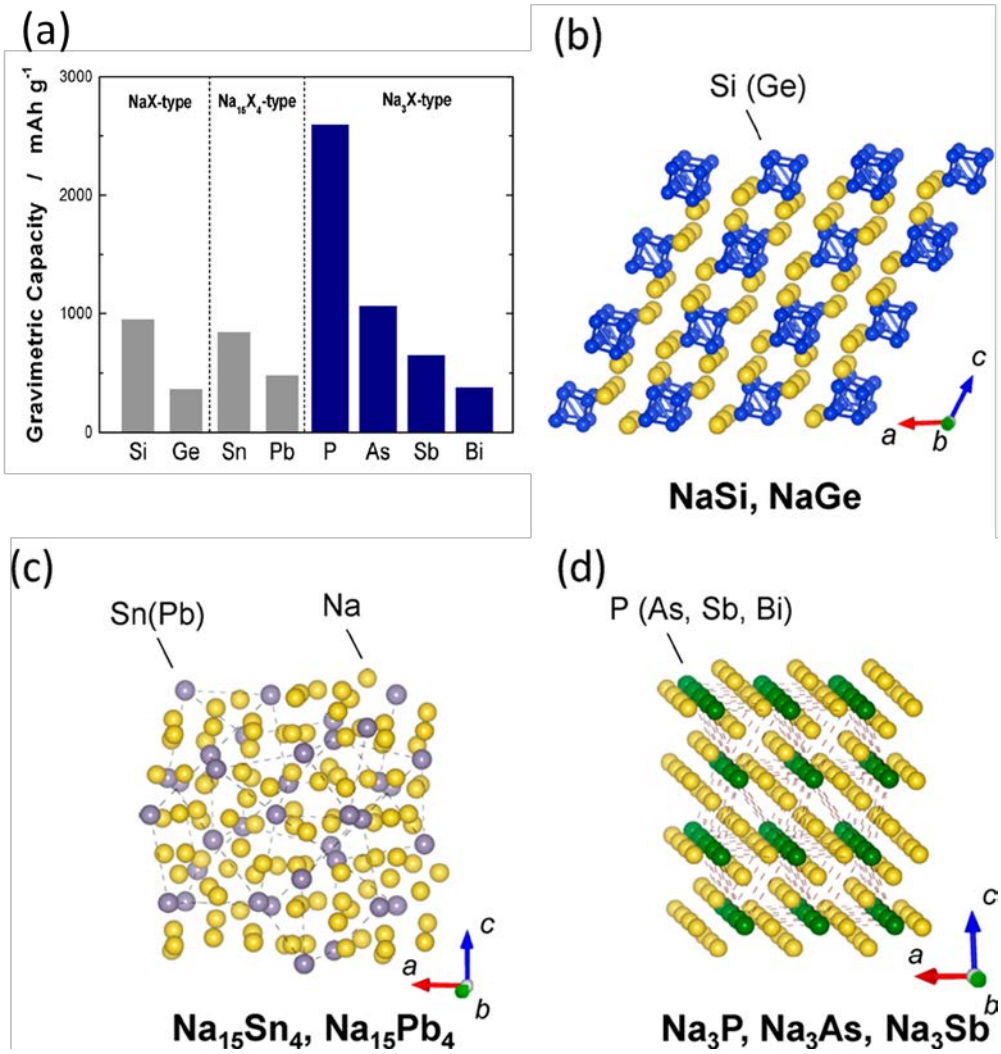


**Figure 2.21** (a) Theoretical gravimetric capacity estimated from phase diagrams for alloy materials; schematic illustrations of the most Na-rich phases for Si and Ge (b), Sn and Pb (c), and P, As, and Sb (d). Data derived from ref[75].

Metals (Sn, Pb, Bi), metalloids (Si, Ge, As, Sb), and a polyatomic non-metal (P), are known to form binary compounds with Na. These electrode materials, alloying with Na or forming Na binary compounds, have been recently studied as potential negative electrodes,[76-80] which offer a much higher capacity than carboneous materials. Large volume expansion, depending on the amount of Na ions incorporated into the structure, is unavoidable in this system, while in many cases the volume expansion for Na insertion materials does not exceed 120%. Therefore, during successive cycles of charge/discharge the alloying/dealloying material suffers from high mechanical stress and repeated passivation. The cracking in the composite electrodes leads to a loss of electrical contact and results in capacity loss.

2.3.2.1 Sb-based

Recently, many research groups have demonstrated that Sb features excellent electrochemical performance such as very stable capacity retention over 100 cycles and high reversible capacity of about 500-600 mAh $g^{-1}$.[81-86] In particular, despite the micronscale size of the bulk Sb particles used, Monconduit's group.[87] demonstrated that Sb reversibly alloys with Na, forming $Na_3Sb$, and showed the excellent cycling performance of Sb, with even better cycling performance for NIBs than for LIBs. They suggested that the better cycle performance of Sb for NIBs is caused by the smaller volume change exhibited by Sb during the insertion/de-insertion of $Na^+$ ions compared to that during the insertion/de-insertion of $Li^+$ ions. Reduction in the volume change improves the cycling performance because large volume changes lead to cracking and pulverization of the alloy materials and deformation of the electrodes, resulting in severe capacity fading. Baggetto *et al.*[81] suggested that the better cycling performance of Sb for Na-ion batteries can attributed to the reduced

| Table 2.2 Typical alloying reaction of Sb with Li and Na in electrochemical cells( *c*: crystalline; *a*: amorphous ) | | |
|---|---|---|
| | Na | Li |
| Discharge | *c*-Sb ⟶ *a*-$Na_xSb$ | *c*-Sb ⟶ *c*-$Li_2Sb$ |
| | *a*-$Na_xSb$ ⟶ *c*-$Na_3Sb$ (hex) | *c*-$Li_2Sb$ ⟶ *c*-$Li_3Sb$ |
| Charge | *c*-$Na_3Sb$ (hex) ⟶ *a*-Sb | *c*-$Li_3Sb$ ⟶ *c*-Sb |

anisotropic mechanical stress due to the repeated formation of only one crystalline phase for Na ($Na_3Sb$) as opposed to the repeated formation of three crystalline phases for Li (Sb, $Li_2Sb$, $Li_3Sb$), as shown by the reaction mechanism of Sb for Na and Li (Table 2.2). In particular, Sb is transformed into hexagonal $Na_3Sb$ through amorphous $Na_xSb$ during sodiation, while it is changed into cubic $Li_3Sb$ through $Li_2Sb$ during lithiation. The improved cycling performance was also suggested to be caused by the formation of stable SEI layers composed of thin NaF-like or fluroalkyl carbonate due to the addition of the fluoroethylene carbonate (FEC) additive. This compact SEI film can protect the Sb particles from the volume changes of the alloy particles during repeated charge and discharge cycling.[84] As shown in Figure 2.22, the Sb/C electrode in the electrolyte with 5% FEC exhibited superior cycling stability than the electrolyte without FEC.

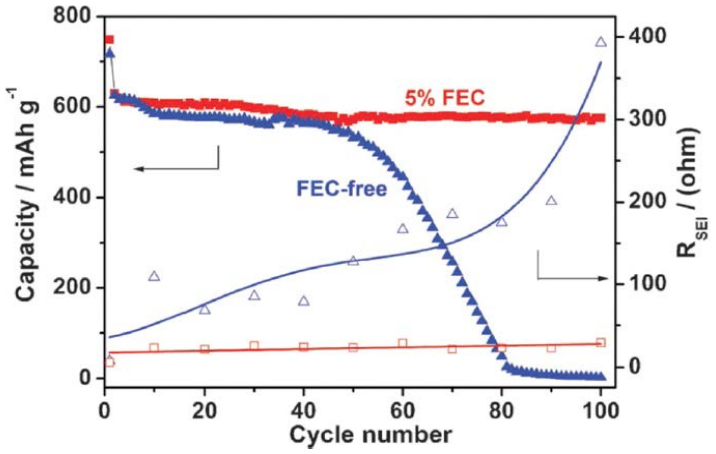


**Figure 2.22** Cycling performance of Sb/C anodes in electrolytes with and without FEC additive.[84]

2.3.2.2 Sn-based

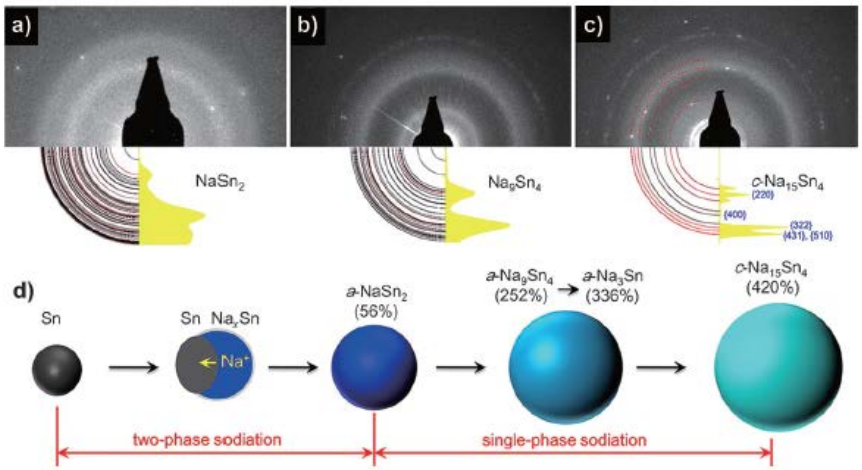


**Figure 2.23** Three *a*-$Na_xSn$ phases in the single-phase sodiation. Electron diffraction pattern (EDP) of (a) the first *a*-$Na_xSn$, (b) the second *a*-$Na_xSn$ phase, and (c) the third *a*-$Na_xSn$ phase; (d) schematic illustration of the structural evolution of Sn nanoparticles during the sodiation process.[84]

According to *in-situ* transmission electron microscope (TEM) analysis results (Figure 2.23), electrochemical alloying/dealloying for the Na−Sn system occurs in a series of phase transitions.[84] Sn nanoparticles (80–400 nm) were first sodiated to form amorphous $NaSn_2$ and Na-rich amorphous phases such as a-$Na_9Sn_4$ and *a*-$Na_3Sn$ through a two-phase reaction and a one-phase reaction, respectively. Afterwards, crystalline $Na_{15}Sn_4$ was finally obtained after full sodiation. The in situ TEM analysis also showed that Sn nanoparticles are expanded by about 420% after full sodiation, and this volume change is detrimental to the cycling performance of Sn. In order to address this large volume change of Sn, polyacrylic acid (PAA), a three–dimension cross-linkable binder, is utilized to inhibit the deformation of electrodes. Furthermore, when FEC is added to the electrolyte, the performance of the Sn electrode with PAA is further improved, owing to the formation of a stable SEI. The cycling performance

of Sn in Na-ion batteries was dependent on the voltage cut-offs shown in Figure 2.24. As the upper voltage limit was changed from 1.5 V to 0.8 V, the capacity retention was greatly improved.[88]

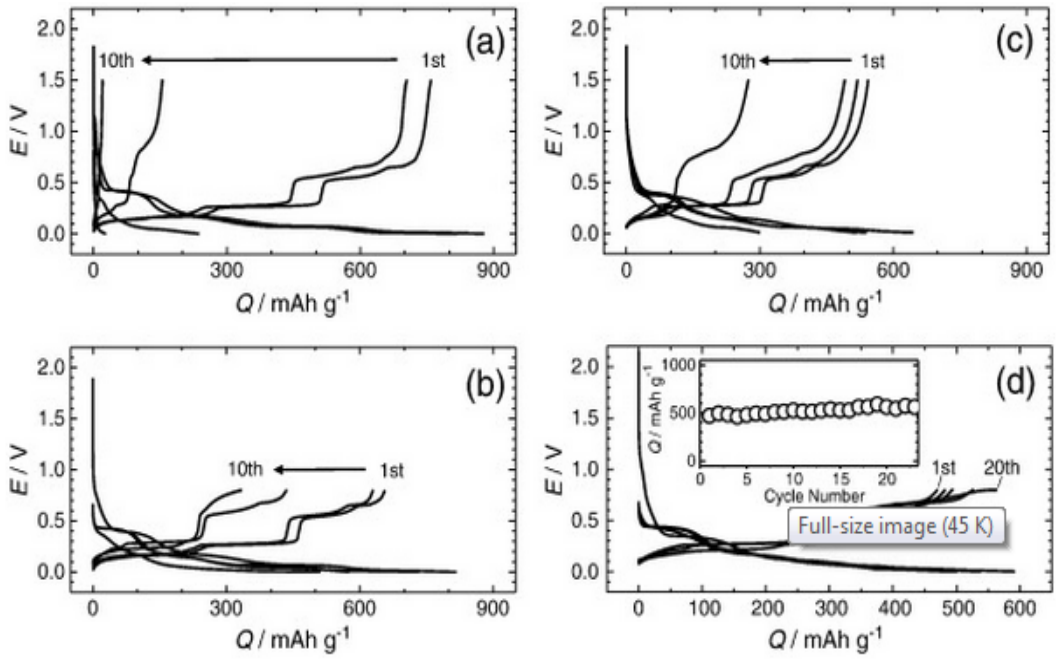


**Figure 2.24** Charge/discharge curves for selected cycles of Sn-PAA electrodes in (a, b) FEC-free and (c, d) FEC-containing electrolyte with the cut-off voltages of (a, c) 1.5-0.0 V and (b, d) 0.85-0.0 V. The inset to (d) shows the corresponding cycling performance.[88]

2.3.2.3 Phosphorus-based materials

In 2013, Lee and co-workers reported for the first time that amorphous red phosphorus/carbon composites showed excellent electrochemical performance in Na-ion batteries.[80] The amorphous red phosphorus/carbon composite powders were obtained by mechanical ball milling using amorphous red phosphorus (P) and Super P carbon. The composite delivered the highest reversible capacity (~ 1890 mAh $g^{-1}$) among all reported anode materials for NIBs. The high reversible capacity and low

redox potential of phosphorus enable Na-ion batteries to have energy densities similar to those of Li-ion batteries. The P/C composite also showed good rate performance, delivering 1540 mAh $g^{-1}$ with stable cyclability over 30 cycles at a current density of 2.86 mA $g^{-1}$. *Ex-situ* XRD analysis of the P/C composite during sodiation and desodiation revealed that $Na_3P$ is formed after full sodiation, which results in a volume change of 491 % between P and $Na_3P$. It is well known that PAA, carboxymethyl cellulose (CMC), and alginate binders are effective in accommodating the large volume changes of high-capacity anode materials such as Si for Li-ion batteries.[89, 90] Phosphorus is also an insulator with very poor electrical conductivity (~ $1\times10^{-14}$ S $cm^{-1}$), and thus the addition of electrically conductive materials such as carbon to phosphorus is necessary to improve the electrochemical performance of phosphorus in Na-ion batteries. Independently and simultaneously, Qian *et al.*[91] reported that an amorphous red phosphorus and carbon composite obtained by ball-milling showed excellent electrochemical performance, including, a high reversible capacity of 1750 mAh $g^{-1}$ and a stable cycle performance over 140 cycles. The improved cycling performance is ascribed to the formation of stable SEI layers because of the addition of the FEC additive. As demonstrated for alloy-based materials, the FEC additive was effective in enhancing the cycling performance of phosphorus. In addition, Li *et al.*[92] demonstrated that a simple mixture of phosphorus and carbon nanotubes (CNTs) obtained by hand-grinding showed good electrochemical performance, but its performance was worse than that of the phosphorus/carbon composite obtained by the mechanical ball milling. Recently, Komaba and co-workers also examined the role of FEC in the electrochemical performance of phosphorus.[93] A more stable reversible capacity of 1890 mAh $g^{-1}$ was obtianed in the phosphorus–carbon composites studied, which were prepared with

PAA binder; and *ex-situ* XRD data show the formation of $Na_3P$ at the end of discharge.[80] In addition, Monconduit and co-workers[94] examined $NiP_3$ for the first time as an anode in Na-ion batteries, and it delivered a high reversible capacity of 1000 mAh $g^{-1}$ with a capacity loss of 11% after 15 cycles. Lee and co-workers[95] recently reported that $Sn_4P_3$ showed excellent electrochemical performance for Na-ion batteries. $Sn_4P_3$ delivered a reversible capacity of about 700 mAh $g^{-1}$ and exhibited very stable cycling performance with negligible capacity fading over 100 cycles. Qian et al. and Li et al. also have recently examined the electrochemical performance of $Sn_4P_3$.[96, 97]

### 2.3.3 Metal oxides and sulfides

The sodium-storage mechanisms for metal oxides and sulfides can be divided into two types. In the first type of reaction, the M in $M_aX_b$ is an electrochemically inactive element such as Fe, Cu, Ni, or Co, and X is O or S. The sodiation/desodiation of these oxides proceeds via a conversion reaction:

$$M_aX_b + 2nNa + 2ne^- \leftrightarrow a\ M + b\ Na_nX\ (X = O, S) \qquad (2.1)$$

As shown in Figure 2.25, this type of reaction results in small volume change, usually leading to high capacity. Most metal oxides with inactive metal elements usually deliver relatively small reversible capacities of less than 400 mAh $g^{-1}$, in spite of their high theoretical capacities, for example, 1007, 674, 715, 1117, and 890 mAh $g^{-1}$ for $Fe_2O_3$, CuO, CoO, $MoO_3$, and $NiCo_2O_4$, respectively. Nanostructured γ-$Fe_2O_3$/α-$Fe_2O_3$ agglomerates delivered a reversible capacity of 300 mAh $g^{-1}$ with stable cycling performance over 60 cycles, while they showed a high polarization of > 1 V in the voltage profile.[98] The reversible capacity of $Fe_3O_4$ for Na-ion

batteries was also compared with that for Li-ion batteries, and it exhibited about 400 and 900 mAh $g^{-1}$, respectively.[99] $MoO_3$[100] and spinel $NiCo_2O_4$[101, 102] also was reported, showing smaller reversible capacities (410 and 200 mAh $g^{-1}$, respectively) than the theoretical values. In contrast, various transition metal sulfides, such as $FeS_2$ (pyrite),[103] CuS,[104] $Ni_3S_2$,

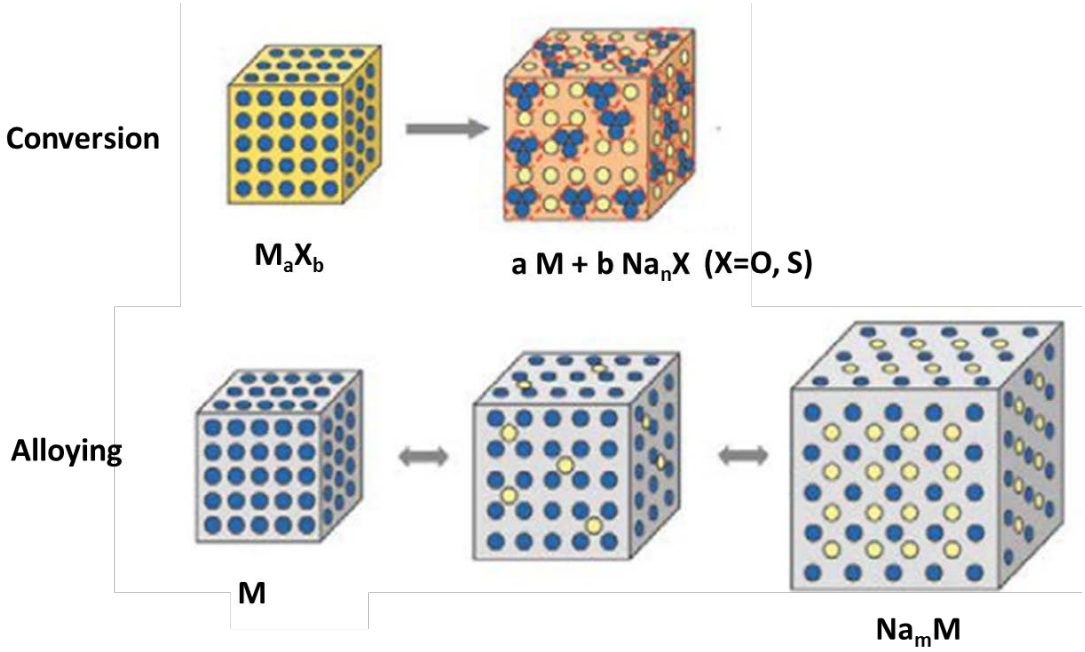


**Figure 2.25** Schematic representation of reaction mechanisms for metal oxides and sulfides in sodium-ion batteries.

[105] and $MoS_2$,[106] have shown promising electrochemical performance. $FeS_2$ and $Ni_3S_2$ delivered high reversible capacities of 630 mAh $g^{-1}$ at about 1.3 V and 420 mAh $g^{-1}$ at about 0.9 V, respectively. The reversible capacity of $MoS_2$ depended on the size of the $MoS_2$ particles and the species of carbon in the composite. The $MoS_2$ embedded in carbon nanofibers obtained by electrospinning had lateral dimensions of 4 nm and a thickness of 0.4 nm (Figure 2.26d) and delivered 1267 mAh $g^{-1}$ at a current density of 100 mA $g^{-1}$. The material exhibited excellent cycling stability at high current

densities (Figure 2.26e). The capacity was 484 mAh $g^{-1}$ at a current density of 1 A $g^{-1}$ after 100 cycles, while the value was 253 mAh $g^{-1}$ even at a current density of 10 A $g^{-1}$.[107] Meanwhile, $MoS_2$/RGO composite was also studied, which showed a reversible capacity of about 400 mAh $g^{-1}$.[108]

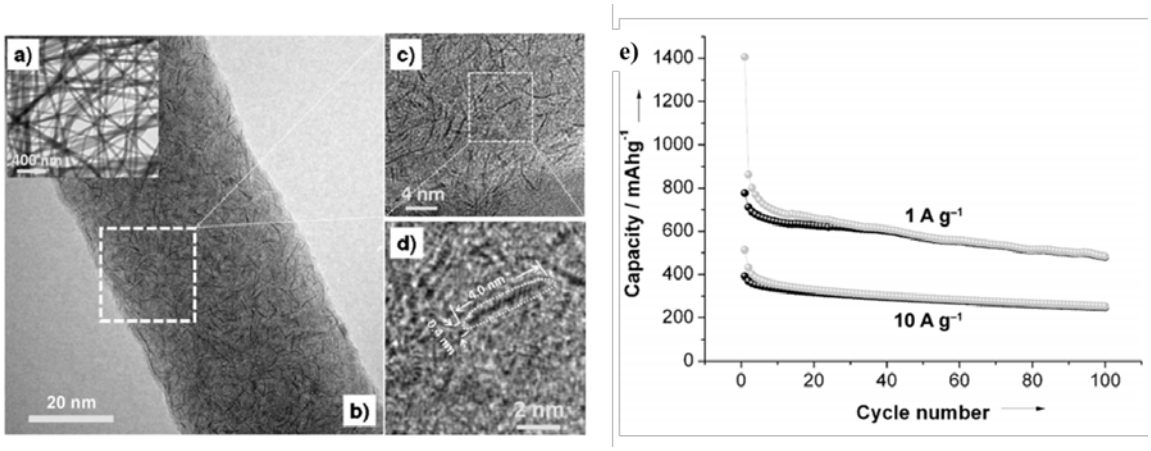


**Figure 2.26** (a) TEM- bright field (TEM-BF) micrograph. (b) High resolution TEM (HRTEM) showing the ultrathin $MoS_2$ embedded in the carbon nanofiber. (c), (d) Corresponding HRTEM images from the marked region in (b) and (c), respectively, to show the detailed structure of single-layered ultra-small $MoS_2$ embedded in the amorphous carbon; (e) cycling performance at different current rates of a single-layered $MoS_2$-carbon nanofiber composite for sodium batteries [107]

In the second type of reaction shown in Figure 2.25, the sodiation/desodiation of these oxides and sulfides proceeds via a conversion reaction and a further alloying reaction:

$$M_aX_b + 2n\ Na + 2\ ne^- \leftrightarrow a\ M + b\ Na_nX\ (X=O, S) \qquad (2.2)$$

$$M + m\ Na + m\ e^- \leftrightarrow Na_mX \qquad (2.3)$$

The reaction and failure mechanisms of $SnO_2$ were studied by in situ TEM analysis with density functional theory calculations.[109] During the discharge process

(sodiation), $SnO_2$ nanowires were changed into amorphous $Na_xSn$ nanoparticles dispersed in the $Na_2O$ matrix. Then, crystalline $Na_{15}Sn4$ was formed accompanied by a large volume expansion (>100% increase in diameter) after full sodiation. During the discharge process (desodiation), $Na_{15}Sn_4$ was transformed into Sn nanoparticles confined in a hollow matrix of $Na_2O$, as shown in Figure 2.27f. The formation of pores after desodiation increases the electrical impedance because of poor contact between the Sn and $Na_2O$, resulting in capacity fading.

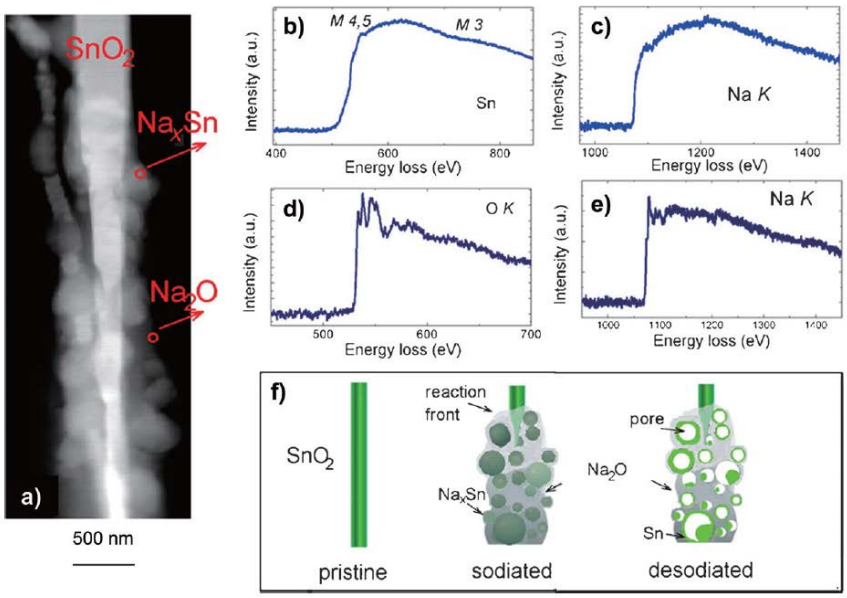


**Figure 2.27** (a) Scanning TEM (STEM) Z-contrast image showing the reaction front of the $SnO_2$ nanowire; and STEM – electron energy loss spectra (STEM-EELS) showing: (b) Sn M edge and (c) Na K edges obtained with the electron beam positioned in the particle with a higher brightness in the Z-contrast image; (d) O K edge and e) Na K edge with the electron beam positioned in the $Na_2O$ matrix region close to the surface, which gives a low brightness in the Z-contrast image; (f) schematic drawing showing the evolution of morphology the $SnO_2$ nanowire upon Na insertion and extraction.[109]

$Sb_2O_4$ thin films were also reported to deliver high reversible capacity of about 800 and 600 mAh $g^{-1}$ at 1/70 and 1/10 C-rates, respectively.[110] RGO/$Sb_2S_3$ composite showed a capacity of about 670 mAh $g^{-1}$, with capacity retention of 495 % after 50 cycles.[111] The reactions between $Sb_2S_3$ and sodium are expected to follow the equations as below:

Conversion reaction: $Sb_2S_3 + 6Na^+ + 6e^- \rightarrow 2Sb+3Na_2S$ (2.4)

Alloying reaction: $2Sb + 6Na^+ + 6e- \rightarrow 2Na_3Sb$ (2.5)

Through the same reaction mechanism, SnS@graphene composite also exhibited outstanding capacity stability, which delivered a specific capacity of 940 mAh $g^{-1}$ after 50 cycles at 30 mA $g^{-1}$, with capacity retention of 92.4 %.[112]

In conclusion, the main problem for Na alloys and compounds as electrode materials lies in the volume expansion of electrode materials correlated with destruction of the structures of starting materials in the reaction with Na. There are more tough challenges in the Na system compared with the Li system because the molar volume of Na is much larger than that of Li. The current research is essentially to control at least the unfavourable effects of volume changes of the electrodes during cycling and to suppress the loss of electronic conduction in the composite electrodes. These issues greatly penalize the cycling life and the kinetics of the charge/discharge reaction for batteries containing these electrode materials. Further optimization of alloy compositions and structures and careful study of the structural changes for the different alloy phases during the electrochemical reactions will lead to further improvement of the electrochemical performance. In addition, selection of binders

and electrolytes, which affect the interphase of the electrode materials, is an effective strategy as well.

## 2.4 Electrolytes

Electrolyte is a key component for battery performance, since it is directly associated with the formation of SEI film and the electron transfer. As compiled for electrolytes of LIBs, a good electrolyte should exhibit: (i) good ionic conductivity, (ii) a large electrochemical window (i.e., high and low onset potential for electrolyte decomposition through oxidation and reduction at high and low voltages, respectively), (iii) no reactivity towards the cell components, and (iv) a large thermal stability window (i.e. melting point and boiling point lower and higher than the standard temperatures for cell utilization, respectively). Finally, it should be intrinsically safe, have as low toxicity as possible and meet cost requirements for the targeted applications. All these features are intrinsically dependent on the nature of the Na-salts, the solvent(s) and the possible use of additives.

### 2.4.1 Sodium salts

The choice of Na-salts mainly affects the electrochemical stability and ionic conductivity. The choice of solvents decides the ion transport in total. Mostly the total ionic conductivity is expressed as the sum over all species *i* of the electrolyte for the 3-part product of: the number of charge carriers, $n_i$, their mobility, $m_i$, and their charge, $z_i$. The problematic point is that while the total ionic conductivity is easily measured, the ion transport itself, and more importantly, the part carried by the species of interest during migration, here $Na^+$, is cumbersome to attain. The sodium transference number ($t_{Na}$) that quantifies the Na transport is defined as:

$$t_{Na} = \mu_{Na} \sum \mu_i \qquad (2.6)$$

where $\mu$ is the relevant chemical potential. Rapid enough ion transport across the electrolyte is one of the fundamental requirements for operation at high power. This is dependent both on a fast enough ion transport in the bulk, to reduce polarisation resistance, and on the delivery and kinetics of the ion intercalation processes at the electrodes (charge transfer) including the transfer across the interfaces. The bulk ion transport properties will somewhat differ from LIBs to NIBs by virtue of different solvation shells, with $Na^+$ often exhibiting larger coordination numbers in solution than $Li^+$.

Table 2.3 Basic properties of the most commonly used Na-salts fro NIB electrolytes

| Salt | Anion chemical structure | $M_w$ [g mol$^{-1}$] | $T_m$ [°C] (Li-salt) | $\sigma$ [mS cm$^{-1}$][a] (Li-salt) |
|---|---|---|---|---|
| $NaClO_4$ |  | 122.4 | 468 (236) | 6.4 (5.6) |
| $NaBF_4$ |  | 109.8 | 384 (293) | (3.4) |
| $NaPF_6$ |  | 167.9 | 300 (200) | 7.98 (5.8) |
| NaTf | 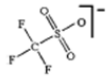 | 172.1 | 248 (>300) | (1.7) |
| NaTFSI | 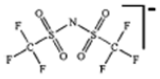 | 303.1 | 257 (234) | 6.2 (5.1) |
| NaFSI | 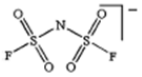 | 203.3 | 118 (130) | |

[a] 1 M NaX (LiX) in PC at 25 °C.

All the commonly used Na-salts are shown in Table 2.3, $ClO_4^-$ is a strong oxidant and therefore more or less banned for any practical cell development; $BF_4^-$ produces less conductive electrolytes by virtue of a stronger interaction with the cation, and thus, fewer charge carriers are present; $PF_6^-$ while being the anion of choice (the best compromise candidate) for LIBs has severe safety issues, especially at elevated temperatures and in the presence of moisture, suffering hydrolysis to yield $PF_5$, $POF_3$,

and HF; trifluoromethane sulfonate (Tf) has the same main problem as $BF4^-$ (less conductive electrolytes), and also corrodes the aluminium current collectors, which is also the main problem for the academically popular bis(trifluoromethanesulfonyl)imide (TFSI) anion. The corrosion has an onset potential at ~ 2.7 V vs. $Li/Li^+$ for Tf in a LIB electrolyte.[112]

### 2.4.2 Solvents

The solvents also need to comply with most of the prerequisites already set for the Na-salts: stable, non-toxic, inexpensive, etc. In addition, the presence of polar groups to dissolve sufficient amounts of Na-salt is a compulsory feature. The families of

Table 2.4 Solvents commonly used. Tm, Tb, Tf, η, ε, and AN/DN stand for the melting point, the boiling point, the flash point, the viscosity, the dielectric constant and the acceptor and donor numbers, respectively.

| Solvent | $T_m$ (°C) | $T_b$ (°C) | $T_f$ (°C) | $\eta$ (cP) 25 °C | $\varepsilon$ 25 °C | AN (DN) |
|---|---|---|---|---|---|---|
| 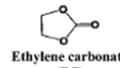 Ethylene carbonate (EC) | 36.4 | 248 | 160 | 1.9 (40 °C) | 89.78 | (16.4) |
| 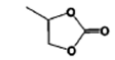 Propylene carbonate (PC) | −48.8 | 242 | 132 | 2.53 | 64.92 | 18.3 (15.1) |
| 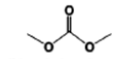 Dimethyl-carbonate (DMC) | 4.6 | 91 | 18 | 0.59 | 3.107 | |
| 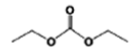 Diethyl carbonate (DEC) | −74.3 | 126 | 31 | 0.75 | 2.805 | (16.0) |
| 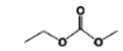 Ethylmethyl carbonate (EMC) | −53 | 110 | | 0.65 | 2.958 | |
| 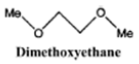 Dimethoxyethane (DME) | −58 | 84 | 0 | 0.46 | 7.18 | 10.9 (18.6) |
| 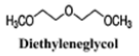 Diethyleneglycol dimethylether (Diglyme) | −64 | 162 | 57 | 1.06 | 7.4 | 9.9 (19.2) |
| 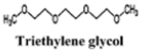 Triethylene glycol dimethyl ether (Triglyme) | −46 | 216 | 111 | 3.39 | 7.53 | 10.5 (14) |

organic solvents investigated are much the same as those used for LIBs:[113] organic carbonates (linear and cyclic), esters and ethers, for which the most significant properties are listed in Table 2.4. The electronic acceptor/donor capability of a solvent is important as it will influence the electrochemical stability window.[114]

### 2.4.3 Additives

The third major component is additives, which are basically new chemicals in small amounts used to address shortcomings of the original electrolyte. The limited amount needed originates from the preferred reactions taking place at the electrolyte/electrode interfaces rather than in the bulk of the electrolyte. Typical interface/surface actions by an additive are to modify the SEI, increase the wetting of the surface, and protect towards overcharging events by redox shuttles taking on the extra charge. There are also additives with actions that are more global to the electrolyte, including flame-retardants, fluidity enhancers/viscosity decreasers, impurity or radical scavengers, etc. Several common additives in LIBs were studied for NIB electrolytes,[115] including fluoroethylene carbonate (FEC), vinylene carbonate (VC), ethylene sulphite (ES) and transdifluoroethylene fluorinated EC (DFEC). The results pointed to a clear advantage of FEC with respect to the others. The film-forming additive, FEC, is noticeably effective to achieve good reversibility of the Na insertion in hard carbon with PC electrolyte, which is presumably associated with formation of a stable passivation layer at the surface of the hard carbon.[8, 115] The addition of FEC was proven to be detrimental in the electrolytes to allow the formation of a high quality SEI film, such as EC:PC, [70] for which a decrease in the reversible capacity and Coulombic efficiency by FEC addition was reported. The reduction process would not be able to access the low potential plateau

(at ~ 0.1 V vs. $Na/Na^+$) region probably due to the highly resistive nature of the surface layer formed by FEC addition with EC/PC mixtures. According to the research, the benefits of FEC stand out for electrode materials undergoing significant volume change, including $SnO_2$, Sn, Sb, SnSb, $Sb_2S_3$, $MoS_2$, and red phosphorus.[79, 87, 88, 111, 116, 117] Water contamination might affect the different influence of FEC. Interestingly, VC, very effective in the field of LIBs, was not found to act in the same way for NIBs.

### 2.4.4 General electrolytes

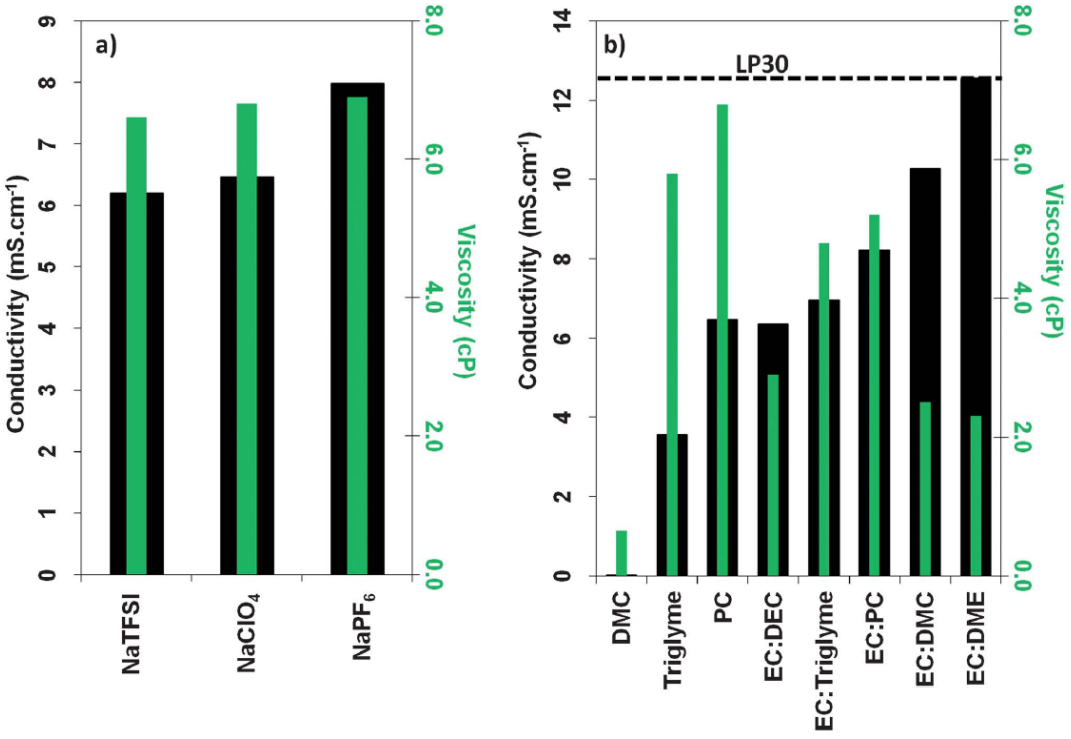


**Figure 2.28** Conductivity (black bars and left-hand-side y axis) and viscosity (green bars and right hand side y axis) values of (a) PC based electrolytes with 1 M of various Na salts and (b) electrolytes based on 1 M $NaClO_4$ dissolved in various solvents and solvent mixtures (LP30: 1M $LiPF_6$ in EC:DMC).[118]

Ponrouch *et al.*[118] did a systematic study on those electrolytes as well, Figure 2.28 illustrates a comparative survey of electrolytes prepared using several solvents (PC, EC, DMC, DME, DEC, THF and triglyme) and solvent mixtures (EC:DMC, EC:DME, EC:PC, and EC:triglyme) in combination with different Na salts, namely $NaClO_4$, $NaPF_6$, and NaTFSI.

The conductivity values for PC-based electrolytes (Figure 2.28a) are relatively similar, ranging from 7.98 mS $cm^{-1}$ for $NaPF_6$ to 6.2 mS $cm^{-1}$ for NaTFSI and intermediate for $NaClO_4$. This dependence upon the nature of the anion is consistent with what was previously reported for Li-based electrolytes.[119] It is associated with the lower polarizing character of the $PF_6^-$ anions, which would improve salt dissociation and enhance ionic mobility. In contrast, larger ionic conductivity variations were found by fixing the salt ($NaClO_4$) and changing the nature of the solvents with σ values following the trend EC:DME > EC:DMC > EC:PC > EC:triglyme > EC:DEC > PC > triglyme (Figure 2.28b). These results confirm that single-solvent-based electrolytes show much lower conductivity than binary-solvent-based electrolytes, this being true even for PC, which presents a very high dielectric constant value of 64.92. The addition of EC as a co-solvent strongly improved the ionic conductivity in all cases. The lowest ionic conductivity for binary mixtures was measured for EC:DEC (~ 6.35 mS $cm^{-1}$) and the highest for EC:DME (~ 12.55 mS $cm^{-1}$). Such differences in the values of ionic conductivity were found to be proportional to the dielectric constant of the EC co-solvent (PC > triglyme > DME > DMC > DEC, see Table 2.4). The only exceptions to this trend are PC and triglyme-based electrolytes which present lower ionic conductivity, most certainly due to their higher viscosity values as compared to other co-solvents (PC > triglyme > DEC >

DMC > DME). In conclusion, the nature of the co-solvent can enhance ionic conductivity through improving the dissociation of the salt (if the dielectric constant is high) and/or by lowering the viscosity of the resulting electrolyte and thus improving the ionic mobility. Similar viscosity values of about 6.8 cP are observed for PC-based electrolytes with 1 M NaTFSI, $NaClO_4$, or $NaPF_6$ (Figure 2.28a), which indicates that counter anions of Na-salts do not have a significant effect on the viscosity. On comparing the values measured for various solvents and solvent mixtures with 1 M $NaClO_4$ (Figure 2.28b), the viscosity of single solvent-based electrolytes (i.e. 1 M $NaClO_4$ in DMC, triglyme or PC) follows the same trend as for the solvent alone (PC > triglyme > DMC, see Table 2.5). The same observation has been made for binary solvent EC-based electrolytes (with 1 M $NaClO_4$), with their viscosities being proportional to that of the co-solvent, thus following the trend: EC:PC > EC:triglyme > EC:DEC > EC:DMC > EC:DME. Amongst single solvent based electrolytes (i.e. 1M $NaClO_4$ in DMC, triglyme or PC), PC possesses the highest ionic conductivity and the highest viscosity, which confirms that dissociation of the salt is the key parameter (i.e. high dielectric constant value). In contrast, for binary solvent-based electrolytes (i.e. 1 M $NaClO_4$ in EC:PC, EC:triglyme, EC:DEC, EC:DMC or EC:DME) the highest ionic conductivity is recorded for EC:DME even though DME does not exhibit the highest dielectric constant value (Table 2.4), yet it presents the lowest viscosity among all the binary-solvent-based electrolytes. This confirms that ion mobility is the most important factor here (i.e. low viscosity value), with the presence of EC already allowing good dissociation of the salt.

Figure 2.29 demonstrates the electrochemical stability window for all the electrolyte formulations studied. A combined plot (Figure 2.29b), which also lists the also

thermal stability values for those exhibiting suitable ionic conductivities and viscosities (Figure 2.28), allows the primary selection of the most suitable electrolytes for use in sodium ion cells. Rather than being rooted in thermodynamics, electrolyte inertness on active electrodes is usually related to kinetic limitations and the existence of chemical passivation layers.

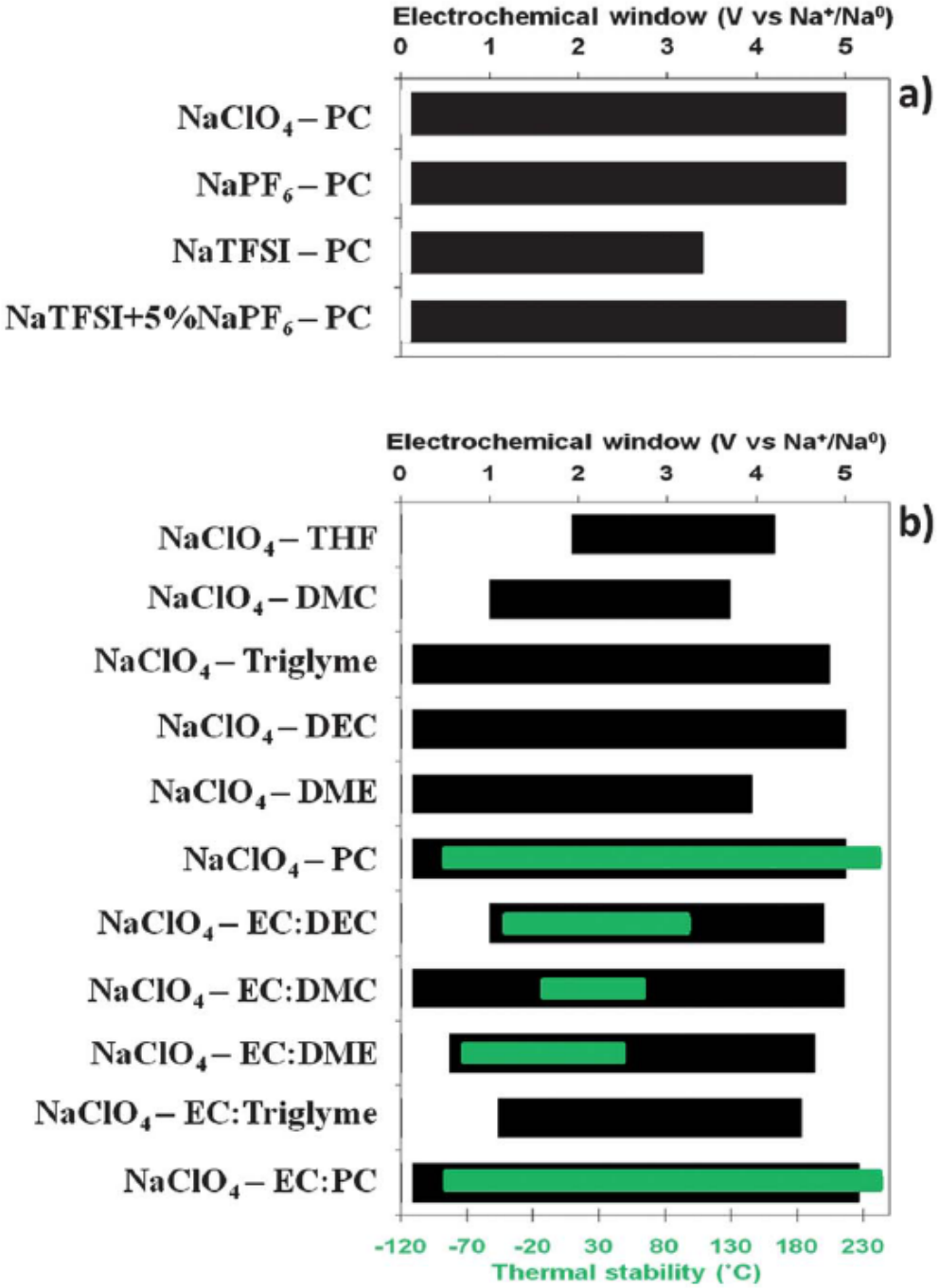


**Figure 2.29** Electrochemical potential window stability (black bars and upper y axis) and thermal range (green bars and lower y axis) values of (a) PC based electrolytes with 1 M of various Na salts, and (b) electrolytes based on 1 M $NaClO_4$ dissolved in various solvents and solvent mixtures.[118]

## 2.5 References


1. J. M. Tarascon and M. Armand, *Nature*, 2001, 414, 359-367.

2. M. Armand and J. M. Tarascon, *Nature*, 2008, 451, 652-657.

3. B. Dunn, H. Kamath and J.-M. Tarascon, *Science*, 2011, 334, 928-935.

4. R. S. Carmichael, *Practical Handbook of Physical Properties of Rocks a nd Minerals*, CRC Press, 1989.

5. F. Risacher and B. Fritz, *Aquatic Geochemistry*, 2009, 15, 123-157.

6. A. Yaksic and J. E. Tilton, *Resources Policy*, 2009, 34, 185-194.

7. M. D. Slater, D. Kim, E. Lee and C. S. Johnson, *Advanced Functional Materials*, 2013, 23, 947-958.

8. S. Komaba, W. Murata, T. Ishikawa, N. Yabuuchi, T. Ozeki, T. Nakayama, A. Ogata, K. Gotoh and K. Fujiwara, *Advanced Functional Materials*, 2011, 21, 3859-3867.

9. S.-W. Kim, D.-H. Seo, X. Ma, G. Ceder and K. Kang, *Advanced Energy Materials*, 2012, 2, 710-721.

10. A. Hayashi, K. Noi, A. Sakuda and M. Tatsumisago, *Nat Commun*, 2012, 3, 856.

11. M. S. Whittingham, *Science*, 1976, 192, 1126-1127.

12. M. S. Whittingham, *Progress in Solid State Chemistry*, 1978, 12, 41-99.

13. M. S. Whittingham, *Mater. Res. Bull.*, 1978, 13, 775-782.

14. G. H. Newman and L. P. Klemann, *Journal of The Electrochemical Society*, 1980, 127, 2097-2099.

15. K. Mizushima, P. Jones, P. Wiseman and J. Goodenough, *Mater. Res. Bull.*, 1980, 15, 783-789.

16. C. Delmas, J.-J. Braconnier, C. Fouassier and P. Hagenmuller, *Solid State Ionics*, 1981, 3, 165-169.

17. K. Abraham, *Solid State Ionics*, 1982, 7, 199-212.

18. C. Delmas, *Materials Science and Engineering: B*, 1989, 3, 97-101.

19. R. Kanno, Y. Takeda, T. Ichikawa, K. Nakanishi and O. Yamamoto, *Journal of Power Sources*, 1989, 26, 535-543.

20. M. Mohri, N. Yanagisawa, Y. Tajima, H. Tanaka, T. Mitate, S. Nakajima, M. Yoshida, Y. Yoshimoto, T. Suzuki and H. Wada, *Journal of Power Sources*, 1989, 26, 545-551.

21. R. Fong, U. von Sacken and J. Dahn, *Journal of The Electrochemical Society*, 1990, 137, 2009-2013.

22. T. Ohzuku, Y. Iwakoshi and K. Sawai, *Journal of The Electrochemical Society*, 1993, 140, 2490-2498.

23. P. Ge and M. Fouletier, *Solid State Ionics*, 1988, 28, 1172-1175.

24. M. M. Doeff, Y. Ma, S. J. Visco and L. C. De Jonghe, *Journal of The Electrochemical Society*, 1993, 140, L169-L170.

25. T. R. Jow, L. W. Shacklette, M. Maxfield and D. Vernick, *Journal of The Electrochemical Society*, 1987, 134, 1730-1733.

26. D. Stevens and J. Dahn, *Journal of The Electrochemical Society*, 2000, 147, 1271-1273.

27. N. Yabuuchi, K. Kubota, M. Dahbi and S. Komaba, *Chemical Reviews*, 2014, 114, 11636-11682.

28. N. Yabuuchi, M. Kajiyama, J. Iwatate, H. Nishikawa, S. Hitomi, R. Okuyama, R. Usui, Y. Yamada and S. Komaba, *Nature materials*, 2012, 11, 512-517.

29. C. Delmas, C. Fouassier and P. Hagenmuller, *Physica B+ C*, 1980, 99, 81-85.

30. R. I. Fielden and M. N. Obrovac, 2012.

31. P. Vassilaras, X. Ma, X. Li and G. Ceder, *Journal of The Electrochemical Society*, 2013, 160, A207-A211.

32. Y. Takeda, J. Akagi, A. Edagawa, M. Inagaki and S. Naka, *Mater. Res. Bull.*, 1980, 15, 1167-1172.

33. Y. Takeda, K. Nakahara, M. Nishijima, N. Imanishi, O. Yamamoto, M. Takano and R. Kanno, *Mater. Res. Bull.*, 1994, 29, 659-666.

34. N. Yabuuchi, H. Yoshida and S. Komaba, *Electrochemistry*, 2012, 80, 716-719.

35. N. Yabuuchi and S. Komaba, *Science and Technology of Advanced Materials*, 2014, 15, 043501.

36. J. J. Braconnier, C. Delmas and P. Hagenmuller, *Mater. Res. Bull.*, 1982, 17, 993-1000.

37. S. Komaba, C. Takei, T. Nakayama, A. Ogata and N. Yabuuchi, *Electrochemistry Communications*, 2010, 12, 355-358.

38. J.-J. Ding, Y.-N. Zhou, Q. Sun and Z.-W. Fu, *Electrochemistry Communications*, 2012, 22, 85-88.

39. X. Xia and J. Dahn, *Electrochemical and Solid-State Letters*, 2011, 15, A1-A4.

40. Y. Wang, Z. Liu and S. Zhou, *Electrochimica Acta*, 2011, 58, 359-363.

41. S.-K. Hu, G.-H. Cheng, M.-Y. Cheng, B.-J. Hwang and R. Santhanam, *Journal of Power Sources*, 2009, 188, 564-569.

42. X. Xia and J. Dahn, *Journal of The Electrochemical Society*, 2012, 159, A647-A650.

43. M. D'Arienzo, R. Ruffo, R. Scotti, F. Morazzoni, C. M. Mari and S. Polizzi, *Physical Chemistry Chemical Physics*, 2012, 14, 5945-5952.

44. J. Ding, Y. Zhou, Q. Sun, X. Yu, X. Yang and Z. Fu, *Electrochimica Acta*, 2013, 87, 388-393.

45. N. Yabuuchi, M. Kajiyama, J. Iwatate, H. Nishikawa, S. Hitomi, R. Okuyama, R. Usui, Y. Yamada and S. Komaba, *Nature Materials*, 2012, 11, 512-517.

46. D. Yuan, W. He, F. Pei, F. Wu, Y. Wu, J. Qian, Y. Cao, X. Ai and H. Yang, *Journal of Materials Chemistry A*, 2013, 1, 3895-3899.

47. K. Zaghib, J. Trottier, P. Hovington, F. Brochu, A. Guerfi, A. Mauger and C. Julien, *Journal of Power Sources*, 2011, 196, 9612-9617.

48. A. Sun, F. R. Beck, D. Haynes, J. A. Poston, Jr., S. R. Narayanan, P. N. Kumta and A. Manivannan, *Materials Science and Engineering B-Advanced Functional Solid-State Materials*, 2012, 177, 1729-1733.

49. P. Moreau, D. Guyomard, J. Gaubicher and F. Boucher, *Chemistry of Materials*, 2010, 22, 4126-4128.

50. M. Avdeev, Z. Mohamed, C. D. Ling, J. Lu, M. Tamaru, A. Yamada and P. Barpanda, *Inorganic Chemistry*, 2013, 52, 8685-8693.

51. M. Casas-Cabanas, V. V. Roddatis, D. Saurel, P. Kubiak, J. Carretero-Gonzalez, V. Palomares, P. Serras and T. Rojo, *Journal of Materials Chemistry*, 2012, 22, 17421-17423.

52. Y. Zhu, Y. Xu, Y. Liu, C. Luo and C. Wang, *Nanoscale*, 2013, 5, 780-787.

53. J. Goodenough, H.-P. Hong and J. Kafalas, *Mater. Res. Bull.*, 1976, 11, 203-220.

54. A. Ignaszak, P. Pasierb, R. Gajerski and S. Komornicki, *Thermochimica Acta*, 2005, 426, 7-14.

55. J. Gaubicher, C. Wurm, G. Goward, C. Masquelier and L. Nazar, *Chemistry of Materials*, 2000, 12, 3240-3242.

56. J. Gopalakrishnan and K. K. Rangan, *Chemistry of Materials*, 1992, 4, 745-747.

57. K. Saravanan, C. W. Mason, A. Rudola, K. H. Wong and P. Balaya, *Advanced Energy Materials*, 2013, 3, 444-450.

58. W. Song, X. Cao, Z. Wu, J. Chen, K. Huangfu, X. Wang, Y. Huang and X. Ji, *Physical Chemistry Chemical Physics*, 2014, 16, 17681-17687.

59. Z. Jian, C. Yuan, W. Han, X. Lu, L. Gu, X. Xi, Y.-S. Hu, H. Li, W. Chen, D. Chen, Y. Ikuhara and L. Chen, *Advanced Functional Materials*, 2014, 24, 4265-4272.

60. K. Saravanan, C. W. Mason, A. Rudola, K. H. Wong and P. Balaya, *Advanced Energy Materials*, 2013, 3, 444-450.

61. K. Chihara, A. Kitajou, I. D. Gocheva, S. Okada and J.-i. Yamaki, *Journal of Power Sources*, 2013, 227, 80-85.

62. R. A. Shakoor, D.-H. Seo, H. Kim, Y.-U. Park, J. Kim, S.-W. Kim, H. Gwon, S. Lee and K. Kang, *Journal of Materials Chemistry*, 2012, 22, 20535-20541.

63. M. Xu, L. Wang, X. Zhao, J. Song, H. Xie, Y. Lu and J. B. Goodenough, *Physical Chemistry Chemical Physics*, 2013, 15, 13032-13037.

64. E. Peled, *Journal of The Electrochemical Society*, 1979, 126, 2047-2051.

65. Y. Kim, K.-H. Ha, S. M. Oh and K. T. Lee, *Chemistry-A European Journal*, 2014, 20, 11980-11992.

66. G. E. Pascal and M. Fouletier, *Solid State Ionics*, 1988, 28, 1172-1175.

67. D. A. Stevens and J. R. Dahn, *Journal of The Electrochemical Society*, 2001, 148, A803-A811.

68. P. Thomas and D. Billaud, *Electrochimica Acta*, 2001, 46, 3359-3366.

69. H. Kim, J. Hong, Y.-U. Park, J. Kim, I. Hwang and K. Kang, *Advanced Functional Materials*, 2014, DOI: 10.1002/adfm.201402984.

70. J. Zhao, L. Zhao, K. Chihara, S. Okada, J.-i. Yamaki, S. Matsumoto, S. Kuze and K. Nakane, *Journal of Power Sources*, 2013, 244, 752-757.

71. A. Ponrouch, A. R. Goni and M. Rosa Palacin, *Electrochemistry communications*, 2013, 27, 85-88.

72. A. Mabuchi, K. Tokumitsu, H. Fujimoto and T. Kasuh, *Journal of The Electrochemical Society*, 1995, 142, 1041-1046.

73. D. A. Stevens and J. R. Dahn, *Journal of The Electrochemical Society*, 2000, 147, 4428-4431.

74. K. Tang, L. J. Fu, R. J. White, L. H. Yu, M. M. Titirici, M. Antonietti and J. Maier, *Advanced Energy Materials*, 2012, 2, 873-877.

75. Y. Cao, L. Xiao, M. L. Sushko, W. Wang, B. Schwenzer, J. Xiao, Z. Nie, L. V. Saraf, Z. Yang and J. Liu, *Nano Letters*, 2012, 12, 3783-3787.

76. H. G. Wang, Z. Wu, F. L. Meng, D. L. Ma, X. L. Huang, L. M. Wang and X. B. Zhang, *ChemSusChem*, 2013, 6, 56-60.

77. J. W. Wang, X. H. Liu, S. X. Mao and J. Y. Huang, *Nano Letters*, 2012, 12, 5897-5902.

78. L. Wu, X. Hu, J. Qian, F. Pei, F. Wu, R. Mao, X. Ai, H. Yang and Y. Cao, *Journal of Materials Chemistry A*, 2013, 1, 7181-7184.

79. L. Baggetto, J. K. Keum, J. F. Browning and G. M. Veith, *Electrochemistry Communications*, 2013, 34, 41-44.

80. A. Darwiche, M. T. Sougrati, B. Fraisse, L. Stievano and L. Monconduit, *Electrochemistry Communications*, 2013, 32, 18-21.

81. Y. Kim, Y. Park, A. Choi, N. S. Choi, J. Kim, J. Lee, J. H. Ryu, S. M. Oh and K. T. Lee, *Advanced Materials*, 2013, 25, 3045-3049.

82. L. Baggetto, P. Ganesh, C.-N. Sun, R. A. Meisner, T. A. Zawodzinski and G. M. Veith, *Journal of Materials Chemistry A*, 2013, 1, 7985-7994.

83. H. Hou, Y. Yang, Y. Zhu, M. Jing, C. Pan, L. Fang, W. Song, X. Yang and X. Ji, *Electrochimica Acta*, 2014, 146, 328-334.

84. M. He, K. Kraychyk, M. Walter and M. V. Kovalenko, *Nano Letters*, 2014, 14, 1255-1262.

85. J. Qian, Y. Chen, L. Wu, Y. Cao, X. Ai and H. Yang, *Chemical Communications*, 2012, 48, 7070-7072.

86. X. Zhou, Z. Dai, J. Bao and Y.-G. Guo, *Journal of Materials Chemistry A*, 2013, 1, 13727-13731.

87. Y. Zhu, X. Han, Y. Xu, Y. Liu, S. Zheng, K. Xu, L. Hu and C. Wang, *ACS Nano*, 2013, 7, 6378-6386.

88. A. Darwiche, C. Marino, M. T. Sougrati, B. Fraisse, L. Stievano and L. Monconduit, *Journal of the American Chemical Society*, 2012, 134, 20805-20811.

89. S. Komaba, Y. Matsuura, T. Ishikawa, N. Yabuuchi, W. Murata and S. Kuze, *Electrochemistry Communications*, 2012, 21, 65-68.

90. B. Koo, H. Kim, Y. Cho, K. T. Lee, N. S. Choi and J. Cho, *Angew. Chem.-Int. Edit.*, 2012, 51, 8762-8767.

91. I. Kovalenko, B. Zdyrko, A. Magasinski, B. Hertzberg, Z. Milicev, R. Burtovyy, I. Luzinov and G. Yushin, *Science*, 2011, 334, 75-79.

92. J. Qian, X. Wu, Y. Cao, X. Ai and H. Yang, *Angew. Chem.-Int. Edit.*, 2013, 52, 4633-4636.

93. W.-J. Li, S.-L. Chou, J.-Z. Wang, H.-K. Liu and S.-X. Dou, *Nano Letters*, 2013, 13, 5480-5484.

94. N. Yabuuchi, Y. Matsuura, T. Ishikawa, S. Kuze, J. Y. Son, Y. T. Cui, H. Oji and S. Komaba, *ChemElectroChem*, 2014, 1, 580-589.

95. J. Fullenwarth, A. Darwiche, A. Soares, B. Donnadieu and L. Monconduit, *Journal of Materials Chemistry A*, 2014, 2, 2050-2059.

96. Y. Kim, Y. Kim, A. Choi, S. Woo, D. Mok, N.-S. Choi, Y. S. Jung, J. H. Ryu, S. M. Oh and K. T. Lee, *Advanced Materials*, 2014, 26, 4139-4144.

97. J. Qian, Y. Xiong, Y. Cao, X. Ai and H. Yang, *Nano Letters*, 2014, 14, 1865-1869.

98. W. Li, S.-L. Chou, J.-Z. Wang, J. H. Kim, H.-K. Liu and S.-X. Dou, *Advanced Materials*, 2014, 26, 4037-4042.

99. M. Valvo, F. Lindgren, U. Lafont, F. Bjorefors and K. Edstrom, *Journal of Power Sources*, 2014, 245, 967-978.

100. S. Hariharan, K. Saravanan, V. Ramar and P. Balaya, *Physical Chemistry Chemical Physics*, 2013, 15, 2945-2953.

101. S. Hariharan, K. Saravanan and P. Balaya, *Electrochemistry Communications*, 2013, 31, 5-9.

102. A. Thissen, D. Ensling, F. J. F. Madrigal, W. Jaegermann, R. Alcantara, P. Lavela and J. L. Tirado, *Chemistry of Materials*, 2005, 17, 5202-5208.

103. R. Alcantara, M. Jaraba, P. Lavela and J. L. Tirado, *Chemistry of Materials*, 2002, 14, 2847.

104. T. Kim, J. Choi, H. Ryu, G. Cho, K. Kim, J. Ahn, K. Cho and H. Ahn, *Journal of Power Sources*, 2007, 174, 1275-1278.

105. J.-S. Kim, D.-Y. Kim, G.-B. Cho, T.-H. Nam, K.-W. Kim, H.-S. Ryu, J.-H. Ahn and H.-J. Ahn, *Journal of Power Sources*, 2009, 189, 864-868.

106. J.-S. Kim, G.-B. Cho, K.-W. Kim, J.-H. Ahn, G. Wang and H.-J. Ahn, *Current Applied Physics*, 2011, 11, S215-S218.

107. Y. N. Ko, S. H. Choi, S. B. Park and Y. C. Kang, *Nanoscale*, 2014, 6, 10511-10515.

108. C. Zhu, X. Mu, P. A. van Aken, Y. Yu and J. Maier, *Angewandte Chemie International Edition*, 2014, 53, 2152-2156.

109. L. David, R. Bhandavat and G. Singh, *ACS Nano*, 2014, 8, 1759-1770.

110. M. Gu, A. Kushima, Y. Shao, J.-G. Zhang, J. Liu, N. D. Browning, J. Li and C. Wang, *Nano Letters*, 2013, 13, 5203-5211.

111. Q. Sun, Q.-Q. Ren, H. Li and Z.-W. Fu, *Electrochemistry Communications*, 2011, 13, 1462-1464.

112. Y. Denis, P. V. Prikhodchenko, C. W. Mason, S. K. Batabyal, J. Gun, S. Sladkevich, A. G. Medvedev and O. Lev, *Nature Communications*, 2013, 4.

113. T. Zhou, W. K. Pang, C. Zhang, J. Yang, Z. Chen, H. K. Liu and Z. Guo, *ACS Nano*, 2014, 8, 8323-8333.

114. S. Y. Hong, Y. Kim, Y. Park, A. Choi, N.-S. Choi and K. T. Lee, *Energy & Environmental Science*, 2013, 6, 2067-2081.

115. A. Ponrouch, D. Monti, A. Boschin, B. Steen, P. Johansson and M. Palacín, *Journal of Materials Chemistry A*, 2015, 3, 22-42.

116. S. Komaba, T. Ishikawa, N. Yabuuchi, W. Murata, A. Ito and Y. Ohsawa, *ACS Applied Materials & Interfaces*, 2011, 3, 4165-4168.

117. Y.-X. Wang, Y.-G. Lim, M.-S. Park, S.-L. Chou, J. H. Kim, H.-K. Liu, S.-X. Dou and Y.-J. Kim, *Journal of Materials Chemistry A*, 2014, 2, 529-534.

118. Y.-X. Wang, K. H. Seng, S.-L. Chou, J.-Z. Wang, Z. Guo, D. Wexler, H.-K. Liu and S.-X. Dou, *Chemical Communications*, 2014, 50, 10730-10733.

119. A. Ponrouch, E. Marchante, M. Courty, J.-M. Tarascon and M. R. Palacin, *Energy & Environmental Science*, 2012, 5, 8572-8583.

120. D. Guyomard and J. Tarascon, *Solid State Ionics*, 1994, 69, 222-237.

# CHAPTER 3 EXPERIMENTAL METHODS

## 3.1 Experimental procedures

The research work in this thesis follows the procedures described in Figure 3.1. Firstly, various active anode materials were synthesized via simple methods that are easy to scale up, such as chemical reaction and the hydrothermal method. Furthermore, different physical characterization techniques were carried out to confirm and observe the properties of the as-prepared samples, including X-ray diffraction (XRD), scanning electron microscopy/ transmission electron microscopy/ energy dispersive X-ray spectroscopy (SEM/TEM/EDS), Raman spectroscopy, thermogravimetric analysis (TGA), and the Brunauer-Emmett-Teller (BET) surface area analysis technique. Finally, the corresponding electrochemical performance for Na-storage was explored, involving galvanostatic cycling, cyclic voltammetry (CV) and electrochemical impedance spectroscopy (EIS). Moreover, some physical characterization techniques (SEM, X-ray photoelectron spectroscopy (XPS), and XRD) were conducted to observe the morphology change and detect the possible reaction mechanism.

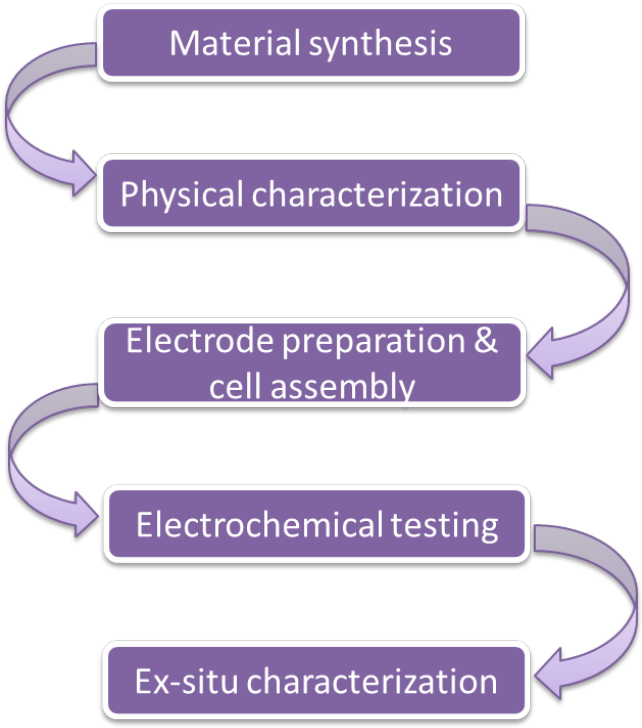


**Figure 3.1** Outline of experimental procedures and techniques conducted in this thesis.

### 3.2 Chemicals

The chemicals used in this thesis are summarized in details in Table 3.1.

Table 3.1 List of chemicals used in the thesis.

| **Chemicals** | **Formula** | **Purity (%)** | **Supplier** |
|---|---|---|---|
| Acetone | $(CH_3)_2CO$ | 99 | Ajax Finechem |
| Aluminium foil | Al | N/A | Vanlead Tech |
| Carbon black | C | Super P | Timcal graphite&Carbon |
| Copper foil | Cu | N/A | Vanlead Tech |
| CR2032 type coin cells | N/A | N/A | China |
| Diethyl carbonate (DEC) | $C_5H_{10}O_3$ | 99+ | Sigma Aldrich, Australia |
| Ethanol | $C_2H_5OH$ | Reagent | Q-store, Australia |
| Ethylene carbonate (EC) | 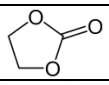 | 99 | Sigma Aldrich, Australia |
| Fluoroethylene carbonate | 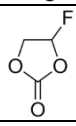 | N/A | Sigma Aldrich, Australia |
| Glucose | $C_{12}H_{22}O_{11}$ | 99 | Sigma Aldrich, Australia |
| Graphite | C | N/A | Sigma Aldrich, Australia |
| Hexane | $CH_3(CH_2)_4CH_3$ | 95 | Sigma Aldrich, Australia |
| Hydrochloric acid | HCl | 36.5 | Sigma Aldrich, Australia |
| Hydrogen peroxide | $H_2O_2$ | 30 | Sigma Aldrich, Australia |
| Milli-Q Water | $H_2O$ | 5 ppb (TOC) | Millipore, USA |
| Molybdenum(IV) sulfide | $MoS_2$ | 99 | Sigma Aldrich, Australia |
| Multi-wall carbon nanotubes (MWCNTs) | C | 95 | NanoAmor |
| n-butyl lithium solution |  | 2.5 M in hexanes | Sigma Aldrich, Australia |
| Nitric acid | $HNO_3$ | 69 | Sigma Aldrich, Australia |
| N-methyl-2-pyrrolidone | 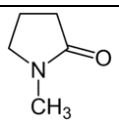 | 99.5 | Sigma Aldrich, Australia |

| | | | |
|---|---|---|---|
| Poly (acrylic acid) (MW=130,000) | 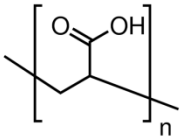 | N/A | Sigma Aldrich, Australia |
| Polyvinylidene difluoride (MW=543,000) | 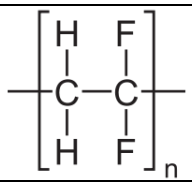 | N/A | Sigma Aldrich, Australia |
| Potassium permanganate | $KMnO_4$ | 99 | Sigma Aldrich, Australia |
| Propylene carbonate | 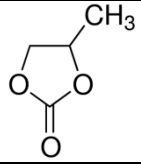 | 99.7 | Sigma Aldrich, Australia |
| Sodium carbonate | $Na_2CO_3$ | 99 | Sigma Aldrich, Australia |
| Sodium carboxymethyl cellulose (MW = 90,000) | 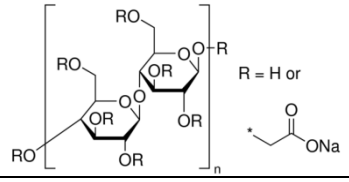 | N/A | Sigma Aldrich, Australia |
| Sodium cubes (stored in mineral oil) | Na | 99.9 | Sigma Aldrich, Australia |
| Sodium ingot | Na | 99.95 | Sigma Aldrich, Australia |
| Sodium nitrate | $NaNO_3$ | 99 | Sigma Aldrich, Australia |
| Sodium perchlorate | $NaClO_4$ | 98 | Sigma Aldrich, Australia |
| Sulfuric acid | $H_2SO_4$ | 98 | Sigma Aldrich, Australia |
| Sulfur | S | 99.5+ | Sigma Aldrich, Australia |
| Tin (II) chloride dihydrate | $SnCl_2\ 2H_2O$ | 96 | Fluka, Australia |
| Tin (II) chloride dihydrate | $SnCl_2\ 2H_2O$ | 96 | Sigma Aldrich, Australia |

## 3.3 Methodology and theory of experiments

### 3.3.1 Liquid exfoliation

Liquid exfoliation is a process of exfoliating layered materials into mono- or few-layers by chemical reaction or intercalation. Such a technique involves introducing guest species in-between the gaps of the host layered materials then separating them. Specifically, graphene oxides were prepared by a modified Hummers' method, treating graphite with a mixture of sulfuric acid ($H_2SO_4$), sodium nitrate ($NaNO_3$), and potassium permanganate ($KMnO_4$). Strong acids are able to insert themselves into the interlayer space of graphite, leading to oxidation of the graphite, enlargement of the layer distance, and disorder of the layered structure. Molybdenum disulfide ($MoS_2$) is a black inorganic layered material with a structure similar to that of graphite. From a similar viewpoint, n-butyl lithium was utilized to intercalate into $MoS_2$ interlayers. When the interacting lithium was washed out from $Li_xMoS_2$, higher disorder degree and larger interlayer distance could be achieved. In addition, ultra-sonication is an important procedure for realizing better exfoliation and guaranteeing homogeneous dispersion. Meanwhile, centrifuging is a key step to remove un-exfoliated impurity.

### 3.3.2 Hydrothermal method

The hydrothermal method is a process to gradually crystallize substances from high-temperature aqueous solutions at high vapour pressures. This method is extremely efficient for crystal growth and nanomaterials synthesis. As shown in Figure 3.2, the device consists of a polytetrafluoroethylene (PTFE) vessel and a stainless steel protector. The composition, morphology, and crystal structure of the products is associated with several factors. The volume of the solvent is related to the pressure of

the autoclave. Generally, the solution volume is controlled to be below 2/3 of the volume of the Teflon-liner due to the safety issue. The concentration of the precursors is responsible for the size and morphology of the products. The temperature for hydrothermal synthesis is a key parameter as well, directly deciding the final resultant. Thus, the relevant parameters should be considered in order to fabricate target materials.

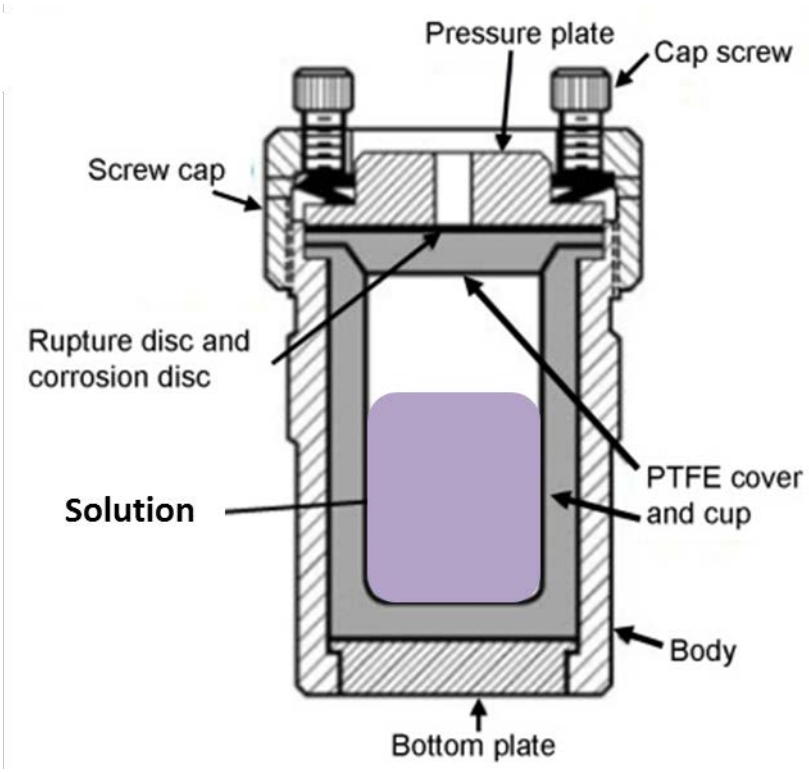


**Figure 3.2** Schematic diagram of stainless steel autoclave.

## 3.4 Characterization and measurement methods

### 3.4.1 X-ray diffraction

X-ray diffraction (XRD) is a direct and powerful experimental technique to determine the structural characterization of materials, using the diffraction of X-rays on powder or microcrystalline samples. X-rays can be considered waves of electromagnetic radiation, and crystals are regular arrays of atoms. When X-rays go through a specimen, the periodic lattice found in crystalline structures acts as a diffraction grating for electromagnetic radiation with wavelengths of a similar order of magnitude. X-rays scattered by ordered features will be scattered coherently "in-phase" in certain directions meeting the criteria for constructive interference, which are determined by Bragg's law:

$$2d\sin\theta = n\lambda \qquad (3.1)$$

where $d$ is the distance between lattice planes, $\lambda$ is the X-ray wavelength of the incident beam, $n$ is any integer, and $\theta$ is the angle of incidence with the lattice plane. The crystal size of materials can also be estimated and calculated according to the Scherrer formula:

$$D = \frac{K\lambda}{\beta\cos\theta} \qquad (3.2)$$

where $K$ represents the shape factor of the average crystallite (with a typical shape factor around 0.9), $\lambda$ represents the X-ray wavelength, $\beta$ represents the half-peak width, and $2\theta$ represents the peak position (°).

In the X-ray diffractometer, the copper anode is irradiated with a beam of high-

energy electrons that is accelerated by a high voltage electric field to a very high speed. A small Be window in the X-ray tube allows the X-rays to exit the tube with little attenuation, while maintaining the vacuum seal required for the X-ray tube operation. In this thesis, X-ray powder diffraction was conducted. Powder samples are loaded onto a small disc-shaped sample holder, which is put on one axis of the diffractometer and tilted by an angle $\theta$, while a detector rotates around it on an arm at a $2\theta$ angle. The XRD devices used in this thesis were a GBC MMA diffractometer in UOW and an EMPYREAN, PAN analytical X-ray diffractometer in KETI, respectively. All the XRD devices use Cu Kα radiation, $\lambda$ = 1.54056 Å.

### 3.4.2 Scanning electron microscopy

The scanning electron microscope (SEM) is a type of electron microscope to scan a sample surface with a high-energy beam of electrons. The electrons interact with atoms in the sample, producing various signals that can be detected and that contain information about the sample's surface topography and composition. Typically, an electron beam is thermionically emitted from an electron gun fitted with a tungsten filament cathode. The electron beam usually has an energy ranging from 0.2 to 40 keV. Then it is focused by one or two condenser lenses to a spot about 0.4 nm to 5 nm in diameter. The beam passes through pairs of scanning coils or pairs of deflector plates in the electron column, typically in the final lens, which deflects the beam with respect to the x and y axes so that it scans in a raster fashion over a rectangular area of the sample surface. The types of signals produced by an SEM include secondary electrons, back-scattered electrons (BSE), characteristic X-rays, light specimen currents, and transmitted electrons. Secondary electron detectors are common used in all SEM, which can offer very high resolution images. The morphology and structure

of samples in this thesis were characterized with a field-emission scanning electron microscope (FESEM; JEOL JSM-7500FA in KETI or JEOL 7500 in UOW, respectively).

### 3.4.3 Transmission electron microscopy

Transmission electron microscopy (TEM) is a technique to observe sample's morphology, lattice spacing, crystal orientation and electronic structure. When a beam of electrons is transmitted through an ultra-thin specimen, the specimen will interact with the electrons, and then an image is collected during the interaction. TEM is capable of significantly higher resolution imaging than light microscopes. Selected area electron diffraction (SAED) is a crystallographic experimental technique, which is often complementary to TEM. The TEM consists of an emission source, which may be a tungsten filament or a lanthanum hexaboride source. By applying a high voltage source (typically 100 – 300 kV), the gun will begin to emit electrons either by thermionic or field electron emission into a vacuum. This extraction is usually aided by the use of a Wehnelt cylinder. Once extracted, the upper lenses of the TEM allow for the formation of the electron probe in the desired size and location for later interaction with the sample. TEM specimen stage designs include airlocks to allow for insertion of the specimen holder into the vacuum with minimal increase in pressure in other areas of the microscope. Standard TEM grid sizes are in the form of a 3.05 mm diameter ring, with a thickness and mesh size ranging from a few μm to 100 μm. The sample is placed on the inner meshed area, having a diameter of approximately 2.5 mm. The grid is placed on the sample holder, which is paired with the specimen stage. The samples for TEM in this work were dispersed in ethanol and then loaded onto a holey carbon support film on a copper

grid. The TEM used in this thesis was a TEM, JEOL 2011, 200 keV. Elemental mapping was performed on the X-ray spectrometer attached to the JEM-2100F instrument.

### 3.4.4 Energy-dispersive X-ray spectroscopy

Energy-dispersive X-ray spectroscopy (EDS) is an analytical technique for the elemental analysis or chemical characterization of a sample. It relies on the interaction of some source of X-ray excitation and the sample, and its characterization capabilities are due in large part to the fundamental principle that each element has a unique atomic structure allowing a unique set of peaks on its X-ray spectrum. To stimulate the emission of characteristic X-rays from a specimen, a high-energy beam of electrons, X-rays or protons is focused onto the sample being studied. In this doctoral work, point and mapping analysis EDS spectroscopy was generally used in both SEM and TEM studies of the materials.

### 3.4.5 Thermogravimetric analysis

Thermogravimetric analysis (TGA) is a method to analyse the chemical changes or physical weight changes of materials with increasing temperature. Commonly, it is used to determine selected characteristics of materials that exhibit mass loss or increase because of decomposition, oxidation, or loss of volatiles. In this doctoral work, TGA was used to determine the carbon contents in the carbon composite materials. TGA was carried out in air atmosphere using a SETARAM Thermogravimetric Analyzer (France) in UOW or a PerkinElmer TG/DTA 6300 in KETI.

### 3.4.6 Brunauer-Emmett-Teller

Brunauer-Emmett-Teller (BET) method is an important analysis technique to explain the physical adsorption of gas molecules on a solid surface and measure the specific surface area of a material. BET analysis is conducted at liquid nitrogen temperature (77 K) over different relative pressures. In order to get accurate results, pre-drying and degassing are necessary. Surface area of samples can be calculated using experimental points at a relative pressure of $P/P_0$ = 0.05-0.25. Pore size distribution can be calculated by the Barrett-Joyner-Halenda (BJH) method, using the amount of nitrogen adsorbed at a relative pressure of $P/P_0$ = 0.99. In this work, nitrogen sorption was measured by a Quanta Chrome Nova 1000 in UOW.

### 3.4.7 Raman spectroscopy

Raman spectroscopy is a spectroscopic technique for analysis of the vibrations of chemical bonds and symmetry of molecules, which is commonly used in chemistry to identify materials. In a Raman spectrometer, a laser light interacts with molecular vibrations, phonons, or other excitations of the sample, resulting in characteristic shifts in laser photons. Specifically, it was used to confirm the identification of obtained materials and estimate the level of graphitization of carbon. The Raman spectra in this thesis work were collected on a JOBIN Yvon Horiba Raman Spectrometer model HR800, employing a 10 mW helium/neon laser at 632.8 nm in UOW; and a Jobin Yvon HR800 Raman spectrometer with a 10 mW He–Ne laser at 632.8 nm excitation in KETI.

### 3.4.8 X-ray photoelectron spectroscopy

X-ray photoelectron spectroscopy (XPS) is a surface-sensitive quantitative

spectroscopic technique to measure the elemental composition, empirical formula, chemical state and electronic state of the elements within a material. XPS spectra are obtained by irradiating a material with a beam of X-rays while simultaneously measuring the kinetic energy and number of electrons that escape from the top surface of the material (0-10 nm). The valence states of elements can be identified and the ratio of each valence state can be estimated from the spectra. In this doctoral work, XPS was carried out on a VG Scientific ESCALAB 2201XL instrument in UOW, and a Thermo Scientific Sigma Probe instrument in KETI using Al Kα X-ray radiation and fixed analyser transmission mode.

## 3.5 Electrode fabrication and cell assembly

### 3.5.1 Electrode preparation

Mixtures were prepared by mixing the active materials, conductive carbon (super P), and binder [polyvinylidene difluoride (PVDF) or carboxymethyl cellulose (CMC) or CMC/polyacrylic acid (PAA)] in specific ratios. After thoroughly grinding with a mortar and pestle, an appropriate solvent [N-methyl-2-pyrrolidone (NMP) for PVDF, $H_2O$ for CMC and CMC/PAA] was added into the mixtures. Homogenous slurry could be obtained after mixing in a rotary mixer. The slurry was then uniformly pasted onto current collectors (Cu foil for anode, Al foil for cathode) by a doctor blade technique with a thickness of 100 μm. The prepared working electrodes were dried in a vacuum oven at 120 °C (PVDF) for 12 h, 80 °C (CMC) for 12 h, or 150°C (CMC/PAA) for 2 h, depending on the solvent and properties of the active materials. The dried electrodes were punched into discs with a diameter of 0.96 cm after a rolling-press procedure. The discs were then ready to be assembled into a testing cell in an argon filled glove box.

### 3.5.2 Cell assembly

Cell assembly was carried out in an Ar-filled glove box using 2032-type coin cells. Compared with lithium foil, sodium foil is prepared by cutting a sodium cube or ingot into thin slices. In order to avoid oxidation and reaction with $H_2O$ by Na, the moisture and oxygen level of the glove box was controlled to less than 0.1 ppm. In the order of assembly shown in Figure 3.3, the cut sodium foil was first placed at the positive cap followed by dripping 2-3 drops of electrolyte; the glass fibre separator was then evenly immersed in the electrolyte, and an extra 1-2 drops of electrolyte were added. The electrode disc was placed onto the glass fibre followed by stainless

steel spacer, spring, and positive cap subsequently. After tight sealing of the coin cell, the batteries were rested for at least 12 hours before electrochemical testing, in order to make certain the full penetration of electrolyte into the electrodes and separator components.

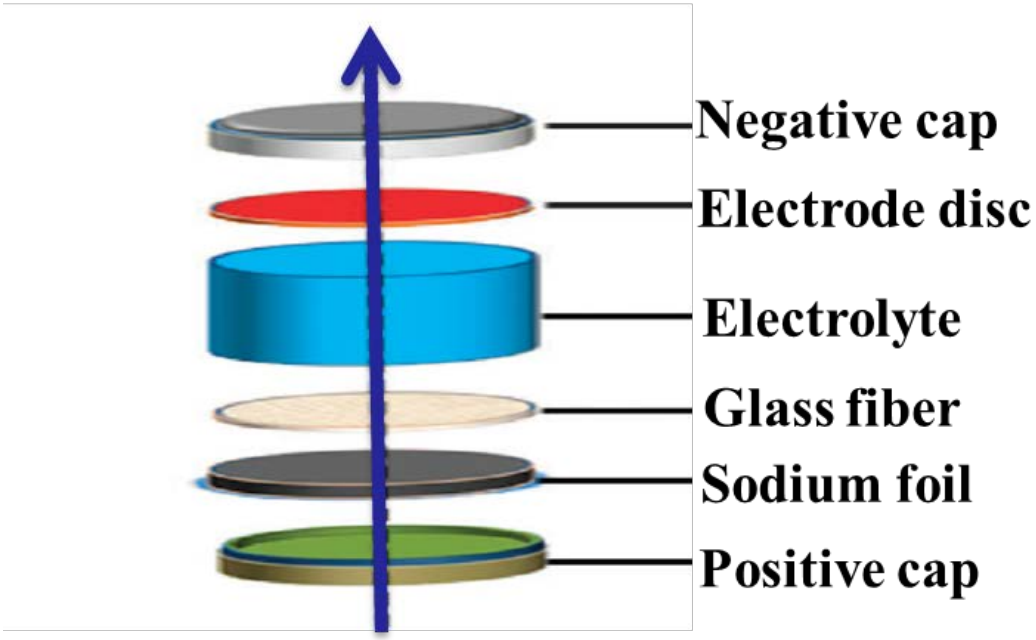


**Figure 3.3** Schematic diagram and order assembly of 2032-type coin cells.

## 3.6 Electrochemical measurements

### 3.6.1 Cyclic voltammetry

Cyclic voltammetry (CV) is an electrochemical technique to investigate the electrochemical reactions in a cell. CV is conducted by cycling the potential of a working electrode at a specified scan rate, and the response current is recorded. For three-electrode system, the working electrode's potential is varied linearly with time, while the reference electrode maintains a constant potential. The counter electrode conducts electricity from the signal source to the working electrode. The current-to-voltage converter measures the resulting current, and the data acquisition system produces the resulting voltammogram. CV testing for coin cells is based on the two-electrode model, in which lithium foil act as both reference electrode and counter electrode. A peak would be observed in both anodic and cathodic curves when a redox reaction occurs. The CV data were acquired on a Biologic VMP-3 electrochemical workstation.

### 3.6.2 Galvanostatic electrochemical testing

The electrochemical performance of a cell can be estimated by galvanostatic testing, in which the cell is charged and discharged during a certain cut-off voltage at a constant current mode. The charge and discharge capacity can be calculated based on the applied current and the total accumulated time for the full charge and discharge process. This testing technique can also be used to evaluate rate capability by applying various current densities over a number of cycles. The instrument used here to obtain the data was a Land battery tester.

### 3.6.3 Electrochemical Impedance Spectroscopy

Electrochemical Impedance Spectroscopy (EIS) is a common method to investigate the inner resistance of a cell. The impedance spectrum for active materials usually includes a high-frequency semicircle and a low-frequency linear tail. The semicircle is related to the kinetic processes reflecting the charge transfer resistance and the double layer capacitance. The linear tail reflects the solid-state diffusion of Na ions into the bulk of the active materials. In this thesis, EIS data were collected on a Biologic VMP-3 electrochemical workstation.

# CHAPTER 4 REDUCED GRAPHENE OXIDE WITH SUPERIOR CYCLING STABILITY AND RATE CAPABILITY FOR SODIUM STORAGE

Sodium ion battery is a promising electrical energy storage system for sustainable energy storage applications due to the abundance of sodium resources and their low cost. In this communication, the electrochemical properties of sodium ion storage in reduced graphene oxide (RGO) were studied in an electrolyte consisting of 1 M $NaClO_4$ in propylene carbonate (PC). The experimental results show that the RGO anode allowed significant sodium ion insertion, leading to higher capacity at high current density compared to the previously reported results for carbon materials. This is due to the fact that RGO possesses higher electrical conductivity and is a more active host, with large interlayer distances and a disordered structure, enabling it to store a higher amount of Na ions. RGO anode exhibits high capacity combined with long-term cycling stability at high current densities, leading to reversible capacity as high as 174.3 mAh $g^{-1}$ at 0.2 C (40 mA $g^{-1}$), and even 93.3 mAh $g^{-1}$ at 1 C (200 mA $g^{-1}$) after 250 cycles. Furthermore, RGO could yield a high capacity of 141 mAh $g^{-1}$ at 0.2 C (40 mA $g^{-1}$) over 1000 cycles.

**Y.-X. Wang,** S.-L. Chou, H.-K. Liu, S.-X. Dou. *Carbon* 2013, 57, 202-208**.**

## 4.1 Introduction

As rechargeable lithium ion battery energy storage technologies have been well developed, lithium ion batteries (LIBs) are extensively applied in various electronic devices, including electric vehicles, portable electrical devices, and smart grids. Large-scale application of LIBs, however, could face challenges related to scarcity of lithium resources and high cost. To achieve long-term energy development, rechargeable sodium ion batteries (NIBs) are gaining recognition as an intriguing candidate for such large-scale and sustainable applications. In contrast to lithium, sodium has an obvious cost advantage because of the natural abundance of Na resources, although sodium has a larger atomic mass and ionic radius than lithium. These properties mean that successful reversible intercalation hosts must possess large enough channels and interstitial sites to accept the large Na ions. Furthermore, sodium shows different thermodynamic parameters, as reflected in the higher standard reduction potential (– 2.71 V vs. standard hydrogen electrode (SHE), compared to ~ 3.04 V for Li), and the gravimetric capacity is lower (1165 mAh $g^{-1}$ compared to 3829 mAh $g^{-1}$ for Li). Although batteries based on metallic sodium anodes would always deliver lower energy densities and exhibit lower operating voltages than those with lithium metal anodes,[1] sodium ion batteries certainly are a promising option for large-scale applications in which cost rather than energy density is the overwhelming factor. Recently, great efforts have been made to find appropriate active materials for both anodes and cathodes of NIBs.[2-9] Many LIB electrode materials should theoretically show a similar electrochemistry to their counterparts in NIBs. Graphite initially drew attention because of its common use in LIBs, however, it does not allow sodium ions to intercalate to any appreciable extent

and is electrochemically irreversible.[10] It is well known that the characteristics of carbon materials, including the degree of graphitization, the structural or textural disorder, and the porosity have a strong influence on the capability for and mechanisms of sodium insertion.[11-13] In recent decades, several types of non-graphitic carbon anodes were proposed for NIBs that possess large interlayer distances and disordered structure favorable to Na-ion insertion-extraction, delivering a low reversible capacity between 100 and 300 mAh $g^{-1}$.[14-16]Although those research proves the feasibility of non-graphitic carbon materials, all of them showed rather poor cycling stability even with low charge-discharge rates at room temperature. Dramatic progresses have been made by Maier's and Liu's groups,[17, 18] whose results show the critical function of microstructure in the carbon materials, in forms such as hollow nanospheres and nanowires. Maier's results showed the hollow carbon nanospheres was tested at 50 mA $g^{-1}$ for first ten cycles and then 100 mA $g^{-1}$ for 100 cycles, a reversible capacity of ~ 160 mAh $g^{-1}$ could be obtained over 100 cycles. Liu's group showed a high reversible capacity of 206.3 mAh $g^{-1}$ after 400 cycles at 0.2 C (50 mA $g^{-1}$).

In this chapter, reduced graphene oxide (RGO) was prepared in large amounts by the simple modified Hummer's method,[19] which can meet the demand for large-scale applications. The results show the RGO anode could deliver high capacity and outstanding rate capability.

## 4.2 Experimental methods

### 4.2.1 Preparation of RGO

Graphite oxide was prepared from natural graphite by the modified Hummers' method.[19] Graphite powder (2 g) was added into 46 mL concentrated $H_2SO_4$ then 1 g $NaNO_3$ was added into the above mixture under stirring and cooling in an ice bath condition for 15 min, followed by slowly adding 6 g $KMnO_4$. Then the mixture was continuously stirred overnight at room temperature, followed by adding 92 mL deionized water, 280 mL warm deionized water and 10 mL 30 wt. % $H_2O_2$ in sequence. The obtained graphite oxide was then washed with 1:10 (v:v) HCl solution once and deionized water three times, followed by ultrasonic treatment for 1 h to further exfoliate the graphene nanosheets. The graphite oxide was collected by dried in a vacuum oven at 45 °C overnight. Reduced graphene oxide (RGO) was fabricated from the obtained graphite oxide through heat-treatment at 450 ℃ for 5 h, then 750 ℃ for 5 h in $H_2$/Ar mixed atmosphere.

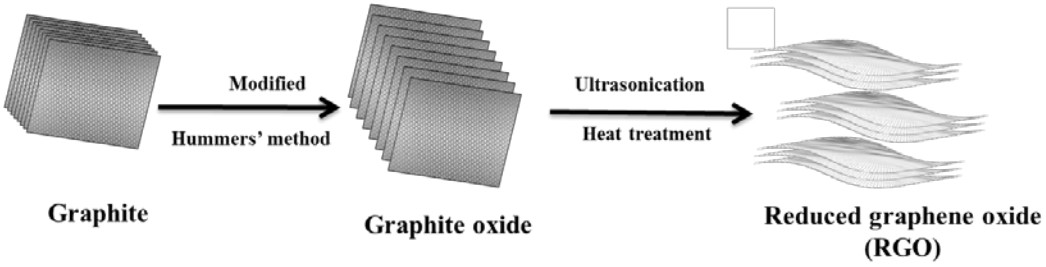


**Figure 4.1** Illustration of the fabrication of reduced graphene oxide.

### 4.2.2 Physical characterization

The morphology of the samples was investigated by field-emission scanning electron microscopy (FESEM; JEOL JSM-7500FA) and transmission electron microscopy (TEM, JEOL 2011, 200 keV). The pass energy was 60 eV for the survey spectra and

20 eV for specific elements. Atomic force microscope (AFM) images were collected by Kelvin probe force microscopy (Asylum Research MFP-3D).The microstructure was characterized by powder X-ray diffraction (XRD; GBC MMA diffractometer) with Cu Kα radiation at a scan rate of $2^{o}$ $min^{-1}$. Raman spectra were collected with a Jobin Yvon HR800 Raman spectrometer with a 10 mW helium/neon laser at 632.8 nm excitation. X-ray photoelectron spectroscopy (XPS) was carried out on a VG Scientific ESCALAB 2201XL instrument using Al Kα X-ray radiation and fixed analyzer transmission mode.

### 4.2.3 Electrochemical measurements

The electrochemical measurements were conducted by first assembling coin-type half cells in an argon-filled glove box. The slurry was prepared by fully mixing 80 wt. % RGO, 10 wt. % carbon black, and 10 wt. % polyvinylidene difluoride (PVDF) by planetary mixer (KK-250S), then pasted on a copper film by a doctor blade with the thickness of 100 μm followed by dried in a vacuum oven overnight at 80 °C . The working electrode was prepared by punching the electrode film into discs of 0.97 cm diameter. The sodium foil was cut by the doctor blade technique from the sodium bulk stored in mineral oil. The sodium foil was employed as both reference and counter electrode. The electrodes were separated by a glass fiber separator. The electrolyte was 1.0 M $NaClO_4$ in propylene carbonate (PC). The electrochemical performance was tested by a Land Battery Test System with a cut-off voltage range from 0.01 V to 2.0 V (vs. $Na/Na^{+}$). Cyclic voltammetry was performed using a Biologic VMP-3 electrochemical workstation between 0.01-2.0 V at a sweep rate of 0.1 mV $s^{-1}$.

### 4.3 Characterization of morphology and structure

The morphology and microstructure of the prepared material was characterized by field emission scanning electron microscopy (FESEM). Low magnification SEM images (Figure.4.2a) show that the particle size of the RGO material is around 10 µm. High magnification images (Figure 4.2b) show that the RGO possesses a layered structure. It is obvious that the RGO nanosheets overlap each other and show a thin, wrinkled structure, resulting in a large amount of free space between the graphene

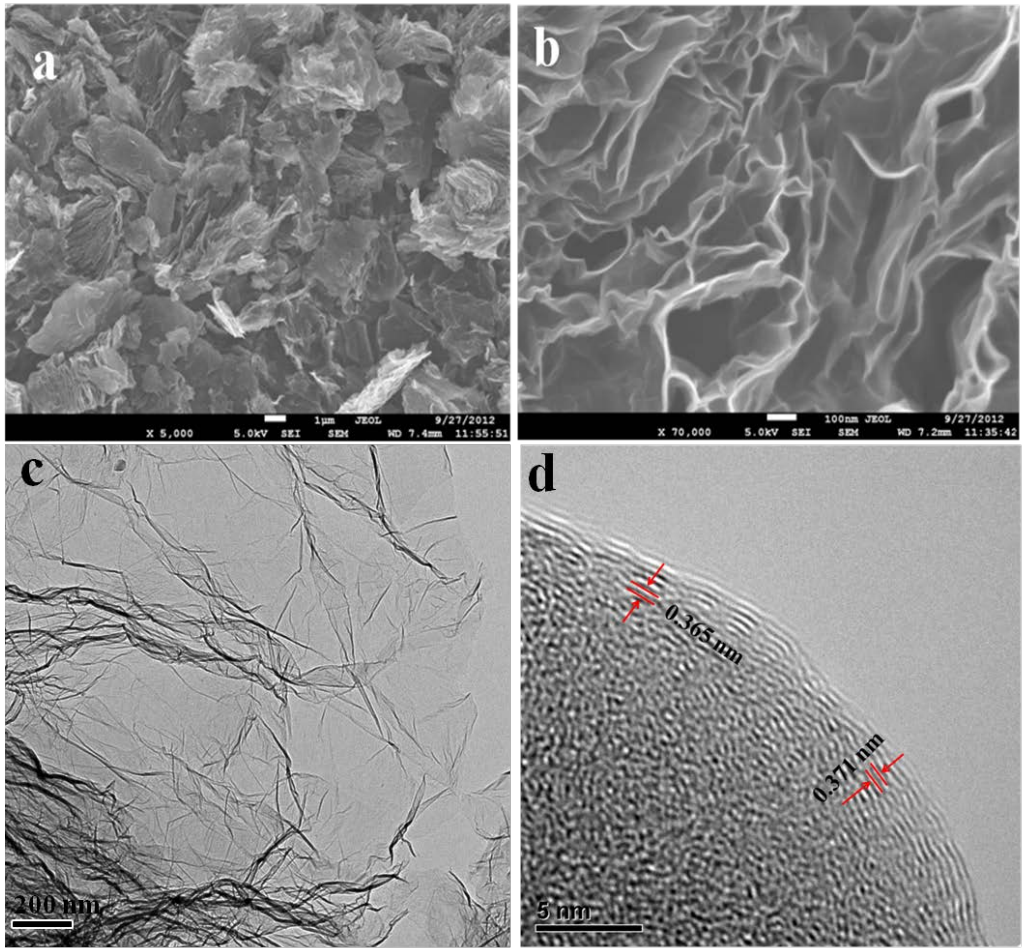


**Figure 4.2** FESEM images of RGO (a) at low magnification (5 K) (b) at high magnification (70 K), TEM images of RGO (c) at low magnification (d) at high resolution.

and some thicker ripples. From the low magnification image presented in Figure 4.2c, the transparency implies that the RGO nanosheets are only a few layers, the dark ripples are due to crumpling of nanosheets. It is reasonable to believe that the larger interlayer distances would facilitate to accommodate larger Na cations.By means of high resolution TEM image (HRTEM, Figure 4.2d), the interlayer spacing of the (002) planes is carefully measured to be 0.371 nm and 0.365 nm at different area. It shows layers and the appearance of nanocavities and/or holes and/or defects, which is favorable to the Na ion insertion.

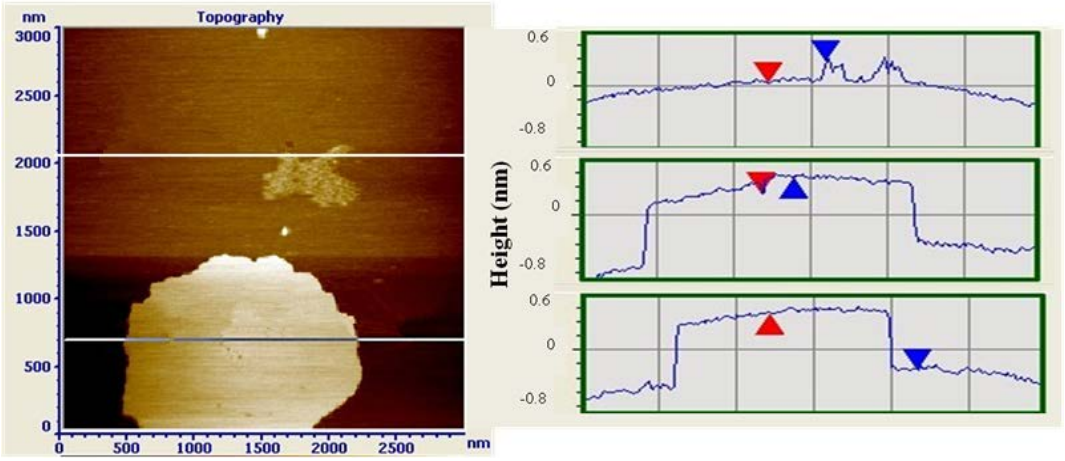


**Figure 4.3** AFM image and profiles of RGO along the indicated lines in different locations.

Atomic force microscope (AFM) images (Figure. 4.3) of RGO were used to further confirm the thickness of the RGO layers. The sample was deposited onto a mica flake from an aqueous dispersion of 0.1 mg $mL^{-1}$ of RGO. The results show that the thickness of the large RGO sheet in the image is ~ 2.0 nm (from point H to point K), which results from the stack of 3–5 graphene layers that is created during the heat reduction process. The RGO sheet possesses nanocavities with single layer graphene ~ 0.6 nm in thickness (G-L). It is found that the defects and single layer graphene

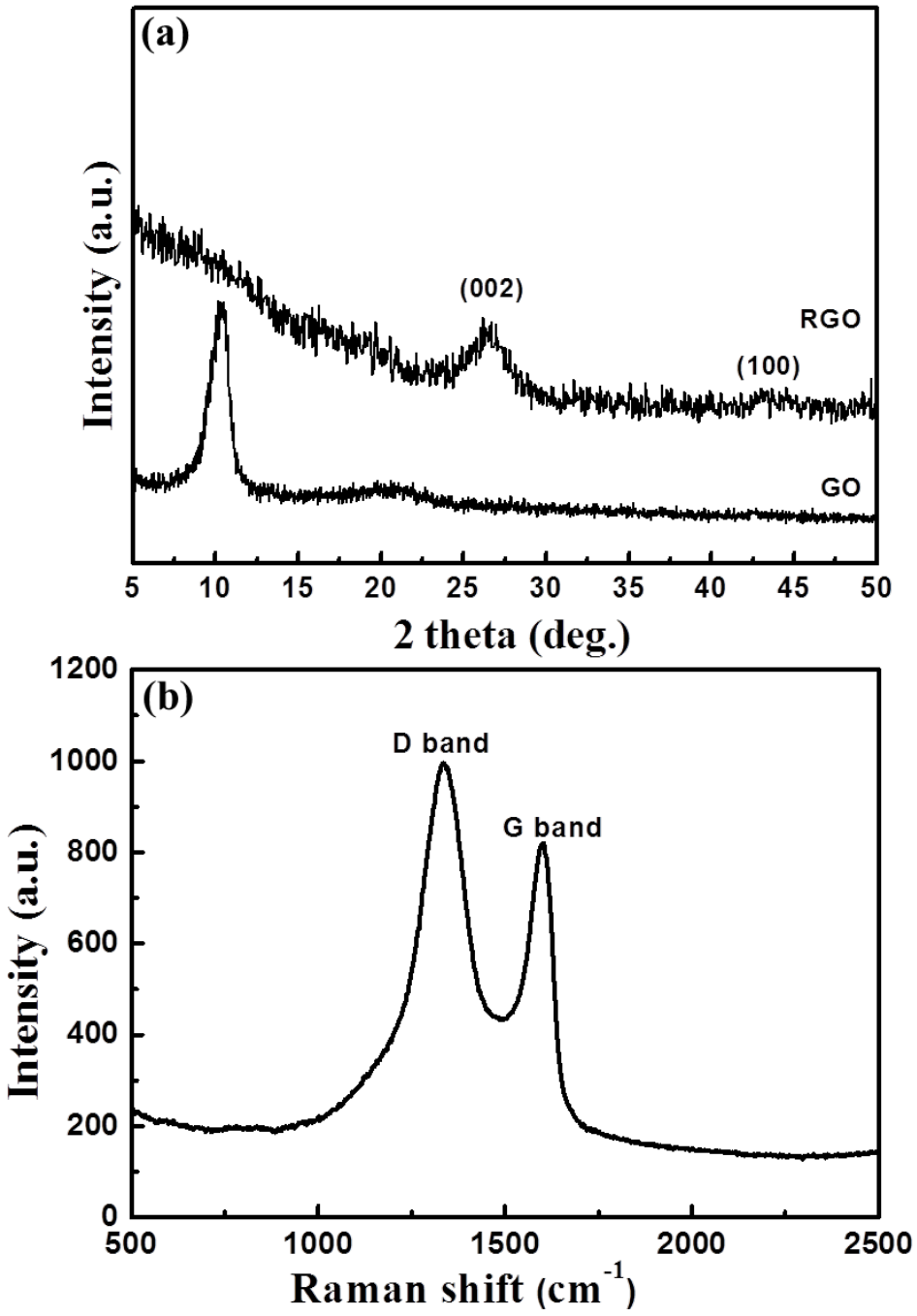


**Figure 4.4** XRD patterns of GO and RGO (a), Raman spectrum of RGO (b), and XPS survey scan of C 1s (c) and O 1s (d) photoelectron spectra of RGO.

co-exist in the RGO host, with a thickness of ~ 0.8 nm for the small RGO sheet (E-F).

The X-ray diffraction (XRD) patterns of RGO and GO are shown in Figure. 4.4a. It

is found that the characteristic diffraction peak of GO at ~ 10° disappears in RGO, which demonstrates that the GO was reduced to RGO during the heat-treatment. The RGO XRD pattern consists basically of two broadened peaks located at around $26^{o}$ and $43^{o}$, corresponding to the (002) diffraction of the graphitic layered structure and the (100) diffraction for graphite, respectively.[17] The XRD pattern in Figure 4.4a is typical of non-graphitic carbon materials with a highly disordered nanocrystalline structure. In addition, the samples show a low signal-to-background ratio, which is probably attributable to incoherent scattering from non-crystalline materials. It is unavoidable that large amounts of hydrocarbons, impurities, and heteroatoms are formed on the graphene surfaces during the oxidative process in strong acid in the modified Hummers' method.[19] Thus, the XRD results suggest that RGO is composed of disordered graphite nanocrystallites with stacked layers of graphene sheets, in agreement with the SEM and AFM observations. The Raman spectra (Figure 4.4b) of RGO exhibit two peaks at about 1334.8 $cm^{-1}$ and 1603.4 $cm^{-1}$, corresponding to the typical D band and G band for carbon material.[20] The D and G band positions are very sensitive to the microstructure of carbon materials, including defects, disorder, edges, and carbon grain size.[21] The intensity ratio of the D band to the G band ($I_D/I_G$) could reflect the degree of disorder of RGO. Large $I_D/I_G$ values (1.22), a prominent D band, and a wide G band indicate the loss of long-range ordering between the graphene sheets, which is consistent with the XRD results. This is probably because a high density of cavities and/or holes and/or defects is present in the graphene nanosheets in the RGO host. In addition, surface area measurements of the RGO via nitrogen gas absorption yield a large Brunauer-Emmett-Teller (BET) value of 330.9 $m^2\ g^{-1}$, further confirming this conclusion. However, RGO anode shows a very low initial Coulombic efficiency mainly owing to the high surface area.

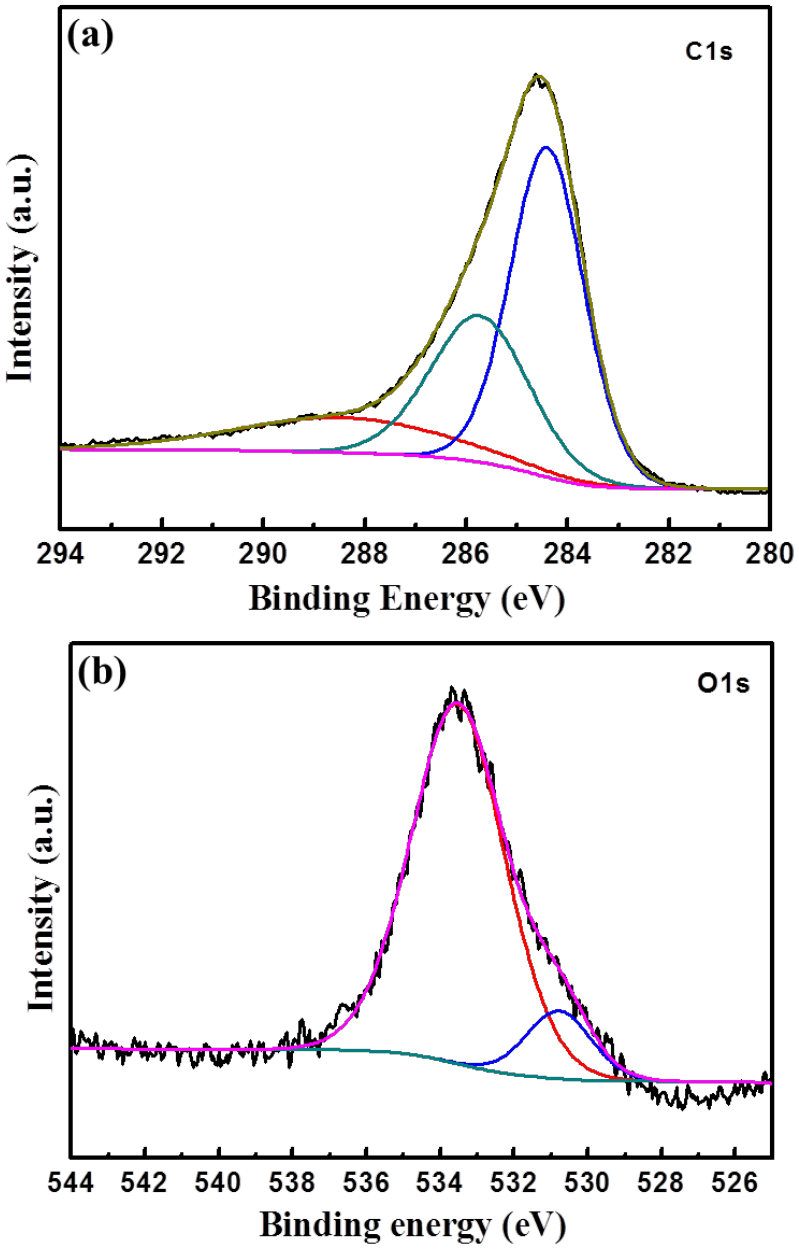


**Figure 4.5** XPS survey scan of C 1s (c) and O 1s (d) photoelectron spectra of RGO.

The X-ray photoelectron spectra (XPS) shown in Figure 4.5a and b were collected to estimate the functionalization of the RGO. Three peaks are obtained from XPS spectra in the C1s region: The main peak is located at 284.4 eV, with a peak area proportion of 52.6 %, corresponding to C-C bonding ($sp^2$ carbon) in defect-free graphite lattice. The peaks at 285.5 eV and 288.1 eV with peak area proportions of 31.1 % and 16.3 % are attributed to C-OH and/or C-C bonding in defective graphite lattice and C=O bonding, respectively. The low proportion of C=O indicates that most of the carboxyl and hydroxyl functional groups were reduced. The O1s spectrum of RGO (Figure 4.5b) shows two peaks located at 533.1 eV and 530.3 eV, assigned to the C-OH and C=O species, respectively.[20, 22] Therefore, the XRD, Raman, and XPS spectra clearly demonstrate that RGO was successfully synthesized by simple heating of GO in a $H_2$/Ar mixed gas atmosphere.

### 4.4 Electrochemical performance

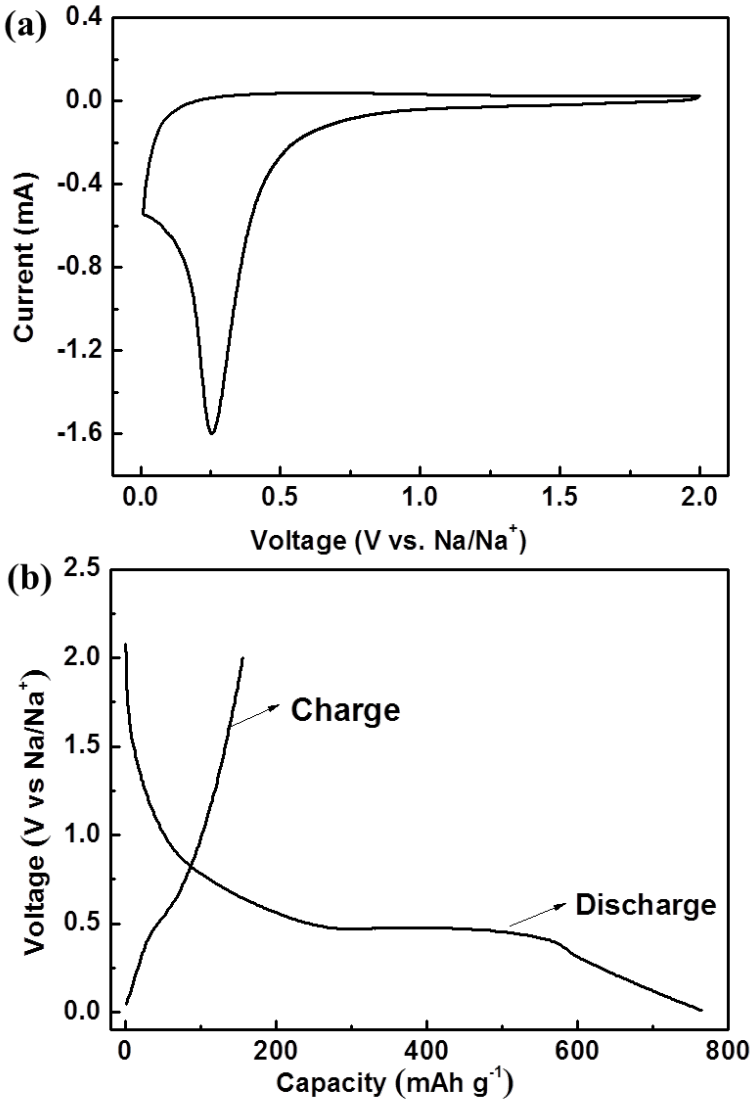


**Figure 4.6** (a) Cyclic voltammogram of RGO in a coin cell at scan rate 0.1 mV $s^{-1}$ and (b) Charge/discharge profiles of RGO in a coin cell at 1 C for first cycle.

The Na-ion storage behavior of RGO is revealed by the cyclic voltammogram and charge-discharge profiles in Figure 4.6. The Na-ion storage behavior of RGO is similar to that of its Li counterpart.[23] The CV curve of first cycle is shown in Figure 4.6a. The RGO anode shows a large irreversible oxidation reaction at about 0.75 V-

0.02 V at the first cycle, which is consistent with a large initial irreversible capacity during discharge/charge processes (Figure 4.6b). it is well known that the decomposition voltage of propylene carbonate (PC) is at ~ 0.7 V in LIBs,[24, 25] which should be much smaller for NIBs due to the standard electrode potential difference ($E^0_{Li/Li+}$ - $E^0_{Na/Na+}$= -0.33 V). A sharp cathodic peak shows up at 0.26 V versus Na+/Na, which is likely to be assigned to the PC decomposition therefore forming a solid electrolyte interphase (SEI) film on the electrode surface. Tang et al. reported a similar result that PC decomposed at 0.36 V in NIBs with hollow carbon nanospheres anode.[17] Similarly, a large irreversible plateau between 0.58 V and 0.75 V is observed in the charge/discharge curve during the first Na-storage. By analogy, it could have originated from the formation of the solid electrolyte interphase (SEI) film on the electrode surface and the reaction of sodium ions with residual-oxygen-containing functional groups.[26]

In the following cycles (Figure 4.7a), the CV curves showed good repeatability, indicating that the sodium ions could reversibly reacted with the RGO and leading to good cycling stability for long cycles. A pronounced cathodic peak is observed at near 0.01 V, in analogy to lithium ion insertion in carbonaceous materials for LIBs,[27, 28] while there is no anodic peak occurs in the reverse cycle. It indicates that the mechanisms of Na in this low-voltage area could be envisaged to the sodium adsorption on the graphene sheets and/or active sites. A pair of small cathodic and anodic peaks can be detected at 0.8 V and 1.57 V, respectively, which gradually disappear in the prolonged cycles. It likely originates from interaction between sodium ion and impurity atoms in RGO. As illustrated in Figure 4.7b, the charge/discharge profiles of subsequent cycles show sloping curves and large

voltage hysteresis between discharge and charge curves, and the reversible capacities decrease slightly over prolonged cycling. The charge/discharge profiles indicate that the reaction between sodium ions and graphene layer resembles capacitive behavior. The discharge capacities of RGO after the 2nd, 10th, 50th, 100th, 200th, and 250th cycles are 177.0, 136, 123.7, 110.3, 97.6, and 94.3 mAh $g^{-1}$ at 1 C, respectively. From those CV and charge/discharge curves, it could be speculated that the Na-storage mechanism of RGO is similar to that of its Li equivalent,

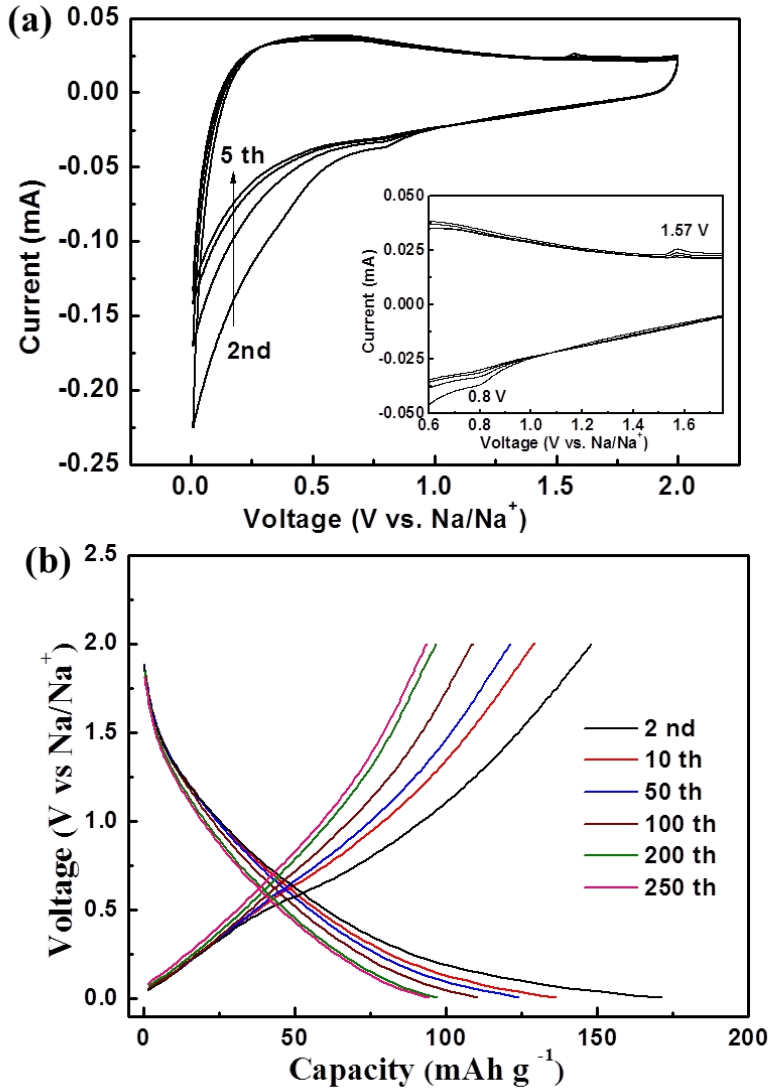


**Figure 4.7** (a) Cyclic voltammogram of RGO in a coin cell at scan rate 0.1 mV $s^{-1}$ for subsequent cycles with zoom-in area (inset); and (b) Charge/discharge profiles of RGO in a coin cell at 1 C for subsequent cycles.

including adsorption on the graphene sheets or interaction with impurity atoms.[15,29]

It can be expected that RGO could show good cycling performance and rate capability due to its adsorption mechanism. The outstanding cycling performance of RGO is shown in Figure. 4.8a. The electrochemical performance was tested at 0.2 C (40 mAh $g^{-1}$) and 1 C (200 mAh $g^{-1}$), respectively. The RGO anode shows similar trends at different current densities: high capacity loss for the first cycle, then good stability over prolonged cycling. After 250 cycles, the electrode exhibits a

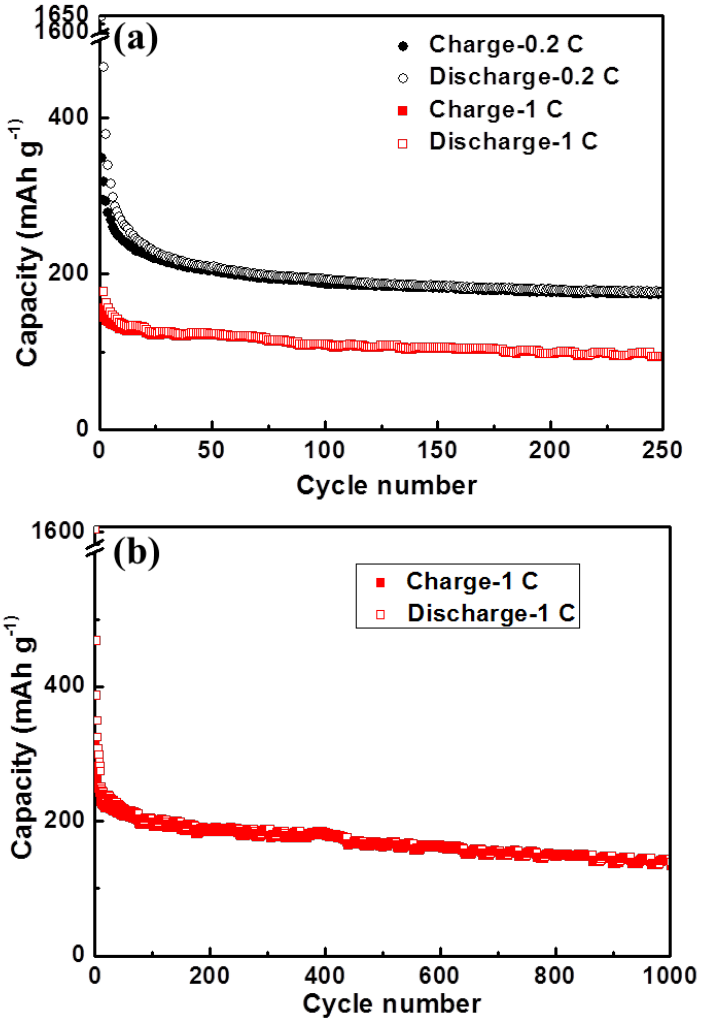


**Figure 4.8** (a) Cycling performance of RGO at 0.2 C and 1 C for 250 cycles (b) cycling performance of RGO at 1 C for 1000 cycles.

reversible capacity of 174.3 mAh $g^{-1}$ at 0.2 C and 93.3 mAh $g^{-1}$ at 1 C. It should be noted that RGO exhibits an excellent cycling performance (Figure 4.8b), remaining a capacity of 141 mAh $g^{-1}$ at 0.2 C over 1000 cycles with a capacity retention ratio of 45.0 %. To the best of our knowledge, it is the best electrochemical performance with long cycling life for carbon anode in NIBs compared with the reported results.[11-18]

The rate performance of RGO is presented in Figure. 4.9a. The average charge capacities are 217.2, 176.4, 150.9, 118.7, and 95.6 mAh $g^{-1}$ at the different current densities of 0.2 C, 0.4 C, 1 C, 2 C, and 5 C, respectively. When the current is finally directly reduced back to 0.2 C, the average capacity can recover to 180.9 mAh $g^{-1}$. RGO shows a superior rate capability presenting capacity decrease of 0.4 times with applied current rate increase of 8 times. Finally, the rate performance of the RGO is compared with the two best results for carboneous anodes of NIBs, hollow carbon nanospheres[17] and hollow carbon nanowires[18] (Figure 4.9b). It is obvious that the hollow carbon naospheres show a relatively low capacity for low current density (< 200 mA $g^{-1}$). Nevertheless, it shows the slightest capacity decay even for applied current of up to 5 A $g^{-1}$. The hollow carbon nanowires show the highest capacity for the similar lower current density while did not report the rate capability for higher current density (> 500 mA $g^{-1}$). The RGO, on the contrary, could provide a medium performance, which provides a higher capacity in lower current density; moreover, it offers slower capacity decay for an applied higher current density as well. The excellent electrochemical performance in terms of Na-ion storage is due to the superior structure of RGO, in which the graphene nanosheets in the RGO host are interconnected so as to minimize the diffusion lengths of Na-ions within the

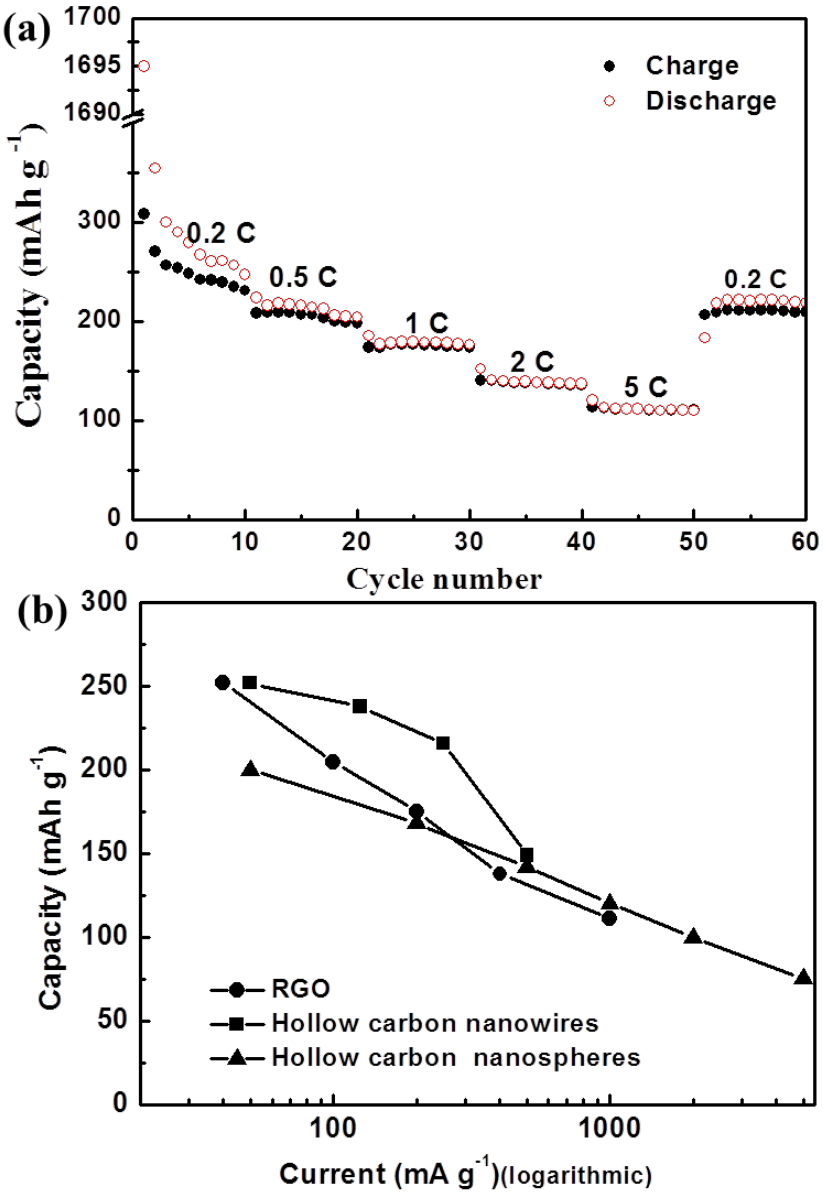


**Figure 4.9** (a) Rate capability of RGO at variant current rates. (b) Comparison of rate capability of RGO with hollow carbon nanowires and hollow carbon nanospheres.(capacity vs. applied current, logarithmic).

electrode. Furthermore, a large number of surface defects, heteroatoms, and hydrocarbons are introduced onto the graphene films byan oxidative process that can play a role in sodium incorporation even though leading to large initial irreversible Coulombic efficiency as well. More importantly, the graphene

nanosheets overlap each other and show a thin wrinkled structure, due to the formation of the nanocavities and/or holes and/or defects, which is favorable to insertion of the relatively large Na ions. It is noteworthy that all of those results show the morphology such as porosity, size of graphene stacks, and purity and so on of carbon anodes plays a key role in improving the electrochemical performance of sodium ion batteries; therefore, modification of the nanostructure of material is a significant strategy to optimize electrochemical properties of electrode. The exact effect of the carbon nanostructure is hard to confirm and is subject to further experimental studies.

## 4.5 Conclusions

RGO was obtained in large quantities by a facile method, which was used as anode material for sodium ion batteries. The prepared RGO anode shows Na-ion insertion properties at room temperature, with excellent cycling stability and rate capability. The experimental results clearly show the significant Na-storage capability of RGO compared to natural graphite, indicating its potential as an anode for the sodium ion battery. It is a big challenge that the irreversible loss at the first cycle is large, which could be reduced in the future by reducing the surface area and oxidized groups. The detailed reaction mechanisms need more experimental research into various nanostructured non-graphitic carbon materials, in particular those with complex nanostructures and activated sites. In addition, it was implied that RGO would be an ideal carbon matrix for those electrode materials, which might be low conductivity and/or undergo large volume change during charge/discharge process. RGO matrix can not only be favorable to construct nanostructure and improve conductivity, but also play a role to accommodate sodium ions in the RGO-based composites.

## 4.6 References


1. M. D. Slater, D. Kim, E. Lee and C. S. Johnson, *Advanced Functional Materials*, 2013, 23, 947-958.

2. J. Qian, Y. Chen, L. Wu, Y. Cao, X. Ai and H. Yang, *Chemical Communications*, 2012, 48, 7070-7072.

3. S. Komaba, Y. Matsuura, T. Ishikawa, N. Yabuuchi, W. Murata and S. Kuze, *Electrochemistry Communications*, 2012, 21, 65-68.

4. Y. Park, D. S. Shin, S. H. Woo, N. S. Choi, K. H. Shin, S. M. Oh, K. T. Lee and S. Y. Hong, *Advanced Materials*, 2012, 24, 3562-3567.

5. P. Senguttuvan, G. Rousse, V. Seznec, J.-M. Tarascon and M. R. Palacin, *Chemistry of Materials*, 2011, 23, 4109-4111.

6. H. Kim, D. J. Kim, D.-H. Seo, M. S. Yeom, K. Kang, D. K. Kim and Y. Jung, *Chemistry of Materials*, 2012, 24, 1205-1211.

7. J. Kang, S. Baek, V. Mathew, J. Gim, J. Song, H. Park, E. Chae, A. K. Rai and J. Kim, *Journal of Materials Chemistry*, 2012, 22, 20857-20860.

8. D. Kim, E. Lee, M. Slater, W. Lu, S. Rood and C. S. Johnson, *Electrochemistry Communications*, 2012, 18, 66-69.

9. L. Zhu, Y. Niu, Y. Cao, A. Lei, X. Ai and H. Yang, *Electrochimica Acta*, 2012, 78, 27-31.

10. P. Ge and M. Fouletier, *Solid State Ionics*, 1988, 28, 1172-1175.

11. L. Joncourt, M. Mermoux, P. Touzain, L. Bonnetain, D. Dumas and B. Allard, *Journal of Physics and Chemistry of Solids*, 1996, 57, 877-882.

12. R. Alcantara, F. Fernandez Madrigal, P. Lavela, J. Tirado, J. Jiménez Mateos, C. Gómez de Salazar, R. Stoyanova and E. Zhecheva, *Carbon*, 2000, 38, 1031-1041.

13. D. Stevens and J. Dahn, *Journal of The Electrochemical Society*, 2000, 147, 1271-1273.

14. R. Alcántara, J. J. Mateos and J. Tirado, *Journal of The Electrochemical Society*, 2002, 149, A201-A205.

15. P. Thomas and D. Billaud, *Electrochimica Acta*, 2002, 47, 3303-3307.

16. R. Alcántara, P. Lavela, G. F. Ortiz and J. L.Tirado, *Electrochemical and Solid-State Letters*, 2005, 8, A222-A225.

17. K. Tang, L. Fu, R. J. White, L. Yu, M. M. Titirici, M. Antonietti and J. Maier, *Advanced Energy Materials*, 2012, 2, 873-877.

18. Y. Cao, L. Xiao, M. L. Sushko, W. Wang, B. Schwenzer, J. Xiao, Z. Nie, L. V. Saraf, Z. Yang and J. Liu, *Nano Letters*, 2012, 12, 3783-3787.

19. W. S. Hummers Jr and R. E. Offeman, *Journal of the American Chemical Society*, 1958, 80, 1339-1339.

20. L. Tang, Y. Wang, Y. Li, H. Feng, J. Lu and J. Li, *Advanced Functional Materials*, 2009, 19, 2782-2789.

21. S. Stankovich, D. A. Dikin, R. D. Piner, K. A. Kohlhaas, A. Kleinhammes, Y. Jia, Y. Wu, S. T. Nguyen and R. S. Ruoff, *Carbon*, 2007, 45, 1558-1565.

22. D. Yang, A. Velamakanni, G. Bozoklu, S. Park, M. Stoller, R. D. Piner, S. Stankovich, I. Jung, D. A. Field and C. A. Ventrice Jr, *Carbon*, 2009, 47, 145-152.

23. C. Wang, D. Li, C. O. Too and G. G. Wallace, *Chemistry of Materials*, 2009, 21, 2604-2606.

24. M. Arakawa and J.-I. Yamaki, *Journal of Electroanalytical Chemistry and Interfacial Electrochemistry*, 1987, 219, 273-280.

25. J.-T. Li, V. Maurice, J. Swiatowska-Mrowiecka, A. Seyeux, S. Zanna, L. Klein, S.-G. Sun and P. Marcus, *Electrochimica Acta*, 2009, 54, 3700-3707.

26. S. Wenzel, T. Hara, J. Janek and P. Adelhelm, *Energy Environ. Sci.*, 2011, 4, 3342-3345.

27. M. Winter, K.-C. Moeller and J. Besenhard, in *Lithium Batteries*, Springer, 2003, pp. 145-194.

28. J. Dahn, T. Zheng, Y. Liu and J. Xue, *Science*, 1995, 270, 590-593.

29. D. Stevens and J. Dahn, *Journal of The Electrochemical Society*, 2001, 148, A803-A811.

# CHAPTER 5 ULTRAFINE $SNO_2$ LOADING ONTO REDUCED GRAPHENE OXIDE AS ANODES FOR SODIUM-ION BATTERIES WITH SUPERIOR RATE AND CYCLIC PERFORMANCE

A structured $SnO_2$ / reduced graphene oxide (RGO) nanocomposite has been synthesized with ultrasmall $SnO_2$ nanoparticles (~ 5 nm) anchored on RGO framework. It has been successfully applied as an anode material in sodium-ion batteries. The electrode delivers a reversible Na-storage capacity of 330 mAh $g^{-1}$ with outstanding capacity retention of 81.3 % over 150 cycles. Moreover, it possesses an outstanding rate capability, exhibiting capacity retention of 25.8 % at high rate (1000 mAh $g^{-1}$). With its combined advantages of low cost and environmental benignity, the $SnO_2$/RGO nanocomposite provides great promise as a suitable anode for Na-ion batteries.

**Y.-X. Wang,** Y.-G. Lim, M.-S. Park, S.-L. Chou, J. H. Kim, H.-K. Liu, S.-X. Dou, Y.-J. Kim. *Journal of Materials Chemistry A* 2014, 2 (2), 529-534.

## 5.1 Introduction

Rechargeable lithium ion batteries (LIBs) are overwhelmingly dominant among the energy storage systems, and they have been widely applied in portable devices. LIBs show great potential for electric vehicles and are expected to play an important part in grid storage as well.[1, 2] Taking the availability and price of lithium resources into account, low-cost sodium ion batteries (NIBs) are recently being revisited and are considered to be the most promising substitute for future large-scale commercial applications.[3-12] In contrast to the case of lithium, the element sodium is abundant in the earth's crust, and sodium metal and other sodium-containing productions are relatively low-cost and easy to obtain. Na cations are about 1.4 times larger in radius than Li cations, however, which undoubtedly is a barrier to reversible sodiation and desodiation of electrode materials. This intrinsic characteristic directly jeopardizes their feasibility for insertion materials, including most cathode and some anode materials. According to previous research on NIBs, the commercial anode in LIBs, graphite, has shown poor $Na^+$ insertion properties and the reaction is electrochemically irreversible.[13] On the other hand, sodium is supposed to be less detrimental to many other anode materials, which achieve their alkali storage (Na or Li) by conversion or alloying/dealloying mechanisms and usually deliver significantly high storage capacities. Furthermore, the electrodes based on the mechanism of conversion or alloying reactions usually deliver a much higher capacity. It is also true, however, for those two types of anodes that the alkali-storage process is accompanied by enormous volume expansion and crystal structure destruction, leading to poor cycling performance and sluggish rate capability. To cope with this challenge, several feasible strategies have been proposed for LIBs,

including reducing particle size,[14] fabricating carbonaceous composites,[15] constructing special electrode nanostructures[16, 17] and exploiting suitable binders.[18] Similarly, those strategies are expected to be functional in the corresponding Na storage system. Currently, researchers have moved to those active anodes such as Sn, Sb, $SnO_2$, SnSb alloy, $Sb_2O_4$, P, and $Fe_3O_4$.[19-26] Komaba et al reported Sn anode with polyacrylic acid (PAA) binder, for which a reversible capacity of ~ 500 mAh $g^{-1}$ was achieved over very short 20 cycles.[27] Qian et al reported a Sb/C nanocomposite for NIBs, which delivers a capacity of 610 mAh $g^{-1}$ over 100 cycles.[28] while it is well known that Sb is highly toxic. Wang's group reported a $SnO_2$ @ multi-walled carbon nanotubes (MWCNTs) nanocomposite, demonstrating a capacity of about 400 mAh $g^{-1}$ at the current density of 50 mA $g^{-1}$ over 50 cycles.[21] Most recently, they also reported the Na-storage properties of $SnO_2$@Graphene nanocomposite, which shows stable capacity of 302 mAh $g^{-1}$ at high current (160 mA $g^{-1}$) in favor of grapheme matrix. However, the $SnO_2$ nanocrystal is large (~ 60 nm), which directly leads to a poor rate capability.[29] To optimize $SnO_2$ anode, it is necessary to further improve its cycling life and rate capability.

$SnO_2$ was selected as the object of our study due to its Na-storage ability, according to the following rational considerations: (1) alloying/dealloying mechanism, (2) low reaction potential for sodium ions, (3) high theoretical capacity (667 mAh $g^{-1}$ for NIBs),[21, 30] and (4) low cost and environmental benignity. The obtained $SnO_2$/ reduced graphene oxide (RGO) nanocomposite possesses buffering space between the small $SnO_2$ nanoparticles (~ 5 nm) and lacunose nanovoids amongst the agglomerated $SnO_2$ cluster. This special nanostructure facilitates fast Na diffusion, shortens diffusion paths and tolerates large volume change. Therefore, it shows a high capacity (330 mAh $g^{-1}$) at the current density of 100 mA $g^{-1}$ over 150 cycles.

Outstanding rate capability is obtained as well, and the capacity can be fully reversed after high C-rate testing.

## 5.2 Experimental methods

### 5.2.1 Preparation of $SnO_2$/RGO nanocomposites

Graphite oxide was prepared from natural graphite by the modified Hummers' method. The specific synthesis process is reported in our previous work.[31] The obtained graphite oxide was then washed with 1:10 (v:v) HCl solution once and deionized water three times. The graphite oxide was dispersed into 500 mL deionized water. The concentration of GO dispersion is estimated to be 3.1 mg/mL. $SnCl_2 \cdot 2H_2O$ was firstly added to a mixture of ethanol and water to reach the concentration of 15.8 mM with magnetic stirring for 1h, and then the appropriate volume of GO dispersion was added to the solution. The pH of the mixed solution was adjusted to be about 11 using $Na_2CO_3$, which is followed by hydrothermal at 120 $^oC$ for 6 h. The obtained products were washed in water and ethanol 3 times, respectively. Finally the $SnO_2$/RGO nanocomposite was obtained after drying at 80 $^oC$ overnight.

### 5.2.2 Physical characterization

The morphology of the samples was investigated by field-emission scanning electron microscopy (FESEM; JEOL JSM-7500FA) and transmission electron microscopy (TEM, JEOL 2011, 200 keV). The microstructure was characterized by powder X-ray diffraction (XRD; GBC MMA diffractometer) with Cu Kα radiation at a scan rate of $2^o$ $min^{-1}$. Raman spectra were collected with a Jobin Yvon HR800 Ranman spectrometer with a 10 mW helium/neon laser at 632.8 nm excitation. X-ray photoelectron spectroscopy (XPS) was carried out on a VG Scientific ESCALAB 2201XL instrument using Al Kα X-ray radiation and fixed analyzer transmission

mode. The amount of $SnO_2$ in the RGO framework was confirmed by using a thermogravimetric analyzer (TGA, PerkinElmer TG/DTA 6300).

### 5.2.3 Electrochemical measurements

The electrochemical measurements were conducted by first assembling coin-type half cells in an argon-filled glove box. The slurry was prepared by fully mixing 80 wt. % $SnO_2$/RGO nanocomposite, 10 wt. % super P, and 10 wt. % mixed binder with carboxymethyl cellulose (CMC) and polyacrylic acid (PAA), then pasted on a copper film by a doctor blade with the thickness of 100 μm followed by dryed in a vacuum oven at 150 ° C for 2 h. The working electrode was prepared by punching the electrode film into discs 0.96 cm in diameter. The sodium foil was cut by the doctor blade technique from sodium bulk. The sodium foil was employed as both reference and counter electrode. The electrodes were separated by a glass fiber separator. The electrolytes were 1.0 M $NaClO_4$ in 1:1 (weight ratio) propylene carbonate (PC) / ethylene carbonate (EC) with and without 5 wt. % fluoroethylene carbonate (FEC) additive. The electrochemical performance was tested by a Land Battery Test System with a cut-off voltage range from 0.005 V to 2.5 V (vs. $Na/Na^+$). Cyclic voltammetry and impedance testing were performed using a Biologic VMP-3 electrochemical workstation from 0.005 V to 2.5 V at a sweep rate of 1 mV $s^{-1}$.

### 5.3 Characterization of morphology and structure

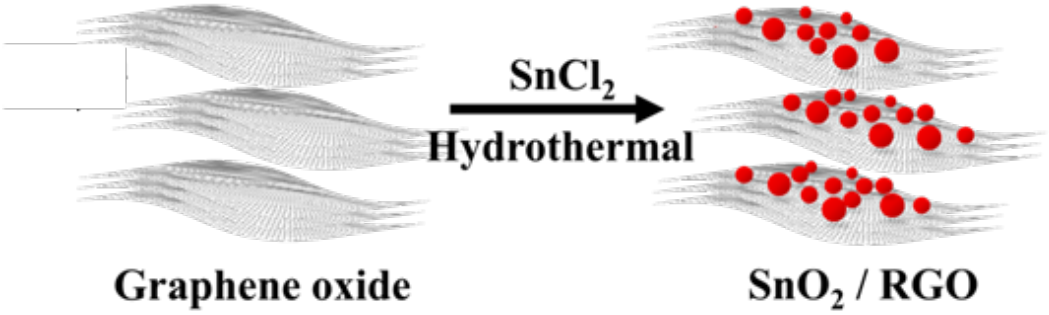


Figure 5.1 A schematic representation of the in-situ synthesis of $SnO_2$/RGO nanocomposite.

The in-situ synthesis of $SnO_2$/RGO nanocomposite is presented in Figure 5.1, commercial graphite was successfully exfoliated into graphene oxide through a modified Hummer's method. Then the $SnCl_2$ was added into the GO dispersion with $Na_2CO_3$ to control hydrolysis. The $SnO_2$ /RGO nanocomposite was obtained by a simple hydrothermal method. The weight ratio was set at 80:20 of $SnO_2$ : RGO. As shown in Figure 5.2, structured $SnO_2$/RGO nanocomposite electrode is designed with the following advantages: (1) small nanosized $SnO_2$ to facilitate fast $Na^+$ diffusion and alleviate the pulverization, (2) highly conductive RGO framework to enhance electronic conductivity of the electrode, (3) large surface area of RGO framework to improve electrolyte wettability and relieve the mechanical stress, and (4) the presence of nanovoids in the composite to accommodate large volume change. All these factors codetermine the superior properties of $SnO_2$/RGO nanocomposite. The overall capacity of the electrode originates from the contribution of the RGO matrix and the $SnO_2$ active materials, including the $Na^+$ adsorption onto the graphene nanosheets and sodium alloying/dealloying with Sn.

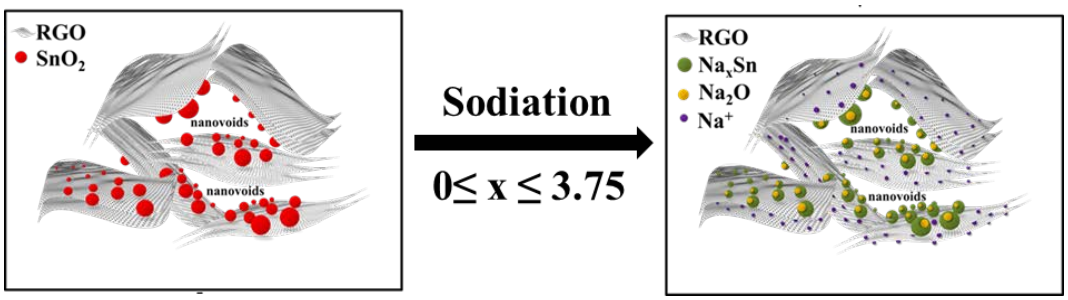


**Figure 5.2** Schematic illustration of sodium storage during charge/discharge process of $SnO_2$/RGO nanocomposite anode.

As illustrated in Figure 5.3, the crystal structure of $SnO_2$/RGO nanocomposite was revealed by X-ray diffraction (XRD). All the diffraction peaks of $SnO_2$/RGO nanocomposite are consistently indexed to the $SnO_2$ tetragonal structure (JCPDS No. 88-0287) without any impurity. Both the (110) peak of $SnO_2$ and the (002) peak of RGO emerged at ~ $26^o$, which overlap in the XRD pattern of the composite. It is obvious that all the typical peaks are broadened and low intensity, which proves that the size of the $SnO_2$ particles is very small. The average crystallite size of the $SnO_2$ nanoparticles has been estimated to be 2.3 nm from the (101) and (110) peaks of $SnO_2$/RGO using Scherrer's equation. The results are in agreement with the transmission electron microscopy (TEM) analysis in Figure 5.4. The accurate weight percentage of $SnO_2$ was evaluated to be 76.4 wt. % by thermogravimetric analysis (TGA), as shown analysis in Figure 5.3b, and the TGA curve of pure RGO is presented as a comparison.

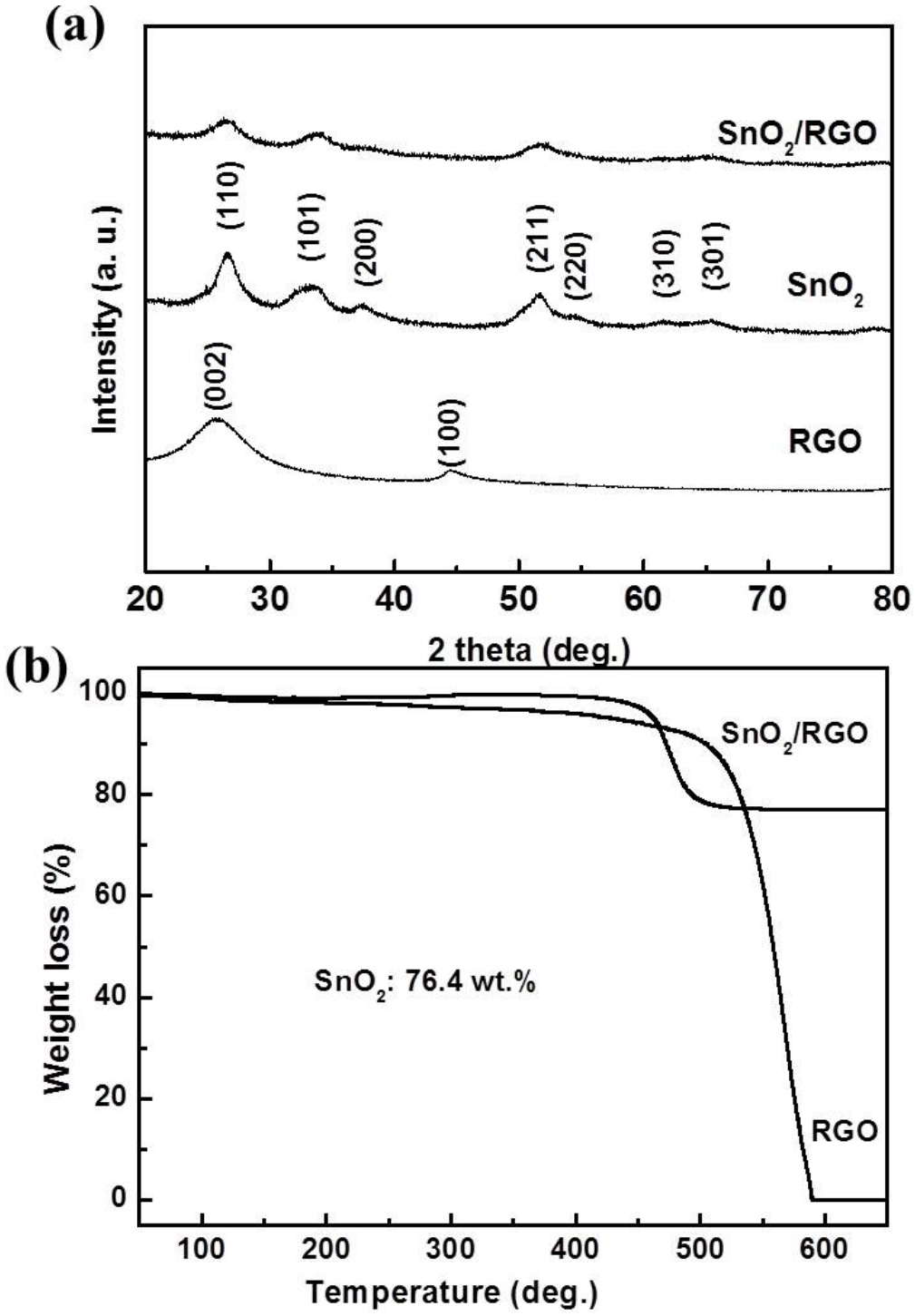


**Figure 5.3** XRD patterns (a) and TGA results (b) for RGO and $SnO_2$/RGO nanocomposite.

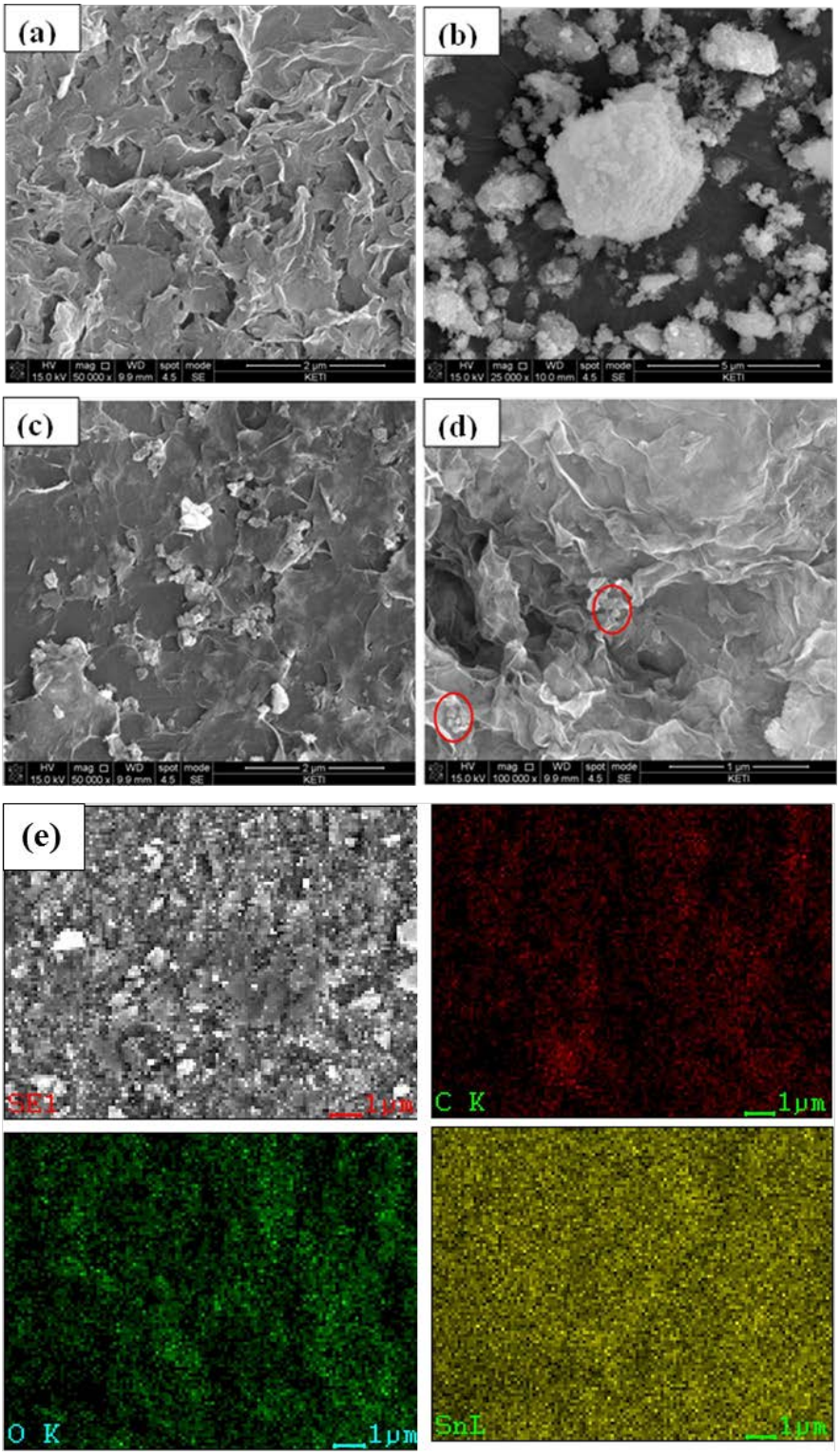


**Figure 5.4** SEM images of RGO (a), pure $SnO_2$ (b); and $SnO_2$/RGO nanocomposite (c), (d) at different magnification; (e) elemental mapping of C, Sn, and O in $SnO_2$/RGO nanocomposite.

The morphologies of the samples were observed by Field emission scanning electron microscopy (FESEM) firstly. As displayed in Figure 5.4, RGO possesses layer structure; and pure $SnO_2$ particles tend to agglomerate together due to the ultrafine particle size. It is manifest that even though the agglomeration phenomenon still occur in the composite, the agglomeration degree of $SnO_2$ particles was alleviated by graphene nanosheets, and the $SnO_2$ particles were evenly anchored on the graphene

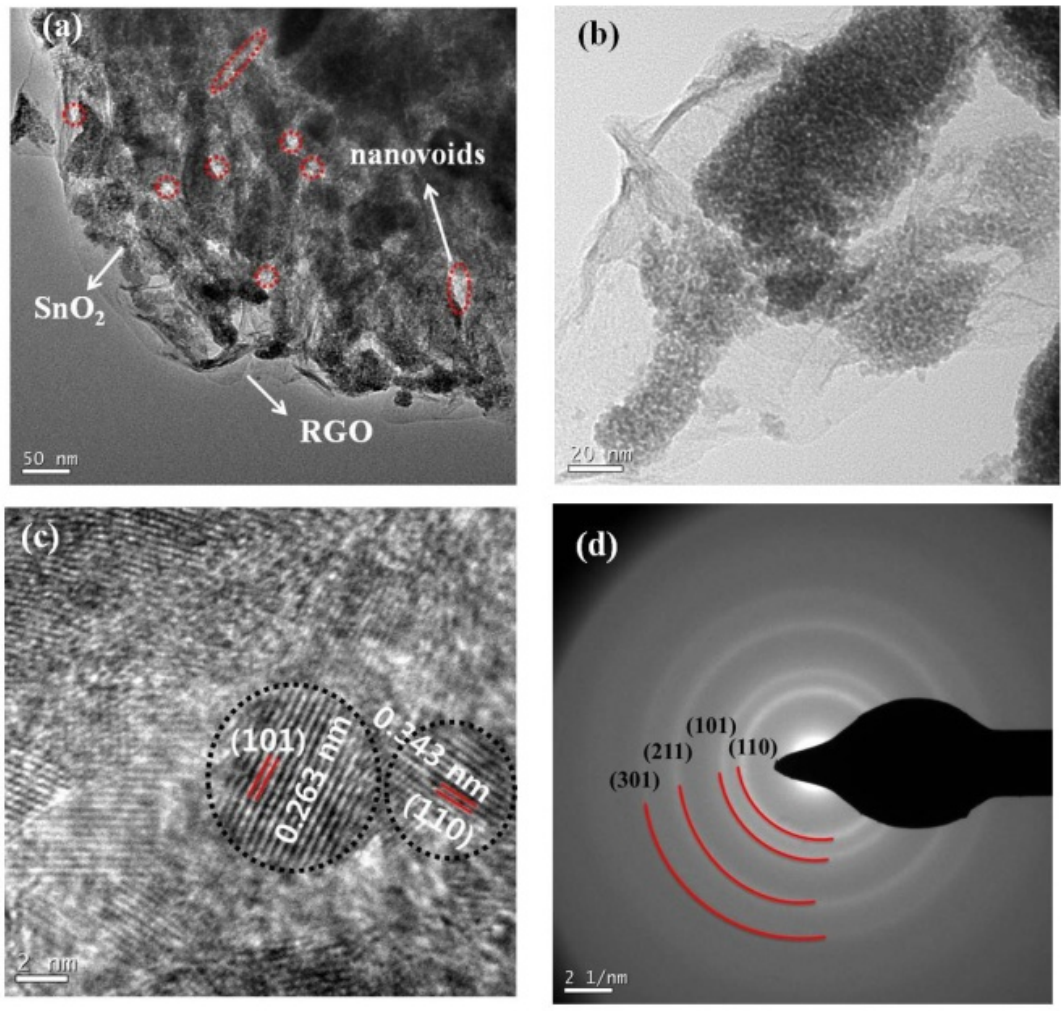


**Figure 5.5** TEM images of $SnO_2$/RGO nanocomposite at low magnification (a), at high magnification (b), at high resolution (HRTEM) (c) and corresponding SAED pattern (d).

matrix. The elemental mappings of Sn, O, and C in Figure 5.4e confirmed that $SnO_2$ nanoparticles were wrapped homogeneously by RGO matrix.

TEM images were shown in Figure 5.5, which confirmed that the nanosized $SnO_2$ particles are uniformLy dispersed on the graphene nanosheets. Importantly, numerous nanovoids are formed among the $SnO_2$ nanoparticles because of their slight aggregation with surrounding particles. Furthermore, excess space exists amongst the $SnO_2$ nanoparticles. The lacunose nanostructure that is formed is extremely favorable for tolerating the large volume change during sodium alloying/dealloying reactions. High resolution TEM (HRTEM), as in Figure 5.5c, shows the (110) and (101) lattice fringes, which are measured to be 0.262 and 0.343

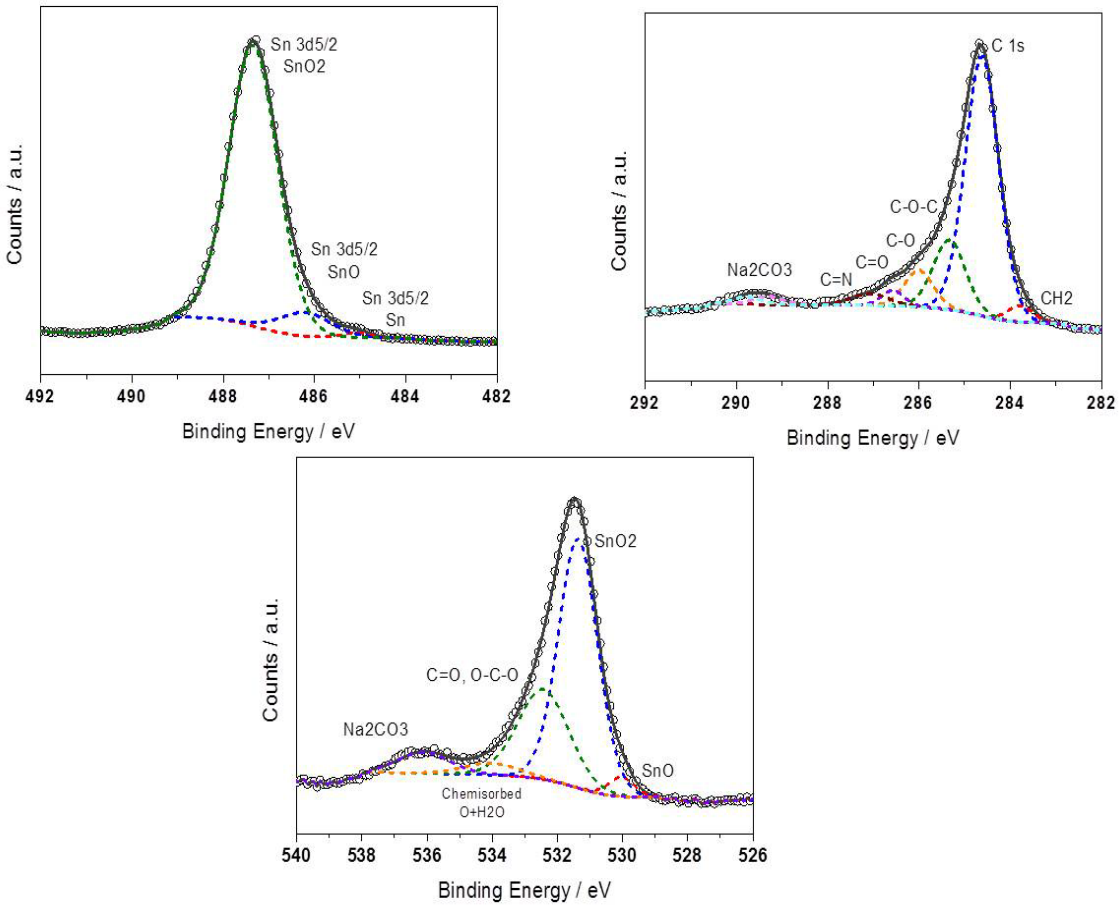


**Figure 5.6** XPS spectra of Sn, C, and O in $SnO_2$/RGO nanocomposite.

nm respectively.Meanwhile, the selected area electron diffraction (SAED) pattern in Figure 5.5d is well indexed to the pure phase of $SnO_2$, corresponding to the diffraction peaks of (110), (101), (211), and (301) planes in the XRD pattern.

X-ray photoelectron spectroscopy (XPS) results (see Figure 5.6) show typical peaks of $Sn^{4+}$, confirming the formation of $SnO_2$ /RGO composite. Furthermore, the Raman spectra of RGO and $SnO_2$/RGO are shown in Figure 5.7, These spectra both show

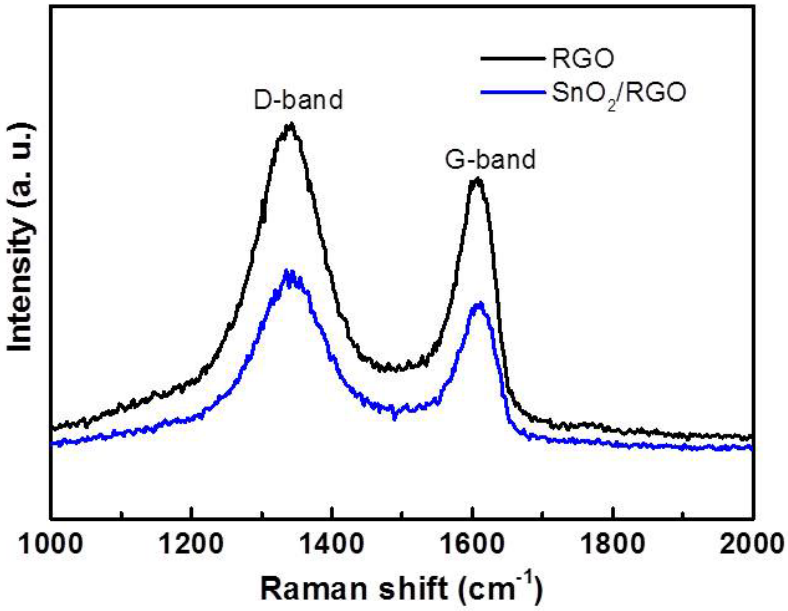


**Figure 5.7** Raman spectra of $SnO_2$/RGO nanocomposite and pure RGO.

two prominent peaks that represent the D and G bands, respectively. The D band is ascribed to the presence of numerous defects in the graphene structure and the G band is related to the $E_{2g}$ mode of phonon vibrations within $sp^2$-bonded carbon materials. The anchored $SnO_2$ nanoparticles in the composite can occupy a large number of defects within the graphene structure, which is responsible for the lower intensity of the D band. The G band of $SnO_2$/RGO is slightly shifted, due to the presence of $SnO_2$ between the graphene layers. The Brunauer-Emmet-Teller (BET)

specific surface area of the $SnO_2$/RGO composite is 107.4 $m^2$ $g^{-1}$ with total pore volume of 0.27 $cm^3$ $g^{-1}$. In contrast, RGO possesses a surface area of 131.7 $m^2$ $g^{-1}$ with the pore volume of 0.16 $cm^3$ $g^{-1}$. It is obvious that the composite shows reduced surface area, which is attributable to the anchoring of the $SnO_2$ particles onto the graphene nanosheets. The much higher pore volume means that the composite possesses a very high porosity due to the formation of nanovoids in the composite architecture, which is consistent with the TEM results.

### 5.4 Electrochemical performance

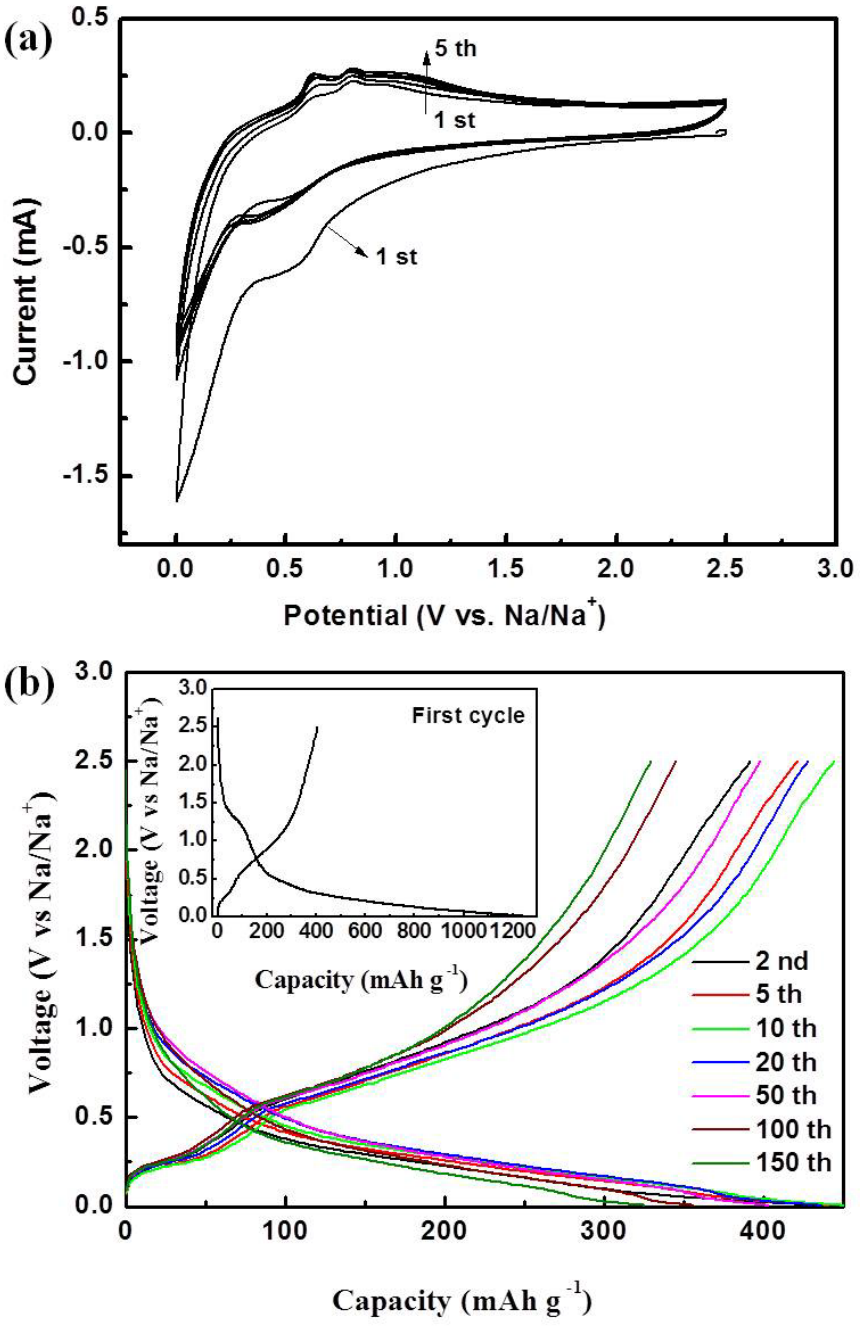


**Figure 5.8** (a) Cyclic voltammogram for the first 5 cycles at scan rate of 1 mV $s^{-1}$. (b) Charge/discharge profiles for selected cycles at 100 mA $g^{-1}$ of $SnO_2$/RGO anode in a coin-cell. The inset shows the charge/discharge profile for the first cycle.

The electrochemical reactions of $SnO_2$/RGO nanocomposite were initially evaluated by cyclic voltammogram (CV). As displayed in Figure 5.8a, there is an irreversible transformation of $SnO_2$ into Sn at the first discharge process. A large irreversibility between 0.01 V and 1.6 V is observed in the first cathodic scan. This is likely to have originated from the formation of the solid electrolyte interphase (SEI) film on the electrode surface and from irreversible reactions between Na and the active materials. The CV profiles in the following cycles show the same pairs of peaks with different intensity, which indicates that the electrochemical reactions in the $SnO_2$-based anode are highly reversible and ensure prolonged cycling stability. In the following cycles, the peaks in the region from 0.6 V to 0.02 V could be related to the transformation of Sn into $Na_xSn$ alloys and the Na-storage of graphene nanosheets. According to the Na-Sn binary alloy phase diagrams and previous reports,[11, 32-36] α-NaSn, $Na_9Sn_4$, $Na_3Sn$, and $Na_{15}Sn_4$ are the main stable phases. It can be speculated that the reductive peak located at 0.4 V corresponds to the formation of two-phase alloy of α-NaSn and $Na_9Sn_4$. Another reductive peak positioned at around 0.00 V is assigned to the formation of single phase of $Na_3Sn$ and $Na_{15}Sn_4$, together with adsorption of Na on the graphene nanosheets. Three anodic peaks are clearly distinguished at approximately 0.28 V, 0.63 V and 0.8 V, which indicate that the phase transition during the dealloying process is more distinct. The Na-Sn alloying/dealloying processes are qualitatively analogous to their Li-Sn counterparts. A hump at 0.28 V can be mainly inferred to belong to the dealloying reaction of $Na_3Sn$, and $Na_{15}Sn_4$, meanwhile, the Na-desorption peak should occur at the similar region as well.[37] The peaks at 0.63 V and 0.8 V are owing to the $Na_9Sn_4$ and α-NaSn dealloying reactions, respectively. The charge/discharge curves of selected cycles are shown in Fig. 3b. In agreement with the CV profiles, the first discharge profiles show an irreversible

plateau at around 1.25 V, which only appears at the first cycle and is likely to be due to the irreversible reaction between $SnO_2$ and Na and the formation of SEI film, which partly leads to the low initial Coulombic efficiency. The large irreversible capacity during the first cycle is also ascribed to the irreversible side reaction with residual functional groups that exist on RGO framework. The following sloping plateau that starts from 0.8 V corresponds to the Na-alloying reaction. Two plateaus at about 0.5 and 0.75 V are observed during the discharge process, which is responsible for the related redox reaction. Therefore, the reactions during the charge /discharge processes mainly involve the irreversible transformation from $SnO_2$ and $Na_xSn$ accompanied by the formation of $Na_2O$ and the reversible alloying/dealloying reaction between Sn and Na. The overall reduction process of $SnO_2$/RGO in NIBs can be described as:

$$SnO_2 + 4\ Na^+ + 4\ e^- \rightarrow Sn + 2Na_2O \qquad (5.1)$$

$$Sn + 3.75\ Na^+ + 3.75\ e^- \leftrightarrow Na_{3.75}Sn \qquad (5.2)$$

$$xC + Na^+ + e^- \leftrightarrow NaC_x \qquad (5.3)$$

According to this reaction, the theoretical sodium storage capacity of $SnO_2$ is 667 mAh $g^{-1}$. The reversible capacity of graphene is about 176 mAh $g^{-1}$ at 100 mA $g^{-1}$.[29] The overall theoretical capacity is 556.9 mAh $g^{-1}$ (theoretical capacity = 667*0.74 + 176*0.36 = 556.9 mAh $g^{-1}$). The electrode delivers a capacity of 406.9 mAh $g^{-1}$ at first cycle, accounting for about 73 % of its theoretical capacity.

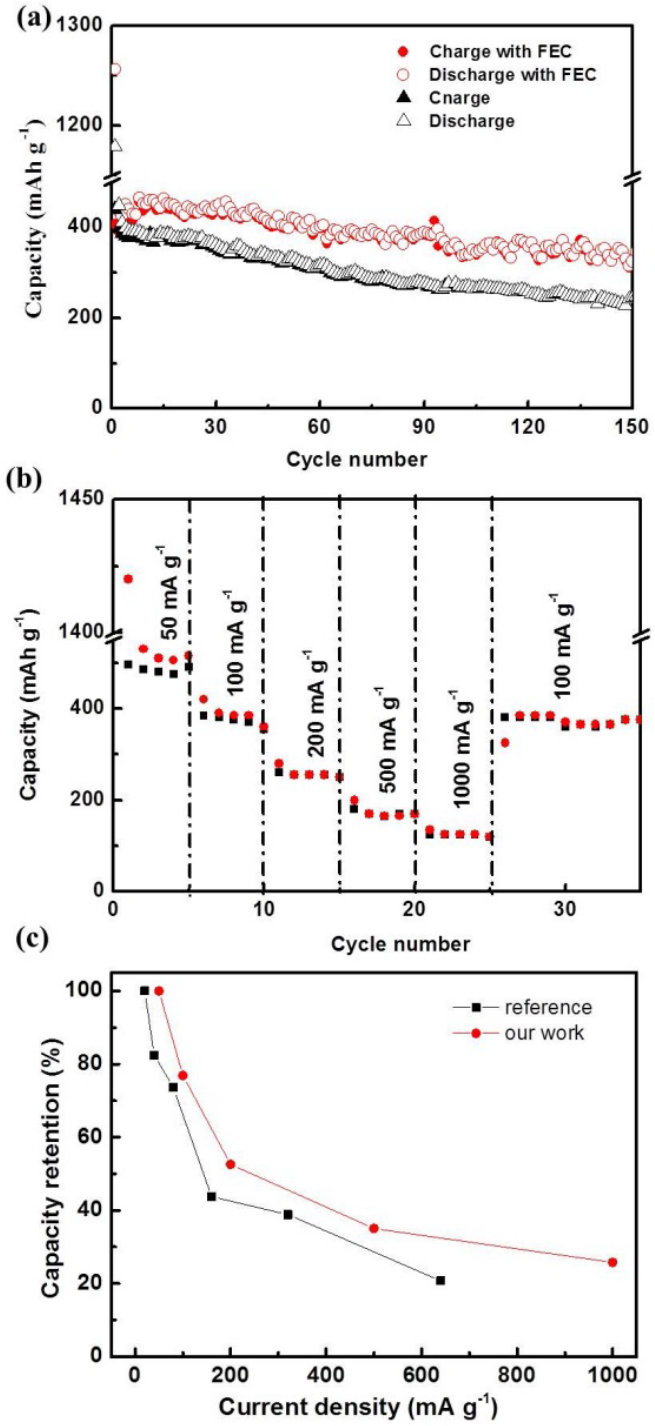


**Figure 5.9** (a) Cycling performance of $SnO_2$/RGO anode in 1 M $NaClO_4$ in EC/PC with and without FEC additive. (b) Rate capability of $SnO_2$/RGO anode in 1 M $NaClO_4$ in EC/PC with FEC additive. (c) Capacity retention of this work and reference[28].

It can be expected that $SnO_2$/RGO composite would show superior electrochemical properties owing to the unique architecture and extremely small $SnO_2$ nanoparticles. The cycling performance was tested at 0.2 C (100 mA $g^{-1}$) over the range of 0.005 ~ 2.5 V for the two electrolyte systems. It is obvious that the electrode shows higher capacity and better cycling stability over prolonged cycling in the electrolyte with fluoroethylene carbonate (FEC) additive. The capacity remains at 330 mAh $g^{-1}$ with capacity retention of 81.3 % over 150 cycles. As a comparison, a capacity of 244.8 mAh $g^{-1}$ and capacity retention of 55.8% is obtained for the electrolyte without FEC. This is because that FEC additive can modify the SEI film. It undergoes preferential reduction (~ 0.7 V) to solvent and forms high quality SEI on active material. The participation of additive molecular moieties in the SEI enhances its stability. Yang's group speculated that the modified film is probably composed of stable alkali fluoride or fluoroalkyl carbonate.[28] Furthermore, the rate capability of $SnO_2$/RGO composite at different current rates in the electrolyte with FEC additive is evaluated in Figure 5.9 b. The electrodes exhibited good C-rate performance. When the electrode was tested at 50 mA $g^{-1}$ (0.1 C), the capacity of about 480 mAh $g^{-1}$ was delivered, then when the current rate increased rapidly to 1000 mA $g^{-1}$ (2 C), the corresponding capacity was maintained at 125 mAh $g^{-1}$. More importantly, the capacity can recover to a great extent, to around 380 mAh $g^{-1}$ at 0.2 C, which is consistent with the obtained results of electrode cycling at 0.2 C in Fig. 4a. The comparison of capacity retention between this work and reported result is presented in Fig. 4c, it is clear that our work shows much better rate capability, which exhibits a capacity retention of 25.8 % at 1000 mAh $g^{-1}$ in contrast with 20.7 % at 640 mAh $g^{-1}$ of the reference[28].

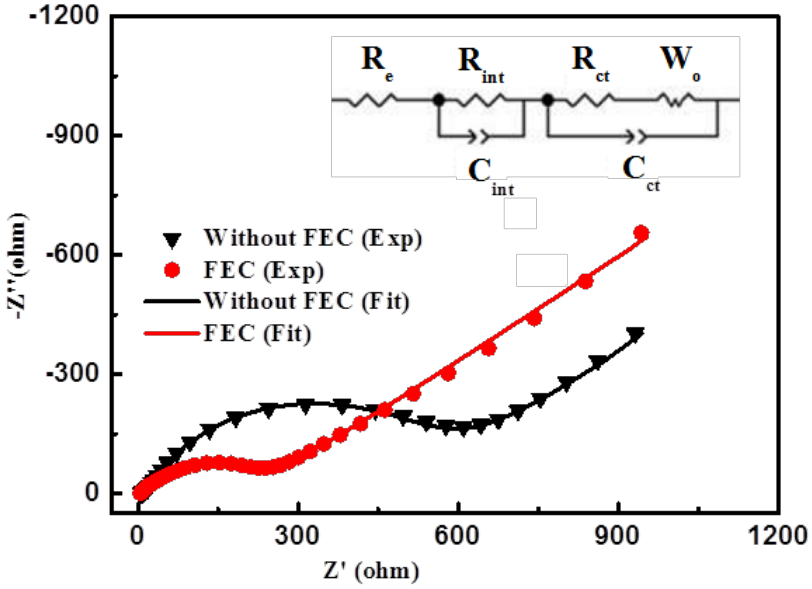


**Figure 5.10** Measured and calculated Impedance plots of $SnO_2$/RGO nanocomposite anode after 150 cycles in the electrolyte with and without FEC. The inset is the equivalent circuit used for the analysis of the impedance plots

Electrochemical impedance spectroscopy (EIS) measurements were also carried out to compare the impedance differences of $SnO_2$/RGO nanocomposite in these electrolytes. The data were collected from 100 kHz to 10 mHz on the coin-cell batteries after charge/discharge for 150 cycles. As shown in Figure 5.10, the EIS spectra are fitted by an equivalent circuit, which exhibit two semi-circles followed by a liner part. The fitted parameters show that both of the cells with and without FEC possess the similar electrolyte resistance ($R_e$) of 3.9 and 5.8 Ω. In contrast, the interface resistance ($R_{int}$) and charge transfer resistance ($R_{ct}$) show significant differences. The $R_{int}$ (88.6 Ω) for the cell with FEC is higher than that without FEC (18.1Ω), which indicates the more discharge products formed on the former electrode. This is in agreement with the much higher capacity in Figure 5.9a. The $R_{ct}$ is believed to be related to Na-ion migration through the SEI films, corresponding to

the conductivity of the discharge product.[10, 16] It is clear that the $R_{ct}$ is much higher than its counterpart in LIBs. This confirms that the $Na^+$ suffers lower kinetics because of its intrinsic properties. $R_{ct}$ in the electrolyte with FEC (~ 62.5 Ω) is much lower than in that without FEC (~ 556.4 Ω), indicating that the kinetic resistance of the charge transfer is much lower for the electrolyte with FEC regardless of more discharge products. This should be attributed to the passivation effects of the additive modified SEI, which is supposed to consist of sodium fluoride and polythelene compounds similar with its lithium counterpart,[38] and therefore, thinner and higher conductive SEI film is formed than in the cell with FEC.

## 5.5 Conclusions

In summary, lacunose $SnO_2$/RGO nanocomposite has been successfully prepared via a simple hydrothermal method. It is believable that the unique architecture and nanosized $SnO_2$ particles in the composite are responsible for such superior electrochemical properties. The overall capacity of the electrode originates from the contribution of the RGO matrix and the $SnO_2$ active materials, including the sodium adsorption onto the graphene nanosheets and sodium alloying/dealloying with Sn. Firstly, the RGO framework can dramatically enhance the conductivity of the anode material. On the other hand, it favors the construction of a lacunose microstructure to tolerate the volume change during the charge/discharge process. Moreover, the graphene nanosheets can effectively prevent the agglomeration of nanoparticles and pulverization of electrode material. Secondly, the RGO framework also plays a part in accommodating the sodium ions because of its large number of active defects, making a stable contribution to overall capacity of the composite. Thirdly, the nanosized particles are vital for accelerating the reaction kinetics and promoting diffusion because of their short transport length. The above explanation proves that both the unique construction and nanosize nature of the $SnO_2$ particle optimized the overall performance by allowing the maximum utilization of electrode material. The experimental results show that the designed $SnO_2$/RGO composite electrode has great potential as an anode for sodium ion batteries. Furthermore, this paper sheds light on that the structure design of promising electrode materials should be paid more attention in the future.

## 5.6 References


1. J.-M. Tarascon and M. Armand, *Nature*, 2001, 414, 359-367.

2. P. G. Bruce, B. Scrosati and J. M. Tarascon, *Angewandte Chemie International Edition*, 2008, 47, 2930-2946.

3. M. S. Islam, D. J. Driscoll, C. A. Fisher and P. R. Slater, *Chemistry of Materials*, 2005, 17, 5085-5092.

4. D. Stevens and J. Dahn, *Journal of The Electrochemical Society*, 2000, 147, 1271-1273.

5. R. Alcántara, M. Jaraba, P. Lavela and J. Tirado, *Chemistry of Materials*, 2002, 14, 2847-2848.

6. S. Komaba, W. Murata, T. Ishikawa, N. Yabuuchi, T. Ozeki, T. Nakayama, A. Ogata, K. Gotoh and K. Fujiwara, *Advanced Functional Materials*, 2011, 21, 3859-3867.

7. V. Palomares, P. Serras, I. Villaluenga, K. B. Hueso, J. Carretero-González and T. Rojo, *Energy & Environmental Science*, 2012, 5, 5884-5901.

8. Y.-X. Wang, Y.-G. Lim, M.-S. Park, S.-L. Chou, J. H. Kim, H.-K. Liu, S.-X. Dou and Y.-J. Kim, *Journal of Materials Chemistry A*, 2014, 2, 529-534.

9. D. Kim, S.-H. Kang, M. Slater, S. Rood, J. T. Vaughey, N. Karan, M. Balasubramanian and C. S. Johnson, *Advanced Energy Materials*, 2011, 1, 333-336.

10. X. Lu, G. Xia, J. P. Lemmon and Z. Yang, *Journal of Power Sources*, 2010, 195, 2431-2442.

11. S. Komaba, C. Takei, T. Nakayama, A. Ogata and N. Yabuuchi, *Electrochemistry Communications*, 2010, 12, 355-358.

12. Y. Cao, L. Xiao, W. Wang, D. Choi, Z. Nie, J. Yu, L. V. Saraf, Z. Yang and J. Liu, *Advanced Materials*, 2011, 23, 3155-+.

13. P. Ge and M. Fouletier, *Solid State Ionics*, 1988, 28, 1172-1175.

14. U. Kasavajjula, C. Wang and A. J. Appleby, *Journal of Power Sources*, 2007, 163, 1003-1039.

15. X. W. Lou, C. M. Li and L. A. Archer, *Advanced Materials*, 2009, 21, 2536-2539.

16. W. M. Zhang, J. S. Hu, Y. G. Guo, S. F. Zheng, L. S. Zhong, W. G. Song and L. J. Wan, *Advanced Materials*, 2008, 20, 1160-1165.

17. N. Zhao, G. Wang, Y. Huang, B. Wang, B. Yao and Y. Wu, *Chemistry of Materials*, 2008, 20, 2612-2614.

18. S.-L. Chou, J.-Z. Wang, C. Zhong, M. Rahman, H.-K. Liu and S.-X. Dou, *Electrochimica Acta*, 2009, 54, 7519-7524.

19. Y. Xu, Y. Zhu, Y. Liu and C. Wang, *Advanced Energy Materials*, 2013, 3, 128-133.

20. A. Darwiche, C. Marino, M. T. Sougrati, B. Fraisse, L. Stievano and L. Monconduit, *Journal of The American Chemical Society*, 2012, 134, 20805-20811.

21. Y. Wang, D. Su, C. Wang and G. Wang, *Electrochemistry Communications*, 2013, 29, 8-11.

22. A. Darwiche, M. T. Sougrati, B. Fraisse, L. Stievano and L. Monconduit, *Electrochemistry Communications*, 2013, 32, 18-21.

23. Q. Sun, Q.-Q. Ren, H. Li and Z.-W. Fu, *Electrochemistry Communications*, 2011, 13, 1462-1464.

24. J. Qian, X. Wu, Y. Cao, X. Ai and H. Yang, *Angew. Chem.-Int. Edit.*, **2013**, 52, 4633-4636.

25. Y. Kim, Y. Park, A. Choi, N.-S. Choi, J. Kim, J. Lee, J. H. Ryu, S. M. Oh and K. T. Lee, *Advanced Materials*, **2013**, 25, 3045-3049.

26. S. Hariharan, K. Saravanan, V. Ramar and P. Balaya, *Physical Chemistry Chemical Physics*, **2013**, 15, 2945-2953.

27. S. Komaba, Y. Matsuura, T. Ishikawa, N. Yabuuchi, W. Murata and S. Kuze, *Electrochemistry Communications*, 2012, 21, 65-68.

28. J. Qian, Y. Chen, L. Wu, Y. Cao, X. Ai and H. Yang, *Chemical Communications*, 2012, 48, 7070-7072.

29. D. Su, H.-J. Ahn and G. Wang, *Chemical Communications*, 2013, 49, 3131-3133.

30. Y. Qi, N. Du, H. Zhang, P. Wu and D. Yang, *Journal of Power Sources*, 2011, 196, 10234-10239.

31. Y.-X. Wang, S.-L. Chou, H.-K. Liu and S.-X. Dou, *Carbon*, 2013, 57, 202-208.

32. L. Xiao, Y. Cao, J. Xiao, W. Wang, L. Kovarik, Z. Nie and J. Liu, *Chem. Commun.*, 2012, 48, 3321-3323.

33. V. Chevrier and G. Ceder, *Journal of The Electrochemical Society*, 2011, 158, A1011-A1014.

34. Y. Liu, Y. Xu, Y. Zhu, J. N. Culver, C. A. Lundgren, K. Xu and C. Wang, *ACS Nano*, 2013, 7, 3627-3634.

35. J. W. Wang, X. H. Liu, S. X. Mao and J. Y. Huang, *Nano Letters*, 2012, 12, 5897-5902.

36. L. Baggetto, P. Ganesh, R. P. Meisner, R. R. Unocic, J.-C. Jumas, C. A. Bridges and G. M. Veith, *Journal of Power Sources*, 2013, 234, 48-59.

37. Y. Cao, L. Xiao, M. L. Sushko, W. Wang, B. Schwenzer, J. Xiao, Z. Nie, L. V. Saraf, Z. Yang and J. Liu, *Nano Letters*, 2012, 12, 3783-3787.

38. H. Nakai, T. Kubota, A. Kita and A. Kawashima, *Journal of The Electrochemical Society*, 2011, 158, A798-A801.

## CHAPTER 6 REVERSIBLE SODIUM STORAGE VIA CONVERSION REACTION IN $MOS_2$/C COMPOSITE

An exfoliated $MoS_2$/C composite (E-$MoS_2$/C) was prepared via simple chemical exfoliation and hydrothermal method. The unique structure and optimized electrolyte effectively promote Na-storage performance. This work suggests a promising new anode and paves the way to further explore its great potential for large-scale applications. Exfoliated $MoS_2$/C composite serves as a novel anode material for the sodium ion battery for the first time, exhibiting high capacity and prolonged cycling life. High capacity (~ 400 mAh $g^{-1}$) at 0.25 C (100 mA $g^{-1}$) is maintained over prolonged cycling life (100 cycles). Outstanding rate capability is also achieved with a capacity of 290 mAh $g^{-1}$ at 5 C.

**Y.-X. Wang,** K. H. Seng, S.-L. Chou, Z. Guo, D. Wexler, H.-K. Liu, S.-X. Dou.
*Chemical Communications* 2014, 50 (73), 10730-10733.

## 6.1 Introduction

Lithium-ion batteries (LIBs) have been widely used as the power sources for the small electronic devices in our daily lives due to their high energy densities.[1, 2] With the increasing demand for Li commodity chemicals and geographically-constrained Li mineral reserves, however, LIBs are confronting a huge challenge to satisfy the demands of the ever growing electronic and electric vehicle markets. Plenty of researches turn to new battery systems, including aqueous batteries,[3, 4] and hybrid batteries.[5] Rechargeable sodium ion batteries (NIBs) are especially regaining interest for use in large-scale applications because of their huge advantages in terms of low cost and the abundance of sodium resources. The ionic radius of sodium (0.102 nm) is larger compared to lithium (0.076 nm), and successfully reversible electrode materials are required to possess large enough channels and/or interstitial sites.[6] Currently, various cathodic host materials have been successfully reported with certain capacity and cycling ability.[7-11] While the options as anodic hosts with higher capacity are merely limited in Sn, Sb and $Sb_2O_4$.[12-14]

Molybdenum disulfide ($MoS_2$) has been extensively investigated for a long time due to its great potential for applications in the field of hydrogen storage,[15] medical and optoelectronics,[16] magnesium ion batteries,[17, 18] and lithium ion batteries.[19-21] As a typical layered transition metal chalcogenide, $MoS_2$ has a graphite-like structure, where Mo and S atoms are covalently bonded to form two-dimensional S-Mo-S tri-layers. These layers are then stacked together through weak van der Waals forces between the $S^{2-}$ layers, forming a sandwich structure. It is not surprising, therefore, that $MoS_2$ could be a desirable intercalation host material because the guest atoms could reversibly intercalate into the weakly bound stacked layers.

The electrochemical performance of $MoS_2$ or $MoS_2$-containing composites with different morphologies for lithium ion batteries have been widely studied, in forms including nanotubes,[22] nanosheets,[20] mesoporous structures,[23] and nanorods.[24] Recently, a number of studies have focused on enlarging the *d*-spacing of the (002) crystal plane, which would facilitate faster lithium intercalation and lead to higher lithium storage. Du *et al.* reported restacked exfoliated $MoS_2$ with enlarged *d*-spacing (0.635 nm), which exhibited a high capacity of 800 mAh $g^{-1}$ for 50 cycles.[25] Hwang *et al.* synthesized $MoS_2$ nanoplates consisting of disordered graphene-like layers with enlarged *d*-spacing (0.69 nm), which showed excellent high rate capability with a capacity of 554 mAh $g^{-1}$ after 20 cycles at applied current density of 53.1 A $g^{-1}$.[26] Liu *et al.* reported highly ordered mesoporous $MoS_2$ with enlarged *d*-spacing (0.66 nm), delivering the high rate electrochemical performance of 608 mAh $g^{-1}$ at a discharge current of 10 A $g^{-1}$.[21] In addition, $MoS_2$ also shows the potential for reversible electrochemical energy storage in rechargeable magnesium batteries. Aurbach's group have reported $MoS_2$ as the cathode material for Mg batteries.[27, 28] Recently, Liang et al. reported highly exfoliated, graphene-like $MoS_2$ for Mg batteries. They found that the battery achieved a high operating voltage (0.8 V) and exhibited stable reversible capacity of 170 mAh $g^{-1}$ after 50 cycles, when coupled with the Mg nanoparticle anode.[18] Recently, Park et. al reported the possibility of commercial $MoS_2$ for sodium-ion storage.[29] However, the $MoS_2$ only delivers a very low capacity of 85 mAh $g^{-1}$ from 0.4 to 2.6 V by intercalation/deintercalation reaction. Based on our recent work, pristine $MoS_2$ can react with Na ions *via* reversible conversion reaction (~ 3 $Na^+$ reaction, ~ 501 mAh $g^{-1}$) when further discharged to lower voltage (0.01 V).[30] Therefore, there is significant room to enhance the reversible capacity of $MoS_2$ via the realization of conversion reaction.

Herein, we study on exfoliated $MoS_2$/C composite (E-$MoS_2$/C) for NIBs with outstanding electrochemical properties. Our strategy to achieve high performance is to use a unique E-$MoS_2$/C composite as an anode material that possesses expanded *d*-spacing to accommodate large sodium ions. In addition, the exfoliated structure could shorten the Na-ion diffusion pathway and also withstand large volume change due to the buffering space created by the crumpled nanosheets. Simultaneously, the carbon component can effectively increase electrode conductivity. On the other hand, various electrolytes were utilized to optimize the cycling performance of E-$MoS_2$/C. The E-$MoS_2$/C is presented as an excellent anode material in 1.0 M $NaClO_4$ with propylene carbonate / ethylene carbonate and 5 wt. % fluoroethylene carbonate additive (PC/EC + 5 wt. % FEC), with an average working voltage of 1.0 V. Coupled with the average capacity of ~ 400 mAh $g^{-1}$ for 100 cycles at applied current of 100 mA $g^{-1}$ (0.25 C) and excellent rate capability (467.7 mAh $g^{-1}$ at 0.125 C and 290.1 mAh $g^{-1}$ at 5 C ), as well as high energy density of 400 Wh $kg^{-1}$, this material could be a promising anode candidate for NIBs at room temperature. Meanwhile, in order to understand the sodium-storage properties of $MoS_2$ in detail, ex-situ XRD and XPS

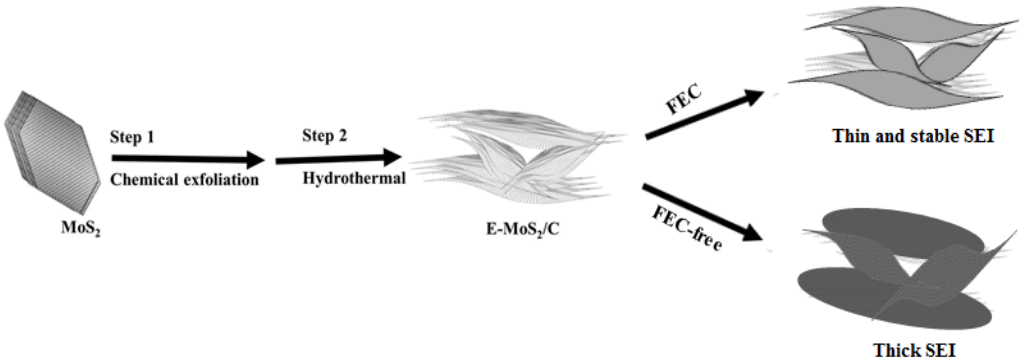


**Figure 6.1** (a) Schematic illustration of preparation of E-$MoS_2$/C and the effect of FEC additive

has been conducted to study the electrochemical reaction mechanism. As shown in Figure 6.1, the synthesis processes consist of two steps, including chemical exfoliation and hydrothermal method. Our strategy to achieve high performance is to use a unique E-$MoS_2$/C as an anode material that possesses expanded *d*-spacing to accommodate large sodium ions. The exfoliated structure could shorten the Na-ion diffusion pathway and also withstand large volume change due to the buffering space created by the crumpled nanosheets. Simultaneously, the carbon component can effectively increase electrode conductivity. On the other hand, various electrolytes were utilized to optimize the cycling performance of E-$MoS_2$/C. The E-$MoS_2$/C is presented as an excellent anode material in 1.0 M $NaClO_4$ with propylene carbonate / ethylene carbonate and 5 wt. % fluoroethylene carbonate additive (PC/EC + 5 wt. % FEC), which is favorable to form thin and stable SEI film due to the FEC reaction with electrolyte.

## 6.2 Experimental methods

### 6.2.1 Material synthesis

Synthesis of exfoliated $MoS_2$/C composite: Firstly, exfoliated $MoS_2$ (E-$MoS_2$) was prepared from pristine $MoS_2$ (P-$MoS_2$) via a modified exfoliation method in a previous report.[31] 1g $MoS_2$ powder was vacuum dried at 120 $^{o}$C for 24 h to remove air and moisture, following by mixing with n-butyl lithium (1 mol $MoS_2$ : 1.5 mol BuLi) in glove box. The mixture was stirred for 3 days at room temperature and transfer into centrifuge tube wash by hexane for 3 times. The obtained solids were dispersed into 500 mL of di-water by stirring for 1 hour. The dispersion was ultra-sonicated for 1-3 hours to ensure the homogenous mixture. The low-speed centrifuge (4400rpm) for 10 minutes was carried out to remove the unexfoliated $MoS_2$. The

obtained $MoS_2$ dispersion was ready to use. The concentration of $MoS_2$ dispersion was estimated by drying method. Exfoliated $MoS_2$/C composite (E-$MoS_2$/C) was fabricated by the hydrothermal method in the second step. Specifically, 0.27 g glucose was dissolved in 20 mL deionized water, and then mixed with 40 mL E-$MoS_2$ dispersion (4.2 mg $mL^{-1}$). The obtained mixture was loaded into a Teflon-lined autoclave, which was then sealed and maintained at 150 $^{o}$C for 5 h, and then allowed to cool down to room temperature naturally. After centrifugation, the black product was then washed three times each with deionized water and absolute ethanol, and dried under vacuum at 80 $^{o}$C overnight. The E-$MoS_2$/C was finally obtained after annealing treatment at 450 $^{o}$C for 2 h and then at 800 $^{o}$C for 2 h in a mixed 5 % $H_2$/Ar atmosphere.

### 6.2.2 Structural characterization

The morphologies of the samples were investigated by field-emission scanning electron microscopy (FESEM; JEOL JSM-7500FA) and transmission electron microscopy (TEM, JEOL 2011, 200 keV). The XRD patterns were collected by powder X-ray diffraction (XRD; GBC MMA diffractometer) with Cu Kα radiation at a scan rate of 1° $min^{-1}$ and 2° $min^{-1}$. Thermogravimetric analysis (TGA) was performed in air with a SETARAM Thermogravimetric Analyzer (France).The X-ray photoelectron spectra (XPS) experiment was carried out using Al Kalpha radiation and fixed analyser transmission mode. The pass energy was 60 eV for the survey spectra and 20 eV for specific elements. The XPS samples were stored in argon box before test to decrease the oxidation.

### 6.2.3 Electrochemical measurements

The electrochemical measurements were conducted by assembling coin-type half

cells in an argon-filled glove box. The slurry was prepared by fully mixing 80 wt. % active materials (P-$MoS_2$, E-$MoS_2$, and E-$MoS_2$/C), 10 wt. % carbon black, and 10 wt. % polyvinylidene difluoride (PVDF) by planetary mixer (KK-250S). Then, the obtained slurry was pasted on a copper film using a doctor blade with a thickness of 100 μm, which was followed by drying in a vacuum oven overnight at 80 °C. The working electrode was prepared by punching the electrode film into discs 0.97 cm in diameter. The sodium foil was cut using a surgical blade from sodium bulk stored in mineral oil. The sodium foil was employed as both reference and counter electrode. The electrodes were separated by a glass fiber separator. Several electrodes with various electrolytes were tested in our work, including P-$MoS_2$ in 1.0 M $NaClO_4$ with PC (P-$MoS_2$ with PC), E-$MoS_2$ in 1.0 M $NaClO_4$ with PC (E-$MoS_2$ with PC), exfoliated $MoS_2$/C in 1.0 M $NaClO_4$ with PC (E-$MoS_2$/C with PC), E-$MoS_2$/C in 1.0 M $NaClO_4$ with PC/EC (E-$MoS_2$/C with PC/EC), and exfoliated $MoS_2$/C in 1.0 M $NaClO_4$ with PC/EC + 5 wt. % FEC (E-$MoS_2$/C with PC/EC+FEC). The electrochemical performance was tested on a LAND Battery Tester. Cyclic voltammetry was performed using a Biologic VMP-3 electrochemical workstation.

### 6.3 Characterization of morphology and structure

The X-ray diffraction (XRD) patterns of pristine $MoS_2$ (P-$MoS_2$), exfoliated $MoS_2$ (E-$MoS_2$), and E-$MoS_2$/C are presented in Figure 6.1a, all of which can be indexed to the hexagonal 2H-$MoS_2$ structure (JPCDS No. 37–1492). P-$MoS_2$ shows more sharp peaks with higher intensity, indicating its good crystallinity with good ordering and well-stacked layered structure. In contrast, E-$MoS_2$ and E-$MoS_2$/C show broadened peaks with weakened (002) diffraction peaks, demonstrating smaller crystallite size and a decrease in the number of stacking layers. Furthermore, as shown in Figure 6.2a the 2 θ value of the (002) diffraction peak has shifted to a lower angle of $13.98^o$ and $14.02^o$ for E-$MoS_2$ and E-$MoS_2$/C, respectively. This corresponds to the increase in the interlayer distance of the (002) plane, which is 0.633 and 0.631 nm, respectively, according to the Bragg equation. Moreover, no characteristic peak of carbon can be detected in E-$MoS_2$/C, indicating the amorphous nature of the carbon.

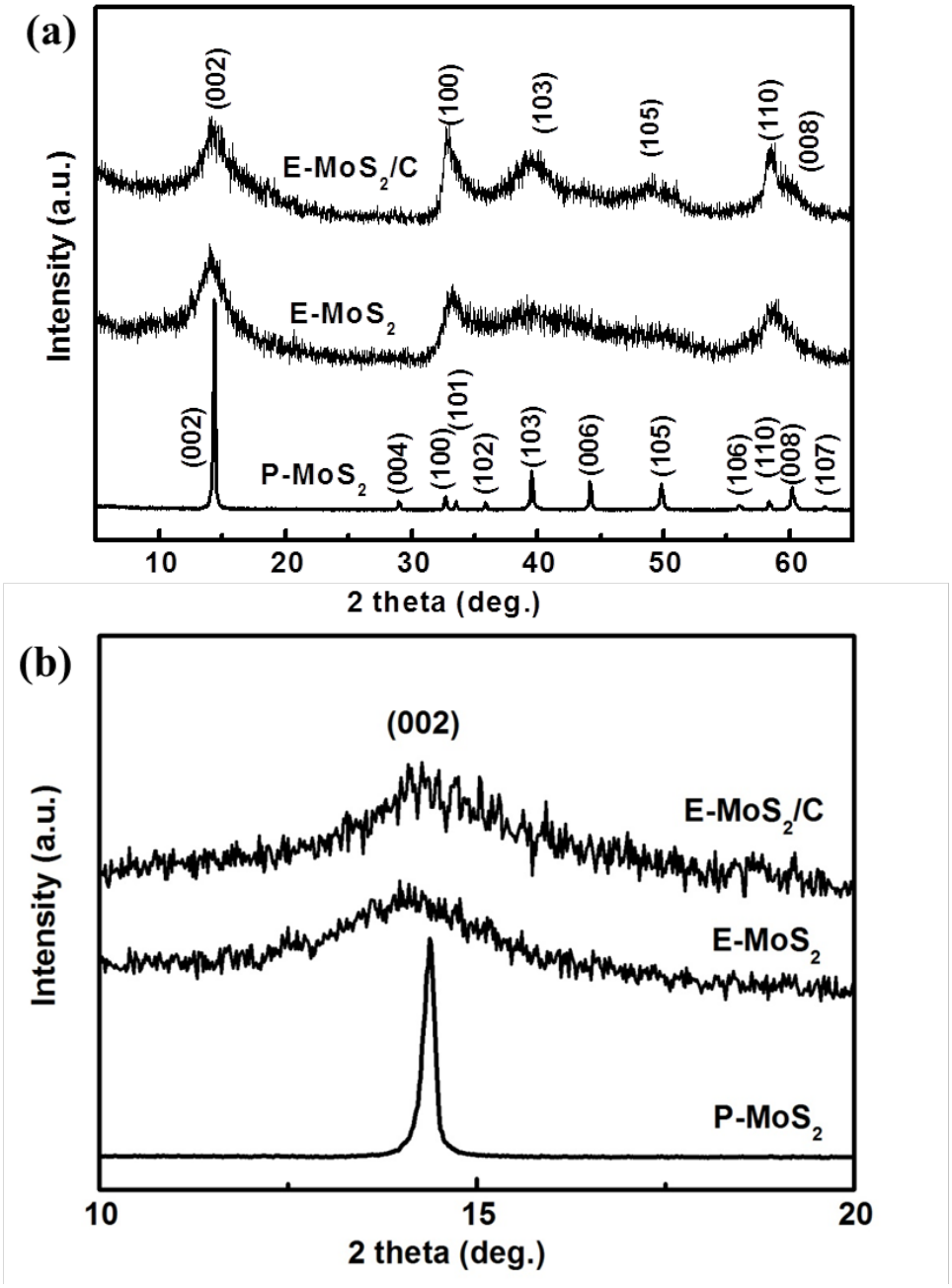


**Figure 6.2** (a) XRD patterns at the range of $5^{o}$ - $65^{o}$; (b) XRD patterns at the range of $10^{o}$ - $20^{o}$ of P-$MoS_2$, E-$MoS_2$, and E-$MoS_2$/C

As shown in Figure 6.3, the TGA curve of P-$MoS_2$ is used as a reference, showing a 10 % weight loss after heating to 650 $^{o}$C in air atmosphere, which indicates that the remaining product after the TGA measurement is pure $MoO_3$. Based on this fact and assuming that the amorphous carbon is completely decomposed after 650 $^{o}$C, it is estimated that the $MoS_2$ content in the composite is approximately 91 wt. %, with successful carbon incorporation of about 9 wt. % in the E-$MoS_2$/C.

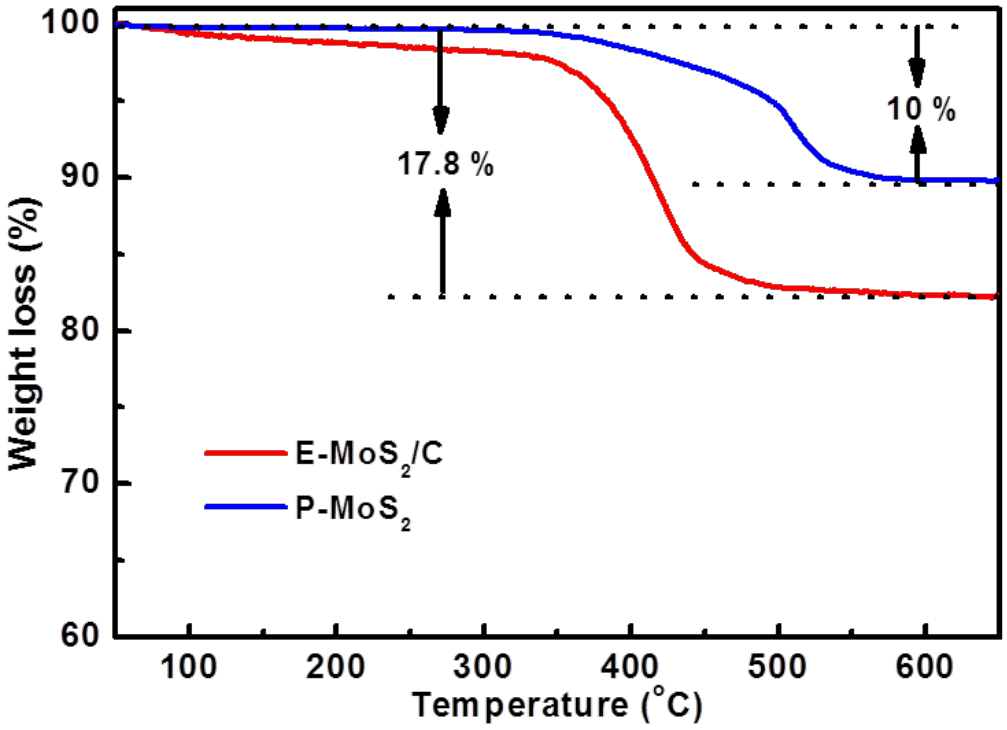


**Figure 6.3** TGA curves of P-$MoS_2$ and E-$MoS_2$/C.

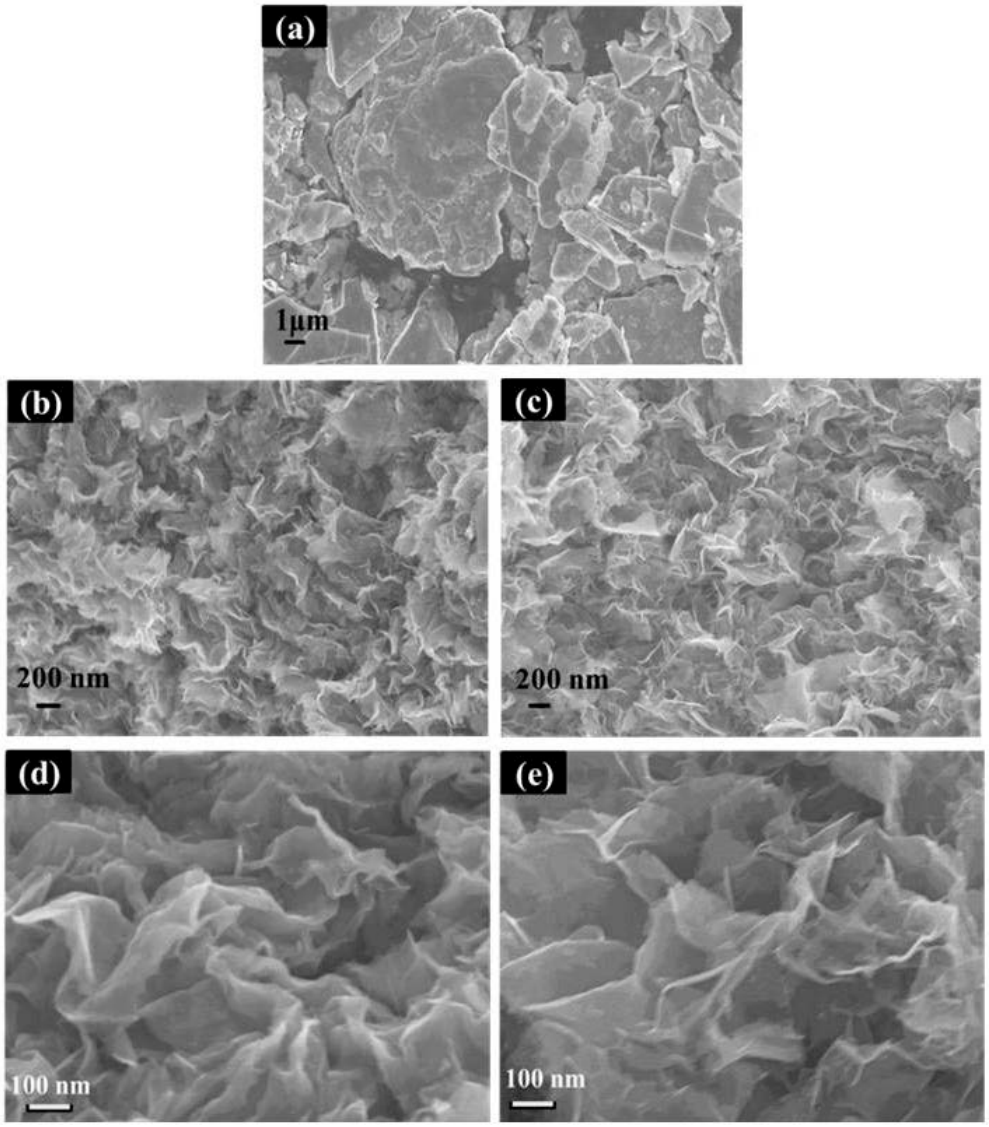


**Figure 6.4** SEM images of (a) P-$MoS_2$, (b) E-$MoS_2$ and (c) E-$MoS_2$/C at low magnification. SEM images of (d) E-$MoS_2$ and (e) E-$MoS_2$/C at high magnification.

Morphological investigations of P-$MoS_2$, E-$MoS_2$, and E-$MoS_2$/C are shown by the SEM images in Figure 6.4. Unlike the P-$MoS_2$ bulk, E-$MoS_2$ and E-$MoS_2$/C are in the form of crumpled sheets. This demonstrates the successful exfoliation of the P-$MoS_2$ into graphene-like nanosheets. Furthermore, it is notable that the nanosheets of E-$MoS_2$/C are thinner than those of E-$MoS_2$, indicating that the E-$MoS_2$/C nanosheets are composed of fewer $MoS_2$ layers and that the incorporation of carbon

restrains the restacking of the $MoS_2$ layers. This can be further confirmed by SEM images at higher magnification.

High resolution transmission electron microscope (HRTEM) images in Figure 6.5 provided insight into the morphology and structure of the P-$MoS_2$, E-$MoS_2$, and E-

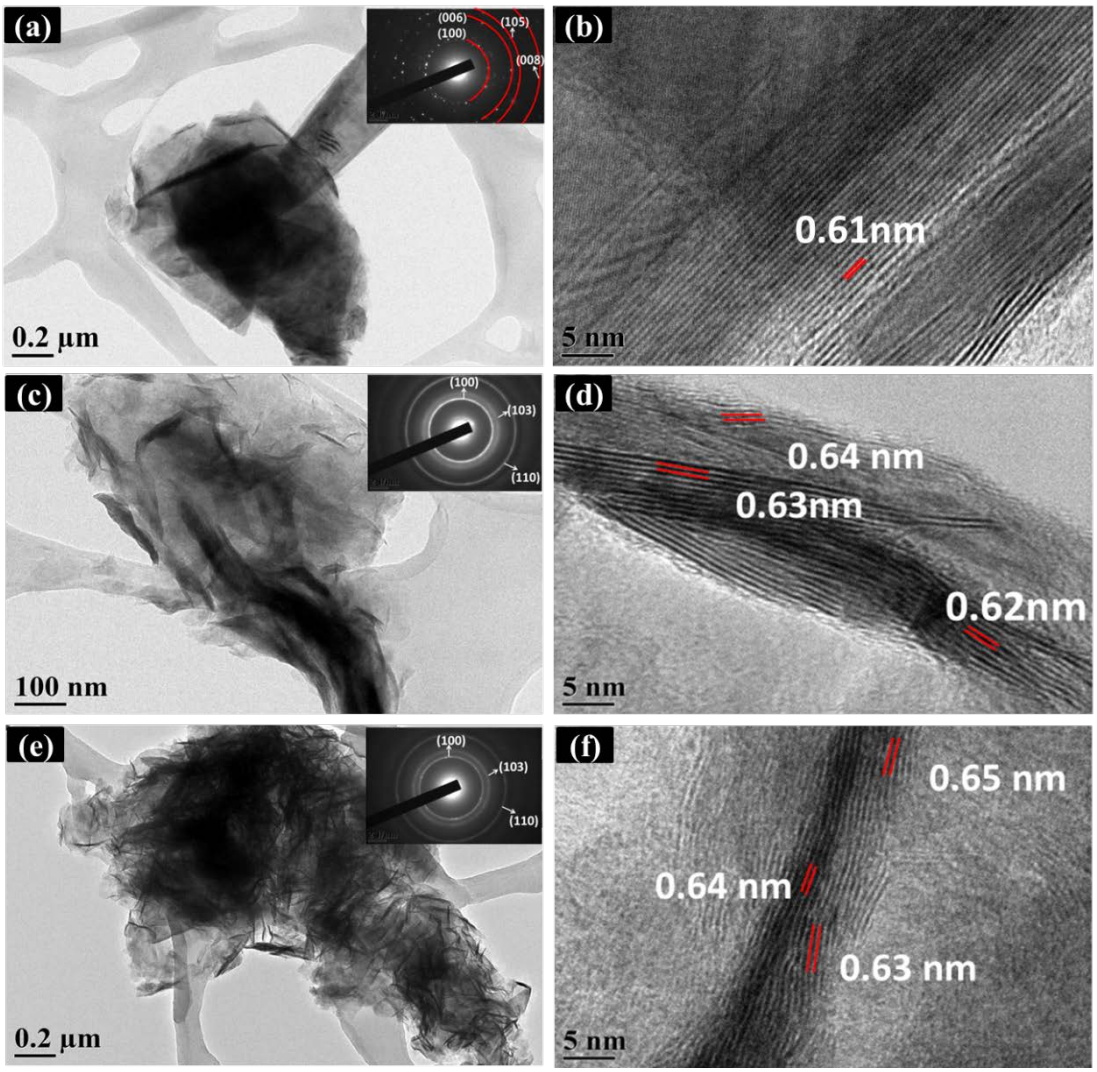


**Figure 6.5** TEM images and corresponding SAED (inset) patterns of (a) P-$MoS_2$, (c) E-$MoS_2$, and (e) E-$MoS_2$/C; and HRTEM images of (b) P-$MoS_2$, (d) E-$MoS_2$, and (f) E-$MoS_2$/C.

$MoS_2$/C. The good crystallization and well-stacked layered structure of P-$MoS_2$ is verified as shown in Figure 6.5a and b, with an interplanar distance of 0.61 nm. In contrast, E-$MoS_2$ and E-$MoS_2$/C (Figure 6.5c and e) displays a relatively loose packing of nanosheets and presents a somewhat transparent appearance. It is also can be seen that the E-$MoS_2$/C possesses much smaller crystal size than P-$MoS_2$ and E-$MoS_2$. Lattice fringes could be observed clearly, measured *d*-spacing of 0.63−0.65 nm and 0.62−0.64 nm for E-$MoS_2$ and E-$MoS_2$/C, respectively, which is consistent with XRD results. The number of restacked layers is less than 10 for E-$MoS_2$/C, which implies that the incorporation of carbon could restrain restacking of the $MoS_2$ layers. It is believed that the larger d-spacing and the smaller crystallite size are favourable to electrochemical storage of the larger sodium.

Energy dispersive X-ray (EDX) analysis in Figure 6.6 at different points reveals that the E-$MoS_2$/C is composed of molybdenum, sulfur, and carbon, and confirms the homogenous dispersion of carbon in the E-$MoS_2$/C.

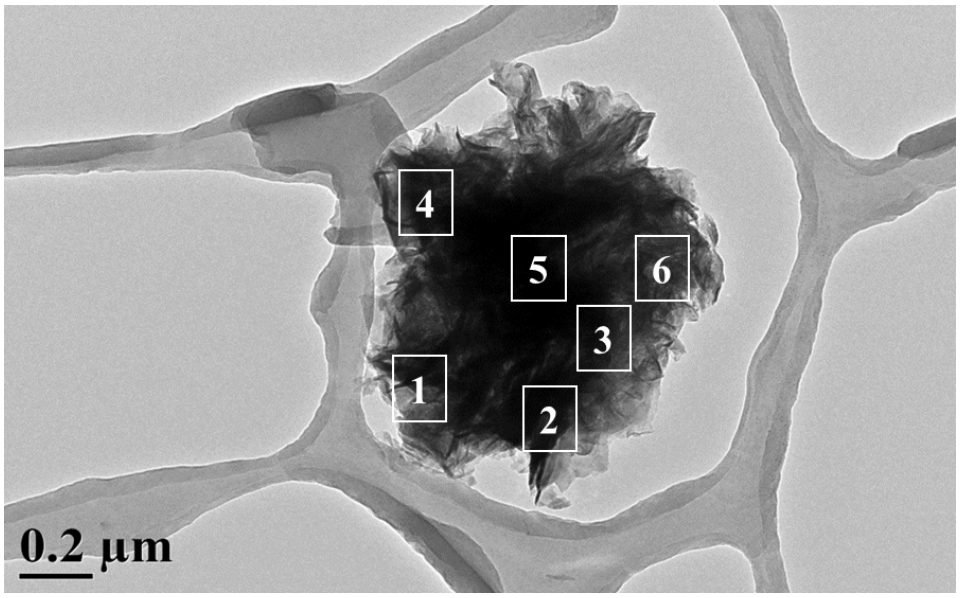


| 1 Element | Mass% | Atom% | 2 Element | Mass% | Atom% |
|---|---|---|---|---|---|
| C K | 17.42 | 55.67 | C K | 15.00 | 60.39 |
| S K | 12.22 | 14.62 | S K | 10.08 | 15.21 |
| Cu K | 7.62 | 4.60 | Cu K | 5.27 | 4.01 |

| Mo L * | 62.74 | 25.10 | Mo L * | 69.66 | 20.39 |
|---|---|---|---|---|---|
| **3** Element | Mass% | Atom% | **4** Element | Mass% | Atom% |
| C K | 19.91 | 58.83 | C K | 43.53 | 81.97 |
| S K | 13.73 | 15.19 | S K | 8.38 | 5.91 |
| Cu K | 7.63 | 4.60 | Cu K | 6.43 | 2.29 |
| Mo L * | 58.72 | 21.72 | Mo L * | 41.66 | 9.82 |
| **5** Element | Mass% | Atom% | **6** Element | Mass% | Atom% |
| C K | 17.66 | 55.01 | C K | 22.40 | 61.41 |
| S K | 15.09 | 17.60 | S K | 15.59 | 16.01 |
| Cu K | 5.86 | 3.45 | Cu K | 7.42 | 3.84 |
| Mo L * | 61.38 | 23.93 | Mo L * | 54.59 | 18.74 |

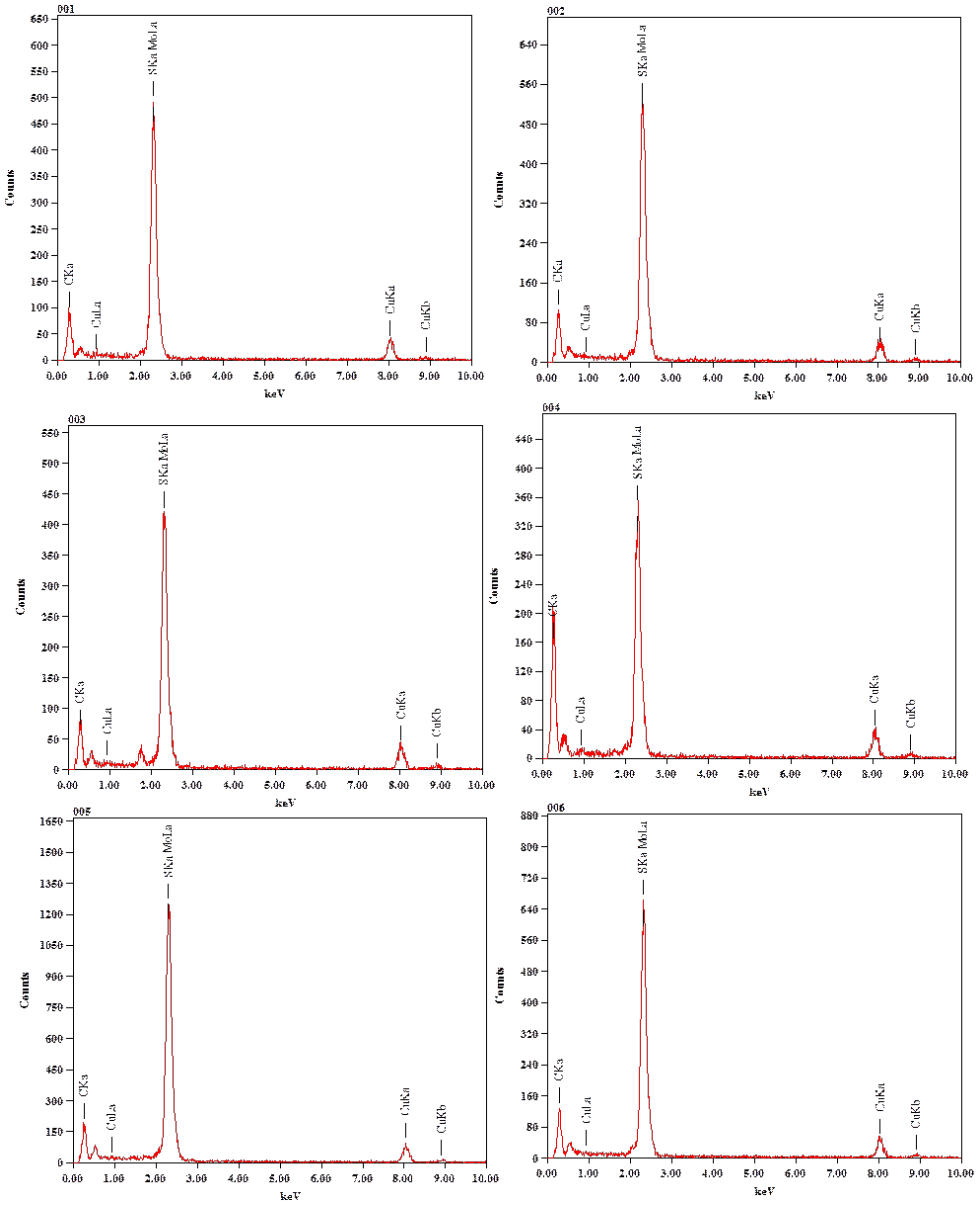


**Figure 6.6** Energy dispersive X-ray (EDX) analysis at selected points.

### 6.4 Electrochemical performance

The electrochemical sodium storage behaviors of these materials were investigated using galvanostatic discharge and cyclic voltammetry measurements. Several electrodes with various electrolytes were tested in our work, including pristine $MoS_2$ in 1.0 M $NaClO_4$ with PC (P-$MoS_2$ with PC), exfoliated $MoS_2$ in 1.0 M $NaClO_4$ with PC (E-$MoS_2$ with PC), exfoliated $MoS_2$/C in 1.0 M $NaClO_4$ with PC (E-$MoS_2$/C with PC), exfoliated $MoS_2$/C in 1.0 M $NaClO_4$ with PC/EC (E-$MoS_2$/C with PC/EC), and exfoliated $MoS_2$/C in 1.0 M $NaClO_4$ with PC/EC + 5 wt. % FEC (E-$MoS_2$/C with PC/EC+FEC). As shown in Figure 6.7, these electrodes show similar charge /dis-

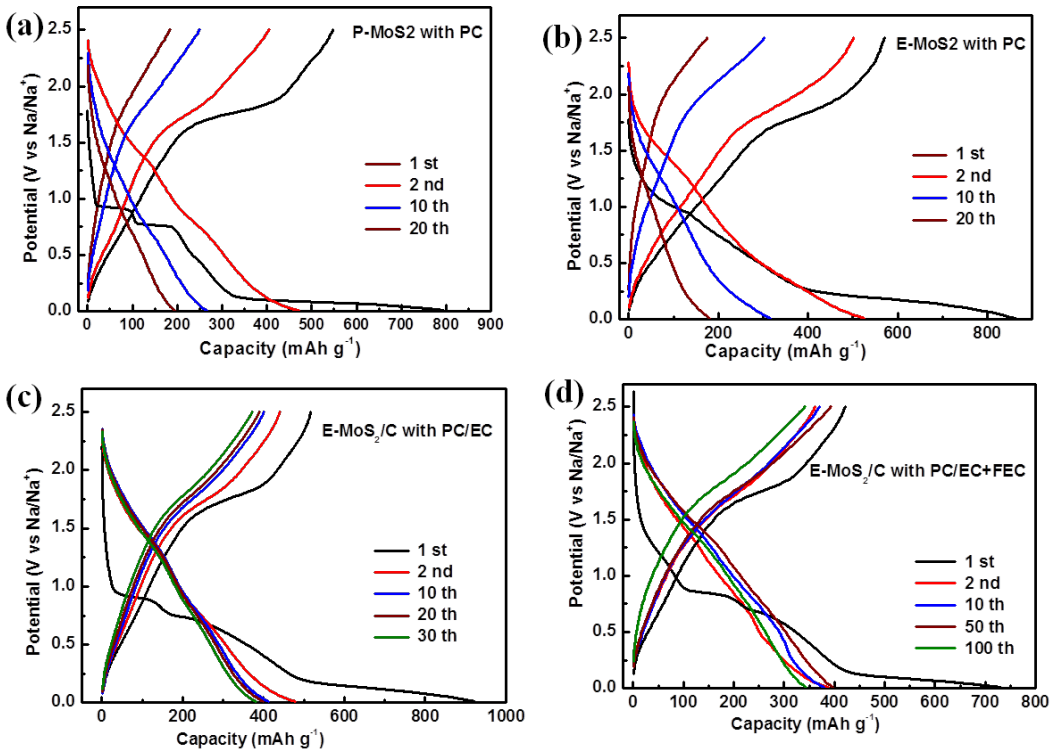


**Figure 6.7** Charge/discharge profiles of (a) P-$MoS_2$ with PC, (b) E-$MoS_2$ with PC, (c) E-$MoS_2$/C with PC/EC and (d) E-$MoS_2$/C with PC/EC+FEC. All the electrodes were tested at a current density of 100 mA $g^{-1}$.

-charge profiles, with slight variation in the plateaus position. The shapes of the charge/discharge profiles are very similar to the report,[11] indicating a similar electrochemical storage mechanism.

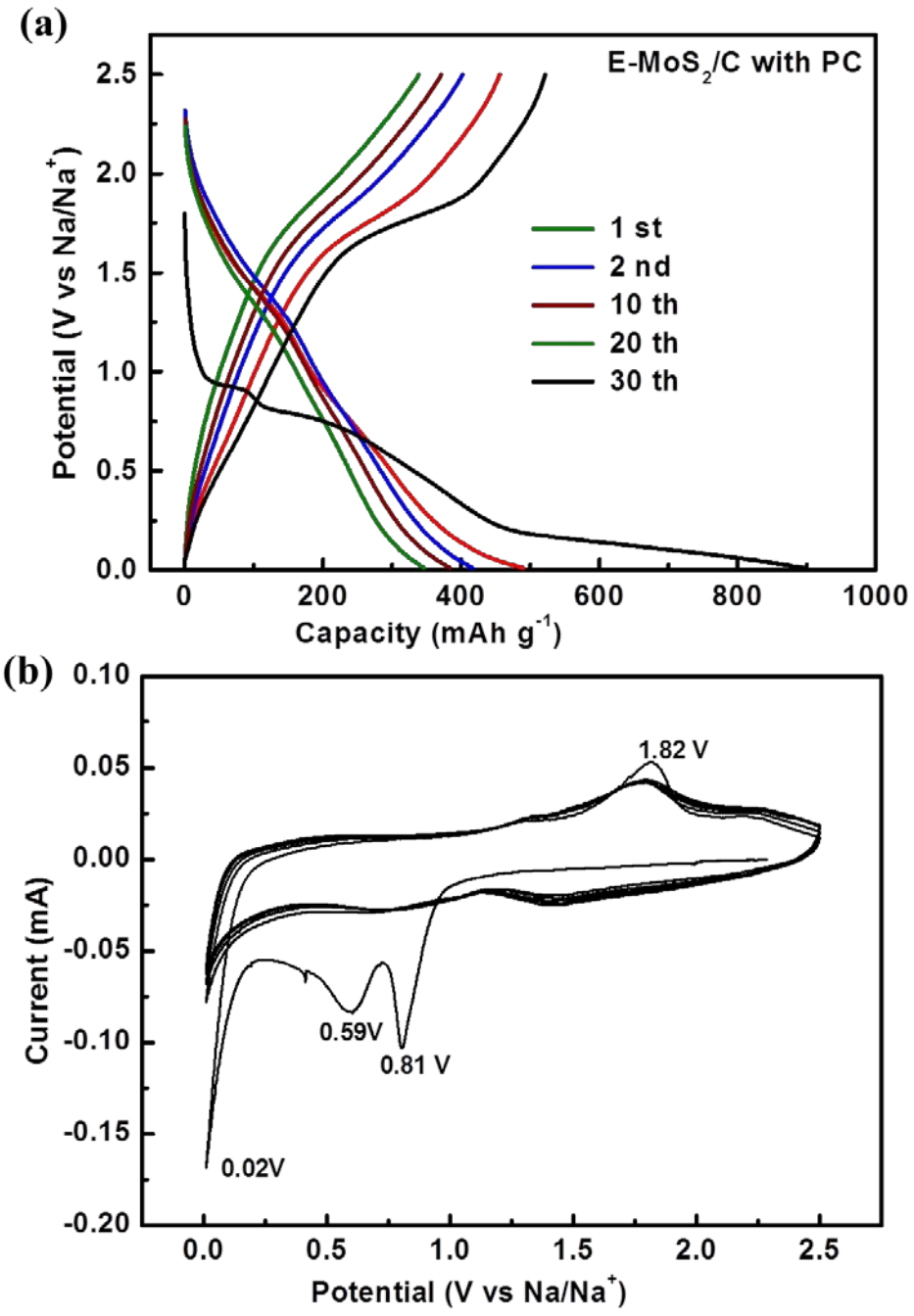


**Figure 6.8** (a) Charge/discharge profiles at a current density of 100 mA $g^{-1}$; (b) Cyclic voltammograms at a scan rate of 0.1 mV $s^{-1}$ for E-$MoS_2$/C in 1.0 M $NaClO_4$ with PC.

We take E-$MoS_2$/C with PC (Figure 6.8) as an example to explain the electrochemical reactions during the charge/discharge process. Three plateaus are observed in Figure 6.8a at ~ 0.9 V, 0.73 V, and 0.1 V during the initial discharge process. The first strongly pronounced plateau at 0.9 V should be indicative of the formation of $Na_xMoS_2$, the plateau at 0.73 V is related to further Na ion reaction with $MoS_2$, and the long 0.1 V plateau should be related to the reduction of $Mo^{4+}$ to Mo metal, accompanied by the formation of $Na_2S$ nanoparticles. In the subsequent discharge process, the discharge profiles turn into sloping curves instead of those three plateaus, which indicate the occurrence of the conversion reaction. During the initial charge process, a plateau at 1.85 V can be seen and is reversible in the following charge cycles, which is supposed to correspond to the redox reaction. There is a corresponding charge plateau at 2.2 V in LIBs.[19-21,32] The difference of ~ 0.3 V is attributed to the standard electrode potential difference ($E^0_{Li/Li^+} - E^0_{Na/Na+} = -0.33$ V). It implies that there is a similar reaction mechanism of $MoS_2$ with both lithium and sodium. In brief, the charge/discharge curves of Na-$MoS_2$ show a sloping profile and voltage hysteresis, which resembles the Li-$MoS_2$ conversion reaction.[19-21,32] The conversion reaction mechanism of Na and E-$MoS_2$/C was further confirmed via *ex-situ* XRD and XPS in Figure. 6.12 and Figure 6.13. As presented in Figure 6.8b, the cyclic voltammogram (CV), which was collected at a scan rate of 0.1 mV $s^{-1}$ in the voltage range from 0.01 V to 2.5 V, show the electrochemical reactions in detail. The peaks are consistent with the potential plateaus observed in the charge/discharge curves. Three reduction peaks appear at 0.81 V, 0.59 V, and 0.02 V in the first cycle, which represent the formation of $Na_xMoS_2$ during the interaction process and the decomposition of $MoS_2$ into Mo and $Na_2S$ through the conversion reaction. In the subsequent oxidation process, a conspicuous peak appears at 1.82 V,

in agreement with the former charge/discharge curves. The CV profiles could be well repeated in following cycles, indicating that the high reversibility of the conversion reaction.

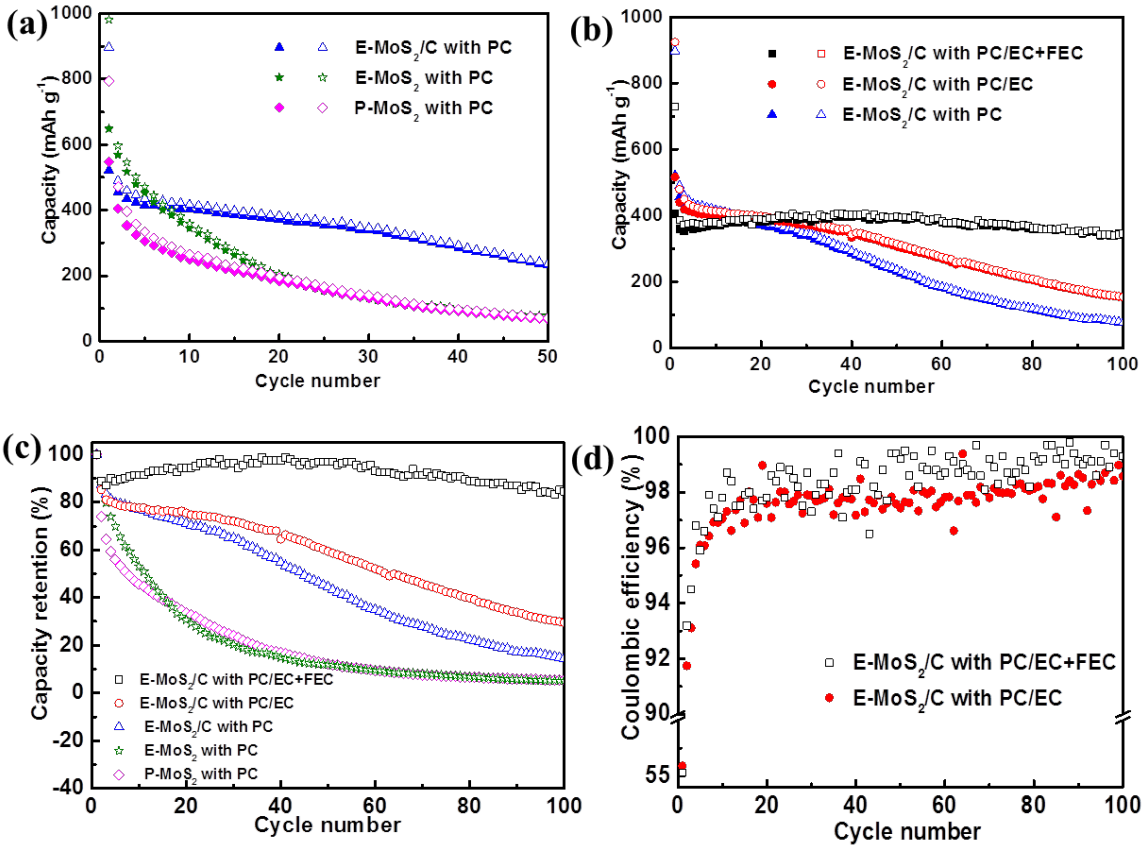


**Figure 6.9 (**a) Cycling performance of P-$MoS_2$, E-$MoS_2$, and E-$MoS_2$/C at 0.01-2.5 V in 1.0 M $NaClO_4$ with PC; (b) Cycling performance of E-$MoS_2$/C at 0.01-2.5 V in various electrolytes; The applied current density was 100 mA $g^{-1}$ for all electrodes; The solid and open symbols represent charge and discharge capacities, respectively; (c) Capacity retention of P-$MoS_2$, E-$MoS_2$, and E-$MoS_2$/C at various electrolytes; (d) Coulombic efficiency of E-$MoS_2$/C in 1.0 M $NaClO_4$ with PC/EC with and without FEC.

The cycling performance of P-$MoS_2$, E-$MoS_2$ and E-$MoS_2$/C were tested in the electrolyte that consisted of 1.0 M $NaClO_4$ with PC. As shown in Figure 6.9a, both

P-$MoS_2$ and E-$MoS_2$ show similar initial Coulombic efficiency (69 % and 66 %) and cycling performance after 20 cycles. E-$MoS_2$ shows higher capacity than P-$MoS_2$, with average reversible capacity of 366.2 mAh $g^{-1}$ and 275.3 mAh $g^{-1}$ in the initial 20 cycles, respectively. This indicates that the E-$MoS_2$ can accommodate more Na ions due to the d-spacing enlargement effect, while it shows almost the same electrochemical performance as P-$MoS_2$ for prolonged cycling as a result of its severe restacking. Interestingly, for E-$MoS_2$/C, the incorporation of carbon can significantly improve the capacity retention with slightly lower initial Coulombic efficiency of 56.1 %. The higher irreversible capacity loss is probably due to its higher specific surface area, leading to more irreversible reactions. It is obvious that E-$MoS_2$/C shows the best electrochemical properties, mainly ascribed to the improved conductivity of the composite. More importantly, they are attributed to the fact that the thinner nanosheets are capable of shortening the Na-ion diffusion length as well. In order to further improve the electrochemical properties of E-$MoS_2$/C in the voltage domain of 0.01 - 2.5 V, different electrolytes were tested. As shown in Fig. 4c, the first cycle Coulombic efficiency of E-$MoS_2$/C is about 56 % in various electrolytes. The reversible capacities with PC and PC/EC are almost the same for the first 20 cycles, with the value of ~ 400 mAh $g^{-1}$, but then decrease to 75.7 mAh $g^{-1}$ and 152.8 mAh $g^{-1}$, respectively, after 100 cycles. Compared to PC, PC/EC solvent has higher conductivity and lower viscosity,[33] so that it can lead to higher capacity retention over longer cycling. Obvious capacity fades are observed for both PC and PC/EC after 30 cycles, which are ascribed to a kinetically limited process, such as electrolyte decomposition.[34] As reported previously, sodium anode would tend to be corroded continuously in the organic electrolytes, rather than allowing a stable SEI film to be formed.[35] In order to improve the performance of electrodes in NIBs, the

film-forming additive, fluoroethylene carbonate (FEC), has recently been used to modify the SEI film of carbon anode [36] and Sb/C anode.[13] FEC has been observed to form a passivation film at 0.7 V on both the carbon and the sodium surfaces, thereby protecting the electrodes from further side reactions with the solvents. A compact SEI film that is likely to be composed of stable alkali fluoride or fluroalkyl carbonate was inferred to be formed on the Sb/C anode. Therefore, E-$MoS_2$/C was further tested in the electrolyte with the addition of 5 wt. % FEC, with the expectation of longer cycling life. As shown in Figure 6.9b, the E-$MoS_2$/C electrode in the electrolyte with 5 wt. % FEC could maintain an almost stable capacity of 390 mAh $g^{-1}$ over 100 cycles. The significant improvement of cycling behavior resulted from

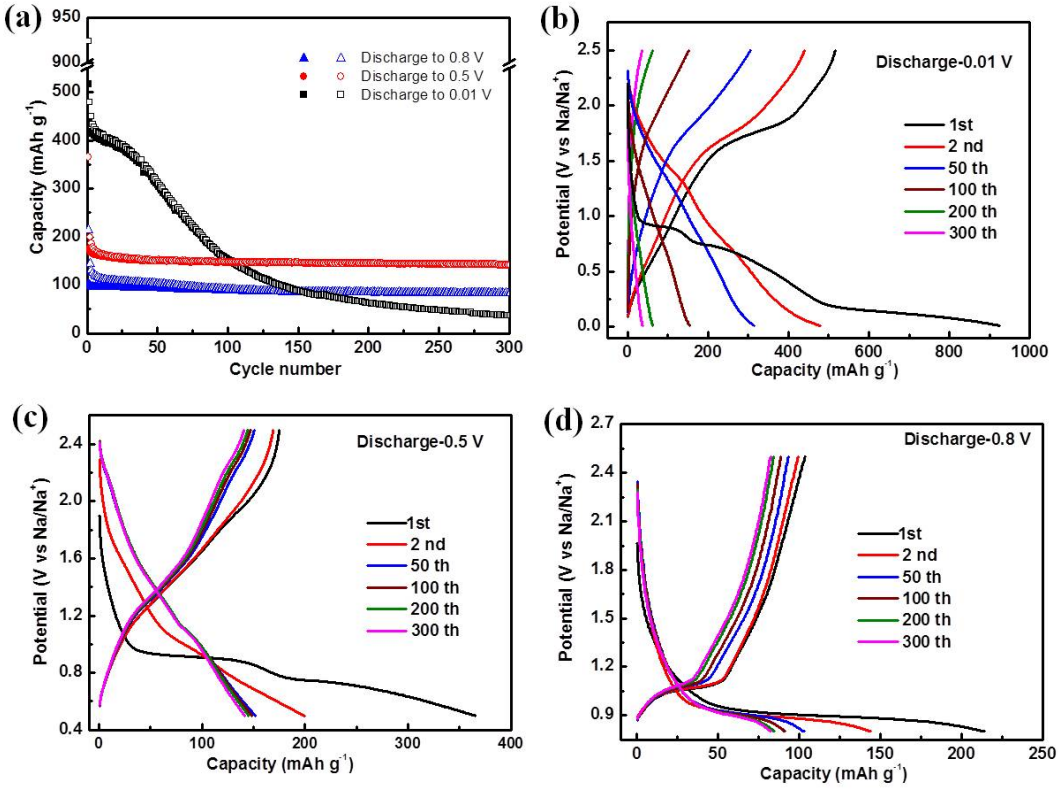


**Figure 6.10** (a) Cycling performance and (b) charge/discharge profiles of E-$MoS_2$/C in the voltage ranges from 2.5 V to 0.8 V, 0.5 V, and 0.01 V in 1.0 M $NaClO_4$ with PC.

the effect of the FEC additive, which could enhance the structural stability of the SEI film and thus curb further electrolyte decomposition. As shown in Figure 6.9c, it is manifest that the capacity retentions increase gradually and significantly by enlarging the interlayer distance of $MoS_2$ and optimizing the electrolyte, thereby leading to a high cycling capacity retention of ~ 82 % over 100 cycles for E-$MoS_2$/C in 1.0 M $NaClO_4$ with PC/EC+FEC. Furthermore, in contrast with the electrolyte without FEC (Figure 6.9d), the Coulombic efficiency of E-$MoS_2$/C is improved to ~ 98 % on average due to the application of FEC additive.

It is worth noting that the E-$MoS_2$/C in 1 M $NaClO_4$ with PC exhibited distinct cycling performance for different discharge cut-off voltages (Figure 6.10a). In the range of 0.01-2.5 V, the electrode delivers the highest average capacity of 375.5 mAh $g^{-1}$ for the initial 50 cycles, while it shows serious capacity degradation in successive cycles. When the discharge voltages are cut off at 0.8 V and 0.5 V, even though the capacities decrease to ~ 83 mAh $g^{-1}$ and ~ 140 mAh $g^{-1}$, respectively, no capacity decay is observed over 300 cycles. It is reasonable to conclude that the cycling stability is attributable to the intercalation reaction and the stability of the electrolyte solution at lower potentials. When it was tested during 2.5 - 0.8 V (Figure 6.10d), the charge/discharge curves show repeatable plateau for 300 cycles, which confirmed the intercalation/deintercalation process with no change of $MoS_2$ layer structure. When discharged to 0.8V, it also showed good cycling stability, which is consistent with the intercalation/deintercalation process with distortion of $MoS_2$ layer structure. Thus, the charge/discharge curves are slope curves instead of obvious plateaus. However, when it was fully discharged to 0.01 V (Figure 6.10b), the distorted $MoS_2$ was further reacted with Na ions, which is corresponding to the

conversion reaction. This process leads to higher capacity and the realization of conversion reaction process for the following cycles.

Furthermore, the rate capabilities of E-$MoS_2$/C with various electrolytes are evaluated in Figure 6.11a. The electrodes were tested at 40, 100, 200, 400, 1000, and 2000 mA $g^{-1}$ (namely, approximately at the C-rates of 0.125, 0.25, 0.5, 1, 2.5, and 5 C), respectively. The electrodes deliver average capacities of 467.7 mAh $g^{-1}$, 509.6 mAh $g^{-1}$, and 460.7 mAh $g^{-1}$ for PC/EC+FEC, PC/EC, and PC at 0.125 C, respectively. The corresponding capacities are 359.4 mAh $g^{-1}$, 334.1 mAh $g^{-1}$, and 209. 1 mAh $g^{-1}$ at 1 C. When the current rate increases gradually to 5 C, the capacities decrease to 290.1 mAh $g^{-1}$, 205.7 mAh $g^{-1}$, and 81.3 mAh $g^{-1}$, respectively. When the current goes directly back to 0.125 C, the average capacity can recover to ~ 440 mAh $g^{-1}$. The capacity retention of the electrodes with different electrolytes at various current rates is presented in Figure 6.11b. The capacity retention is 62.0 %, 40.3 %, and 17.6 % for PC/EC+FEC, PC/EC, and PC at 5 C, respectively. It is obvious that E-$MoS_2$/C with PC/EC+FEC shows the best capacity retention with increasing current rate. The excellent rate capability with FEC additive is likely to be due to the higher ionic conductivity of the SEI film. From its first charge/discharge curve (Figure 6.7d), we can only infer that a stable SEI film is probably formed within the range of 0.80-1.25 V. Further investigations of the components, the formation process, and the ionic conductivity for this SEI layer are needed in the future.

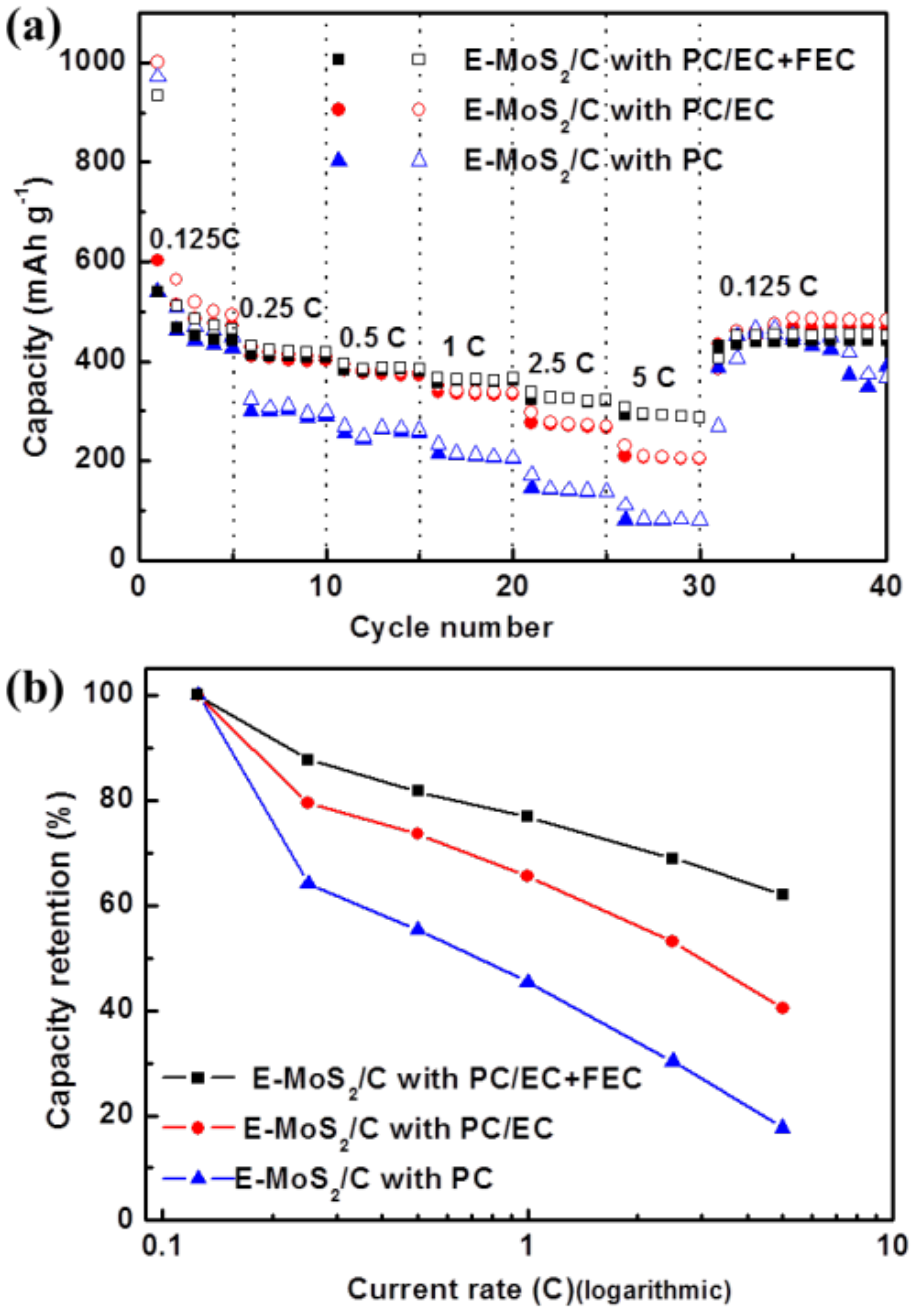


**Figure 6.11** (a) Rate capability, (b) capacity retention of E-$MoS_2$/C in various electrolytes at different current densities.

### 6.5 Sodium-storage mechanism

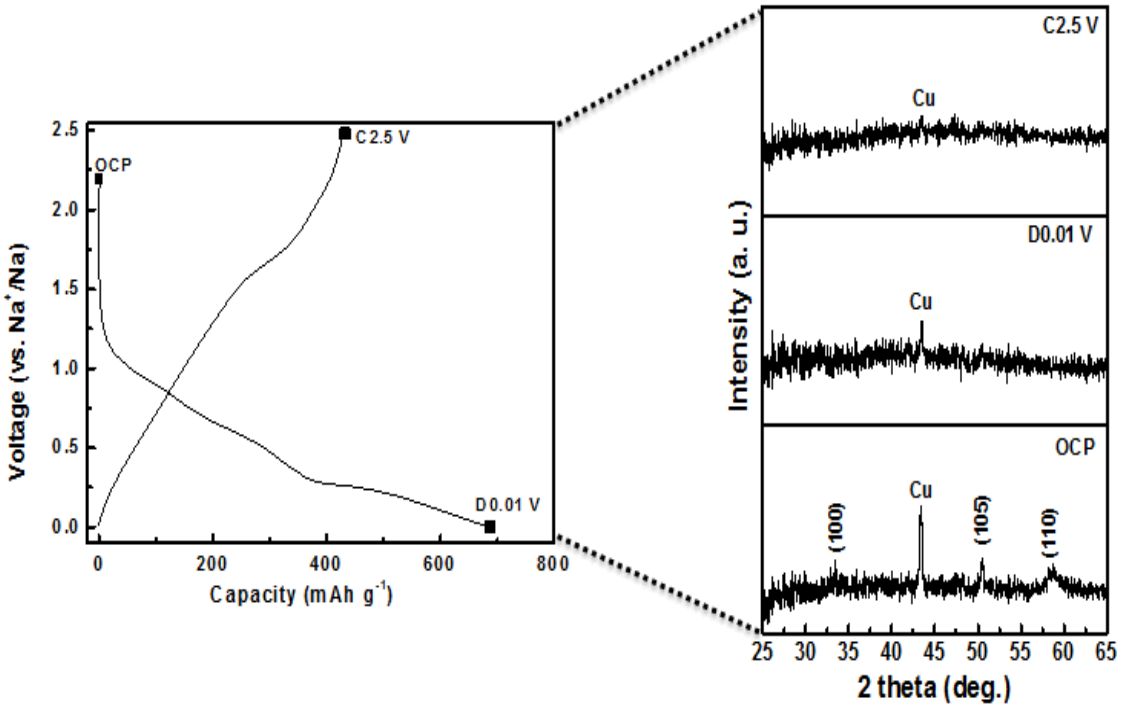


**Figure 6.12** (a) First charge/discharge curves at specified states at current rate of 10 mA $g^{-1}$ and (b) corresponding ex-situ XRD patterns at a scan rate of $1^{o}$ $min^{-1}$ for different states of E-$MoS_2$/C in 1.0 M NaClO4 with PC: OCP (open circuit potential), D0.01 V(discharged to 0.01 V) and C2.5 V (charged back to 2.5 V).

The XRD samples were prepared by peeling the electrode materials off the Cu current collector, followed with sealing it onto XRD holder by kapton tape. This process can avoid the disturbance of strong Cu peaks and the oxidation of electrode material. The XRD pattern shown in Figure 6.12b has deducted the background of kapton tape. The fresh electrode coated by kepton tape can show several typical peaks of E-$MoS_2$/C, which were (100), (105), and (110). In addition, a small peak located at ~ 43.5 $^{o}$ originates from the Cu trace from the current collector. When the electrode was fully discharged to 0.01 V, all of the peaks disappeared and the electrode material showed the amorphous nature. It maintained amorphous nature

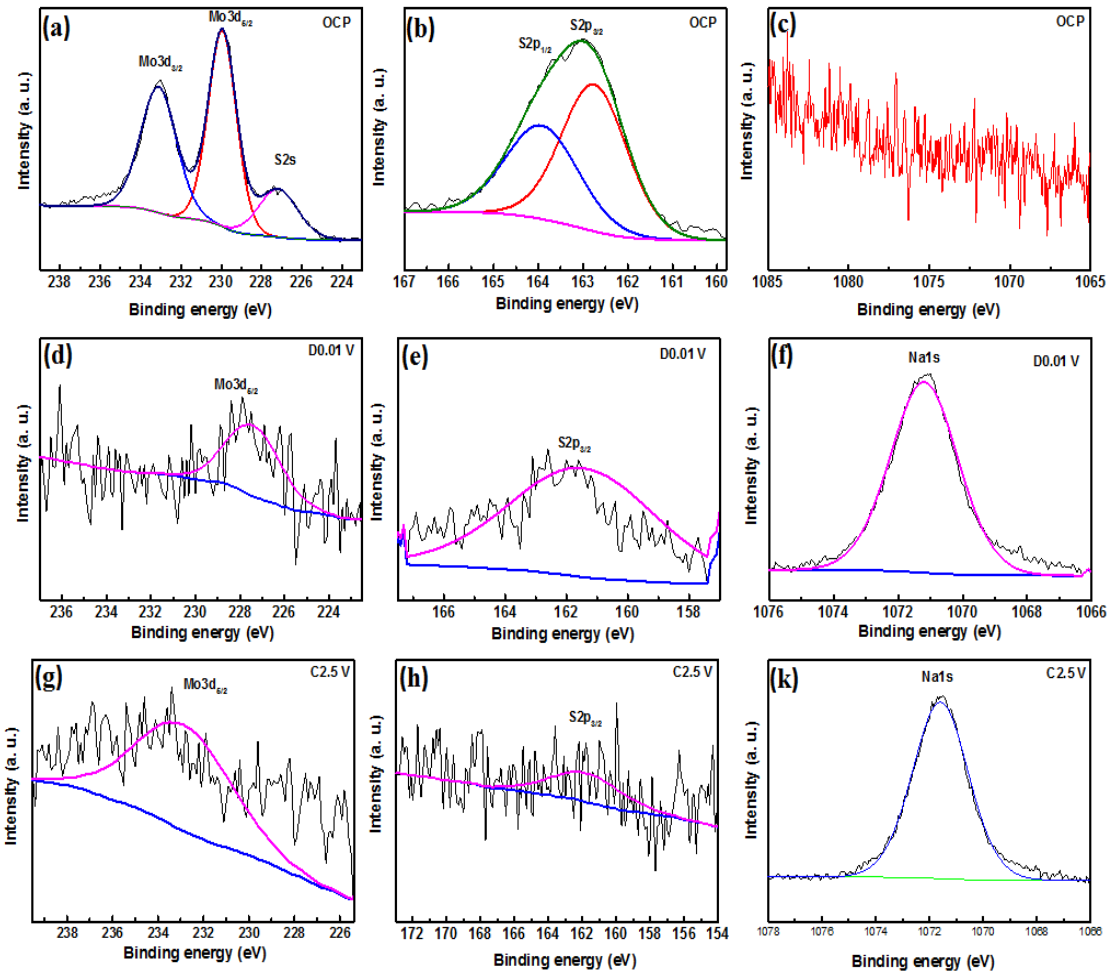


with PC: (a), (d), and (g) Mo 3d spectrum at OCP, D0.01 V, and C2.5 V; (b), (e), and (h) S 2p spectrum at OCP, D0.01 V, and C2.5 V; (c), (f), and (k) Na 1s at OCP, D0.01 V, and C2.5 V.

when the electrode material was fully charged back to 2.5 V. The results proved that E-$MoS_2$/C underwent a conversion reaction during the charge/discharge process. Further evidence for $MoS_2$-Na conversion reaction was provided from XPS analysis. For the E-$MoS_2$/C electrode at OCP state, the Figure 6.13a shows the predominant peaks at ca. 229.7 and 232.8 eV, which is ascribed to $Mo3d_{5/2}$ and $Mo3d_{3/2}$ binding energies, respectively. Correspondingly, the peaks at ca. 162.5 and 163.4 eV can be attributed to $S2p_{3/2}$ and $S2p_{1/2}$ binding energies, respectively. The well-defined spin-coupled Mo and S doublets demonstrate the hexagonal $MoS_2$ state. No sodium

element is observed for the fresh electrode. When the electrode was charged to 0.01 V, the $Mo3d_{5/2}$ peak (Figure 6.13a) shifts to ~ 227.5 eV; it is corresponding to the reduction of $Mo^{4+}$ into Mo. A distinguished peak at ca.1071.2 in Figure 6.13c can be indexed to the Na1s. The $S2p_{3/2}$ peak shifts to 161.5 eV, which indicates the presence of $Na_2S$. When it was charged to 2.5 V, the $Mo3d_{5/2}$ peak appears at higher binding energy (~ 232.6 eV), which is ascribed to the existence of $Mo^{6+}$. The Na1s peak at ca. 1072.58 eV is probably corresponding to $Na^+$ in $Na_2O$. This is due to high activity of charge products ($Mo^{4+}$ and Na), which was tend to be oxidized in air during sample preparation. Combining the ex-situ XRD and XPS of E-$MoS_2$/C electrode, it is obvious that the E-$MoS_2$/C underwent a conversion reaction during sodiation/desodiation.

## 6.6 Conclusions

In summary, we successfully applied $MoS_2$ with highly improved capacity through conversion reaction in a rechargeable sodium battery. Several strategies were exploited to progressively optimize its Na-storage properties, including the exfoliation of $MoS_2$ layers, the incorporation of carbon, and the optimization of the electrolyte system. As a result, E-$MoS_2$/C in 1.0 M $NaClO_4$ with PC/EC+FEC achieved a high reversible capacity and exhibited excellent rate capability. Our findings have therefore revealed a promising anode material candidate for a high-capacity and long-life sodium ion battery.

## 6.7 References


1. J.-M. Tarascon and M. Armand, *Nature*, 2001, 414, 359-367.

2. J. B. Goodenough and Y. Kim, *Chemistry of Materials*, 2009, 22, 587-603.

3. X. Wang, Q. Qu, Y. Hou, F. Wang and Y. Wu, *Chemical Communications*, 2013, 49, 6179-6181.

4. B. Zhang, Y. Liu, X. Wu, Y. Yang, Z. Chang, Z. Wen and Y. Wu, *Chemical Communications*, 2014, 50, 1209-1211.

5. H. Zhang, X. Wu, T. Yang, S. Liang and X. Yang, *Chemical Communications*, 2013, 49, 9977-9979.

6. S.-W. Kim, D.-H. Seo, X. Ma, G. Ceder and K. Kang, *Advanced Energy Materials*, 2012, 2, 710-721.

7. J. H. Lee, R. Black, G. Popov, E. Pomerantseva, F. H. Nan, G. A. Botton and L. F. Nazar, *Energy & Environmental Science*, 2012, 5, 9558-9565.

8. D. Kim, S. H. Kang, M. Slater, S. Rood, J. T. Vaughey, N. Karan, M. Balasubramanian and C. S. Johnson, *Advanced Energy Materials*, 2011, 1, 333-336.

9. Y. Cao, L. Xiao, W. Wang, D. Choi, Z. Nie, J. Yu, L. V. Saraf, Z. Yang and J. Liu, *Advanced Materials*, 2011, 23, 3155-3160.

10. R. Berthelot, D. Carlier and C. Delmas, *Nature Materials*, 2011, 10, 74-80.

11. M. Sathiya, K. Hemalatha, K. Ramesha, J.-M. Tarascon and A. Prakash, *Chemistry of Materials*, 2012, 24, 1846-1853.

12. L. Xiao, Y. Cao, J. Xiao, W. Wang, L. Kovarik, Z. Nie and J. Liu, *Chem. Commun.*, 2012, 48, 3321-3323.

13. J. Qian, Y. Chen, L. Wu, Y. Cao, X. Ai and H. Yang, *Chemical Communications*, 2012, 48, 7070-7072.

14. Q. Sun, Q.-Q. Ren, H. Li and Z.-W. Fu, *Electrochemistry Communications*, 2011, 13, 1462-1464.

15. A. B. Laursen, S. Kegnæs, S. Dahl and I. Chorkendorff, *Energy & Environmental Science*, 2012, 5, 5577-5591.

16. R. Tenne, *Nat. Nanotechnol.*, 2006, 1, 103-111.

17. Z. Lu, A. Schechter, M. Moshkovich and D. Aurbach, *Journal of Electroanalytical Chemistry*, 1999, 466, 203-217.

18. Y. Liang, R. Feng, S. Yang, H. Ma, J. Liang and J. Chen, *Advanced Materials*, 2011, 23, 640-643.

19. K. Chang and W. Chen, *Chemical Communications*, 2011, 47, 4252-4254.

20. S. Ding, D. Zhang, J. S. Chen and X. W. D. Lou, *Nanoscale*, 2012, 4, 95-98.

21. H. Liu, D. Su, R. Zhou, B. Sun, G. Wang and S. Z. Qiao, *Advanced Energy Materials*, 2012, 2, 970-975.

22. Q. Wang and J. Li, *The Journal of Physical Chemistry C*, 2007, 111, 1675-1682.

23. X. Fang, X. Yu, S. Liao, Y. Shi, Y.-S. Hu, Z. Wang, G. D. Stucky and L. Chen, *Microporous and Mesoporous Materials*, 2012, 151, 418-423.

24. C. Zhang, H. B. Wu, Z. Guo and X. W. D. Lou, *Electrochemistry Communications*, 2012, 20, 7-10.

25. G. Du, Z. Guo, S. Wang, R. Zeng, Z. Chen and H. Liu, *Chemical Communications*, 2010, 46, 1106-1108.

26. H. Hwang, H. Kim and J. Cho, *Nano Letters*, 2011, 11, 4826-4830.

27. D. Aurbach, Z. Lu, A. Schechter, Y. Gofer, H. Gizbar, R. Turgeman, Y. Cohen, M. Moshkovich and E. Levi, *Nature*, 2000, 407, 724-727.

28. O. Chusid, Y. Gofer, H. Gizbar, Y. Vestfrid, E. Levi, D. Aurbach and I. Riech, *Advanced Materials*, 2003, 15, 627-630.

29. J. Park, J.-S. Kim, J.-W. Park, T.-H. Nam, K.-W. Kim, J.-H. Ahn, G. Wang and H.-J. Ahn, *Electrochimica Acta*, 2013, 92, 427-432.

30. Y.-X. Wang, S.-L. Chou, D. Wexler, H.-K. Liu and S.-X. Dou, *Chemistry – A European Journal*, 2014, 20, 9607-9612.

31. P. Joensen, R. Frindt and S. R. Morrison, *Mater. Res. Bull.*, 1986, 21, 457-461.

32. K. Chang, W. Chen, L. Ma, H. Li, H. Li, F. Huang, Z. Xu, Q. Zhang and J.-Y. Lee, *Journal of Materials Chemistry*, 2011, 21, 6251-6257.

33. A. Ponrouch, E. Marchante, M. Courty, J.-M. Tarascon and M. R. Palacin, *Energy & Environmental Science*, 2012, 5, 8572-8583.

34. A. Ponrouch, P.-L. Taberna, P. Simon and M. R. Palacín, *Electrochimica Acta*, 2012, 61, 13-18.

35. M. D. Slater, D. Kim, E. Lee and C. S. Johnson, *Advanced Functional Materials*, 2013, 23, 947-958.

36. S. Komaba, T. Ishikawa, N. Yabuuchi, W. Murata, A. Ito and Y. Ohsawa, *ACS Applied Materials & Interfaces*, 2011, 3, 4165-4168.

# CHAPTER 7 HIGH-PERFORMANCE SODIUM-ION BATTERIES AND SODIUM-ION PSEUDOCAPACITORS BASED ON $MOS_2$/GRAPHENE COMPOSITES

Sodium-ion energy storage, including sodium-ion batteries (NIBs) and electrochemical capacitive storage (NICs), is considered as a promising alternative to lithium-ion energy storage. It is an intriguing prospect, especially for large-scale applications, due to its low cost and abundance. $MoS_2$ sodiation/desodiation with Na ions is based on the conversion reaction, which is not only able to deliver higher capacity than intercalation reaction, but is also supposed to be applied in capacitive storage due to its typically sloping charge/discharge curves. Here we construct NIBs and NICs based on expanded $MoS_2$/graphene composite ($MoS_2$/G). The enlarged *d*-spacing, participation of graphene matrix, and the unique properties of the $MoS_2$/G substantially optimize Na storage behaviors, accommodating large volume changes and facilitating fast ion diffusion as well. $MoS_2$/G can exhibit a stable capacity of ~ 350 mAh $g^{-1}$ over 200 cycles at 0.25 C in half cells, and delivers a capacitance of 50 F $g^{-1}$ over 2000 cycles at 1.5 C in pseudocapacitors with a wide voltage window of 0.1-2.5 V.

**Y.-X. Wang,** S.-L. Chou, D. Wexler, H.-K. Liu, S.-X. Dou. *Chemistry-A European Journal* 2014, 20, 9607-9612.

## 7.1 Introduction

Considering current rechargeable battery systems for renewable energy storage, lead acid, nickel/cadmium, and vanadium-redox flow batteries all suffer from serious environmental problems; use of sodium/sulfur battery is limited because of the high operating temperature (~ 350 $^{o}$ C); rechargeable lithium-ion batteries (LIBs), as the mainstay of energy storage, have been successfully commercialized in portable electronic devices.[1, 2] LIBs, however, are encountering an inevitable challenge with respect to large-scale energy storage due to both lithium resources and cost. Thus, it is significant and urgent to develop an essentially new battery system, which needs to be low cost, environmentally friendly, and safe. Sodium, located in the same main group in the periodic table after lithium, is one of the most attractive elements to replace lithium. It is 4-5 orders of magnitude more abundant than lithium, and the cost of the sodium-based materials is much lower than for the lithium-based materials. In addition, the standard potential of $Na^{+}$/Na (- 2. 71 V) is slightly higher than that of $Li^{+}$/Li (- 3.05 V). These features point to the great potential of sodium-ion batteries for renewable energy and smart grids.[3, 4] To date, various cathode materials, including layered transition metal oxides,[5-8] organic polymers,[3,9,10] and polyanion fluorophosphates,[11-15] have been reported to reversibly accommodate Na ions. Anode research is mainly focused on carbonaceous material,[16-18] alloyable metals,[19] metal oxides/sulfides [20-25] and non-metal materials.[26-28] Furthermore, electrochemical capacitors are receiving great attention as well, because of their significantly higher power density than batteries with prolonged cycle life, although they also have relatively lower energy density than batteries.[29, 30] To combine the advantages of both batteries and capacitors, Na-based electrochemical capacitors

have been proposed and are also a fascinating alternative for future energy storage.[31, 32]

Molybdenum disulfide ($MoS_2$), with an analogous structure to graphite, has attracted extensive interest in terms of energy storage, hydrogen storage, catalysis, and solid lubricants. This layer-structured material possesses S-Mo-S sandwich layers, with the sandwiches stacked together via weak van der Waals interactions. Specifically, atoms within the layers of $MoS_2$ are bound by strong covalent bonds, whereas the individual layers are bound together by weak van der Waals interactions. Many reports have involved the application of $MoS_2$ in lithium-ion batteries, since lithium ions can intercalate between the layers.[33-35] Remarkably, expanded $MoS_2$, fabricated via lithiation method with an enlarged c lattice parameter, has achieved higher capacity with longer cycling span than commercial $MoS_2$ (C-$MoS_2$). The expanded $MoS_2$ tends to be prone to serious restacking, however, due to its high surface energy. Moreover, the poor electronic/ionic conductivity between adjacent S-Mo-S sheets further obstructs its application as electrode material. Thus, many researchers have turned to assembling graphene sheets with expanded $MoS_2$ to construct three-dimensional (3D) architectures. The obtained $MoS_2$/G composite would offer high specific surface area, strong mechanical strength, and fast mass transport kinetics. More importantly, the graphene matrix can not only effectively enhance the conductivity and stability of the active materials, but also can significantly inhibit the aggregation of exfoliated $MoS_2$ sheets. The reported studies show that $MoS_2$/G composite possesses synergistic effects between the layered $MoS_2$ and the graphene, which result in good electrochemical properties in LIBs.[36, 37] This strategy is capable of capitalizing on the advantages of $MoS_2$ anode. Recently, the research on $MoS_2$ has

been extended to the sodium-ion battery, and the intercalation mechanism of $MoS_2$ and Na has been confirmed over the narrow voltage range of 0.4-2.6 V, with the electrode delivering a low capacity of 85 mAh $g^{-1}$ over 100 cycles.[38] Most recently, Singh's group explored the electrochemical performance of free-standing $MoS_2$/G composite paper. However, the best electrode with 73 wt. % $MoS_2$ in the composite only delivers a low capacity of 218 mAh $g^{-1}$ after 20 cycles.[39]

Expanded $MoS_2$/G composite ($MoS_2$/G), which was prepared by the attachment of expanded $MoS_2$ layers onto graphene sheets by a simple hydrothermal method, results in excellent electrochemical properties in both the sodium ion battery and the sodium-ion pseudocapacitor. The sodium ion battery is able to deliver a high capacity of 313 mAh $g^{-1}$ over 200 cycles at 0.25 C (1 C = 400 mA $g^{-1}$), with capacity retention of 81%. As for the sodium ion pseudocapacitor, the sodium-ion capacitor (NIC) full cell shows excellent cycling performance over 2000 cycles with relatively stable capacitance (~ 50 F $g^{-1}$) at 1.5 C. Hence, $MoS_2$/G can achieve good energy and power density, high rate capability, and good cycling stability in Na-ion electrodes and pseudocapacitors, providing a promising candidate for high-performance and sustainable energy storage systems.

## 7.2 Experimental sections

### 7.2.1 Synthesis of $MoS_2$/G composite

Expanded $MoS_2$ (E-$MoS_2$) dispersion was prepared from commercial $MoS_2$ (C-$MoS_2$) via an expanded lithiation method [40] and the graphene oxide dispersion was achieved by a modified Hummers' method.[41] $MoS_2$/G composite ($MoS_2$/G) was synthesized by a facile hydrothermal method, followed by adding 60 mL E-$MoS_2$ aqueous dispersion (~ 3 mg/mL) and 30mL graphene oxides aqueous dispersion (~ 5 mg/mL). The obtained mixture was ultrasonicated for 3 min, and then loaded into Teflon-lined autoclaves, which were then sealed and maintained at 180 $^{o}$C for 5 h. After cooling down to room temperature naturally, the black product was centrifuged, washed three times each with deionized water and absolute ethanol, and dried under vacuum at 80 $^{o}$C overnight. The $MoS_2$/G was finally obtained after annealing treatment at 450 $^{o}$C for 2 h and then at 800 $^{o}$C for 2 h in a mixed 5 % $H_2$/Ar atmosphere.

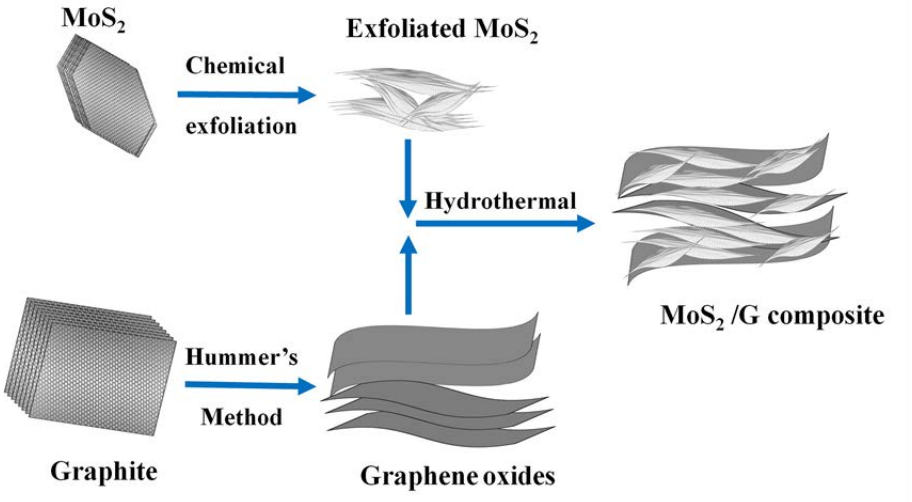


**Figure 7.1** Schematic diagram of synthesis method to prepare $MoS_2$/G composite via exfoliation and hydrothermal strategies.

### 7.2.2 Physical characterization

The morphologies of the samples were investigated by field-emission scanning electron microscopy (FESEM; JEOL JSM-7500FA) and transmission electron microscopy (TEM, JEOL 2011, 200 keV). The XRD patterns were collected by powder X-ray diffraction (XRD; GBC MMA diffractometer) with Cu Kα radiation at a scan rate of 0.5° $min^{-1}$ and 2° $min^{-1}$. Thermogravimetric analysis (TGA) was performed in air with a SETARAM Thermogravimetric Analyzer (France). Raman spectra were collected with a Jobin Yvon HR800 Ranman spectrometer with a 10 mW helium/neon laser at 632.8 nm excitation.

### 7.2.3 Electrochemical measurements

The electrochemical measurements were conducted by assembling coin-type half cells in an argon-filled glove box. The slurry was prepared by fully mixing 80 wt. % active materials, 10 wt. % carbon black, and 10 wt. % polyvinylidene difluoride (PVDF) using a planetary mixer (KK-250S). Then, the obtained slurry was pasted on a copper film by a doctor blade in a thickness of 100 μm, which was followed by drying in a vacuum oven overnight at 80 °C. The working electrode was prepared by punching the electrode film into discs 0.97 cm in diameter. Sodium foils were cut using a surgical blade from sodium bulk to act as both reference and counter electrode. The electrodes were separated by a glass fiber separator. The electrolytes were 1.0 M $NaClO_4$ in 1:1 (weight ratio) propylene carbonate (PC) / ethylene carbonate (EC*)* with 5 wt. % fluoroethylene carbonate (FEC) additive. The electrochemical performance was tested on a LAND Battery Tester.

### 7.3 Characterization of morphology and structure

As shown by the schematic illustration in Figure 7.2a, in spite of the large lattice mismatch between expanded $MoS_2$ and graphene, the $MoS_2$ layers are attached to the graphene sheets matrix, presumably via van der Waals interactions. Besides the unique properties mentioned above, more interestingly, the $MoS_2$/G interfaces show intriguing phenomena according to *ab initio* calculations,[42] which indicate an energetic preference for Li atom intercalation ($MoS_2$/Li/G), in comparison with Li atoms on the $MoS_2$ surface (Li/$MoS_2$ and Li/$MoS_2$/G), thus leading to higher Li storage capacity in the $MoS_2$/G composite. It is reasonable that the $MoS_2$/G interface

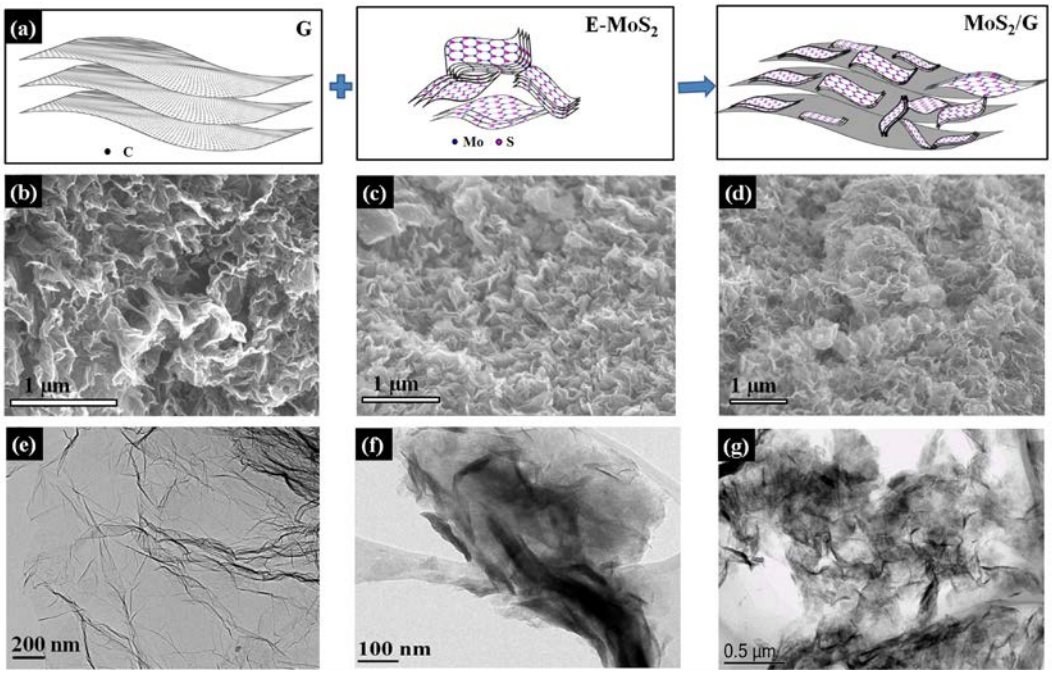


**Figure 7.2** Morphologies of graphene, E-$MoS_2$ and $MoS_2$/G composite: (a), Schematic illustrations of the synthesis of $MoS_2$/G composite; (b), (c), (d), SEM micrographs; (e), (f), (g), TEM micrographs of graphene, expanded $MoS_2$ and $MoS_2$/G composite.

is able to facilitate the accommodation of Na ions, exhibiting higher capacity than $MoS_2$. It can be seen that G, expanded $MoS_2$ and $MoS_2$/G composite show similar layered structures, and no significant morphological changes observed between $MoS_2$ and $MoS_2$/G composite. As shown in Figure 7.2b, the graphene sheets overlap each other with a crumpled structure, which allows plenty of free room between the graphene layers. The free room can accommodate the adherence of $MoS_2$ layers. Furthermore, the obtained graphene nanosheets are very thin and have a large size, as shown in Figure 7.2e, which implies that the graphene nanosheets are only stacked in a few layers and allow $MoS_2$ layers to be quite uniformly dispersed on their surface.

As could be seen in Figure 7.2c, there are $MoS_2$ bulks in the expanded $MoS_2$ (E-

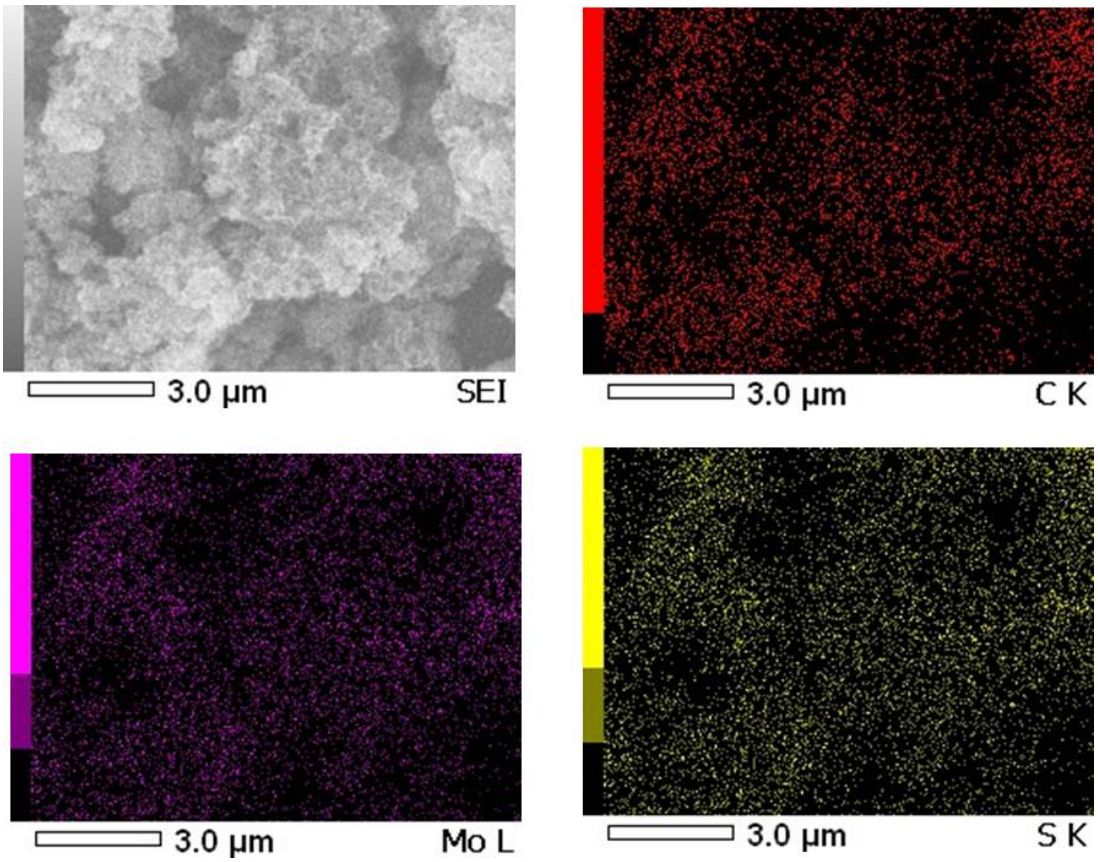


**Figure 7.3** Elemental mappings of C, $M_{O,}$ and S in $MoS_2$/G composite.

$MoS_2$), which are ascribed to the restacking/agglomeration effect of the exfoliated $MoS_2$ layers. In contrast, the $MoS_2$/G shown in Figure 7.2d has a much looser packing of nanosheets and presents a more transparent appearance. The TEM images in Figure 7.2f and g further confirm that the $MoS_2$ layers tend to adhere to the graphene sheets, hindering the restacking of exfoliated $MoS_2$. Elemental mappings (Figure 7.3) verify the even dispersion of $MoS_2$ layers on a graphene matrix.

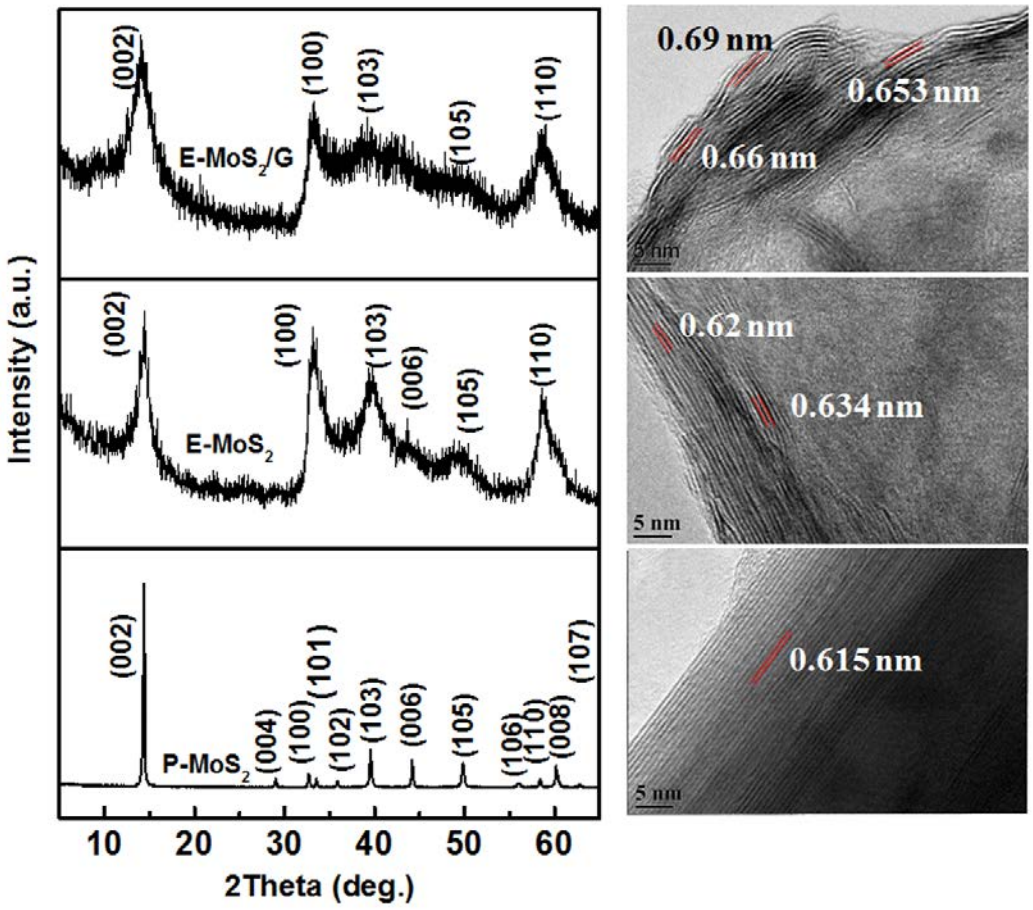


**Figure 7.4** XRD phase analyses and HRTEM characterization: XRD patterns and corresponding HRTEM micrographs of C-$MoS_2$ (bottom), E-$MoS_2$ (middle) and $MoS_2$/G composite (top)

The physical characteristics of C-$MoS_2$, E-$MoS_2$, and $MoS_2$/G were further observed by X-ray diffraction (XRD) analysis and high resolution transmission electron microscopy (HRTEM), respectively. The results in Figure 7.4 reveal that the incorporation of graphene can effectively inhibit the restacking/agglomeration of E-$MoS_2$ layers. In addition, it is noteworthy that the (002) diffraction peak of G cannot be detected in $MoS_2$/G, indicating that the graphene layers are separated by $MoS_2$ layers in the composite. All samples display a similar crystalline structure, congruent with a hexagonal structure (JPCDS No. 37–1492). In contrast to well crystallized C-$MoS_2$, E-$MoS_2$ and $MoS_2$/G present broadened and weakened peaks, indicating smaller crystallite size and a higher disordered degree of the $MoS_2$ layers after the exfoliation process. The *d*-spacing of the (002) planes can be calculated by the Bragg equation, which are 0.616, 0.621 and 0.630 nm (with the corresponding 2 $\theta$ values: 14.37, 14.20, 14.085), respectively. The HRTEM image of C-$MoS_2$ indicates a d-spacing is about 0.62 nm and the well stacking layers of $MoS_2$ layers are estimated to be more than 40. The lattice fringes of $MoS_2$ (E-$MoS_2$) and $MoS_2$/G are distorted and lattice distances are expanded to be ~ 0.63 and ~ 0.66 nm, respectively. In contrast to E-$MoS_2$ (<20 layers), $MoS_2$/G displays higher disordered degree with less restacking (<10 layers). Raman spectra of $MoS_2$/G, E-$MoS_2$, and G are illustrated in Figure 7.5a. In contrast to the E-$MoS_2$, the composite of presents the D-band and G-band of G at 1342 and 1593 $cm^{-1}$, respectively, confirming the existence of G in the composite. Thermogravimetric analysis (TGA) (Figure 7.5b) was carried out between 50-650 $^{o}$C in the air atmosphere to measure the ratio $MoS_2$ to graphene. The commercial $MoS_2$ was tested as well, which showed ~ 10 % weight loss due to the formation of $MoO_3$. Assuming the G can be completely burn out; the $MoS_2$ is estimated to be ~ 77 wt. % in the composite.

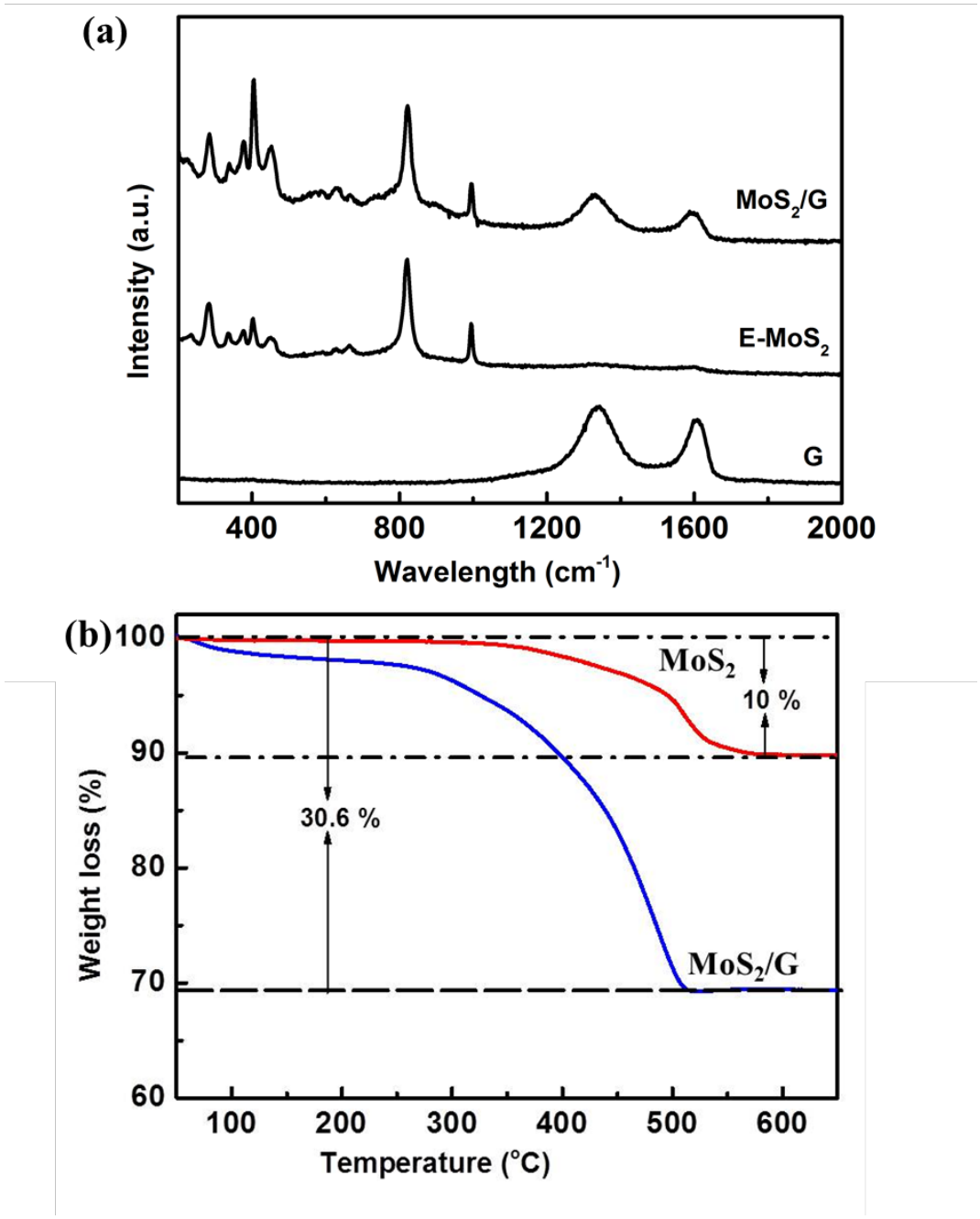


**Figure 7.5** (a) Raman spectrum of G, E-$MoS_2$, and $MoS_2$/G composites; (b) thermogravimetric analysis of curves of C-$MoS_2$ and $MoS_2$/G composites.

### 7.4 Electrochemical performance

In order to evaluate the sodium-ion storage properties of $MoS_2$/G, the electrochemical performance of sodium ion half-cell and pseudocapacitor were tested, respectively. As shown in Figure 7.6a, the half-cell is composed of $MoS_2$/G anode and Na plate separated by glass fiber separators. In contrast to C-$MoS_2$, $MoS_2$/G shows a dramatic enhancement on electrochemical performance (Figure 7.6), delivering a much better cycling stability and capacity retention of 81 % over 200 cycles at 100 mA $g^{-1}$ (0.25 C). The initial charge/discharge capacity is 386.0 and 604.3 mAh $g^{-1}$, respectively; the low Coulombic efficiency (~ 65 %) is mainly ascribed to the formation of solid electrolyte interphase (SEI) and the occurrence

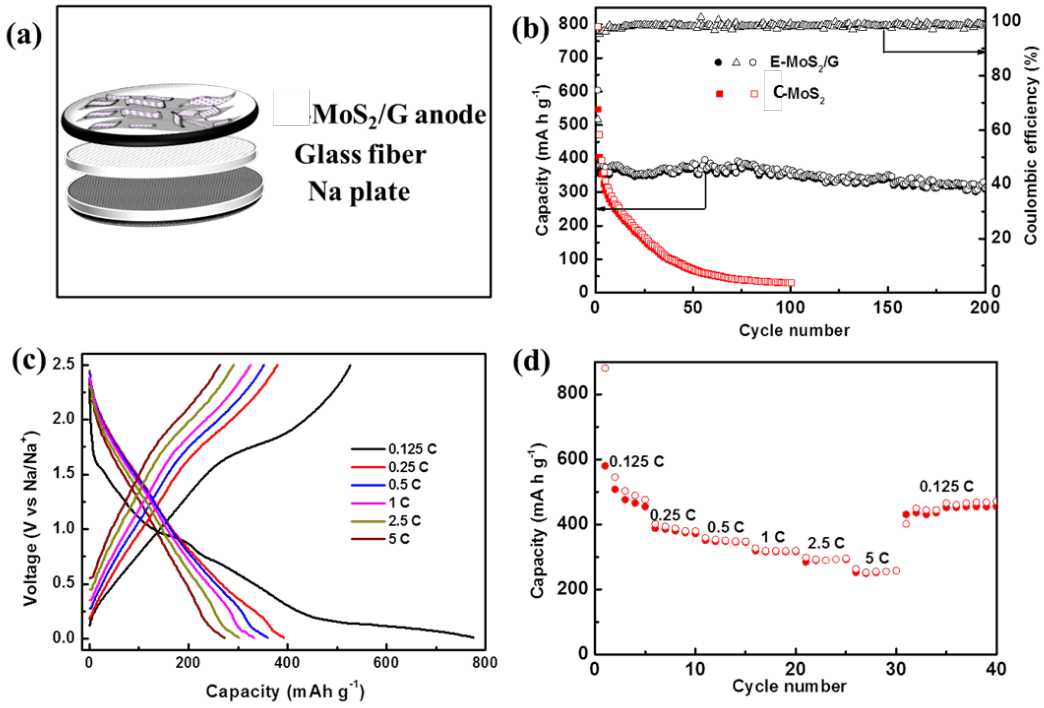


**Figure 7.6** Electrochemical performance of half cells**:** (a) schematic structure of sodium-ion battery; (b) cycling performance of C-$MoS_2$ and $MoS_2$/G composite at 100 mA $g^{-1}$ (0.25 C); and Coulombic efficiency of $MoS_2$/G composite; (c) charge/discharge curves and (d) rate capability of $MoS_2$/G at various current rate.

of irreversible reactions. The Coulombic efficiency retains above 97 %, implying that the mechanism acting in first cycle is possibly different from that in the subsequent cycles. Furthermore, excellent rate capability is achieved as shown in Figure 7.6c and d. It was tested at different current rate of 0.125, 0.25, 0.5, 1, 2.5, and 5 C, with the capacity corresponding to 491.7, 355.6, 327.8, 302.8, 280.6, and 247.2 mAh $g^{-1}$, respectively. Along with the increase in the current rate, interestingly, the charge/discharge curves show more obvious capacitive characteristics, with sloping curves and large voltage hysteresis. Thus, we can speculate that it is feasible to apply $MoS_2$/G in a capacitor system. The charge/discharge curves for the first discharge process show inconspicuous plateaus during 1.7-0.5 V, which disappear from the second cycle. This indicates a different mechanism in the following cycles. An obvious long plateau at about 0.3 V is observed, which implies that the reaction in this step is partially reversible in subsequent cycles. During the charge process, a conspicuous plateau occurs at about 1.85 V, which is corresponding to the redox reaction.

A Na-ion pseudocapacitor was constructed and examined. As shown in Figure 7.7a, the electrodes were sodium-doped $MoS_2$/G ($Na_nMoS_2$/G), which was prepared by galvanostatically discharging the half-cell from open circuit potential (OCP) to 0.01 V. Na ions were accommodated in the $MoS_2$ by the pre-sodiation process, which transformed $MoS_2$ into amorphous $Na_nMoS_2$. After disassembling two half-cells, the sodium-ion pseudocapacitor was reassembled into a coin-cell containing 1M $NaClO_4$ in propylene carbonate (PC) / ethylene carbonate (EC) + fluoroethylene carbonate (FEC) electrolyte, along with $Na_nMoS_2$/G positive and negative electrodes. The

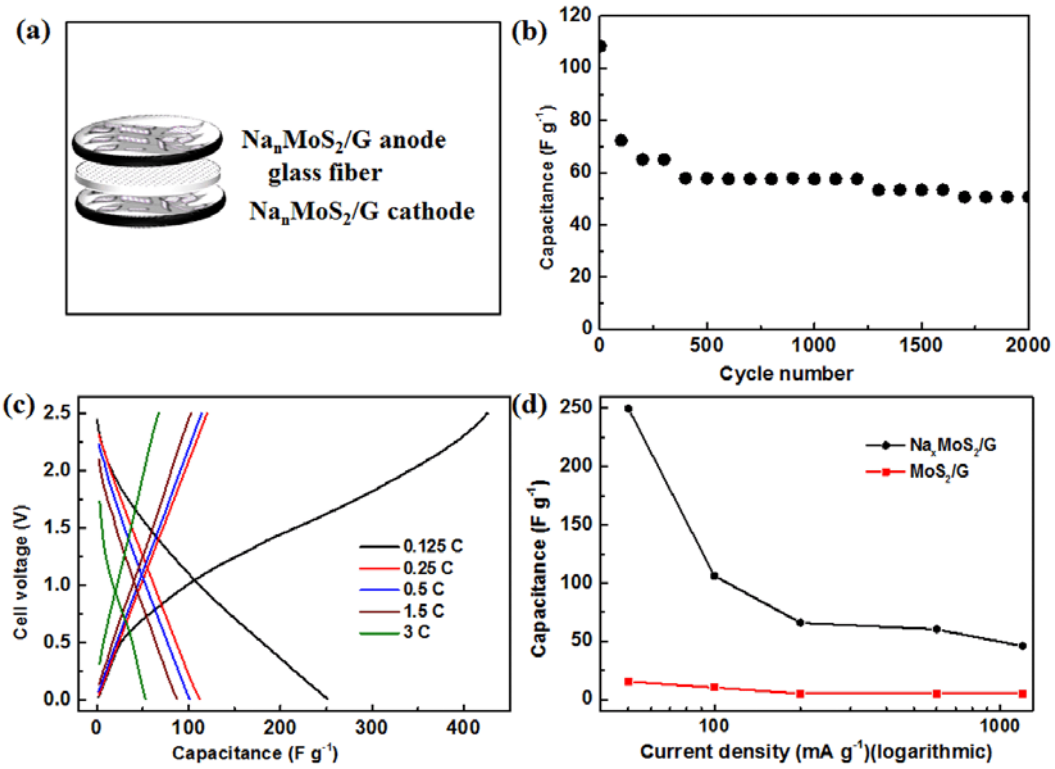


**Figure 7.7** Electrochemical performance of full cells**:** (a) schematic structure of sodium-ion pseduocapacitor; (b) capacitance of NICs at 1.5 C with prolonged cycling; (c) charge/discharge curves of NICs at various current rates; (d) comparison of capacitance between $MoS_2$ NICs and $Na_nMoS_2$ NICs at various current rates.

specific capacitance ($C_m$) of such full cell can be calculated by the following formula: $C_m = Q/\Delta V \times 3.6$, where $Q$ (mAh g$^{-1}$) represents the specific capacity; and $\Delta V$ (V) is the charge/discharge voltage variation (excluding the IR drop). As shown in Figure 7.6b, the NIC full cell showed excellent cycling performance over 2000 cycles with relatively stable capacitance (~ 50 F g$^{-1}$) at 1.5 C. The charge/discharge curves are shown in Figure 7.7c for different current rates. With increasing current rate from 50 to 1200 mA g$^{-1}$, the specific capacitance decreases from 250 to 45 F g$^{-1}$. It is noteworthy that the initial irreversible capacity is very high, which results from the irreversibility of the intercalation reaction of first cycle. Meanwhile, the NIC with

$MoS_2$/G and $MoS_2$/G electrodes was tested in comparison as shown in Figure 7.7d , which delivered a very low capacitance (5-15 F $g^{-1}$), similar to the energy density of electric double layer capacitors (EDLCs). It implies that only a non-faradaic reaction takes place in this capacitor. It is obvious that $Na_nMoS_2$/G NIC exhibits significantly higher capacitance than that of $MoS_2$/G, which arises from the occurrence of the faradaic reaction in the $Na_nMoS_2$/G NIC.

### 7.5 Na-storage mechanism

The Na-storage mechanism was deduced in detail by ex-situ XRD of C-$MoS_2$, based on its good crystallization and high intensity diffraction peaks. As shown in Figure 7.8a, C-$MoS_2$ shows similar charge/discharge curves to $MoS_2$/G (Figure 7.6c), demonstrating that they are likely to be subject to the same mechanism. In addition,

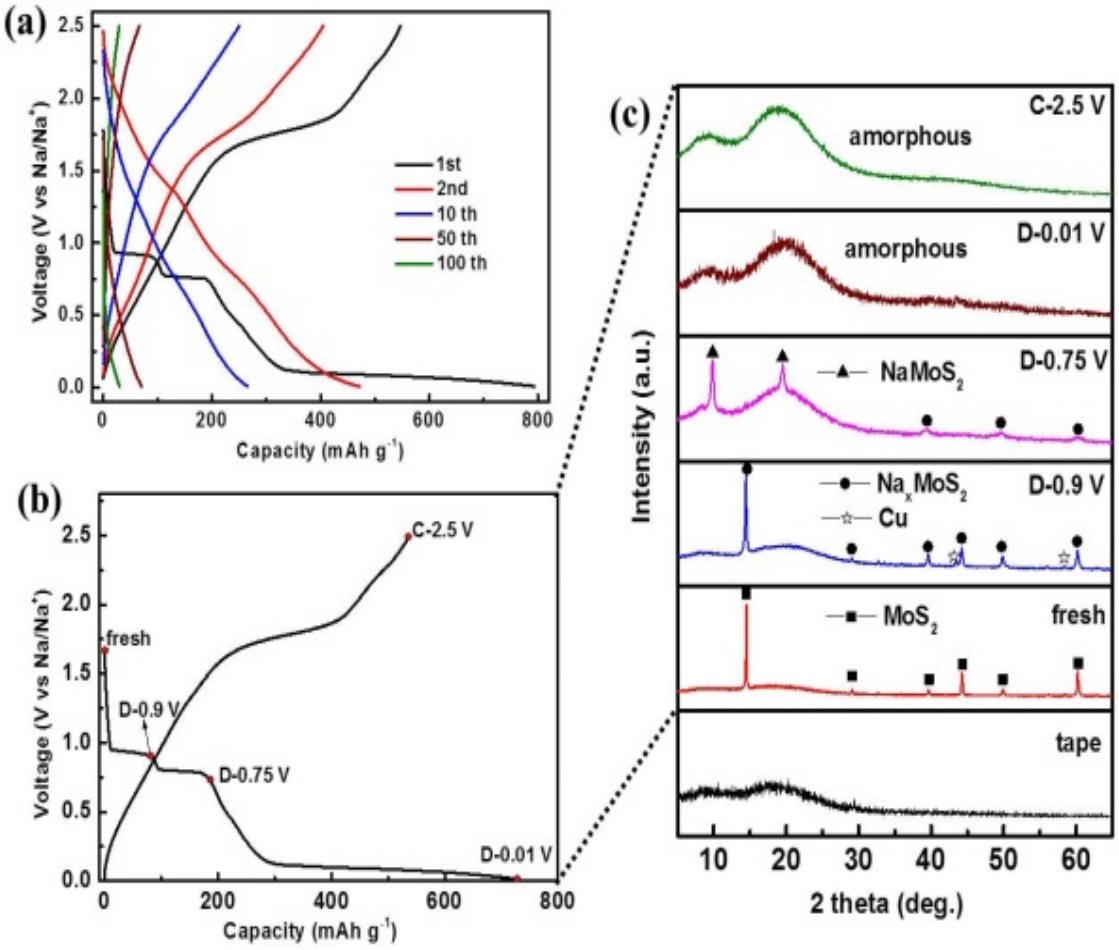


**Figure 7.8** Mechanism of Na storage in $MoS_2$**:** (a) charge/discharge curves of C-$MoS_2$ in different cycles at 100 mA $g^{-1}$; (b) first charge/discharge curves at specified states at 10 mA $g^{-1}$ and (c) corresponding *ex-situ* XRD patterns at a scan rate of 0.5$^o$ $min^{-1}$ for different states of C-$MoS_2$ in 1.0 M $NaClO_4$ with PC.

two pronounced plateaus at ~ 0.9 and ~ 0.75 V are observed in the first discharge profile, which is due to the ordered stacking of its layered structure and good crystallization. Powder samples of *ex-situ* XRD were collected by shaving off the electrode materials from the Cu current collectors under the respective corresponding conditions. *Ex-situ* XRD was conducted at five different states of charge and discharge as presented in Figure 7.8b and c. When discharged to 0.9 V, corresponding to the end of the first plateau, the (002) diffraction peak shows a slight shift towards lower angle. This indicates expansion of the interlayer spacing between the (002) planes due to Na ion intercalation into the layer sites of $MoS_2$. The specific capacity recorded at the end of this plateau was 84 mAh $g^{-1}$, which can be related to the formation of $Na_{0.5}MoS_2$. When the electrodes are discharged to 0.75 V, the diffraction peaks of 2H-$MoS_2$ are no longer observed. Two diffraction peaks appear at 9.54° and 19.8°, which are indexed to $NaMoS_2$ (JCPDS Card No. 18-1257). The capacity recorded after the second plateau is 175mAh $g^{-1}$, which is similar to the theoretical capacity of one $Na^+$ intercalation (167 mAh $g^{-1}$), confirming the formation of $NaMoS_2$. When fully discharged to 0.01 V, no obvious peaks can be observed, apart from two broadened peaks, which indicates the amorphous nature of the product $Na_{x+1}MoS_2$ ($x \leq 3$). There is no doubt that a conversion reaction takes place during this process, so the theoretical capacity should be 668.0 mAh $g^{-1}$ for the 4 $Na^+$ reactions. The capacity recorded is 720 mAh $g^{-1}$, with the exceed capacity mostly due to the formation of a SEI film. As the cells are discharged/charged at 0.01-2.5 V for 1 cycle, the diffraction pattern is amorphous, similar to that of the one discharged to 0.01 V, in agreement with the conversion reaction. The corresponding capacity is 535 mAh $g^{-1}$, which is equivalent to the desodiation of 3.2 $Na^+$ during the charge process, proving the irreversibility of the intercalation reaction (1 $Na^+$) and the high

reversibility of the conversion reaction. In addition, two Cu peaks at 43.4° and 58.4° can be observed in the XRD patterns, an impurity arises from the Cu current collector. Based on the ex-situ XRD analysis, the sodium storage mechanism of $MoS_2$ in sodium ion batteries can be summarized as follows:

1st discharge process:

1st plateau: intercalation reaction

$$MoS_2 + 0.5\ Na^+ + 0.5e^- \longrightarrow Na_{0.5}MoS_2 \qquad (7.1)$$

2nd plateau: intercalation reaction

$$Na_{0.5}MoS_2 + 0.5\ Na^+ + 0.5e^- \longrightarrow NaMoS_2 \qquad (7.2)$$

3rd plateau: conversion reaction

$$NaMoS_2 + xNa^+ + xe^- \longrightarrow 2\ Na_{x+1}MoS_2\ (x\leq 3) \qquad (7.3)$$

1st charge process: conversion reaction

$$Na_{x+1}MoS_2 \longrightarrow Na_{x-2}MoS_2 + 3\ Na^+ + 3e^- \qquad (7.4)$$

Subsequent cycles: conversion reaction

$$Na_{x-2}MoS_2 + yNa \underset{\text{Charge}}{\overset{\text{Discharge}}{\longleftrightarrow}} Na_{x+y-2}MoS_2\ (y\leq 3) \qquad (7.5)$$

As for the sodium-ion pseudocapacitors, the occurred reaction can be represented by:

$$Na_nMoS_2\ (n\leq 3) \leftrightarrow Na_{n-m}MoS_2 + mNa^+ + me^-\ (m<n) \qquad (7.6)$$

The Na doped $MoS_2$ ($Na_nMoS_2$) can provide more sodium ions for this system and ensure the conversion reaction take place in the following cycles. On the other hand,

the conversion reaction is highly reversible, and thus able to maintain long cycling life with good capacitance retention. In addition, the graphene matrix plays a key role in capacity/capacitance improvement in both systems, which can adsorb and desorb Na ions reversibly due to its large surface area and good electrical conductivity.

## 7.6 Conclusions

The graphene-like $MoS_2$/G composite was assessed with respect to its feasibility for Na-ion batteries and pseudocapacitors. The electrode is capable of delivering a high capacity of ~ 400 mAh $g^{-1}$ over 200 cycles. The low initial Coulombic efficiency and ex-situ XRD results confirm that the $MoS_2$ and Na undergo an irreversible intercalation reaction during the first charge, followed by a highly reversible conversion reaction. Interestingly, the conversion reaction, with typical high capacity and voltage hysteresis, can be applied in advanced NIC systems. In contrast to the $MoS_2$/G based capacitor, the capacitance of the $Na_nMoS_2$/G capacitor is significantly enhanced by 7 to 17 times at different currents, which is ascribed to the transformation of conventional EDLCs into advanced sodium-ion pseudocapacitors, so that the battery-like faradaic reaction can take place. Accordingly, we believe that $MoS_2$/G has great potential for Na storage due to its advantages of nanostructure and its reversible conversion reaction mechanism.

## 7.7 References


1 B. Dunn, H. Kamath, J.-M. Tarascon, *Science* 2011, *334*, 928-935.

2 M. Armand, J.-M. Tarascon, *Nature* 2008, *451*, 652-657.

3 M. Dubois, D. Billaud, *Journal of Solid State Chemistry* 1996, *127*, 123-125.

4 J. Barker, R. Gover, P. Burns, A. Bryan, *Electrochemical and Solid-State Letters* 2006, *9*, A190-A192.

5 Y. Cao, L. Xiao, W. Wang, D. Choi, Z. Nie, J. Yu, L. V. Saraf, Z. Yang, J. Liu, *Advanced Materials* 2011, *23*, 3155-3160.

6 R. Berthelot, D. Carlier, C. Delmas, *Nature Materials* 2011, *10*, 74-80.

7 D. Kim, S. H. Kang, M. Slater, S. Rood, J. T. Vaughey, N. Karan, M. Balasubramanian, C. S. Johnson, *Advanced Energy Materials* 2011, *1*, 333-336.

8 T. Kobayashi, Y. Kobayashi, M. Tabuchi, K. Shono, Y. Ohno, Y. Mita, H. Miyashiro, *ACS Applied Materials & Interfaces* 2013, *5*, 12387-12393.

9 W. Deng, X. Liang, X. Wu, J. Qian, Y. Cao, X. Ai, J. Feng, H. Yang, *Scientific Reports* 2013, *3*, 2671.

10 L. Zhu, Y. Shen, M. Sun, J. Qian, Y. Cao, X. Ai, H. Yang, *Chemical Communications* 2013, *49*, 11370-11372.

11 B. Ellis, W. Makahnouk, Y. Makimura, K. Toghill, L. Nazar, *Nature Materials* 2007, *6*, 749-753.

12 J. Zhao, J. He, X. Ding, J. Zhou, Y. o. Ma, S. Wu, R. Huang, *Journal of Power Sources* 2010, *195*, 6854-6859.

13 H. Kim, I. Park, D.-H. Seo, S. Lee, S.-W. Kim, W. J. Kwon, Y.-U. Park, C. S. Kim, S. Jeon, K. Kang, *Journal of The American Chemical Society* 2012, *134*, 10369-10372.

14 Z. Jian, L. Zhao, H. Pan, Y.-S. Hu, H. Li, W. Chen, L. Chen, *Electrochemistry Communications* 2012, *14*, 86-89.

15 Z. Jian, W. Han, X. Lu, H. Yang, Y. S. Hu, J. Zhou, Z. Zhou, J. Li, W. Chen, D. Chen, *Advanced Energy Materials* 2013, *3*, 156-160.

16 D. Stevens, J. Dahn, *Journal of The Electrochemical Society* 2000, *147*, 1271-1273.

17 S. Komaba, T. Ishikawa, N. Yabuuchi, W. Murata, A. Ito, Y. Ohsawa, *ACS Applied Materials & Interfaces* 2011, *3*, 4165-4168.

18 Y.-X. Wang, S.-L. Chou, H.-K. Liu, S.-X. Dou, *Carbon* 2013, *57*, 202-208.

19 L. Xiao, Y. Cao, J. Xiao, W. Wang, L. Kovarik, Z. Nie, J. Liu, *Chem. Commun.* 2012, *48*, 3321-3323.

20 Y.-X. Wang, Y.-G. Lim, M.-S. Park, S.-L. Chou, J. H. Kim, H.-K. Liu, S.-X. Dou, Y.-J. Kim, *Journal of Materials Chemistry A* 2014, *2*, 529-534.

21 Y. Denis, P. V. Prikhodchenko, C. W. Mason, S. K. Batabyal, J. Gun, S. Sladkevich, A. G. Medvedev, O. Lev, *Nature Communications* 2013, *4*.

22 D. Su, H.-J. Ahn, G. Wang, *Chemical Communications* 2013, *49*, 3131-3133 10.1039/c3cc40448j.

23 H. Pan, X. Lu, X. Yu, Y.-S. Hu, H. Li, X.-Q. Yang, L. Chen, *Advanced Energy Materials* 2013, *3*, 1186-1194.

24 Y. Sun, L. Zhao, H. Pan, X. Lu, L. Gu, Y.-S. Hu, H. Li, M. Armand, Y. Ikuhara, L. Chen, *Nature Communications* 2013, *4*, 1870.

25 Y. Wang, X. Yu, S. Xu, J. Bai, R. Xiao, Y.-S. Hu, H. Li, X.-Q. Yang, L. Chen, X. Huang, *Nature Communications* 2013, *4*.

26 L. Zhao, J. Zhao, Y. S. Hu, H. Li, Z. Zhou, M. Armand, L. Chen, *Advanced Energy Materials* 2012, *2*, 962-965.

27 J. Qian, X. Wu, Y. Cao, X. Ai, H. Yang, *Angewandte Chemie-International Edition* 2013, *52*, 4633-4636.

28 W.-J. Li, S.-L. Chou, J.-Z. Wang, H.-K. Liu, S.-X. Dou, *Nano Letters* 2013, *13*, 5480-5484.

29 P. Simon, Y. Gogotsi, *Nature Materials* 2008, *7*, 845-854.

30 M. D. Stoller, S. Park, Y. Zhu, J. An, R. S. Ruoff, *Nano Letters* 2008, *8*, 3498-3502.

31 K. Kuratani, M. Yao, H. Senoh, N. Takeichi, T. Sakai, T. Kiyobayashi, *Electrochimica Acta* 2012, *76*, 320-325.

32 Z. Chen, V. Augustyn, X. Jia, Q. Xiao, B. Dunn, Y. Lu, *ACS Nano* 2012, *6*, 4319-4327.

33 L. Ye, C. Wu, W. Guo, Y. Xie, *Chemical Communications* 2006, 4738-4740 10.1039/b610601c.

34 S.-K. Park, S.-H. Yu, S. Woo, B. Quan, D.-C. Lee, M. K. Kim, Y.-E. Sung, Y. Piao, *Dalton Transactions* 2013, *42*, 2399-2405.

35 J. Z. Wang, L. Lu, M. Lotya, J. N. Coleman, S. L. Chou, H. K. Liu, A. I. Minett, J. Chen, *Advanced Energy Materials* 2013, *3*, 798-805.

36 K. Chang, W. Chen, *ACS Nano* 2011, *5*, 4720-4728.

37 K. Chang, D. Geng, X. Li, J. Yang, Y. Tang, M. Cai, R. Li, X. Sun, *Advanced Energy Materials* 2013, *3*, 839-844.

38 J. Park, J.-S. Kim, J.-W. Park, T.-H. Nam, K.-W. Kim, J.-H. Ahn, G. Wang, H.-J. Ahn, *Electrochimica Acta* 2013, *92*, 427-432.

39 L. David, R. Bhandavat, G. Singh, *ACS Nano* 2014, *8*, 1759-1770.

40 R. Bissessur, P. K. Liu, S. F. Scully, *Synthetic Metals* 2006, *156*, 1023-1027.

41 W. S. Hummers Jr, R. E. Offeman, *Journal of the American Chemical Society* 1958, *80*, 1339-1339.

42 R. H. Miwa, W. L. Scopel, *Journal of Physics: Condensed Matter* 2013, *25*, 445301.

# CHAPTER 8 CONCLUSIONS AND OUTLOOK

## 8.1 General conclusions

A highly cost-efficient energy storage system, sodium-ion batteries, is currently capturing extensive attention with increasing worldwide energy demands. A bright and optimistic future is expected for the positive electrode side. In terms of the full cells, however, tough challenges remain for the negative electrode side to compete with the Li system. In this doctoral work, several promising anode materials have been investigated. Layered materials, such as graphite and graphite-like $MoS_2$, were proven to be capable of sodiation/desodiation via the exfoliation method. The anode materials featuring the conversion reaction are usually able to deliver high capacity in LIBs. Their counterparts were expected to deliver high capacity in NIBs, including $MoS_2$ and $SnO_2$. The effects of carbon matrixes, amorphous carbon, and reduced graphene oxide were studied in $MoS_2$/C, $MoS_2$/G and $SnO_2$/G nanocomposites, respectively. Constructing nanostructured materials is an important method for improving electrochemical Na-storage properties. Meanwhile, various electrolyte solutions were utilized to optimize the capacity and stability of those anode materials.

Reduced graphene oxide (RGO) was fabricated via the well-known Hummers' method, and it was applied as an anode in NIBs for the first time. Due to its properties, including high conductivity, large interlayer distance, and large surface area, RGO is capable of delivering a capacity of 140 mAh $g^{-1}$ over 1000 cycles, which is a significant improvement compared with inactive graphite. Even though the reversible capacity of RGO is too low for practical application, hard carbon is more promising with higher reversible capacity (> 300 mAh $g^{-1}$); it is a favourable

carbon matrix for the materials with low conductivity and big volume changes during charge/discharge processes.

Ultrafine $SnO_2$ nanoparticles (~ 5 nm) loaded on nanosheets of RGO were prepared via an environmentally friendly and facile hydrothermal method. Nanosized particles are vital for accelerating the reaction kinetics and promoting diffusion because of their short transport length. The unique nanostructure, formed with numerous nanovoids and excess space amongst the $SnO_2$ nanoparticles, is extremely favourable for tolerating the large volume changes during sodium alloying/dealloying reactions with Sn. On the other hand, the RGO framework can dramatically enhance the conductivity of the anode material. Furthermore, graphene nanosheets can effectively protect $SnO_2$ nanoparticles from agglomeration and pulverization. Of course, it is beneficial that the RGO framework is also suitable to accommodate sodium ions. As a result, a decent Na-storage performance with 330 mAh $g^{-1}$ over 150 cycles is achieved.

Graphene-like $MoS_2$/C composite was fabricated by simple chemical exfoliation and the hydrothermal method. In order to realize the superior electrochemical performance of $MoS_2$ in NIBs, several strategies were explored. Firstly, in order to accommodate large sodium ions, the interlayer distance of the (002) plane was enlarged by chemical exfoliation; the obtained graphene-like structure is favourable to shorten the Na-ion diffusion pathways and mitigate large volume changes. Furthermore, the carbon matrix, amorphous carbon, was introduced by the hydrothermal method, which can effectively increase electrode conductivity. As well as the efforts directed towards the nanostructure of the active materials, the applied electrolyte solutions received attention as well. The experimental results proved that the exfoliated $MoS_2$/C electrode in

electrolyte of 1.0 M $NaClO_4$ + PC/EC with 5 wt. % FEC could maintain an almost stable capacity of 390 mAh $g^{-1}$ over 100 cycles.

Considering the analogous structures of exfoliated $MoS_2$ and RGO, and the superior properties of RGO, $MoS_2$/G composite was synthesised by attaching $MoS_2$ layers on a graphene sheet matrix, likely via van der Waals interactions. Three-dimensional (3D) architectures of $MoS_2$/G composite offer high specific surface area and mechanical strength, and fast mass transport kinetics. More importantly, it was reported that $MoS_2$/G composite possesses synergistic effects between the layered $MoS_2$ and the graphene, thereby enhancing the reversible capacity and cycling stability of the electrode. The conversion reaction mechanism of $MoS_2$/G composite featured high capacity, and obvious voltage hysteresis was applied in a sodium-ion pseudocapacitor. The sodium-ion capacitor (NIC) full cell delivers excellent cycling performance over 2000 cycles with relatively stable capacitance (~ 50 F $g^{-1}$) at 1.5 C. Moreover, the Na-storage mechanisms of $MoS_2$ were investigated thoroughly by *ex-situ* XRD, which confirmed that the mechanism is the intercalation reaction for the first discharge process, followed by reversible conversion reactions for subsequent cycles.

The materials in this thesis are generally nanosized and possess larger surface area and more active sites than their bulk counterpart, which enable more electrolytes to decompose and result in more and thicker SEI film. Moreover, in case of reduced graphene oxides, there are residual carboxyl and hydroxyl functional groups, which would irreversibly react with Na ions, leading to low Coulombic efficiency as well. It is obvious that the superior electrochemical performance of nanosized materials need to compromise with lower initial Coulombic efficiency. Of course, there is a balance

point between them. To improve initial Coulombic efficiency, it is the most direct strategy is to decrease the surface area of active materials. For RGO materials, we can decrease the surface area and realize high quality of reduction by increasing the heat-treatment temperature, such as 600, 800 $^{o}$C instead of 450 $^{o}$C in our work. This strategy is feasible for $SnO_2$/RGO nanocomposite, it is favourable to further treat the obtained $SnO_2$/RGO in tube furnace at high temperature (~ 450 $^{o}$C) with Ar atmosphere. On the other hand, it should be pointed that the agglomeration of $SnO_2$ nanoparticles would get more serious with higher temperature. It is also easy to decrease the nanosized degree of $MoS_2$/C and $MoS_2$/G samples via weaken the exfoliation process, which could be achieved by utilizing less n-butyl lithium, applying less reaction time, and decreasing the sonication time. Likewise, high-temperature treatment can result in low surface area with the occurrence of stacking and agglomeration.

## 8.2 Outlook

For practical applications, hard carbon is one of the most promising anodes for commercial NIBs, even though its volumetric energy density is smaller than that of graphite in LIBs. Another potential candidate is titanium oxide, which is expected to deliver higher volumetric energy density due to its higher density. The solid electrolyte interphase (SEI) film is an important issue to address on the anode side. Passivation of the material surface is beneficial to maintain cycling stability, while leading to low Coulombic efficiency. Comprehensive studies, including electrolyte solutions, additives, and binders to effectively passivate the surface of oxides and carbonaceous materials added as a conductive agent, which are exposed to the highly reducing conditions, are needed. More anodes based on the alloying/dealloying mechanism, such as phosphorus, hold a great promise with high capacity, but alleviating their large volume change is the toughest challenge. In contrast, for the anodes with the conversion reaction, the lower initial Coulombic efficiency is the biggest barrier to their commercialization.

For application in electrical energy storage (EES), the selection of electrodes is supposed to be based on cost (elemental abundance). Due to the natural abundance of Fe and Mn, P2-type $Na_x[Fe_{1/2}Mn_{1/2}]O_2$ delivers approximately 190 mAh $g^{-1}$ of reversible capacity and is one candidate as a positive electrode material for EES, even though compensation for deficient sodium ions is needed to achieve full capacity.

The electrolyte plays a role in the possible interfaces to the electrodes, deciding the electrochemical stability window of the cell, and thereby affecting full cell performance. $NaClO_4$ is commonly used for academic research because of its cost.

$NaPF_6$ is relatively safe and enables comparisons with many LIB studies. Solvents such as EC, DEC, and PC are utilized in NIBs as these solvents are used in LIB electrolyte. Systematic research on the potential electrolytes for NIBs is urgently required and of great value.

It is anticipated that the demonstration of NIBs as rechargeable batteries at the industrial level will start in the near future, even though we still have many tough challenges. Competing with the state-of-the-art and high-energy LIBs (graphite/$LiCoO_2$ system) does not seem to be easy, especially in the case of the volumetric energy density. Innovations in materials are still needed. Nevertheless, sodium-ion-based technology has great advantages for both high-power and cost-effective systems, as discussed in this review. NIBs can be potentially be used as battery systems for hybrid electric vehicles and electrical energy storage, which requires high-power and cost-effective batteries, respectively, if the cycle life of batteries and the safety are competitive with the lithium system. It is believed that NIBs will become a vital rechargeable battery system in our daily lives, complementarily to the high-energy lithium system.

## APPENDIX A: LIST OF PUBLICATIONS

1. **Y.-X. Wang,** K. H. Seng, S.-L. Chou, Z. Guo, D. Wexler, H.-K. Liu, S.-X. Dou. Reversible sodium storage *via* conversion reaction of a $MoS_2$–C composite; *Chemical Communications* 2014, 50 (73), 10730-10733; **Citations: 10; Impact Factor: 6.718.**
2. **Y.-X. Wang,** S.-L. Chou, D. Wexler, H.-K. Liu, S.-X. Dou. High-performance sodium-Ion batteries and sodium-ion pseudocapacitors based on $MoS_2$/graphene composites; *Chemistry-A European Journal* 2014, 20, 9607-9612; **Citations: 5; Impact Factor: 5.696.**
3. **Y.-X. Wang,** Y.-G. Lim, M.-S. Park, S.-L. Chou, J. H. Kim, H.-K. Liu, S.-X. Dou, Y.-J. Kim. Ultrafine $SnO_2$ nanoparticle loading onto reduced graphene oxide as anodes for sodium-ion batteries with superior rate and cycling performance; *Journal of Materials Chemistry A* 2014, 2 (2), 529-534; **Citations: 47； Impact Factor: Pending.**
4. **Y.-X. Wang,** S.-L. Chou, H.-K. Liu, S.-X. Dou. Reduced graphene oxide with superior cycling stability and rate capability for sodium storage; *Carbon* 2013, 57, 202-208; **Citations: 58; Impact Factor: 6.160.**
5. **Y.-X. Wang,** S.-L. Chou, H.-K. Liu, S.-X. Dou. The electrochemical properties of high-capacity sulfur/reduced graphene oxide with different electrolyte systems; *Journal of Power Sources* 2013, 244, 240-245; **Citations: 12; Impact Factor: 5.211.**
6. **Y.-X. Wang,** S.-L. Chou, J. H. Kim, H.-K. Liu, S.-X. Dou. Nanocomposites of silicon and carbon derived from coal tar pitch: Cheap anode materials for lithium-ion batteries with long cycle life and

enhanced capacity; *Electrochimica Acta* 2013, 93, 213-221; **Citations: 15; Impact Factor: 4.086.**

7. **Y.-X. Wang,** L. Huang, L.-C. Sun, S.-Y. Xie, G.-L. Xu, S.-R. Chen, Y.-F. Xu, J.-T. Li, S.-L. Chou, S.-X. Dou, S.-G. Sun. Facile synthesis of a interleaved expanded graphite-embedded sulfur nanocomposite as cathode of Li–S batteries with excellent lithium storage performance; *Journal of Materials Chemistry* 2012, 22 (11), 4744-4750; **Citations: 91; Impact Factor: 6.626.**

**8.** S.-L. Chou, **Y.-X. Wang,** J. Xu, J.-Z. Wang, H.-K. Liu, S.-X. Dou. A hybrid electrolyte energy storage device with high energy and long life using lithium anode and $MnO_2$ nanoflake cathode； *Electrochemistry Communications* 2013, 31, 35-38; **Citations: 9; Impact Factor: 4.287.**

**9.** C. Zhao, S.-L. Chou, **Y.-X. Wang,** C. Zhou, H.-K. Liu, S.-X. Dou. A facile route to synthesize transition metal oxide/reduced graphene oxide composites and their lithium storage performance; *RSC Advances* 2013, 3 (37), 16597-1660; **Citations: 18; Impact Factor: 3.708.**

**10.** F.-X. Xiang, X.-L. Wang, X. Xun, K. S. B. De Silva, **Y.-X. Wang**, S.-X. Dou; Evidence for transformation from $\Delta T_c$ to $\Delta \ell$ pinning in $MgB_2$ by graphene oxide doping with improved low and high field $J_c$ and pinning potential; *Applied Physics Letters* 2013, 102, 152601; **Citations: 3; Impact Factor: 3.515.**

## Contributions statement

Y.X.W. conducted the experiments and wrote the main manuscripts for all the first-author papers. Y.X.W. did the experiments of electrochemical performance for the second-author and third-author papers. Y.X.W. supplied graphene oxide materials for the last co-author paper in the publication list.

## APPENDIX B: AWARDS RECEIVED

1 ISEM Postgraduate Student Excellence Award, University of Wollongong, 2014.

2 Chinese government scholarship, China Scholarship Council, 08/2011-08/2014.

3 Top-up scholarship, University of Wollongong, 08/2011-until now.